

USAAMRDL-TR- 75-37

12  
DH



## AXIAL-CENTRIFUGAL COMPRESSOR PROGRAM

General Electric Company  
Aircraft Engine Group  
1000 Western Ave.  
Lynn, Mass. 01910

ADA 018078

October 1975

Approved for public release;  
distribution unlimited.

DEC 9 1975  
RECEIVED  
A

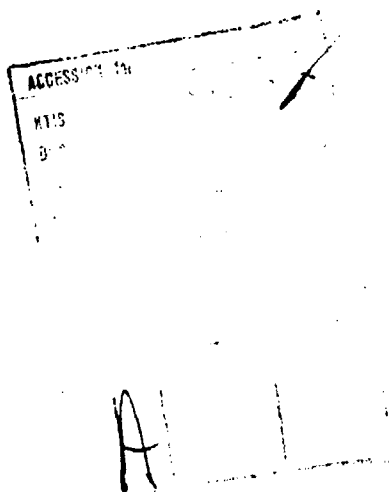
Prepared for

EUSTIS DIRECTORATE  
U. S. ARMY AIR MOBILITY RESEARCH AND DEVELOPMENT LABORATORY  
Fort Eustis, Va. 23604

EUSTIS DIRECTORATE POSITION STATEMENT

This report documents a step in evolving advanced gas turbine engine compressor technology. While the demonstrated compressor performance fell short of the contractual targets, basic data are provided on the matching and performance of a small, highly loaded machine and are considered to be useful as such. The results of this program will be factored into future Eustis Directorate engine cycle analysis efforts.

Robert A. Langworthy of the Propulsion Technical Area, Technology Applications Division served as project engineer for this effort.



DISCLAIMERS

The findings in this report are not to be construed as an official Department of the Army position unless so designated by other authorized documents.

When Government drawings, specifications, or other data are used for any purpose other than in connection with a definitely related Government procurement operation, the United States Government thereby incurs no responsibility nor any obligation whatsoever; and the fact that the Government may have formulated, furnished, or in any way supplied the said drawings, specifications, or other data is not to be regarded by implication or otherwise as in any manner licensing the holder or any other person or corporation, or conveying any rights or permission, to manufacture, use, or sell any patented invention that may in any way be related thereto.

Trade names cited in this report do not constitute an official endorsement or approval of the use of such commercial hardware or software.

DISPOSITION INSTRUCTIONS

Destroy this report when no longer needed. Do not return it to the originator.

UNCLASSIFIED

SECURITY CLASSIFICATION OF THIS PAGE (When Data Entered)

REPORT DOCUMENTATION PAGE		READ INSTRUCTIONS BEFORE COMPLETING FORM
1. REPORT NUMBER <b>18</b> USAAMRDL TR-75-37	2. GOVT ACCESSION NO.	3. RECIPIENT'S CATALOG NUMBER
4. TITLE (and Subtitle) <b>6</b> AXIAL-CENTRIFUGAL COMPRESSOR PROGRAM,	5. TYPE OF REPORT & PERIOD COVERED <b>12</b> 275 p.	
7. AUTHOR(s) <b>10</b> Lawrence W./Blair David J./Tapparo	8. CONTRACT OR GRANT NUMBER(s) <b>15</b> DAAJ02-71-C-0050	
9. PERFORMING ORGANIZATION NAME AND ADDRESS General Electric Company Aircraft Engine Group 1000 Western Ave. Lynn, Mass. 01910	10. PROGRAM ELEMENT, PROJECT, TASK AREA & WORK UNIT NUMBERS 62207A 1G162207AA7102 004EK	
11. CONTROLLING OFFICE NAME AND ADDRESS Eustis Directorate U.S. Army Air Mobility R & D Laboratory Fort Eustis Directorate, Va. 23604	12. REPORT DATE <b>11</b> Oct 1975	
14. MONITORING AGENCY NAME & ADDRESS (if different from Controlling Office)	13. NUMBER OF PAGES 273	
	15. SECURITY CLASS. (of this report) Unclassified	
16. DISTRIBUTION STATEMENT (of this Report) Approved for public release; distribution unlimited. <b>14</b> DA-1-G-162207-AA-711		
17. DISTRIBUTION STATEMENT (of the abstract entered in block 20, if different from Report) <b>17</b> 1-G-162207-AA-1102		
18. SUPPLEMENTARY NOTES		
19. KEY WORDS (Continue on reverse side if necessary and identify by block number) Axial-Centrifugal Compressors Axial Stage Centrifugal Stage Instrumentation Fabrication Test		
20. ABSTRACT (Continue on reverse side if necessary and identify by block number) This report presents the component test results and analysis for Phases III, IV and V of the 5-lb/sec axial-centrifugal compressor. Separate component tests were carried out to evaluate the two-stage axial compressor, the centrifugal compressor, and the combined axial-centrifugal compressor. Additional static blow tests were also conducted on the axial and centrifugal stage inlet guide vanes to determine their performance characteristics.		

DD FORM 1 JAN 73 1473

EDITION 1 NOV 65 IS OBSOLETE

UNCLASSIFIED

SECURITY CLASSIFICATION OF THIS PAGE (When Data Entered)

NOV 75

DN  
402299

UNCLASSIFIED

SECURITY CLASSIFICATION OF THIS PAGE(When Data Entered)

20. Continued

The assembly procedure, buildup clearances, and test procedure are described herein, as well as the instrumentation, data reduction procedure, and test facilities. The test results are presented for all component tests carried out in this program as well as for tests from a related centrifugal compressor development program. The analysis of the test results are reported herein as well as recommendations for future development programs.

This program demonstrated the feasibility of designing a 5-lb/sec, two-stage axial-centrifugal compressor in the 15:1 pressure ratio class and provided insight into the matching of axial-centrifugal compressors.

UNCLASSIFIED

SECURITY CLASSIFICATION OF THIS PAGE(When Data Entered)

## PREFACE

This axial-centrifugal compressor program was carried out for the Eustis Directorate, U.S. Army Air Mobility Research and Development Laboratory (Contract DAAJ02-71-C-0050, Task 1G162207AA7102) in five distinct phases:

1. Phase I - Parametric Study.
2. Phase II - Design.
3. Phase III - Fabrication and Test.
4. Phase IV - Evaluation.
5. Phase V - Redesign and Test.

This report presents the Phase III, IV, and V results of the fabrication, evaluation, and test of the axial, centrifugal, and axial-centrifugal compressor configurations.

We wish to acknowledge other personnel in the General Electric Aircraft Engine Group who have made significant contributions to this program: A. Brooks as overall program manager, L.H. King and A.C. Bryans on the aerodynamic design, Dr. A.I. Bellin and his staff on the mechanical design, and Roger Kress on the vehicle design and fabrication. In the Evaluations and Test Operation we wish to recognize the Evendale Testing under W.T. Martin, Jr. and the Lynn Testing under L. Ottaviano. We also wish to thank Robert Langworthy of the Eustis Directorate for his timely assistance and constructive guidance.

TABLE OF CONTENTS

	<u>Page</u>
PREFACE . . . . .	3
LIST OF ILLUSTRATIONS . . . . .	7
LIST OF TABLES. . . . .	17
INTRODUCTION. . . . .	19
PROGRAM CHRONOLOGY. . . . .	23
FABRICATION OF TEST HARDWARE. . . . .	30
Axial Component Test Vehicle (ACV) . . . . .	30
Centrifugal IGV Blow Test Vehicle. . . . .	37
Axial IGV Blow Test Vehicle. . . . .	39
Centrifugal Component Test Vehicle . . . . .	41
Combined Compressor Test Vehicle (FCV-I) . . . . .	44
Combined Compressor Test Vehicle (FCV-II). . . . .	48
INSTRUMENTATION . . . . .	50
Vehicular Instrumentation. . . . .	50
Aerodynamic Instrumentation. . . . .	53
IGV Blow Test. . . . .	66
Blade and Vane Strain Gages. . . . .	69
TEST EQUIPMENT AND PROCEDURE. . . . .	75
Compressor Drives. . . . .	75
Stator Actuation . . . . .	75
Lubrication Systems. . . . .	78
Thrust Balance System. . . . .	79
Compressor Bleed Control . . . . .	81
Inlet Temperature and Pressure Control System. . . . .	82
Data Acquisition Systems . . . . .	83
COMPRESSOR DATA REDUCTION . . . . .	85
Stage Performance. . . . .	85
Traverse Data. . . . .	86
TEST RESULTS. . . . .	88
Axial Compressor Test (ACV). . . . .	88
Centrifugal IGV Blow Test. . . . .	132
Axial IGV Blow Test. . . . .	141

TABLE OF CONTENTS - Continued

	<u>Page</u>
Centrifugal Compressor Test (CCV-I) . . . . .	151
Combined Compressor Test (FCV-I) . . . . .	177
Combined Compressor Test (FCV-II) . . . . .	196
RELATED CENTRIFUGAL COMPRESSOR PROGRAM. . . . .	218
Centrifugal Aerodynamic Design . . . . .	218
CCV-II Compressor Design . . . . .	221
CCV-III Compressor Design. . . . .	221
CCV-IV Compressor Design . . . . .	227
CCV-V Compressor Design. . . . .	227
PHASE V MATCHING STUDIES. . . . .	242
CONCLUSIONS . . . . .	244
RECOMMENDATIONS . . . . .	247
REFERENCES. . . . .	248
APPENDIX - TEST DATA TABLES . . . . .	249
LIST OF SYMBOLS . . . . .	271

LIST OF ILLUSTRATIONS

<u>Figure</u>		<u>Page</u>
1	Axial-Centrifugal Compressor Program Schedule . . . . .	24
2	Compressor Performance at 10% Stall Margin. . . . .	29
3	Compressor Stator Assembly. . . . .	31
4	Axial Compressor Rotor Assembly . . . . .	33
5	Tie Bolt. . . . .	34
6	Axial Compressor Rotor Assembly Runouts . . . . .	34
7	CCV Blow Test Setup . . . . .	38
8	Axial Blow Test Setup . . . . .	40
9	Centrifugal Compressor Test Impeller. . . . .	42
10	Centrifugal Compressor Impeller Shroud. . . . .	42
11	Centrifugal Compressor Diffuser . . . . .	43
12	Centrifugal Compressor Deswirl Vane Row and Vane Cover. . . . .	43
13	Axial Compressor Casing Inserts . . . . .	44
14	Sketch of Stage 1 and Stage 2 Blisk Contour Forging Outline . . . . .	45
15	Titanium Blisk Redesign . . . . .	46
16	FCV-I Strain Gage Lead Wire Routing . . . . .	47
17	Rework of Impeller Leading Edge . . . . .	49
18	Load Cell . . . . .	51
19	Load Cell Calibration . . . . .	51
20	Compressor Skin Thermocouples . . . . .	52
21	Axial-Centrifugal Compressor Instrumentation Planes . . . . .	55

LIST OF ILLUSTRATIONS - Continued

<u>Figure</u>		<u>Page</u>
22	Wake Rake . . . . .	58
23	Unwrapped Casing Drawing. . . . .	59
24	ACV Centrifugal Inlet Instrumentation Locations . . .	61
25	Centrifugal Static Pressures - CCV-I and FCV-I. . . .	62
26	Plane E Total Pressure Rake . . . . .	64
27	Plane E Total Temperature Rake. . . . .	64
28	Plane E Instrumentation . . . . .	65
29	Cobra Probe . . . . .	66
30	Bellmouth Airflow . . . . .	67
31	Axial Outlet Traverse Setup . . . . .	68
32	Axial Outlet Traverse Modes . . . . .	70
33	ACV Stator Strain Gage Locations. . . . .	71
34	FCV Stator Strain Gage Locations. . . . .	72
35	FCV Rotor Strain Gage Locations . . . . .	73
36	Strain Gage Locations - Stress Distribution . . . . .	74
37	Aero Component Test Facility Layout - Cell A9 . . . .	76
38	Stator Vane Actuation System Schematic. . . . .	77
39	FCV-I Vane Tracking Schedule. . . . .	78
40	Lynn Thrust Balance System Schematic. . . . .	80
41	Air Refrigeration System Schematic. . . . .	82
42	Maximum Allowable Bearing and Sump Temperature Differential. . . . .	92
43	Campbell Diagram for ACV Stage 1 and 2 Blades - 1st Mode. . . . .	94

LIST OF ILLUSTRATIONS - Continued

<u>Figure</u>		<u>Page</u>
44	Campbell Diagram for ACV Stage 1 Blades - Higher Modes. . . . .	95
45	Campbell Diagram for ACV Stage 2 Blades - Higher Modes. . . . .	96
46	Campbell Diagram for IGV. . . . .	97
47	Campbell Diagram for Stage 1 Vane . . . . .	98
48	Campbell Diagram for Stage 2 Vane . . . . .	99
49	Aft Bearing Stress Spectrum - 8-1/3 Hours Total Time. . . . .	101
50	Aft Bearing Stress Spectrum - 38-1/2 Hours Total Time. . . . .	102
51	Failed Thrust Bearing . . . . .	103
52	Closeup of Bearing Inner Race Damage. . . . .	103
53	Closeup of Ball and Cage Damage . . . . .	104
54	Aft Bearing Housing and Lube Jets . . . . .	104
55	Front View of Failed Compressor . . . . .	107
56	Outer Casing View Showing Damaged IGV Levers. . . . .	107
57	Damaged Rotor and Casing Hardware . . . . .	108
58	Stator Casing Half (FLA). . . . .	110
59	Stator Casing Half (ALF). . . . .	110
60	SEM Examination of Stage 1 Blade Stub - 1000 X Magnification. . . . .	112
61	Fatigue Striations in A286 Material - 5000 X Magnification. . . . .	112
62	ACV-I Axial Compressor Performance Nominal Stator Schedule . . . . .	116

LIST OF ILLUSTRATIONS - Continued

<u>Figure</u>		<u>Page</u>
63	Axial Compressor Performance - 100% Speed. VG Optimization . . . . .	117
64	Axial Compressor Performance - 95% Speed, VG Optimization . . . . .	118
65	Axial Compressor Performance - 85% Speed, VG Optimization . . . . .	119
66	Axial Compressor Performance - Low Speed. . . . .	120
67	Axial Compressor Performance - Optimum Stator Schedule . . . . .	121
68	FCV-I Stator Schedule A . . . . .	122
69	Axial Compressor Effectivity - 100% Speed . . . . .	123
70	Axial Compressor Effectivity - 95% Speed. . . . .	123
71	Axial Compressor Effectivity - 85% Speed. . . . .	124
72	Axial Compressor Normalized Stage Characteristics - 100% Corrected Speed. . . . .	126
73	Axial Compressor Normalized Stage Characteristics - 95% Corrected Speed . . . . .	127
74	Axial Compressor Normalized Stage Characteristics - 85% Corrected Speed . . . . .	128
75	Axial Compressor Static Pressure Distribution - 100% Corrected Speed. . . . .	130
76	ACV-I Plane C Traverse Data . . . . .	131
77	ACV-I Plane C Traverse Data . . . . .	131
78	ACV-I Plane C Traverse Data . . . . .	132
79	Total $\Delta P/P$ and Absolute Angle vs Annulus Height . . .	134
80	Total $\Delta P/P$ and Absolute Angle vs Annulus Height . . .	134

LIST OF ILLUSTRATIONS - Continued

<u>Figure</u>		<u>Page</u>
81	Total $\Delta P/P$ and Absolute Angle vs Annulus Height . . .	135
82	Total $\Delta P/P$ and Absolute Angle vs Annulus Height . . .	135
83	Total $\Delta P/P$ and Absolute Angle vs Annulus Height . . .	136
84	Total $\Delta P/P$ and Absolute Angle vs Annulus Height . . .	136
85	Total $\Delta P/P$ and Absolute Angle vs Annulus Height . . .	137
86	Total $\Delta P/P$ and Absolute Angle vs Annulus Height . . .	137
87	Total Pressure Recovery Factor vs Corrected Inlet Flow . . . . .	138
88	Wall Static Pressure Ratio vs Axial Distance Along Duct. . . . .	140
89	Angle Data Match for Block I Duct . . . . .	140
90	Absolute Air Angle at Rotor 1 Inlet . . . . .	142
91	Inlet to First Rotor Pressure Loss. . . . .	142
92	Axial IGV Blow Test - 4.5% Immersion. . . . .	143
93	Axial IGV Blow Test - 19.7% Immersion . . . . .	143
94	Axial IGV Blow Test - 42.0% Immersion . . . . .	144
95	Axial IGV Blow Test - 67.8% Immersion . . . . .	144
96	Axial IGV Blow Test - 91.0% Immersion . . . . .	145
97	Rotor 1 Inlet Air Angle - Tip . . . . .	145
98	Rotor 1 Inlet Air Angle - Pitch . . . . .	146
99	Rotor 1 Inlet Air Angle - Hub . . . . .	146
100	Axial IGV Total Pressure Loss . . . . .	147

LIST OF ILLUSTRATIONS - Continued

<u>Figure</u>		<u>Page</u>
101	Axial Blow Test - Outlet Angle Contours. . . . .	148
102	IGV Blow Test - Outlet Angle Contours. . . . .	149
103	IGV Blow Test - Pressure Loss Contours . . . . .	150
104	Load Cell Strain Gage Wiring . . . . .	153
105	Campbell Diagram for Impeller Vane . . . . .	154
106	Centrifugal Compressor Inlet Guide Vane Nodal Patterns and Natural Frequencies. . . . .	155
107	Campbell Diagram for Centrifugal Compressor Inlet Guide Vane . . . . .	156
108	Centrifugal Compressor Performance Map for Various IGV Settings . . . . .	157
109	Centrifugal Compressor Choke Flow vs Corrected Speed - Nominal IGV Setting. . . . .	159
110	Shroud Normalized Static Pressure vs Meridional Distance - 100% Speed (Throttle). . . . .	159
111	Shroud Normalized Static Pressure vs Meridional Distance - 100% Speed (Effect of IGV) . . . . .	160
112	Shroud Normalized Static Pressure vs Meridional Shroud Distance Along Operating Line. . . . .	161
113	Impeller Performance for Nominal IGV Settings. . . . .	162
114	Impeller Slip Factor . . . . .	162
115	Diffuser Static Pressure - 100% Speed Nominal IGV. . . . .	164
116	Diffuser Static Pressure - 100% Speed Nominal IGV Effect of Throttle . . . . .	165
117	Diffuser Pressure Recovery and Loss Coefficient vs Absolute Air Angle . . . . .	166

LIST OF ILLUSTRATIONS - Continued

<u>Figure</u>		<u>Page</u>
118	Deswirlor Wake Survey. . . . .	167
119	CCV-I Plane E Mach No. - Nominal IGV, No Bleed . . .	167
120	Impeller Exit Bleed. . . . .	168
121	Intercompressor Duct Bleed . . . . .	169
122	Effect of Impeller Exit Bleed on Slip Factor . . . .	172
123	Calculated and Measured Wall Static Pressure Ratio .	173
124	Calculated Enthalpy Rise Through Impeller. . . . .	174
125	Calculated Entrophy Rise Through Impeller. . . . .	175
126	Estimated FCV-I Compressor Performance Using ACV and CCV-I Test Data. . . . .	176
127	Campbell Diagram for FCV-I Rotor Blade . . . . .	179
128	FCV-I Rotor Blade Stall Stresses . . . . .	181
129	Flow Function Correlation. . . . .	185
130	FCV-I Overall Compressor Performance . . . . .	185
131	FCV-I Axial Compressor Performance . . . . .	186
132	Centrifugal Compressor Performance . . . . .	187
133	Effect of Stator 2 Schedule on Overall Compressor Performance - 100% Speed . . . . .	188
134	Effect of Stator 2 Schedule on Overall Compressor Performance - 95% Speed. . . . .	189
135	Effect of Stator 2 Schedule on Overall Compressor Performance - 90% Speed. . . . .	189
136	Effect of Stator 2 Schedule on Axial Compressor Performance - 100% Speed . . . . .	190

LIST OF ILLUSTRATIONS - Continued

<u>Figure</u>		<u>Page</u>
137	Effect of Stator 2 Schedule on Axial Compressor Performance - 95% Speed. . . . .	190
138	Effect of Stator 2 Schedule on Axial Compressor Performance - 90% Speed. . . . .	191
139	Effect of Stator 2 Schedule on Centrifugal Compressor Performance - 100% Speed . . . . .	192
140	Effect of Stator 2 Schedule on Centrifugal Compressor Performance - 95% Speed. . . . .	193
141	Effect of Stator 2 Schedule on Centrifugal Compressor Performance - 90% Speed. . . . .	193
142	Axial Compressor Static Pressure Distribution - 100% Speed . . . . .	194
143	FCV-II Overall Performance Results . . . . .	198
144	FCV-II Overall Performance - Low Speed . . . . .	199
145	FCV-II Plane E Mach No . . . . .	200
146	FCV-II Axial Compressor Results With Plane B Rakes. . . . .	201
147	FCV-II Axial Compressor Data . . . . .	202
148	Effect of Increased Axial Rotor Tip Clearance. . . . .	203
149	FCV-II Centrifugal Compressor Data . . . . .	205
150	FCV-II Centrifugal Compressor Data With Plane B Rakes. . . . .	206
151	FCV-II Diffuser Static Pressure Rise at 100% $N\sqrt{\theta}_A$ Throttle Line. . . . .	207
152	Impeller Static Pressure Rise for FCV-II and CCV-I. . . . .	208
153	CALCOMP Plot of Test Data (50% Immersion). . . . .	209
154	Plane B Traverse - Total Pressure Contours . . . . .	211

LIST OF ILLUSTRATIONS - Continued

<u>Figure</u>		<u>Page</u>
155	FCV-II Traverse Results - Axial Outlet, Plane B at 100% $N_c$ . . . . .	212
156	FCV-II Traverse Results - Axial Outlet, Plane B at 100% $N_c$ . . . . .	212
157	FCV-II Traverse Results - Axial Outlet, Plane B at 100% $N_c$ . . . . .	213
158	FCV-II Traverse Results - Axial Outlet, Plane B Pressure Ratio . . . . .	213
159	FCV-II Traverse Results - Axial Outlet, Plane B at 95% $N_c$ . . . . .	214
160	FCV-II Traverse Results - Axial Outlet, Plane B at 85% $N_c$ . . . . .	214
161	Impeller Metal Angles and Calculated Data Match Inlet Air Angles . . . . .	215
162	FCV-II Test Results - Comparison of Plane B Rake and Traverse Data. . . . .	217
163	Flow Chart of Design Process . . . . .	219
164	CCV-I, CCV-II, and CCV-III Impeller Flow Paths . . . . .	222
165	Blade Velocity Diagrams Along the Shrouds. . . . .	225
166	CCV-I and CCV-IV Impeller Flow Paths . . . . .	228
167	Hub Static Pressure Coefficient. . . . .	230
168	CCV-IV Impeller Disk and Blade Stresses. . . . .	231
169	CCV-IV and CCV-V Test Results. . . . .	233
170	CCV-V and FCV-II Centrifugal Stage Performance . . . . .	234
171	Centrifugal Stage Performance. . . . .	235
172	CCV-IV Impeller Performance. . . . .	236
173	Slip Factor for CCV-I and CCV-IV Impellers . . . . .	236

LIST OF ILLUSTRATIONS - Continued

<u>Figure</u>		<u>Page</u>
174	CCV-IV Impeller Shroud Static Pressures. . . . .	237
175	Effect of Vaneless Space Bleed at 95% $N_c$ . . . . .	238
176	Effect of Vaneless Space Bleed at 90% $N_c$ . . . . .	239
177	CCV-V Diffuser Performance . . . . .	240
178	CCV-V Diffuser Outlet Mach Number. . . . .	241
179	Combined Axial-Centrifugal Compressor. . . . .	243

LIST OF TABLES

<u>Table</u>		<u>Page</u>
1	Axial Compressor Performance Summary . . . . .	20
2	Centrifugal Stage Performance Summary. . . . .	21
3	Overall Performance Summary. . . . .	22
4	Axial Compressor Clearance Measurements. . . . .	36
5	Axial Compressor Clearance Summary . . . . .	37
6	Centrifugal Compressor Clearance Summary . . . . .	39
7	Combined Compressor Clearance Summary. . . . .	39
8	Plane B Rake Sensor Locations. . . . .	54
9	CCV-I Impeller Shroud Statics. . . . .	63
10	Lubrication Requirements . . . . .	79
11	Axial Compressor Vehicle Run Time Summary. . . . .	89
12	Axial Compressor Vehicle Stall Summary . . . . .	90
13	Tensile Specimens. . . . .	113
14	AM355 Chemical Analysis. . . . .	114
15	Centrifugal Compressor Vehicle Time Summary. . . . .	151
16	Comparison of Design and Measured Performance. . . . .	170
17	Combined Compressor Stress Summary. . . . .	180
18	CCV-I Impeller Principal Design Details . . . . .	223
19	CCV-II Impeller Principal Design Details. . . . .	224
20	CCV-III Impeller Principal Design Details . . . . .	226
21	CCV-IV Impeller Principal Design Details. . . . .	229
22	Axial Compressor Test Data (ACV). . . . .	249
23	Centrifugal Test Data (CCV-I) . . . . .	254

LIST OF TABLES - Continued

<u>Table</u>		<u>Page</u>
24	Combined Compressor Data Settings (FCV-I) . . . . .	257
25	Combined Compressor Test Results (FCV-I) . . . . .	260
26	Combined Compressor Data Settings (FCV-II) . . . . .	262
27	Combined Compressor Test Results (FCV-II) . . . . .	266

## INTRODUCTION

The trend in small gas turbine engine compressors has been in the direction of higher pressure ratios from fewer compressor stages. The U.S. Army has sponsored exploratory research on small size, advanced technology axial and centrifugal compressor stages as well as analytical studies directed at matching high-pressure-ratio, single-shaft, axial-centrifugal compressors. This program is directed at the design, fabrication, and test of a 5-lb/sec axial-centrifugal compressor. The overall pressure ratio of 15:1 was designed with a two-stage axial compressor followed by a centrifugal compressor.

During this program separate axial and centrifugal component tests were carried out followed by two combined compressor tests. Of prime importance in this program is the understanding of compressor matching to achieve best efficiency in the 60% power region. To attain this goal, complete variability of the axial compressor vanes was employed as well as intercompressor bleed. Recent advancements to obtain wider axial compressor flow range and higher centrifugal stage efficiency are incorporated by using casing treatment and diffuser vaneless space bleed, respectively.

The mechanical design includes considerations for a potential engine application of this compressor while maintaining the flexibility required for a component development vehicle. A front shaft drive capability has been factored into the design.

The component development program was carried out in five phases.

The documentation of the initial parametric studies and design, Phases I and II, was completed as a separate design report.<sup>1</sup> The design point performance levels established in Phase II are shown in Tables 1 and 2 for the axial and centrifugal compressors, respectively. The overall design point data are shown in Table 3. This report presents the results for the Phase III and Phase V component tests and the Phase IV evaluation of these data. Also included are the test results and analysis on a related centrifugal compressor program (CCV-II through CCV-V). The specific tests included in this report are as follows:

1. Axial Component Test (ACV).
2. Axial and Centrifugal Inlet Guide Vane Blow Tests.
3. Centrifugal Component Tests (CCV-I to V).
4. Combined Axial-Centrifugal Component Tests (FCV-I and FCV-II).

---

1. Blair, L.W., and Tapparo, D.J., AXIAL-CENTRIFUGAL COMPRESSOR PROGRAM - PHASES I AND II, USAAMRD L TR-72-24, U.S. Army Air Mobility Research and Development Laboratory, Fort Eustis, Virginia, February 1973, CONFIDENTIAL.

TABLE 1. AXIAL COMPRESSOR PERFORMANCE SUMMARY

Item	Design Point
<u>OVERALL</u>	
Pressure Ratio	2.4967:1
Inlet Temperature - °R	518.688
Exit Temperature - °R	704.85
Actual Enthalpy Rise - Btu/lb	44.752
Adiabatic Efficiency	0.8307
Polytropic Efficiency	0.8508
Intercompressor Duct Pressure Recovery	0.99575
<u>INLET GUIDE VANE</u>	
Pressure Recovery	0.9939
<u>STAGE ONE</u>	
Pressure Ratio	1.6082:1
Inlet Temperature - °R	518.69
Exit Temperature - °R	608.97
Actual Enthalpy Rise - Btu/lb	21.651
Adiabatic Efficiency	0.8356
Polytropic Efficiency	0.8462
<u>STAGE TWO</u>	
Pressure Ratio	1.5620:1
Inlet Temperature - °R	608.97
Exit Temperature - °R	704.85
Actual Enthalpy Rise - Btu/lb	23.101
Adiabatic Efficiency	0.8593
Polytropic Efficiency	0.8678

The axial component test, the CCV-I centrifugal component test, and the two inlet guide vane (IGV) blow tests were carried out at the Evendale Aero Component Laboratory. The other related centrifugal tests and the combined compressor tests were completed at the Lynn compressor test facilities. These component tests were initiated in May 1972 and concluded in January 1975.

Throughout this report, the illustrations refer to an acronym for the compressor, ATACC, which stands for Advanced Technology Axial Centrifugal Compressor.

TABLE 2. CENTRIFUGAL STAGE PERFORMANCE SUMMARY

Item	Design Point
<u>OVERALL</u>	
Inlet Total Pressure - psia	36.538
Inlet Total Temperature - °R	704.85
Exit Total Pressure - psia	220.44
Exit Static Pressure - psia	218.57
Exit Total Temperature - °R	1265.69
Corrected Inlet Airflow - lb/sec	2.34
Actual Airflow - lb/sec	5.0
Corrected Speed - rpm	51800
Actual Speed - rpm	60400
Adiabatic Efficiency (total-to-total)	.810
Adiabatic Efficiency (total-to-static)	.805
Pressure Ratio (total-to-total)	6.033
Pressure Ratio (total-to-static)	5.982
Polytropic Efficiency (total-to-total)	.8495
Specific Speed	71
<u>IMPELLER</u>	
Inlet Prewhirl - ft <sup>2</sup> /sec	22.0
Pressure Ratio (total-to-total)	6.850
Adiabatic Efficiency (total-to-total)	.8838
Polytropic Efficiency (total-to-total)	.9095
Actual Enthalpy Rise - Btu/lb	139.354
Temperature Ratio	1.796
Impeller Slip Factor ( $C_{\theta_2}/U_2$ )	.91
Impeller Wheel Speed - ft/sec	1992.2
Impeller Tip Radius - in.	3.780
Blade Tip Metal Angle - deg	0
Number of Blades	28/28
<u>DIFFUSER</u>	
Total Pressure Loss ( $\Delta P/q_c$ )	.193
Static Pressure Recovery ( $\Delta p/q_c$ )	.795
Exit Mach Number	.112
Exit Flow Angle - deg	16.6

TABLE 3. OVERALL PERFORMANCE SUMMARY

Item	Design Point
Design Speed - rpm	60400
Design Airflow - lb/sec	5.0
Pressure Ratio (total-to-total)	15.00
Pressure Ratio (total-to-static)	14.87
Adiabatic Efficiency (total-to-total)	.787
Adiabatic Efficiency (total-to-static)	.783
Inlet Temperature - °R	518.688
Exit Temperature - °R	1265.59
Enthalpy Rise - Btu/lb	184.1
Inlet Total Pressure - psia	14.696
Outlet Total Pressure - psia	220.44
Outlet Static Pressure - psia	218.57

## PROGRAM CHRONOLOGY

The events of the axial-centrifugal compressor program occurred over a 45-month period of performance; due to the complex nature of this program there was considerable interaction between the various tasks. The impact of unexpected results or situations is also presented.

The program was started in June 1971, and had five major phases.

At the end of the planned Phase V component test, the program was extended to conduct matching studies and to prepare recommendations for additional areas of investigation and test. Concurrent with this compressor program, the contractor carried out a related centrifugal compressor program; and these results are also presented herein.

A schedule of the major program tasks is shown in Figure 1 with the initially planned and actual milestones. At the conclusion of the 45 months of effort, this program was within 2 months of the proposed schedule.

### PHASE I - PARAMETRIC STUDY

The purpose of Phase I was to carry out a parametric study to finalize the compressor design RPM and pressure ratio split. This was completed slightly ahead of schedule in July 1971. The results of this study were reported in the Phase I and II design report (see Reference 1). Permission was granted in Phase I to order long lead time rotor forgings and antifriction bearings.

### PHASE II - DESIGN

This phase generated the detailed mechanical and aerodynamic designs of the axial and centrifugal compressors. These mechanical designs included the structural analysis of the static and rotating parts as well as the detail and final assembly drawings. Since the design RPM was rather high (60,400 rpm), there was considerable design effort and design review placed on the analysis of the compressor rotor system and its associated mechanical drive. The aerodynamic design of the axial compressor was based on existing technology for high tip speed transonic axial compressors. The results of earlier company-sponsored centrifugal compressor programs were the basis for the centrifugal compressor design.

▲ PLANNED  
 ▲ ACTUAL

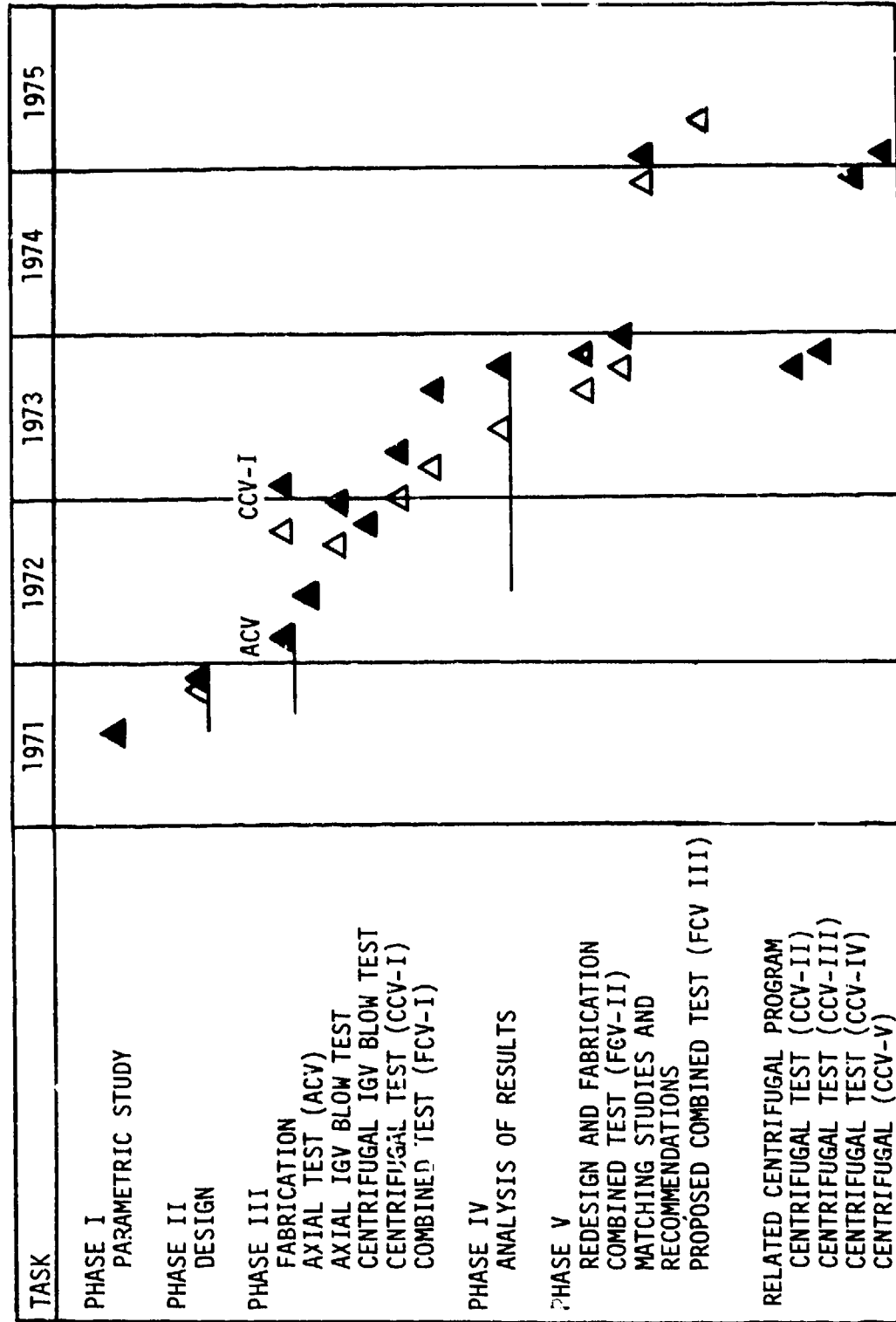


Figure 1. Axial-Centrifugal Compressor Program Schedule.

### PHASE III - FABRICATION

The fabrication of the axial compressor was completed on schedule. The facility high speed drive system was successfully demonstrated in a no-load test while the test vehicle for the axial compressor test (ACV) was being assembled in the Evendale Aero Component Test Area.

### PHASE III - AXIAL COMPRESSOR TEST (ACV)

The axial test was started on schedule in the Evendale Cell A9E test facility. The test vehicle operated successfully to 100% corrected speed (61,000 rpm) without any vibration problems. The compressor mapping and stator schedule optimization proceeded normally for the first 36 hours of test. At that time the strain gages on the aft bearing squirrel cage became increasingly noisy, so chip detectors were installed in the forward and aft bearing oil scavenge lines as a precautionary measure. A possible explanation of this noisy signal was a problem with the thrust bearing, but rollover checks did not indicate any unusual noise from the bearings. After three more hours of test, the noise level increased in intensity on the aft squirrel cage strain gages, so the vehicle was shut down to inspect the chip detectors. Two small chips were found on the aft sump chip detector, but they were not large enough to trigger the alarm circuit. These chips were analyzed as M50 bearing material, which was a positive indication of a bearing beginning to fail. The vehicle was pulled forward and the aft bearing was changed in the test facility. A failure analysis of this bearing indicated one of the four oil jets had poor orientation, which was corrected. Also, the thrust loads were high but not excessive, so it was decided to continue the testing at reduced thrust load and improved lube jet orientation. This bearing design had a shallow design contact angle, hence little margin for overloads, so a longer term action plan was instituted to rework the spare bearings for a higher contact angle prior to any subsequent tests. No further bearing problems occurred over the remainder of this development program.

While mapping various stator schedules at 100% corrected speed, the axial compressor experienced a failure of the first stage rotor blades. An investigation determined the cause of this failure to be high blade root stresses coupled with marginal material properties. The high blade end-effect stresses had reduced the allowable vibrat stress margin, and material inclusions of manganese sulfide acted as fatigue nucleation sites. Experience on similar axial compressors indicated that this mechanical design should be adequate, so the recovery plan was directed at improved materials using the present design. A triple vacuum melt 6-4 titanium material was contour-forged for the replacement rotors instead of using the previous AM355 pancake-forged material. Furthermore, a "superclean" AM355 material specification was instituted for use in future high mean stress rotor blades. All necessary axial test data was gathered prior to the failure, so a second axial test was not required. The

essential matching data and centrifugal inlet conditions were obtained in this test. A total of 208 data readings were logged in the 48 hours of testing.

#### PHASE III - IGV BLOW TESTS

The blow tests were conducted to determine the outlet conditions from the axial and the centrifugal inlet guide vanes (IGV's). The axial IGV blow test was delayed two months while replacement axial hardware was being procured. The centrifugal IGV's simulated the residual swirl from the axial compressor so these vane pressure losses and flow angles were measured to confirm the design.

The axial IGV blow test was completed in December 1973. Traverse surveys were obtained in both the radial and circumferential directions for various vane settings in order to more fully define the flow field into the first stage rotor. A unique test apparatus was designed to accomplish this task within the allotted funds.

#### PHASE III - CENTRIFUGAL COMPONENT TEST (CCV-I)

This test was carried out in the Evendale test facility (Cell A9E) in April 1973 where a total of 108 data points were recorded in 23 hours of testing. These test results were below the objective levels in efficiency, but the pressure ratio and flow range for the 5° open IGV setting appeared adequate for matching with the axial compressor.

The CCV-I centrifugal impeller had unusually high slip factors (approx 1.0) which accompanied below-design impeller efficiency. The diffuser static pressure recovery was also low, but the impeller outlet flow conditions were suspected as part of this lower recovery.

#### PHASE III - COMBINED COMPRESSOR TEST (FCV-I)

The first test of the strain-gaged combined compressor was started on 17 July 1973. This test acquired 99 data points in 12 test runs where data were acquired up to 100% corrected speed. The stress mapping for the axial compressor was conducted early in the test program because of the expected limited life of the strain gages. The test was carried out in the Lynn Small Engine Compressor Test Facility because it had adequate power and capability for a slip ring installation. After four test runs the strain gage lead wires were refurbished at the rear terminus from the rotor. The fifth test run completed the stress mapping of the rotors over the anticipated range of stator schedules and corrected speeds. No serious stress levels were noted during this testing. The inlet was refrigerated at the 95% and 100% corrected speed conditions to lower the physical speed so that the life of the rotor strain gage instrumentation would be extended, and to reduce the mean blade stresses in the event high

vibratory stresses were encountered during this test.

The matching of the axial and centrifugal compressors required some intercompressor bleed at higher speeds because of a reduced flow capacity in the centrifugal stage from the CCV-I component test levels. The testing acquired data up to a total pressure ratio of 14.34:1 at 100% corrected speed, but the efficiency was below predicted levels because of reduced performance in this centrifugal compressor. Opening the second stage stator vanes to load up the centrifugal stage was not effective. After 67 hours of test a peculiar compressor rotor vibration was encountered while operating at 90% corrected speed and an inlet temperature of 403°R. Since only rotor traversing remained in this test program, it was decided to defer that test item to the next Phase V component test. The test vehicle final balance levels and rotor runouts were normal at teardown, and no rubs were detected. An investigation revealed the probable cause to be a partial loss of the rotor tie-bolt clamping while operating at a low speed and a low inlet temperature. Future tests would include a higher initial clamping load from the tie bolt to assure proper clamping at all times. Subsequent tests did not incur any further vibration incidents.

#### PHASE IV - EVALUATION

The analysis of the Phase III test results was carried out in Phase IV. This phase also included design studies for the recommended redesigned compressor which was tested in Phase V.

#### PHASE V - FCV-II COMPONENT TEST

The CCV-I centrifugal impeller was cut back at the inducer leading edge to improve the calculated inlet flow angles as determined from the axial test traverse data. The diffuser throat area was also increased 6.4% for a greater flow capacity. This assembly did not require strain gages, but it was decided to conduct most of the high speed testing at reduced inlet pressure and temperature.

This test got under way on 13 December 1973, and 158 data points were acquired in 56 hours of test. All work items were completed, including the axial rotor traverse data and full corrected speed operation using ambient inlet conditions. Additional traverse data were also obtained in between the axial and centrifugal compressors in order to define the interstage flow conditions in the presence of a centrifugal stage. Previous Phase III axial IGV blow test data had indicated the need for traverse data in both the radial and circumferential directions because of strong circumferential gradients resulting in dubious accuracy of a single radial traverse downstream of a stationary blade row. At the end of the test, the axial rotor tip clearance was increased to determine the effects of clearance on the axial stage performance. This clearance

shift was achieved without disturbing the compressor installation which was important because of the small anticipated efficiency effects,

The performance testing of this compressor demonstrated a satisfactory match of the axial and centrifugal stages without intercompressor bleed. The machine was tested up to full speed, but the indicated efficiency levels were not at predicted levels because of low performance in the centrifugal stage.

To improve the centrifugal stage performance, the related centrifugal compressor development program was scheduled to evaluate two design configurations toward the end of 1974. A new impeller was designed using the flow conditions from the FCV-II Plane B traverse data. This design incorporated a reduced impeller hub loading which was the suspected area of high loss in previous designs (CCV-I, II, and III). In addition, a smooth shroud was incorporated to reduce the shroud frictional heating which was suspected as a partial cause of the high slip factors observed during previous tests. A new diffuser was designed with a 7% larger pipe tangency circle to lower the Mach number in the quasi-vaneless section and to reduce possible interactions between the diffuser and the impeller tip.

#### PHASE V MATCHING STUDIES AND RECOMMENDATIONS

The Phase V program was extended to carry out matching studies with the redesigned centrifugal stage and to prepare recommendations for future work. The redesigned centrifugal compressor program demonstrated a significant improvement in centrifugal stage efficiency and flow range. This was especially evident in the CCV-V test where objective flow range and broad areas of peak efficiency were demonstrated. The impeller efficiency at the design corrected speed and airflow was 87.2% at a pressure ratio of 7.05:1 versus the design objective of 88.4% at a pressure ratio of 6.85:1. The matching studies indicated a 3.5-4.0 point gain in typical operating line efficiency (see Figure 2) and resulted in useable performance levels similar to other advanced compressors like the AMRDL-P&W 10:1 pressure ratio centrifugal stage (see Reference 2).

The redesigned impeller appeared to perform reasonably well, but some additional work could be carried out on pipe diffusers to reduce the losses ahead of the diffuser throat. This is the high Mach number region in the quasi-vaneless space where increased vaneless space bleed during the CCV-V test produced markedly higher static pressure recoveries ( $\Delta p / (P - p)$ ), from the nominal level of 0.72 to a maximum

2. Reeves, G.B., and Schweitzer, J.K., MODIFIED CENTRIFUGAL COMPRESSOR, USAAMRDL TR-74-96, U.S. Army Air Mobility Research and Development Laboratory, Fort Eustis, Virginia, November 1974, ADA004002.

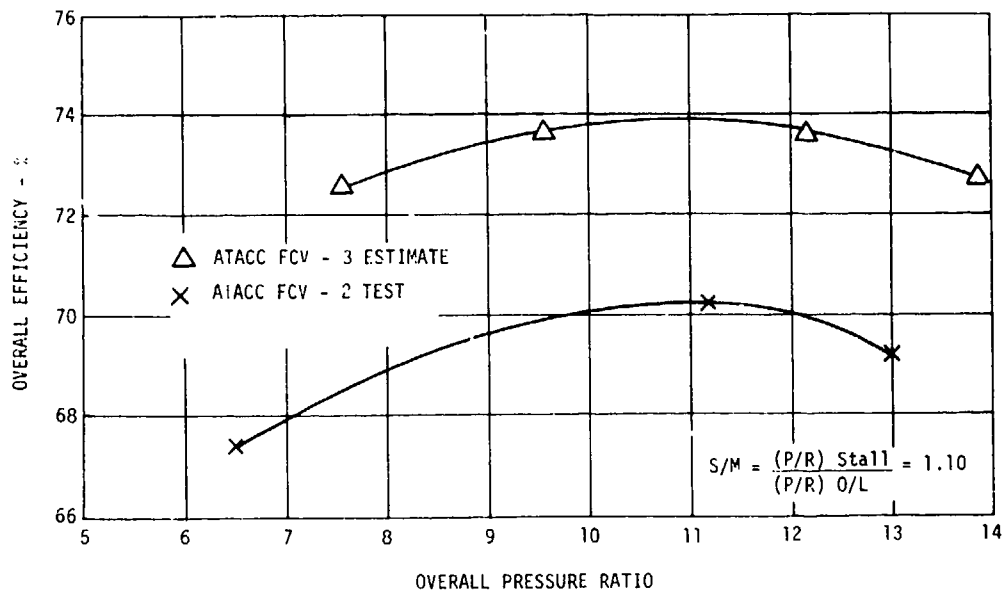


Figure 2. Compressor Performance at 10% Stall Margin.

bleed level of 0.78 at an inlet Mach number of 1.28. Achieving this diffuser recovery at design vaneless space bleed is an objective for future programs, since it would result in an efficiency of 79% for the centrifugal stage at an overall pressure ratio of 6.1:1. This would result in a combined compressor efficiency of about 77% at a compressor pressure ratio of 15:1.

In summary, this program demonstrated the feasibility of designing a 5-lb/sec two-stage axial-centrifugal compressor in the 15:1 pressure ratio class, and provided insights into the matching of axial-centrifugal compressors. Other significant technical issues touched by this program were:

1. Stress-material properties interplay at the design limits.
2. Design of high speed rotor and drive systems.
3. Impeller shroud surface finish.

## FABRICATION OF TEST HARDWARE

### AXIAL COMPONENT TEST VEHICLE (ACV)

#### Hardware Manufacturing

Except for the vane actuation hardware, the compressor parts for the axial component test were machined from AM355 pancake forgings and bar stock. The manufacturing technique used for the blisk and vane airfoils was a pantograph milling process which utilizes a larger scale model to trace the airfoil shape. The 32-microinch surface finish was generated by hand polishing.

Vane actuation hardware including lever arms, bushings, washers, and nuts for the IGV and Stage 1 vanes was obtained from other engine programs. Actuation rings for the IGV and Stage 1 were manufactured from box section extruded 6061-T6 aluminium, while the Stage 2 actuation ring was machined from 321 stainless steel plate stock.

#### Compressor Assembly

Stator Assembly: The assembled compressor stator is shown in Figure 3. The Stage 2 vane tips were ground to length with the casing mounted at the forward flange and rabbet. The aft flange surface and rabbet were indicated to verify the casing setup prior to grinding. The vanes were wrapped with polyvinyl chloride tubing to dampen vibrations generated by the grinding process.

Vane angles were measured using a periscope-like device where the operator rotates an eyepiece until a hairline is tangent to the airfoil at the tip. The rotational angle of the eyepiece is displayed on a digital readout which is initially zeroed by sighting on the casing split line. The position where the vane angles are measured is determined by a close-fitting pin which is inserted through an actuator ring into a slot in the compressor casing. These pin positions were used during the test to verify and zero the vane angle readouts. Vane angle variation in each stage was minimized by changing the actuator ring and casing concentricity using the adjusting screws and buttons. The amount of button adjustment was determined by a least-square error analysis of the measured vane angles. Vane angle variations from average are presented below:

<u>Stage</u>	<u>Max Closed</u>	<u>Max Open</u>	<u>Standard Deviation</u>
IGV	42'	52'	22'
1	1°25'	1°35'	51'
2	1°55'	1°45'	57'

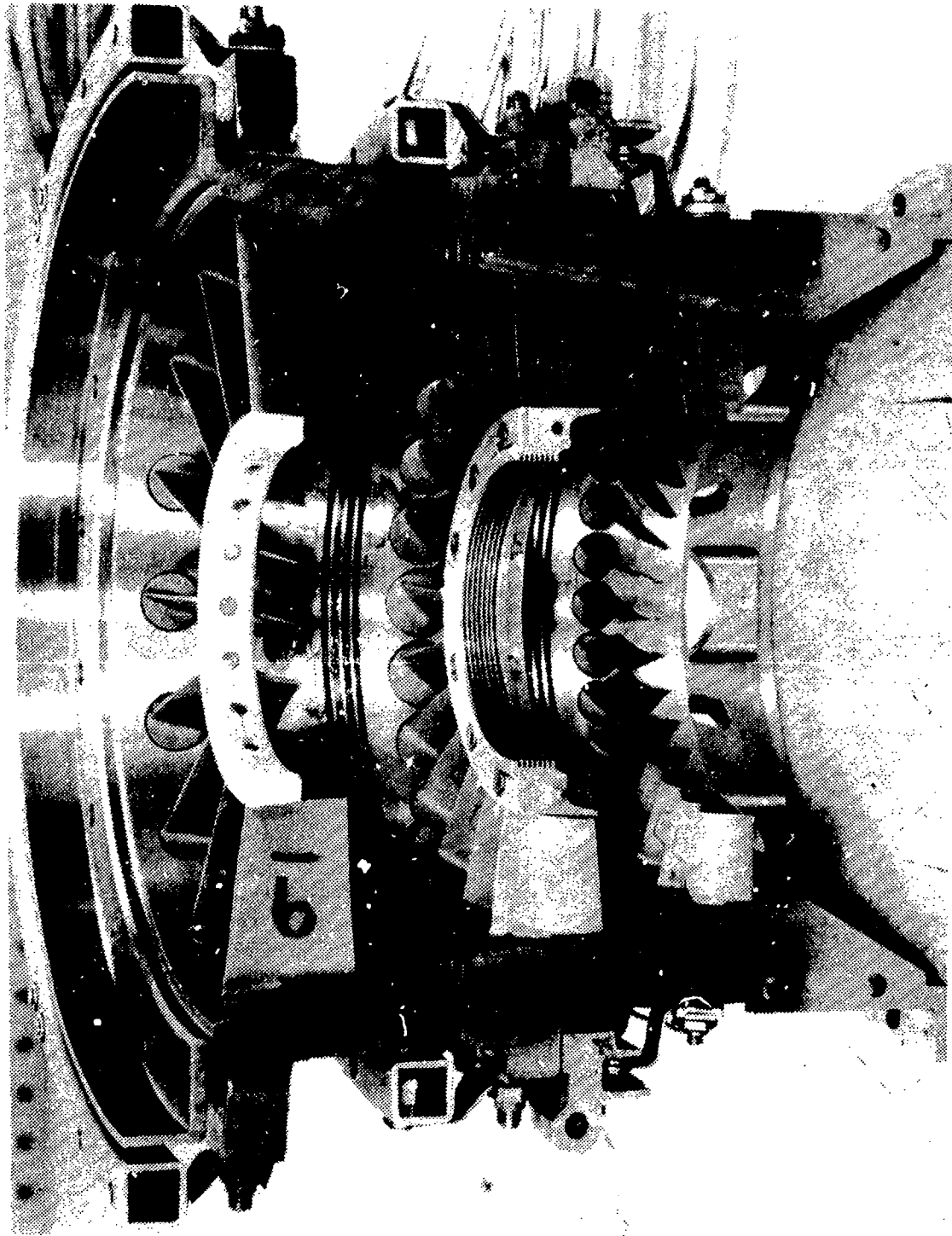


Figure 3. Compressor Stator Assembly.

The Stage 2 vane angle can be set to any one of seven fixed pin positions. The average angle relative to aerodynamic nominal at each of the positions was  $+0^{\circ}2'$ ,  $-4^{\circ}24'$ ,  $-9^{\circ}41'$ ,  $-15^{\circ}15''$ ,  $+5^{\circ}18'$ ,  $+9^{\circ}15'$ ,  $+14^{\circ}45'$ .

Rotor Assembly: The assembled compressor rotor is shown in Figure 4. The rotor is clamped together by a center tie bolt (see Figure 5). To obtain the desired preload in the tie bolt, it was first threaded hand-tight into position. A 1/2-inch-diameter heater was inserted to heat and elongate the hollow-ended tie bolt. It was then threaded an additional 1/3 turn and the heater removed. Tie bolt preload was calculated to be 6900 pounds based on a 0.013-inch measured tie bolt stretch. Rotor compression due to the tie-bolt load was 0.005 inch.

The initial build of the rotor was made to determine the optimum relative circumferential positions for the blisks and dummy impeller. Several positions were tried and runouts made with the rotor supported in V-blocks at the forward bearing journal and dummy impeller aft flange.

The balance piston shaft was then added and runouts were minimized by indexing this part relative to the dummy impeller. For these runouts the rotor was supported at the forward and aft bearing journals. The position producing minimum runouts was match marked and used in subsequent assemblies. Final runout total indicator readings are presented in Figure 6.

The Stage 1 and 2 blade tips were then ground to length in a lathe equipped with a small grinder mounted on the carriage at the desired blade tip angle. The amount of material removed was measured with a height gage resting on the lathe bed. To determine the amount to be ground, the rotor was set in the stator casing with the blade tips resting on the casing inside diameter. The axial position of the rotor relative to the stator was measured. The material removal required to obtain the blade tip angle with the desired clearance was calculated from the axial position.

After the blade tips were ground, the rotor was disassembled and each piece was balanced separately. The compressor rotor assembly (consisting of the blisks, dummy impeller, and tie bolt) was then balanced. Finally, the balance piston was added and the entire rotor assembly was balanced.

The final balance was made using slave bearing races at the forward and aft bearings. The forward locknut, the spline adapter coupling, and the aft locknut were removed after balance for installation of the vehicle bearings. The other rotor parts were not disassembled after balancing.

All parts and assemblies were balanced to the limits of the balance machine which was 0.10 gram-inch. The uncorrected unbalance of the final rotor assembly was 0.04 gram at the forward end and 0.03 gram at the aft end.

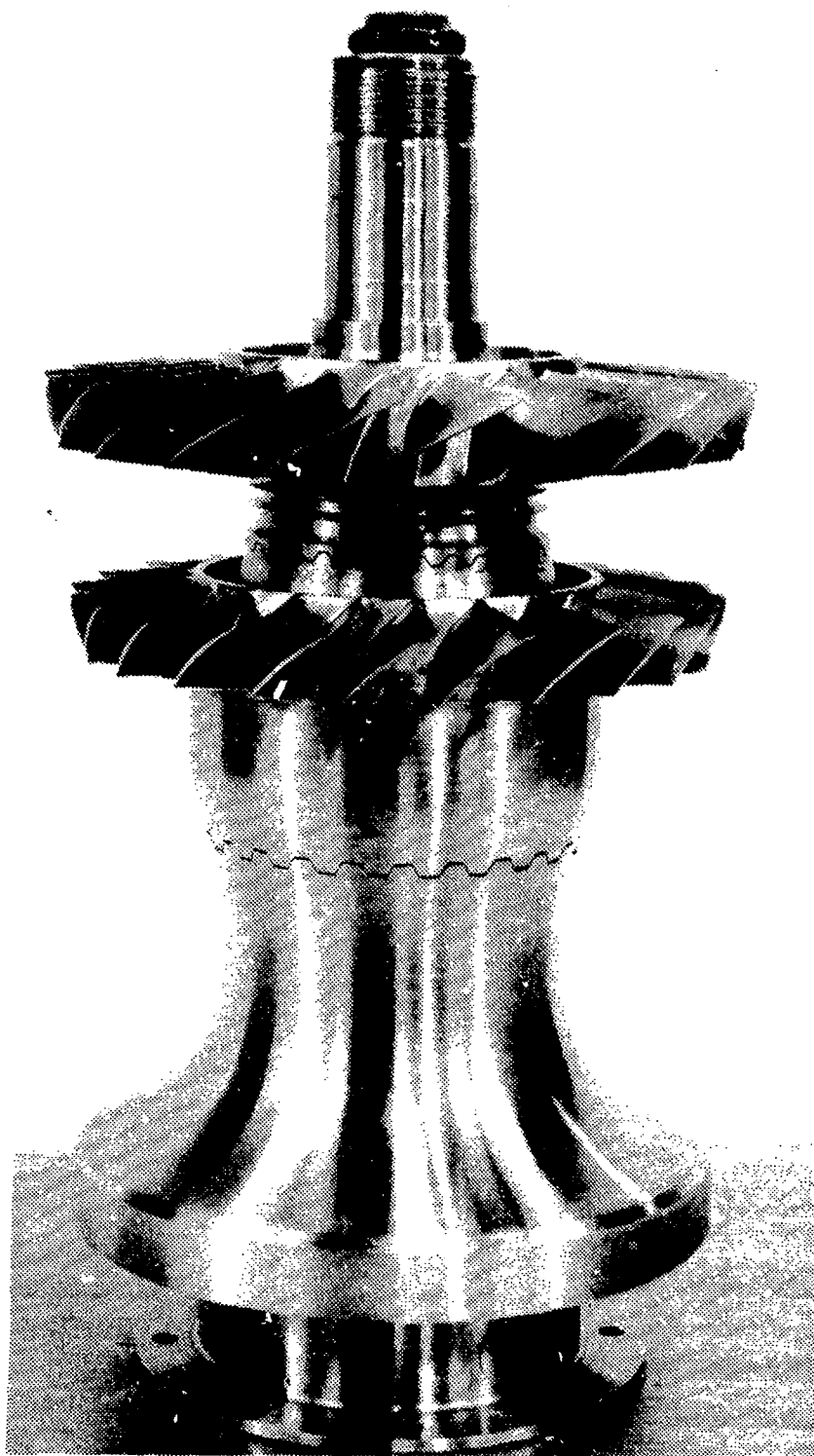


Figure 4. Axial Compressor Rotor Assembly.

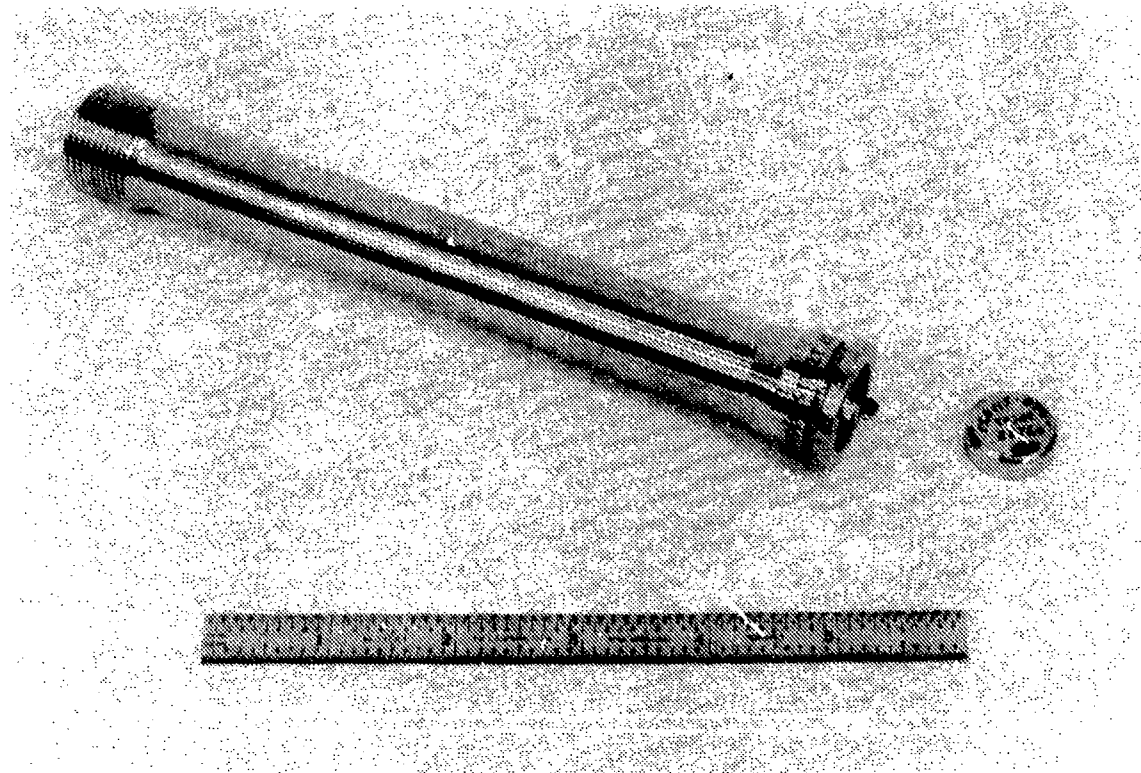


Figure 5. Tie Bolt.

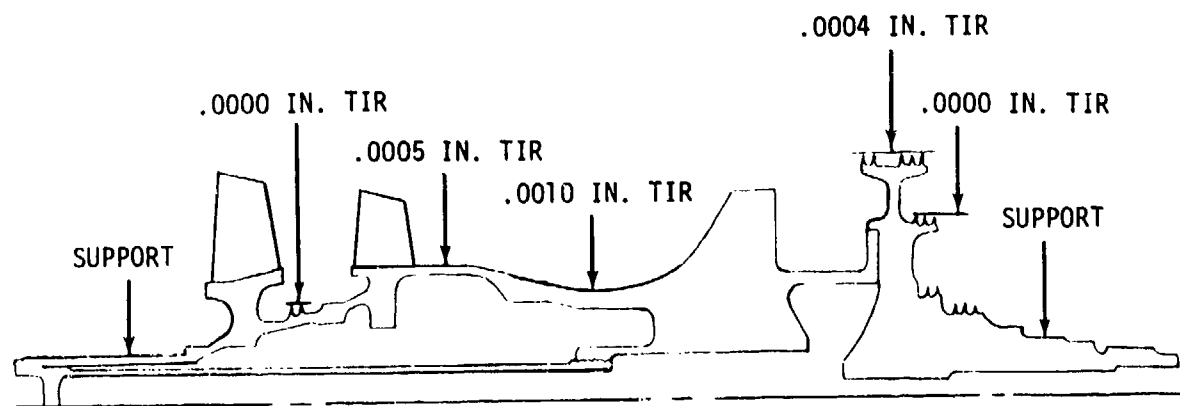


Figure 6. Axial Compressor Rotor Assembly Runouts.

### Clearances

After completion of the tip grinding operation, clearances between the rotor blade tips and the compressor casing were measured by the following three methods:

1. Measurement of the relative axial position between the rotor and the stator with the blade tips touching the compressor casing: The clearance is calculated from the difference between the above axial position and the axial position set at final assembly. Since Stage 1 contacted the casing before Stage 2, the axial position was remeasured with shims between the Stage 2 blade tips and the casing to calculate the Stage 2 clearance.

For these measurements the rotor was automatically centered in the casing. This setup could not be used to determine the minimum clearances because the minimum clearance would be affected by rotor-to-stator eccentricity. Subsequent wax checks and split line shim checks established this eccentricity.

2. Wax check measurements: Four wax patches were put on each casing half for both stages. The casing halves were assembled and bolted into position and the rotor was turned one complete revolution. The casing halves were removed and the thickness of the wax patches was measured.
3. Split line shim check: As each casing half was removed for the wax measurement, the clearance of the other half was measured with shim stock at the split line.

Clearance between the Stage 2 vane tips and the rotor was measured by wax checks and split line shim checks as well as the diameter measurements made during the tip grinding.

Results of the above clearance measurements are presented in Table 4, while the cold and hot clearances are summarized in Table 5. Clearances between the stator vanes and casing and shrouds are also presented in Table 5. These clearances were measured with the vanes in the open position. The inlet guide vanes required benching to provide adequate clearance with the compressor casing when the vanes were in the full open position.

TABLE 4. AXIAL COMPRESSOR CLEARANCE MEASUREMENTS

STAGE 1 BLADES											
Wax Checks Location (O'clock)	Right Casing Half			Left Casing Half			AVG				
	12:00	3:00	6:00	6:00	7:00	10:00	12:00	12:00	12:00	AVG	
Leading Edge (in.)	.012	-	.010	.009	.010	.011	.009			.0102	
Trailing Edge (in.)	.0115	.010	.0105	.010	.011	.012	.010			.0108	
Split Line Shim Checks											
Location (O'clock)	Right Casing Half			Left Casing Half			AVG				
Clearance (in.)	12:00	6:00	12:00	6:00	12:00	6:00	12:00			.010	
Axial Position Check (in.) - .0098	.010	.010	.010	.010	.010	.010	.010			.010	
STAGE 2 BLADES											
Wax Checks Location (O'clock)	Right Casing Half				Left Casing Half				AVG		
	12:00	1:30	3:00	4:30	6:00	6:00	7:00	9:00	12:00	12:00	AVG
Leading Edge (in.)	.010	.010	.010	.009	.008	-	.009	.011	.009		.0095
Trailing Edge (in.)	.008	.010	.009	.0085	-		.009	.010	.009		.0085
Split Line Shim Checks											
Location (O'clock)	Right Casing Half				Left Casing Half				AVG		
Clearance (in.)	12:00	6:00	12:00	6:00	12:00	6:00	12:00	6:00	12:00		.010
Axial Position Check (in.) - .0098	.010	.010	.010	.010	.010	.010	.010	.010	.010		.010
STAGE 2 VANES											
Wax Checks Location (O'clock)	Right Casing Half		Left Casing Half		AVG						
	2:00	4:00	8:00	10:00	8:00	10:00					
Leading Edge (in.)	.0080	.0080	.0075	.0085	.0085	.0085					
Trailing Edge (in.)	.0090	.0090	.0075	.0100	.0089	.0089					
Split Line Shim Checks											
Location (O'clock)	Right Casing Half		Left Casing Half		AVG						
Clearance (in.)	12:00	6:00	12:00	6:00	12:00	12:00					
Diameter Checks at Grind (in.) - .0114	.009	.012	.009	.012	.010	.010					

TABLE 5. AXIAL COMPRESSOR CLEARANCE SUMMARY							
Stage	Cold		Change	Span	Hot		%C1/L Avg (in.)
	Min (in.)	Avg (in.)	Cold - Hot (in.)		Min (in.)	Avg (in.)	
R1	.009	.010	.0060	1.231	.0030	.0040	.32
R2	.0093	.010	.0065	.875	.0028	.0035	.40
S2	.009	.011	.0048	.763	.0044	.0062	.81
IGV (OD)	-	.0015	-	1.46	-	.0015	.10
S1 (OD)	-	.0114	-	.97	-	.0114	1.18
S1 (ID)	-	.0099	.0014	.97	-	.0085	.88
S2 (OD)	-	.0095	-	.75	-	.0095	1.27

#### CENTRIFUGAL IGV BLOW TEST VEHICLE

This assembly was comprised of the following hardware that was part of the other component tests:

1. Inlet casing and vane assembly for CCV.
2. Dummy impeller shroud from ACV.
3. Dummy axial rotor for CCV.
4. Dummy impeller rotor for ACV.
5. Centrifugal inlet instrumentation from ACV.
6. Standard vehicle front frame, midframe, and inlet bellmouth.

An adaptor plate was also constructed to centrally mount the dummy rotors from the impeller flange. The assembled hardware is shown in Figure 7.

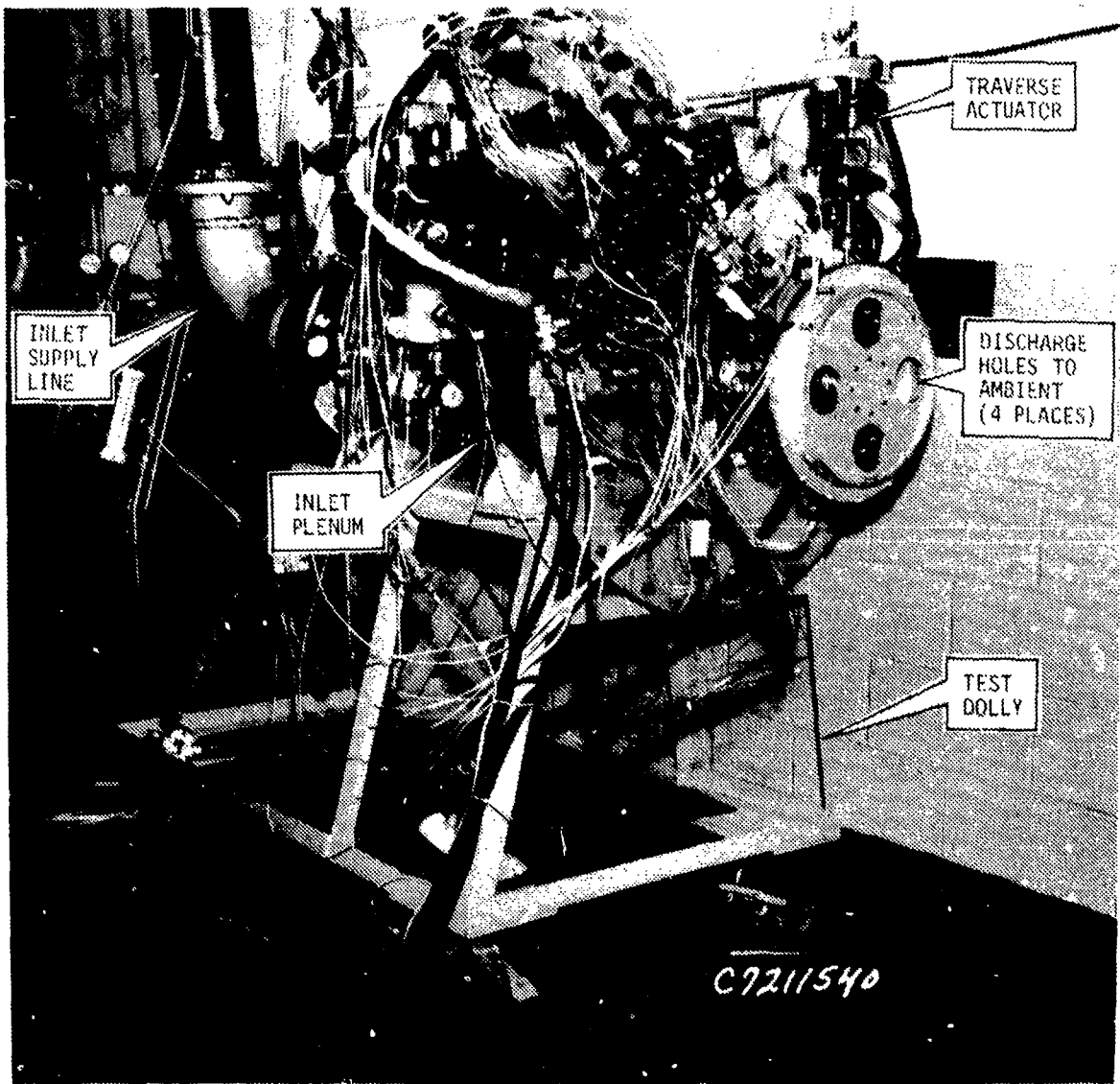


Figure 7. CCV Blow Test Setup.

The buildup data for the vane assembly is presented in Table 6.

TABLE 6. CENTRIFUGAL COMPRESSOR CLEARANCE SUMMARY							
Location	Cold		Change	Span	Hot		%C1/L
	Min. (in.)	Avg (in.)	Hot - Cold (in.)		Min. (in.)	Avg (in.)	
IGV	.0070	.0080	.0035	.763	.0035	.0045	.59
Impeller Inlet	.0030	.0050	.0020	.919	.0010	.003	.33
Impeller	.0065	.0075	.0043	.210	.0020	.0032	1.52*

\* Touch probes on the impeller shroud indicated that the impeller rubbed the shroud during operation. This was confirmed at disassembly by slight rub marks on the shroud.

#### AXIAL IGV BLOW TEST VEHICLE

The standard axial compressor casing was assembled with the replacement vanes used for the FCV-I test. This vane buildup is presented in the FCV-I fabrication data (see Table 7). The casing, front frame, and inlet bellmouth were used with the instrumentation hardware described in the IGV Blow Test instrumentation section to comprise the blow test assembly shown in Figure 8.

TABLE 7. COMBINED COMPRESSOR CLEARANCE SUMMARY							
Stage	Limits		Cold	Wax Checks		Hot	
	Min. (in.)	Max Avg (in.)	Dia Checks Avg (in.)	Min. (in.)	Avg (in.)	Avg (in.)	%C1/L
R1	.0141	.0171	.0152	.0140	.0143	.0080	.65%
R2	.0113	.0143	.0119	.0110	.0119	.0046	.53%
S2	.0084	.0114	.0120	.0085	-	.0082	1.08%
IND	.0054	.0094	-	.0080*	.0085*	.0064	.69%

\*Shim Checks

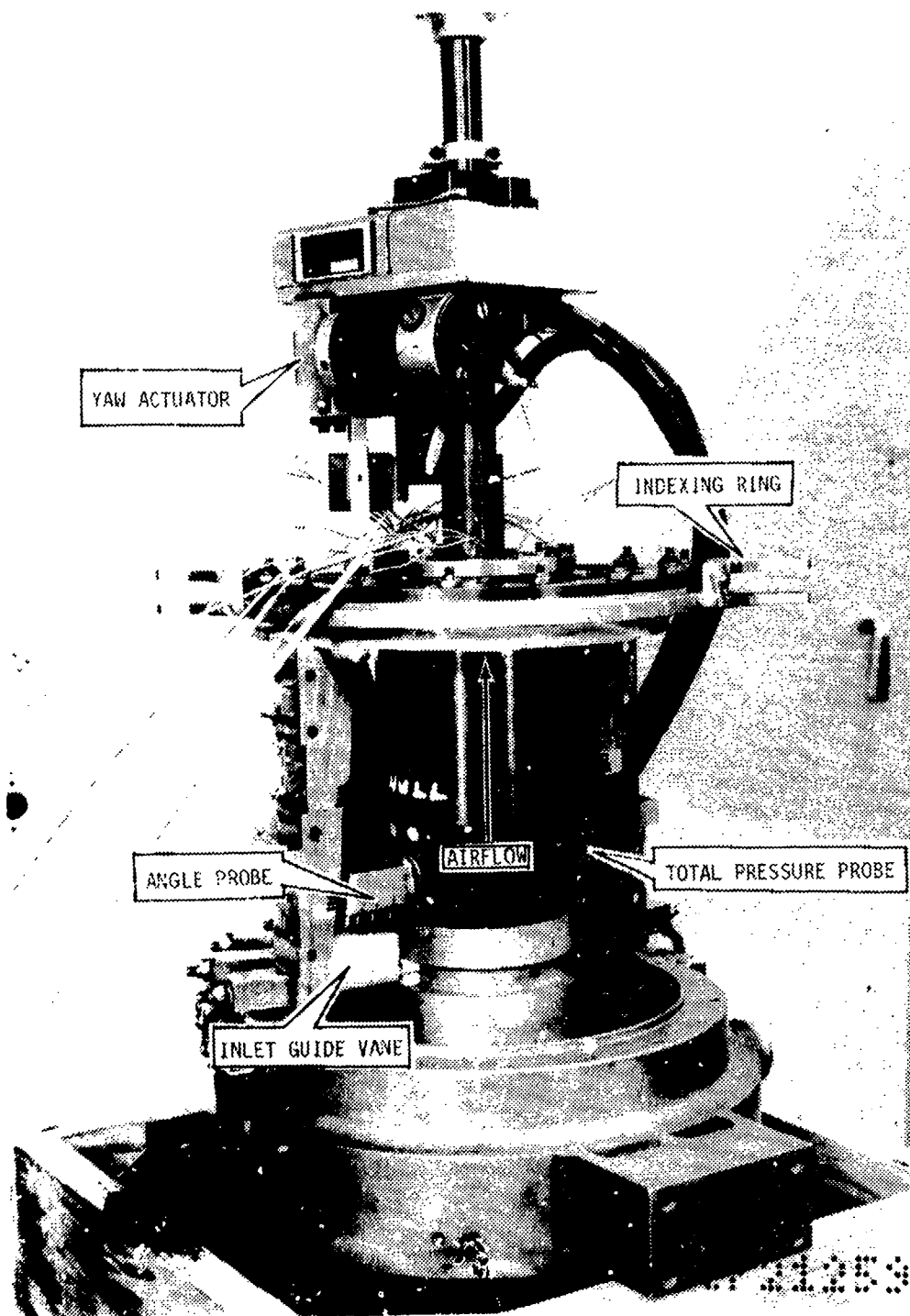


Figure 8. Axial Blow Test Setup.

## CENTRIFUGAL COMPONENT TEST VEHICLE (CCV-I)

### Hardware Manufacturing

All of the centrifugal compressor parts were machined from AM355 pancake forgings. The impeller and deswirl vanes were machined by the pantograph milling process. The diffuser was machined by the Electro Discharge Machining (EDM) process. The inlet guide vanes were made with the same process used for the axial compressor Stage 2 vanes.

A new inlet casing was made for the centrifugal test so the axial compressor, stator vanes would not have to be disassembled. The actuator hardware for the inlet guide vanes was identical to that used on the Stage 2 axial compressor vanes.

The centrifugal compressor hardware items appear in Figures 9 through 12.

### Compressor Assembly

The stator assembly procedure was essentially the same as the axial compressor, including tip grinding of the inlet guide vanes and vane angle measurement.

The IGV angles at the five pin positions were  $-1^{\circ}9'$ ,  $-5^{\circ}14'$ ,  $-9^{\circ}59'$ ,  $+3^{\circ}46'$ , and  $+7^{\circ}56'$ . The maximum vane-to-vane variation from the average was  $+53'$  and  $-49'$  and the standard deviation was  $28'$ .

The rotor was assembled using essentially the same procedure carried out for the axial compressor. Final rotor balance was to the sensitivity limits of the balance machine.

A critical assembly in the centrifugal compressor stage was the alignment of the impeller shroud to the diffuser inlet and the setting of the impeller-to-shroud cold clearance. These positions were set by adjusting the thickness of shims. The shroud-to-diffuser alignment was checked by sliding a dial indicator from the diffuser passage to the shroud. The impeller-to-shroud clearance for the CCV-I test was measured with wax patches painted on the shroud. These patches were cut by the impeller with the rotor loaded in the forward direction. The inlet guide vane tip clearance was measured with feeler gages. All of the centrifugal compressor clearances are summarized in Table 6.

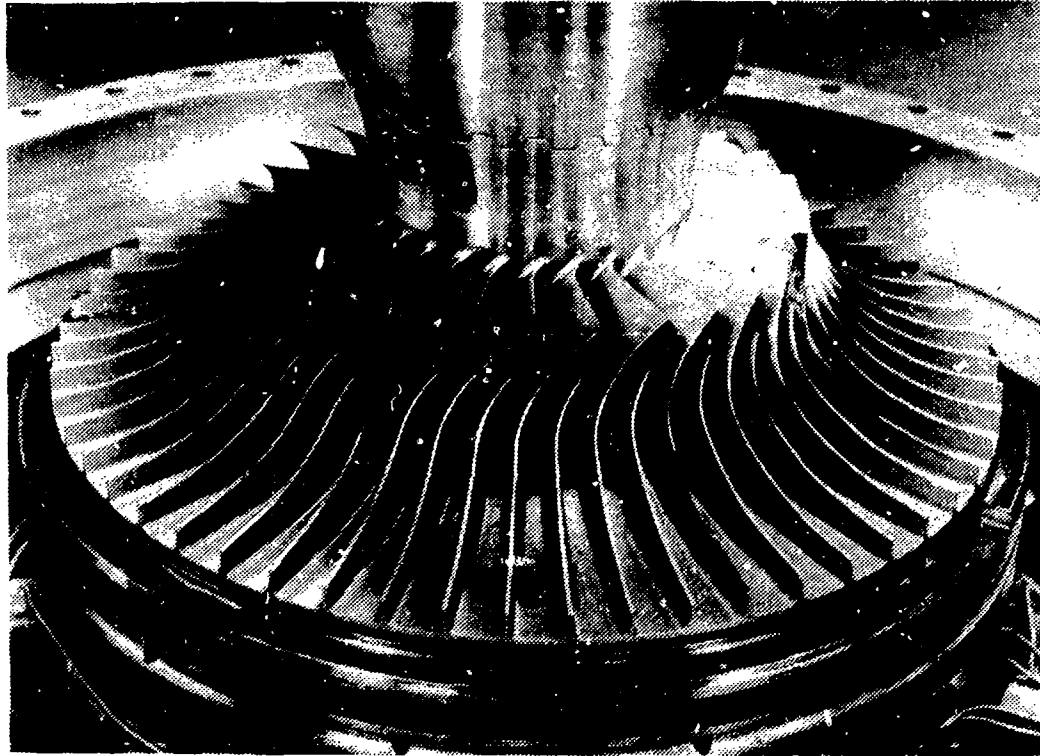


Figure 9. Centrifugal Compressor Test Impeller.



Figure 10 Centrifugal Compressor Impeller Shroud.



Figure 11. Centrifugal Compressor Diffuser.

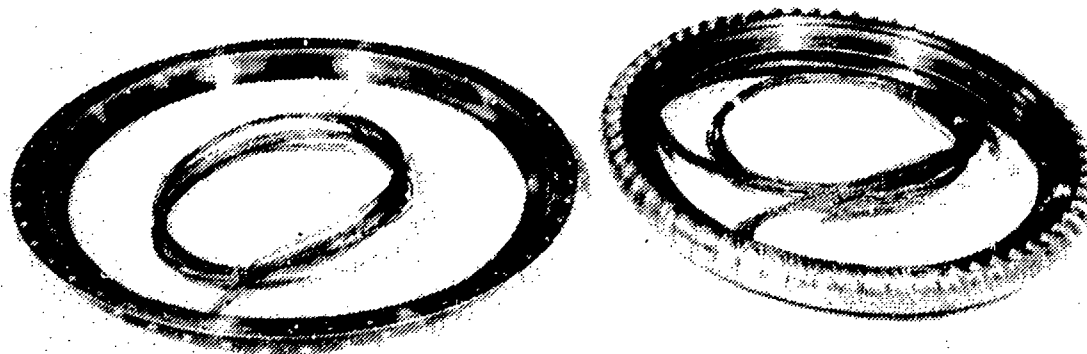


Figure 12. Centrifugal Compressor Deswirl Vane Row and Vane Cover.

## COMBINED COMPRESSOR TEST VEHICLE (FCV-I)

### Hardware Manufacturing

Since the original axial compressor hardware was damaged in the axial compressor failure, it had to be replaced for the combined compressor test. The three stages of vanes were replaced with parts of the same design and material. The actuator levers and bushings were also replaced with identical parts; however, the actuator rings were reused.

The compressor casing treatment over the Stage 1 and 2 blades was destroyed in the failure and had to be replaced. Inserts were machined from AM355 forged stock and installed in the compressor casing as shown in Figure 13. The rest of the compressor casing flow path was polished to remove all raised metal, small nicks, and scratches. No significant dimensional changes occurred in the casing.

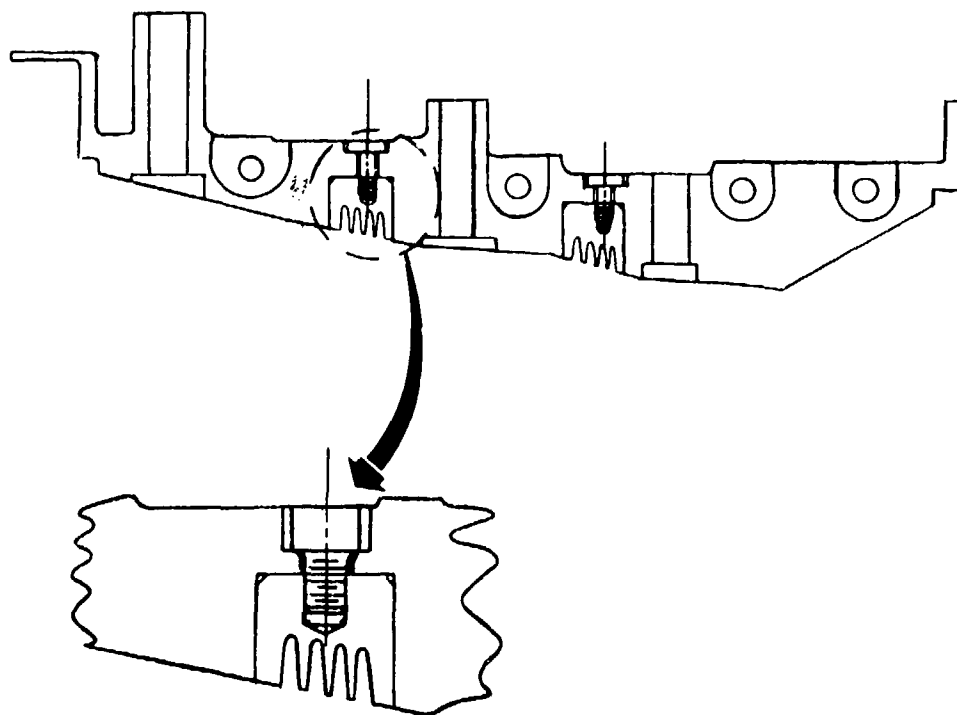


Figure 13. Axial Compressor Casing Inserts.

The AM355 Stage 1 and 2 blisks were replaced with parts of the same aerodynamic design machined from 6Al-4V Titanium contour forgings (see Figure 14). A triple vacuum melt titanium alloy was chosen to provide maximum insurance against impurities in the forgings. The structural shape of the blisks was changed as shown in Figure 15 to maintain the rotor frequency margin with the lower modulus of titanium. The same tooling and process used on the original blisks were used for the titanium parts.

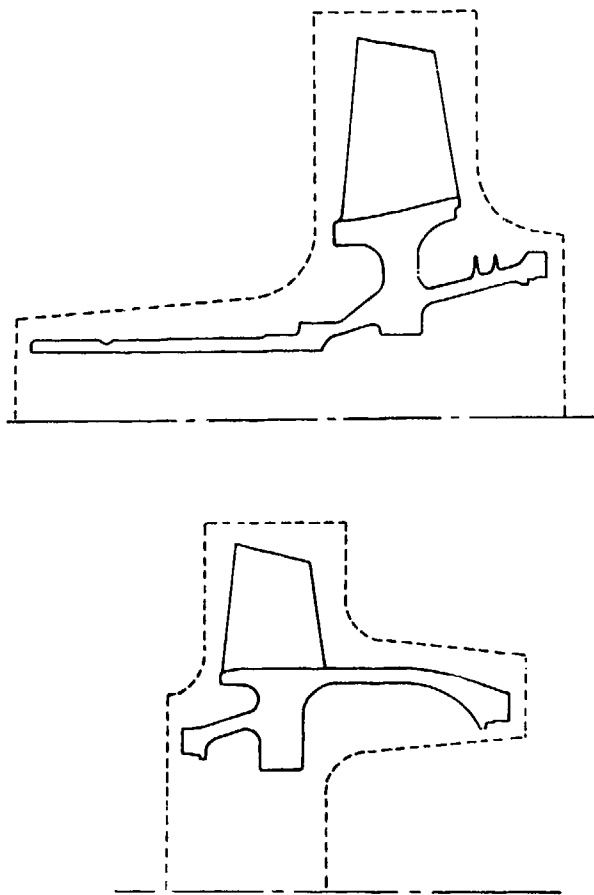


Figure 14. Sketch of Stage 1 and Stage 2 Blisk Contour Forging Outline.

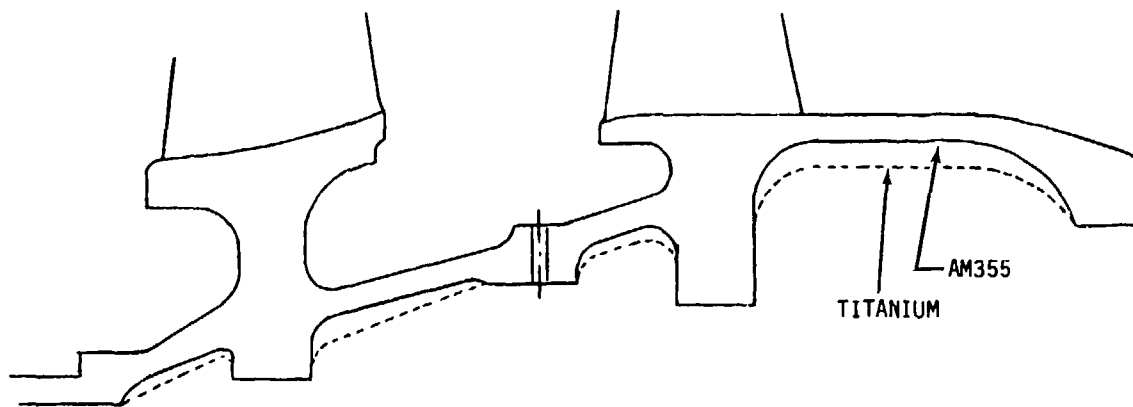


Figure 15. Titanium Blisk Redesign.

#### Compressor Assembly

Assembly of the axial compressor stator for the full compressor test was the same as for the axial test. The Stage 2 vanes were tip ground to length after assembly into the casing. Vane angles were measured on each of the three stages with the following angle variations from the average.

<u>Stage</u>	<u>Max Closed</u>	<u>Max Open</u>
IGV	39'	23'
1	53'	59'
2	1°7'	55'

The seven Stage 2 vane angle pin positions relative to aerodynamic nominal were  $-0^{\circ}26'$ ,  $4^{\circ}25'$ ,  $9^{\circ}28'$ ,  $14^{\circ}33'$ ,  $-5^{\circ}29'$ ,  $-11^{\circ}12'$ , and  $-14^{\circ}59'$ .

The Stage 1 and 2 rotor blade tips were ground to length with the blisks assembled to the dummy impeller as was done for the axial compressor build. The grinding procedure was the same; however, the amount of material to be removed was determined by diameter measurements of the blisks and casing.

After tip grinding, the individual blisks were balanced and then the blade strain gages were applied. Final rotor assembly was similar to that of the axial compressor rotor but it had the added complexity of routing the

strain gage lead wires (see Figure 16). Holes were drilled through the rotors for lead wires routed along the inside contour to the aft end of the assembly. The entire rotor assembly, including the balance piston shaft and spline adapter coupling, was then balanced on slave bearings.

Most of the centrifugal compressor stator assembly from the centrifugal compressor test was not disassembled prior to buildup of the combined compressor test vehicle. The shroud had to be removed for the rotor assembly, and the shim between the shroud and diffuser casing was reused to assure the same shroud-to-diffuser alignment. The shim at the adapter casing and rear frame interface was increased by 0.004 inch to set the impeller axial clearance to a 0.005-inch hot running clearance.

The Stage 1 and 2 rotor blade and Stage 2 stator vane tip clearances were determined using diameter measurements and also by wax checks prior to final assembly. The impeller inducer radial tip clearance was measured by shim checks. The cold and hot clearances are summarized in Table 7.

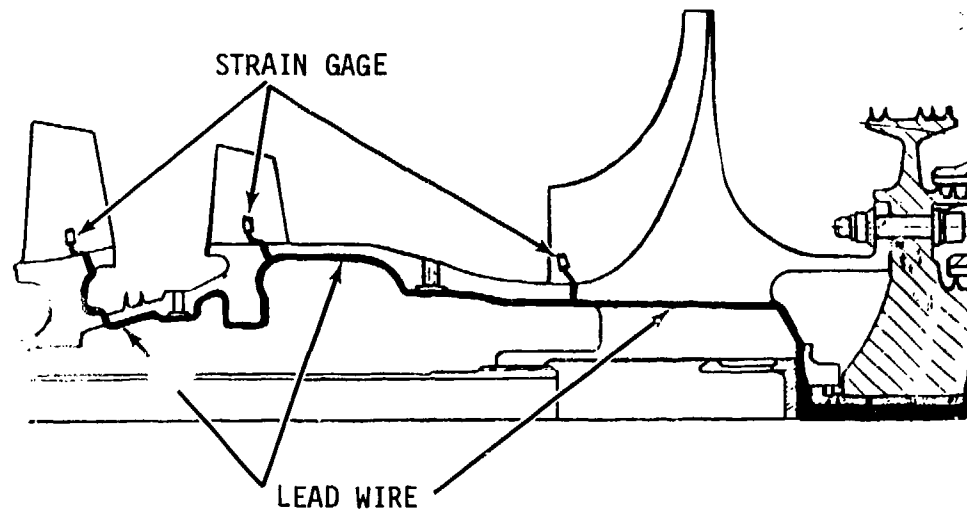


Figure 16. FCV-I Strain Gage Lead Wire Routing.

## COMBINED COMPRESSOR TEST VEHICLE (FCV-II)

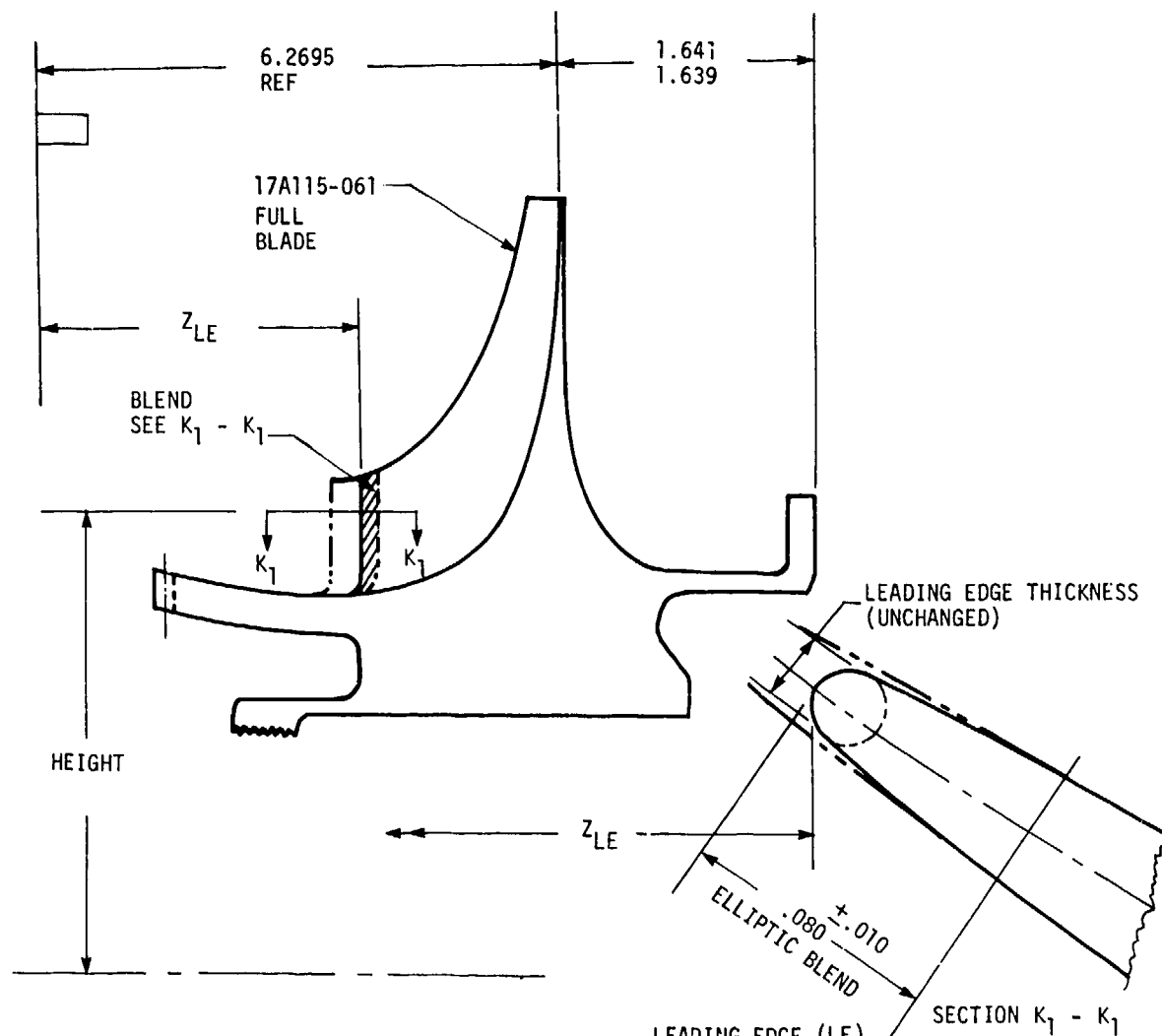
### Hardware Rework

The results of the Phase III test data were used to define the hardware redesign for evaluation in the Phase V, FCV-II combined compressor component test. This hardware rework consisted of a cutback of the inducer leading edge and an increased throat area in the pipe diffuser. The impeller rework is shown in Figure 17 where the leading edge was cut back and blended to a leading edge thickness equal to the initial design.

The pipe diffuser throat area was increased 6.4% to a nominal diameter of 0.2501 in. while maintaining the same passage width at the tangency circle. The actual measured throat diameter in the reworked diffuser was 0.2508 in. and within the allowable tolerance band.

### Compressor Assembly

The strain gages and the lead wires were removed prior to assembly; any holes were plugged or patched with nichrome strips. The rotor clearances were maintained for this assembly, and the rotor bearings were replaced with new bearings. The special conduit hardware for the strain gage wires was not required. During the rotor assembly, the tie-bolt preload was increased to 9600 lb. This higher tie bolt load was a preventative measure against any possible looseness under extremely low ambient inlet temperatures (i.e., 400°R). Traverse probes were installed on this build to measure the outlet flow from the first and second stage axial rotors using three-element Cobra probes. Another traversing apparatus was installed on a Plane B bleed boss to traverse the axial outlet flow in the transverse direction at various immersions with a three-element Cobra probe. The assembly and balancing were normal, and clearance checks were made to assure proper assembly and repeatability of the FCV-I measurements.



HEIGHT (IN)	Z (LE) (IN)	LEADING EDGE (LE) THICKNESS (IN)
1.30	4.97	.0235
1.40	5.00	.0218
1.50	5.023	.0201
1.60	5.04	.0184
1.70	5.05	.0167
1.80	5.05	.0150
1.90	5.05	.0133
2.00	5.05	.0116
2.10	5.05	.0099
2.20	5.05	.0082

Figure 17. Rework of Impeller Leading Edge.

## INSTRUMENTATION

### VEHICULAR INSTRUMENTATION

The vehicular instrumentation is defined as equipment mounted on the test vehicle for monitoring and controlling the test. Specific instrumentation includes:

1. Vibration indicators.
2. Bearing load, temperature, and lube supply.
3. Vehicle skin temperatures.
4. Vehicle cavity pressures.

The vibration indicators consisted of six accelerometers located on the front frame and midframe in the vertical, horizontal, and axial directions. Also, the front and rear squirrel cages were strain-gaged to measure the rotor-to-stator vibrational amplitude. Since the rotor system was soft-mounted, these strain gages provided a better indication of vibration level than the casing-mounted accelerometers. Two proximity probes were used to measure the flexible coupling vibration at the gearbox and vehicle ends, and these were oriented in approximately a vertical plane.

The aft bearing axial load was determined using a three-pedestal load cell (see Figure 18). The load cell had a temperature compensated strain gage bridge circuit in each pedestal to measure the compressive stress. The load cell was statically calibrated in the bearing support housing prior to test. The results of the calibration are shown in Figure 19. Periodic static checks of this calibration were made during the test by applying external air pressure to the balance piston. The check calibrations were made to reset the zero on the electronic readout equipment and to verify the signal at a 200-lb load.

The forward and aft bearing outer race temperatures were observed using Chromel-Constantan thermocouples mounted in the bearing housing. Two thermocouples were used for each bearing. A further monitor of the bearing condition was established by measuring the lube oil supply and scavenge temperatures.

A magnetic chip detector was installed in each scavenge line. These detectors would close an alarm circuit after a number of particles were captured. During the axial component test only a few particles were observed on the aft detector, but an analysis of these particles indicated M50 bearing material and positively identified a thrust bearing problem.

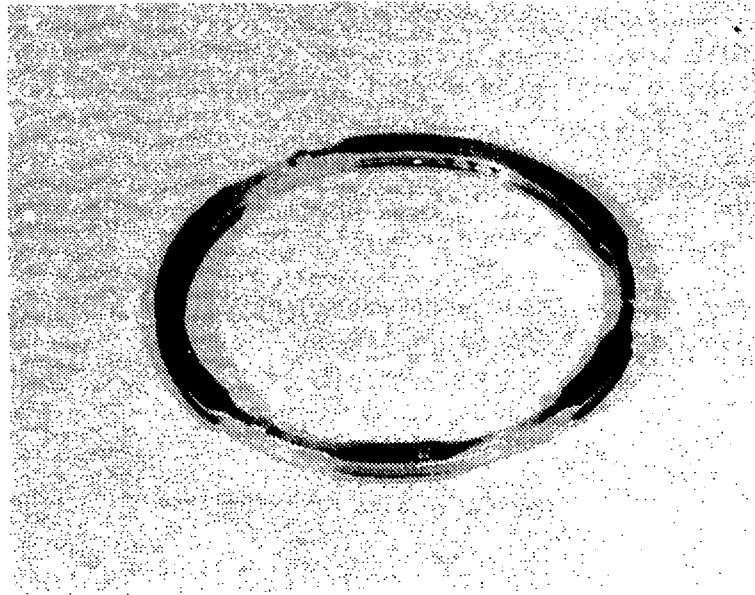


Figure 18. Load Cell.

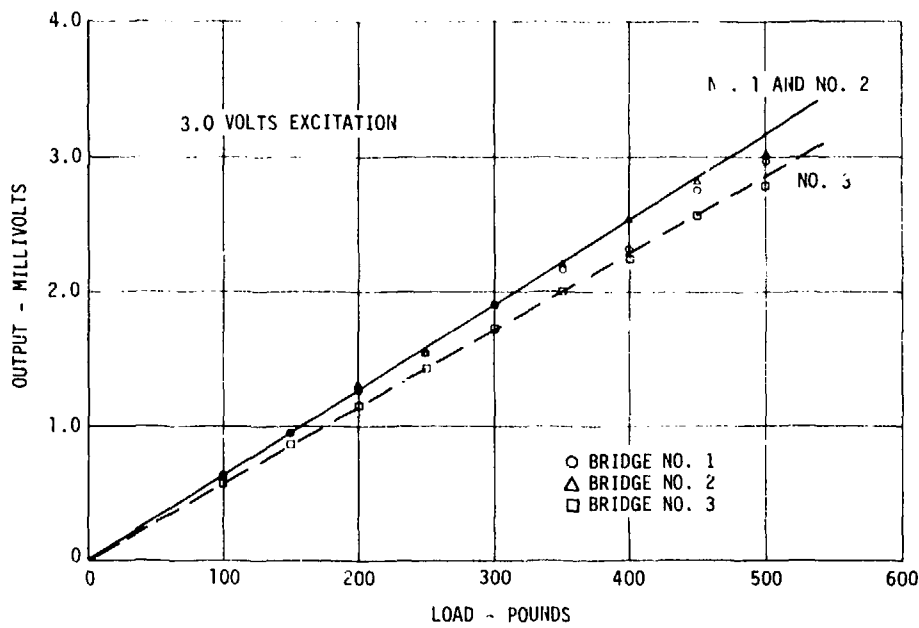


Figure 19. Load Cell Calibration.

The lube supply temperatures to the bearings and oil dampers were measured with Chromel-Alumel thermocouples mounted in the supply lines. Additional thermocouples were located in the oil scavenge lines from the forward and aft sumps.

A total of nine skin temperature thermocouples were located on the test vehicle as shown in Figure 20. These Chromel-Constantan thermocouples were used on the CCV-I and FCV-I tests.

A total of 15 vehicle cavities were instrumented for observing the various internal seal supply and vent pressures.

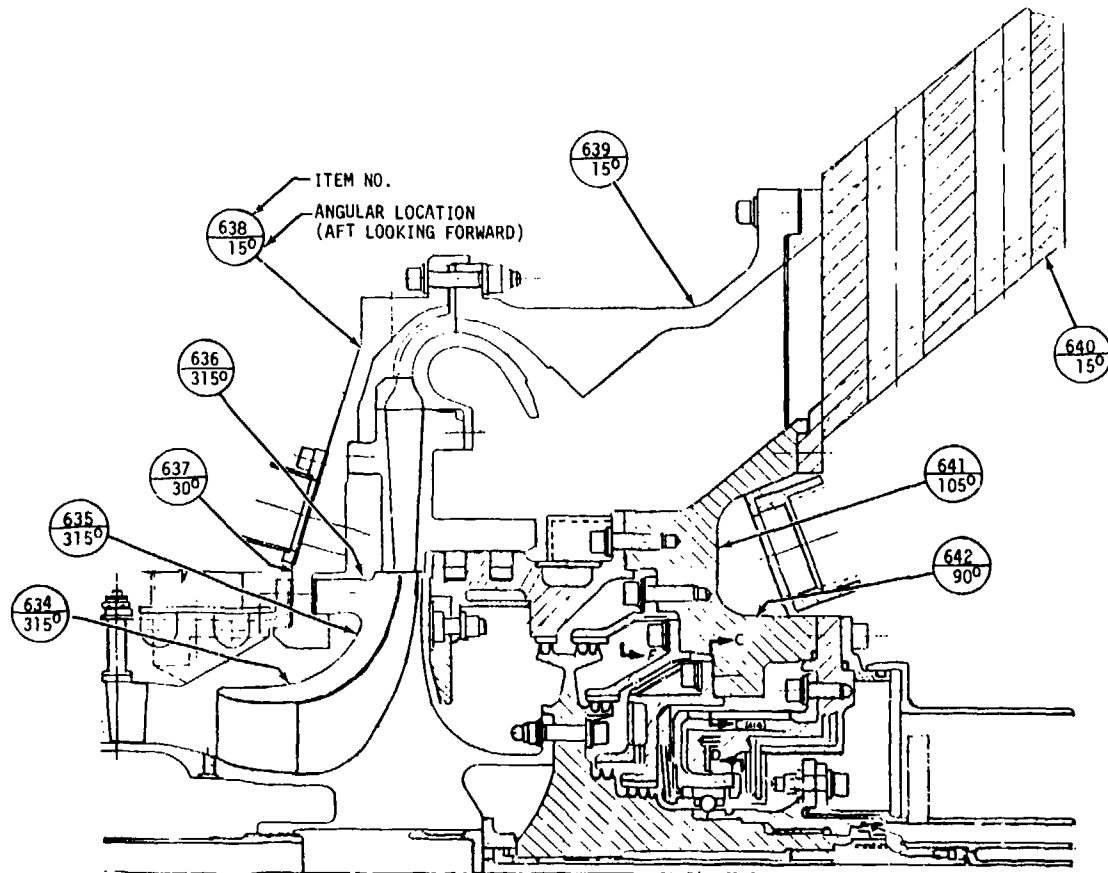


Figure 20. Compressor Skin Thermocouples.

## AERODYNAMIC INSTRUMENTATION

The various aerodynamic measurement planes are shown schematically in Figure 21.

### Thermocouple Measurement System

The thermocouples were connected to the automatic data recording system through an intermediate reference junction constructed of a solid copper biscuit which was heavily insulated from the environment to produce an isothermal junction. The reference junction was mounted on the vehicle so that the thermocouple lead wires could be connected directly to the copper block, thereby eliminating all external connections which are sources of measurement error. Copper lead wires were used to connect with the data recording system to avoid errors associated with spurious EMF's. An ice junction was also connected to the reference junction to determine the potential of the reference junction relative to ice. The temperature level of any thermocouple could then be determined by summing the reference-to-ice and reference-to-thermocouple potentials. Separate ice junctions were used to establish the reference junction potential for the Chromel-Constantan and Chromel-Alumel thermocouples.

It should be noted that the corrections for thermocouple error from standard are a function of millivolt signal level and not temperature level. Therefore, the wire calibration was applied to the reference-to-thermocouple potential level and not to the thermocouple-to-ice potential level.

### Compressor Inlet Instrumentation (Plane A)

The compressor inlet instrumentation consisted of 24 inlet screen-mounted thermocouples, 8 inlet bellmouth throat static pressures, and 3 inlet total pressures. The inlet thermocouples were constructed using insulated Chromel-Constantan thermocouple wire and were calibrated to 150°F. The eight inlet static pressures were equally spaced around the bellmouth throat. The inlet stagnation pressure was the test tank inlet plenum pressure. The stagnation pressure for the ACV test was recorded using two baskets attached to the inlet screen and one basket mounted from the test tank wall. The FCV test had four total pressure sensors mounted at the inlet screen where one sensor was used for facility control. The pressures on the inlet screen were averaged for the inlet total pressure. Barometric pressure was recorded using a precision instrument.

The bellmouth was calibrated during the inlet guide vane static blow tests. Using the nominal throat area of 31.548 in<sup>2</sup>, the flow coefficient was determined as

$$C_D = .984 - .07 (P_A - P_A)/P_A \quad (1)$$

### Axial Discharge Instrumentation (Plane B)

The axial discharge instrumentation consisted of total pressure and temperature rakes and casing wall static pressures. The rakes were positioned to observe the flow at the center of six equal annulus areas in two circumferential locations. The casing had provisions for three rakes each for total pressure and temperature, so three different rake configurations were required. The requirement for six immersions was determined from the Phase II Design Study<sup>1</sup> in order to have significantly lower bias error. The three rake configurations, Types A, B, and C, are shown in Table 8.

Immersion % Depth	Type A	Type B	Type C
7.05	yes	yes	-
21.68	yes	-	yes
37.10	-	yes	yes
53.47	yes	yes	-
70.97	yes	-	yes
89.89	-	yes	yes

The design passage for the probe spacing had a tip radius of 2.3390 in. and a hub radius of 1.5733 in. Six-element probes were not used because it would result in excessive probe blockage.

The total temperature rakes were constructed from 0.040-in.-diameter magnesium oxide (MgO) insulated Type E thermocouple wire. The design used a semiclosed bead construction. The rakes were calibrated for recovery and wire error. An additional check was made on the wire lot to be sure it was within the inhomogeneity tolerance (spurious EMF's from external wire temperature gradients).

The total pressure rakes were fabricated from 0.032-in. OD x 0.005-in. wall tubing, and the tube ends were chamfered to a 50-degree included angle for better off-angle recovery. The rakes were each calibrated for total pressure recovery versus pitch and yaw angle.

The Plane B static pressure was determined from six taps located at the following angles (aft-looking-forward): 31°15', 76°15', 121°15', 211°15', and 301°15'. These taps were unequally located to avoid interference with the Plane B bleed air bosses and rake instrumentation pads.

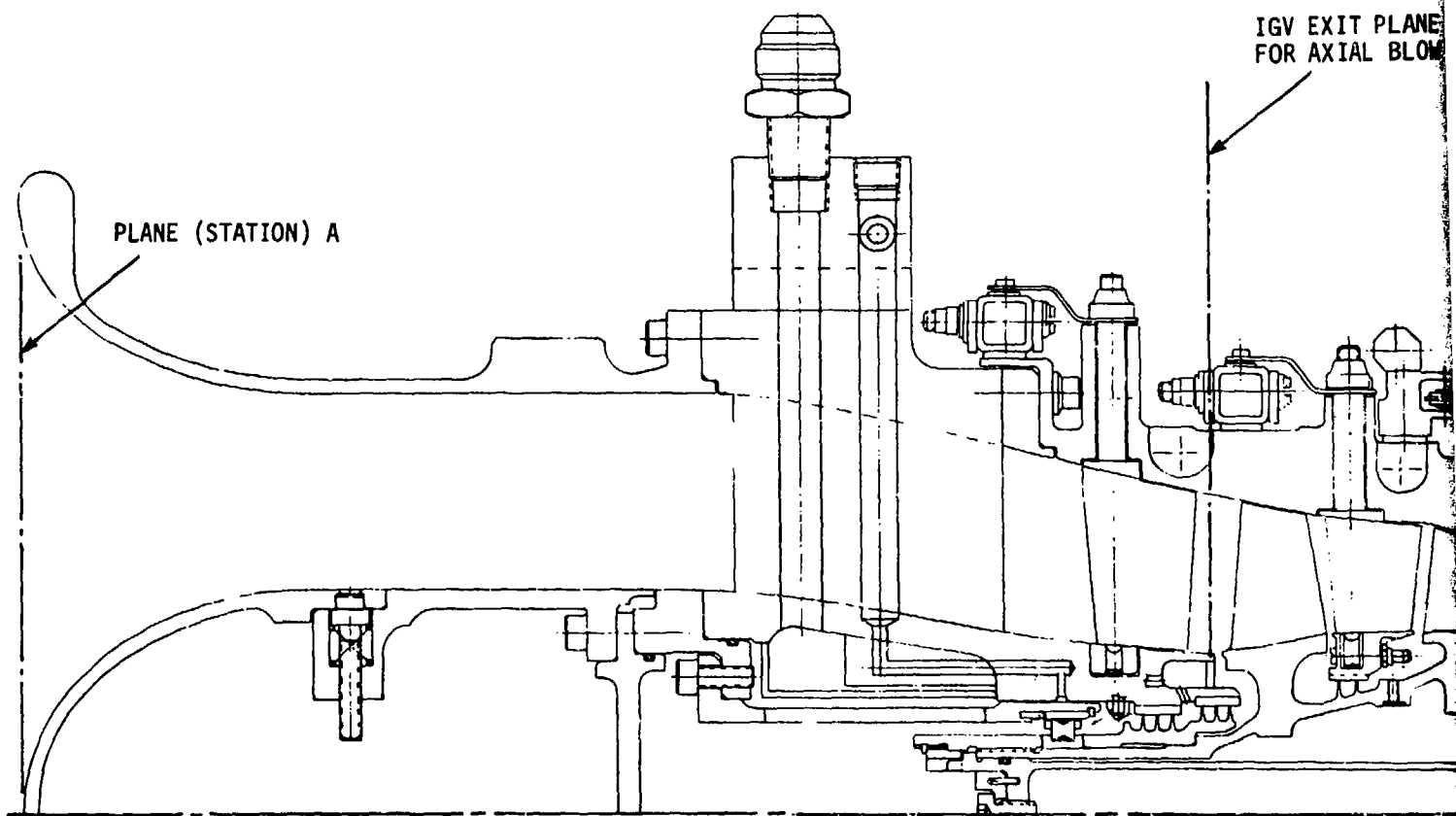
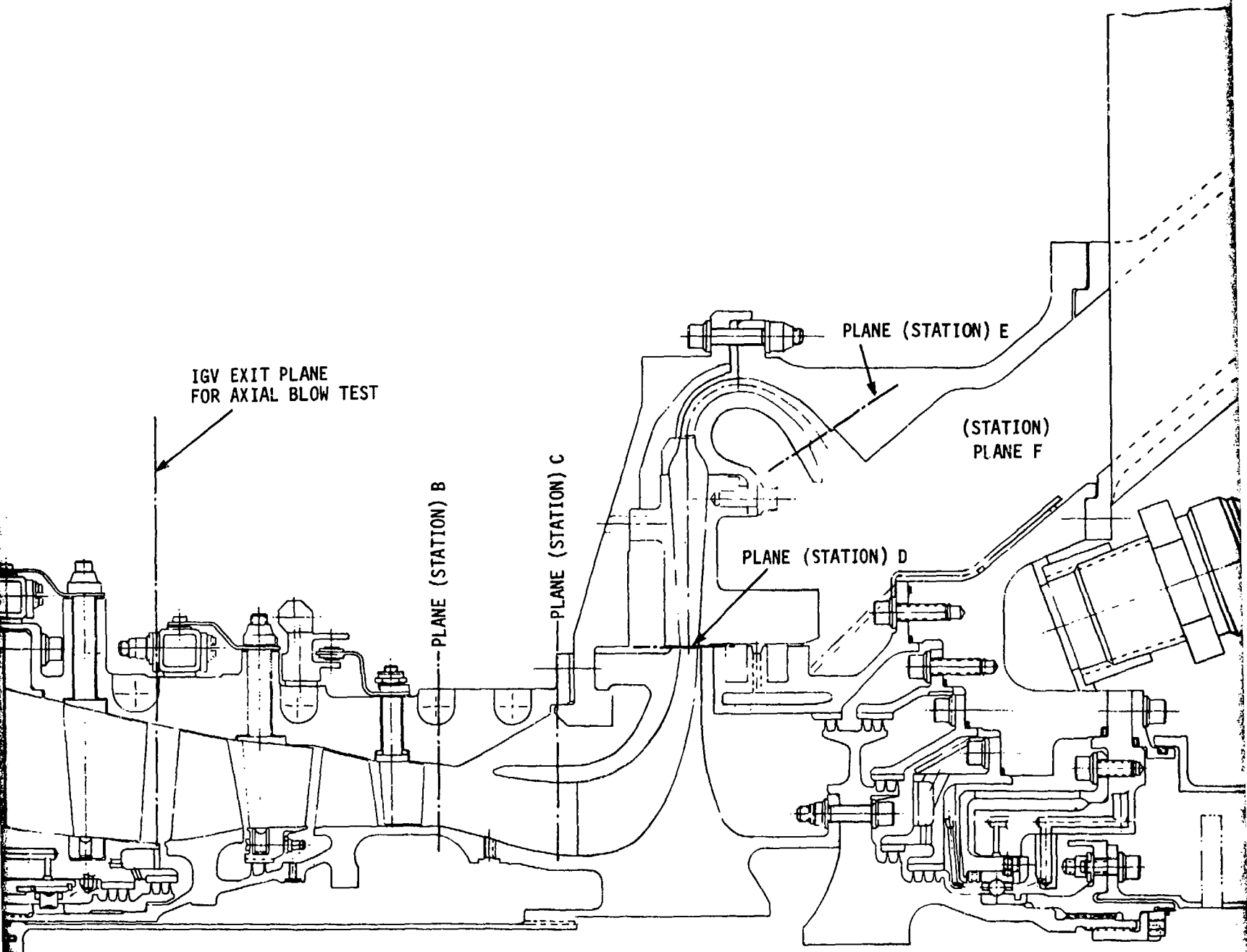
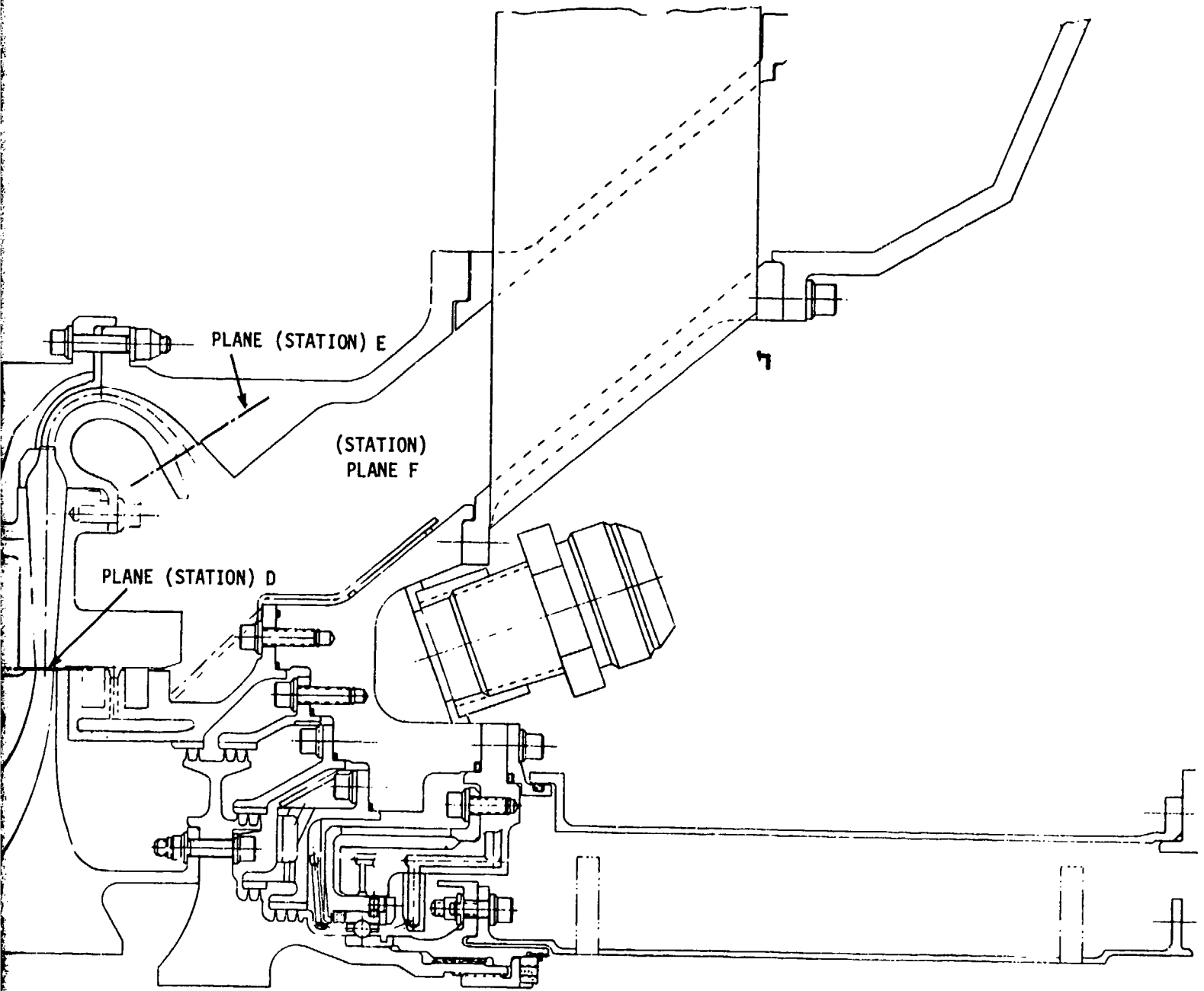


Figure 21. Axial-Centrifugal Compressor Instrumentation Planes.



mes.

2



The construction of the tap was a double-drilled hole 0.066-0.071 in. diameter to within 0.080 in. of the flow path and drilled through using a 0.017- to 0.022-in.-diameter drill. The edge of the drilled hole was left sharp and any burrs were stoned smooth with the flow path.

The axial location of the Plane B static pressure taps was between the second stator trailing edge and the slot for intercompressor bleed air. The sensing plane of the rakes was near the leading edge of the slot because the rakes were installed through this bleed slot to avoid special holes and flush plugs when the rakes were not in place. The flow path radii at the Plane B static pressure taps were 2.3604-in. OD and 1.6151-in. ID.

#### Centrifugal Impeller Inlet (Plane C)

The inlet of the centrifugal impeller was instrumented with six shroud static pressures which were equally spaced about the circumference. For the tests when the impeller was not installed, additional instrumentation was included (ACV test and centrifugal IGV blow test). This additional instrumentation consisted of a 3-parameter Cobra probe and a 15-element wake rake. The 3-parameter, 0.125-in.-diameter Cobra probe measured total pressure, angle, and temperature, and the probe was calibrated for angle and recovery.

The wake rake had 15 elements spaced along a radial arc to span about 2 blade pitches (see Figure 22). This wake rake was actuated in the radial direction to determine radial and circumferential total pressure profiles. The wake rake elements were connected to the automatic data recording system and were included on every data reading. During most of the ACV test, the probe was at 47% immersion (50% nominal annulus area).

#### Compressor Static Pressures

The static pressures can be grouped into three major areas: (1) axial compressor casing, (2) impeller shroud, and (3) centrifugal diffuser. This section describes the size and location of the static pressure taps in the above sequence. Unless otherwise specified, all static taps were constructed using an 0.066-to 0.071-in.-diameter counterbore up to within 0.080 in. of the flow path, and the sensing hole was drilled through at a diameter of 0.017-0.022 in. All holes were smooth with the flow path and had sharp edges.

The axial casing was used on the ACV, FCV, and axial IGV blow tests. The centrifugal casing was used on the CCV and centrifugal IGV blow tests.

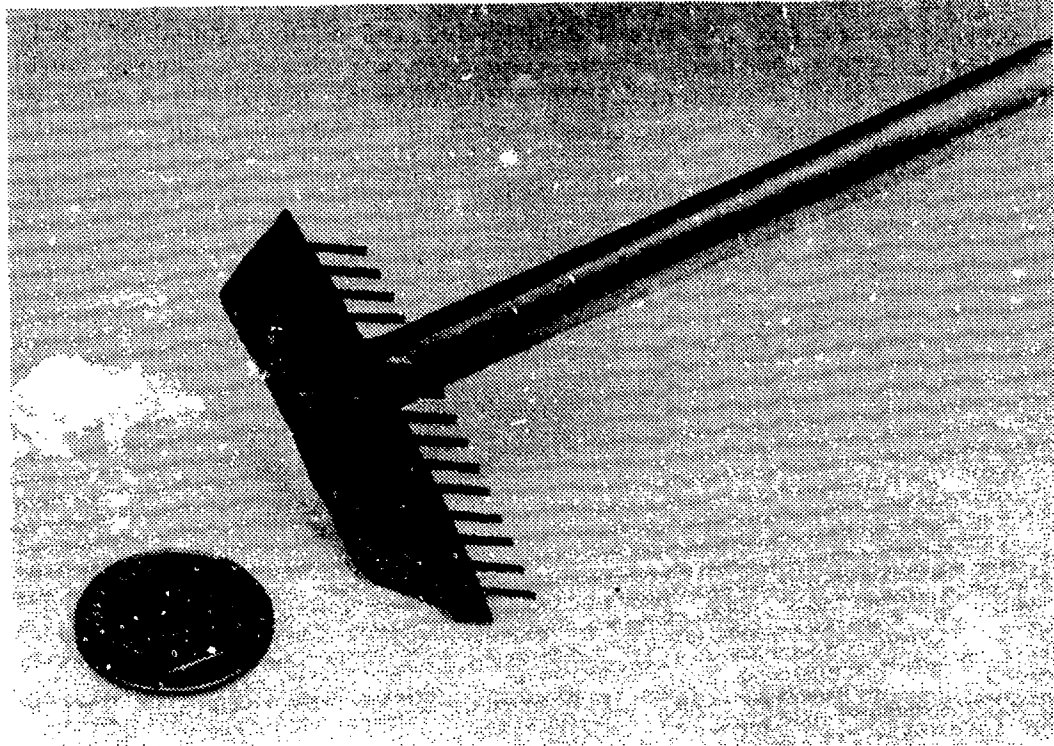


Figure 22. Wake Rake.

An unwrapped axial casing drawing is shown in Figure 23 which identifies the tap locations for the axial compressor casing. Figure 23 also shows the spatial relationship between static taps, rakes, strain gages, and vane-mounted thermocouples used on the ACV test. The item numbers shown in Figure 23 correspond to the identification printed out on the ACV data sheets. Static taps were located at the inlet and exit of each vane row in three clusters of four taps for a total of 12 taps per axial station.

The static pressure taps on the centrifugal inlet casing had three clusters of four taps installed at the IGV inlet and exit. The remaining nine taps were distributed along the flow path.

The partial impeller shroud, used for the ACV and centrifugal IGV blow tests, is shown in Figure 24. This partial shroud formed part of the intercompressor duct and the centrifugal inducer flow path. The wall static tap locations are indicated in Figure 24.

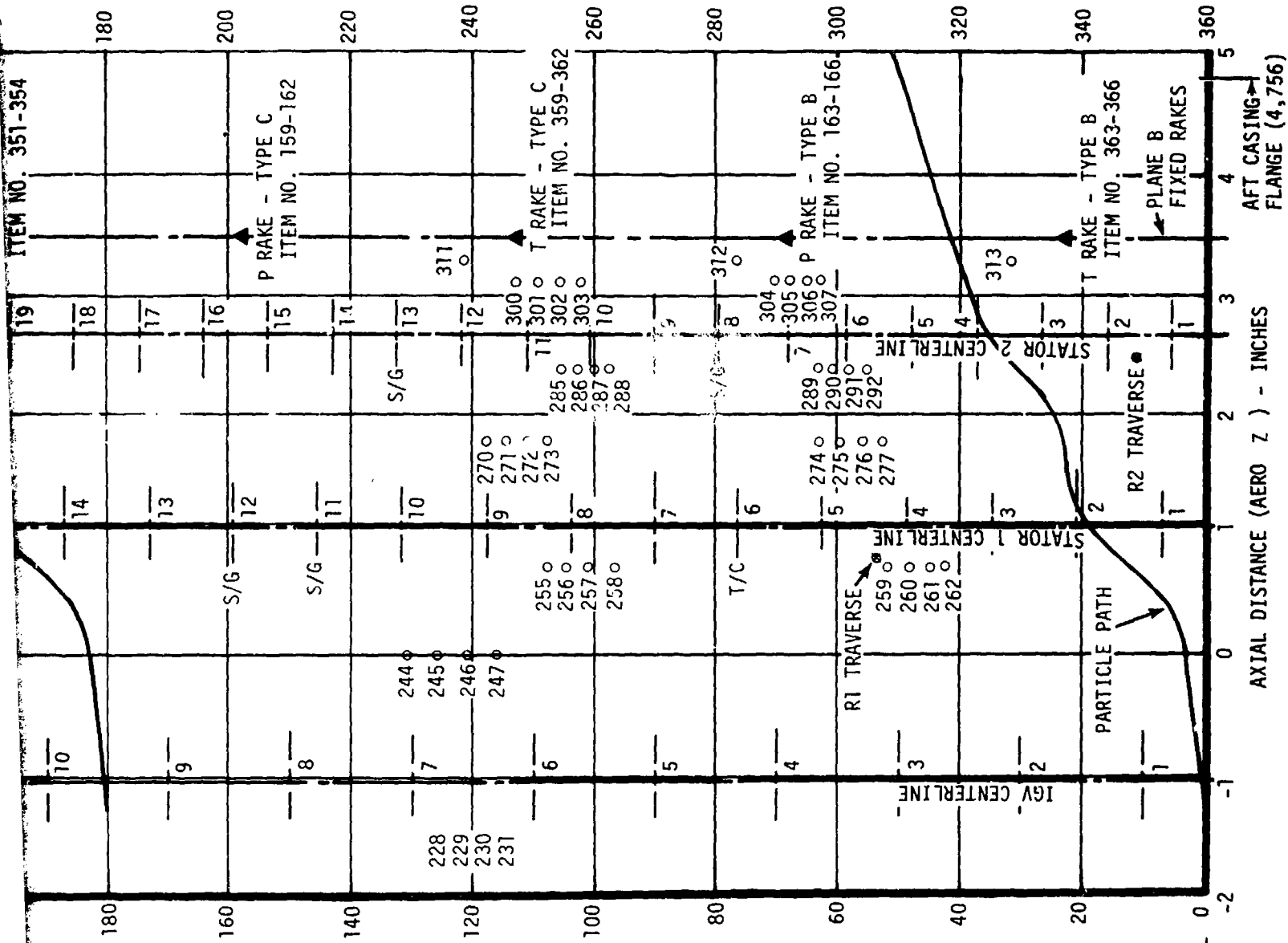


ANGULAR POSITION IN DEGREES, AFT LOOKING

CASING  
BOTTOM

CASING TOP ZERO DEGREES

ANGULAR POSITION IN DEGREES, FORWARD LOOKING



2

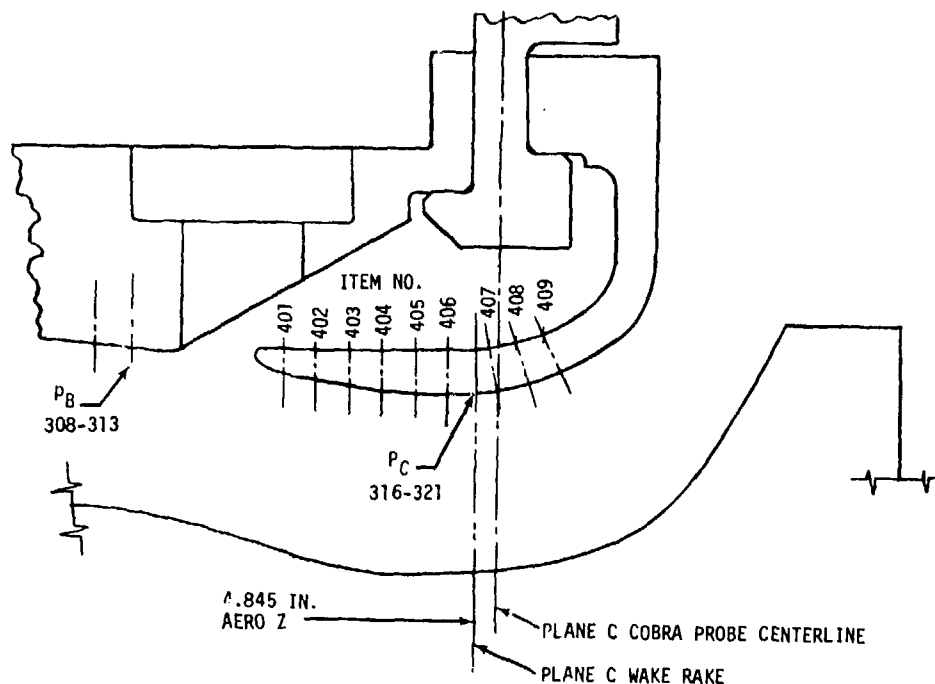


Figure 24. ACV Centrifugal Inlet Instrumentation Locations.

The impeller shroud taps were constructed differently because the nickel-graphite coating applied to the shroud would not form a sharp-edged hole. This problem was overcome by drilling 0.049-0.046 in. diameter through holes for metal tubing which was made flush to flow path contour. The tubing produced sharp-edged holes and was routed directly to the data recording system. A schematic of the static pressure taps is shown on Figure 25, and Table 9 provides data on the tap location as a percentage of the shroud length from impeller leading edge to trailing edge.

Diffuser static pressure taps were provided along a single conical passage with three additional passages instrumented for inlet and throat static pressure for a total of 29 static taps. The flow from the diffuser entered a deswirl vane row. Alternate deswirl vane row passages were instrumented to observe wake flow and core flow passages, since there were twice the number of vanes in the deswirl row as there were passages in the diffuser. The meridional locations of the various diffuser static taps are shown in Figure 25. Twelve static taps were used at the discharge of the exit annular diffuser with six equally spaced taps on the outer wall opposing six taps on the inner wall. The average of these twelve taps was used to determine the compressor outlet static pressure.

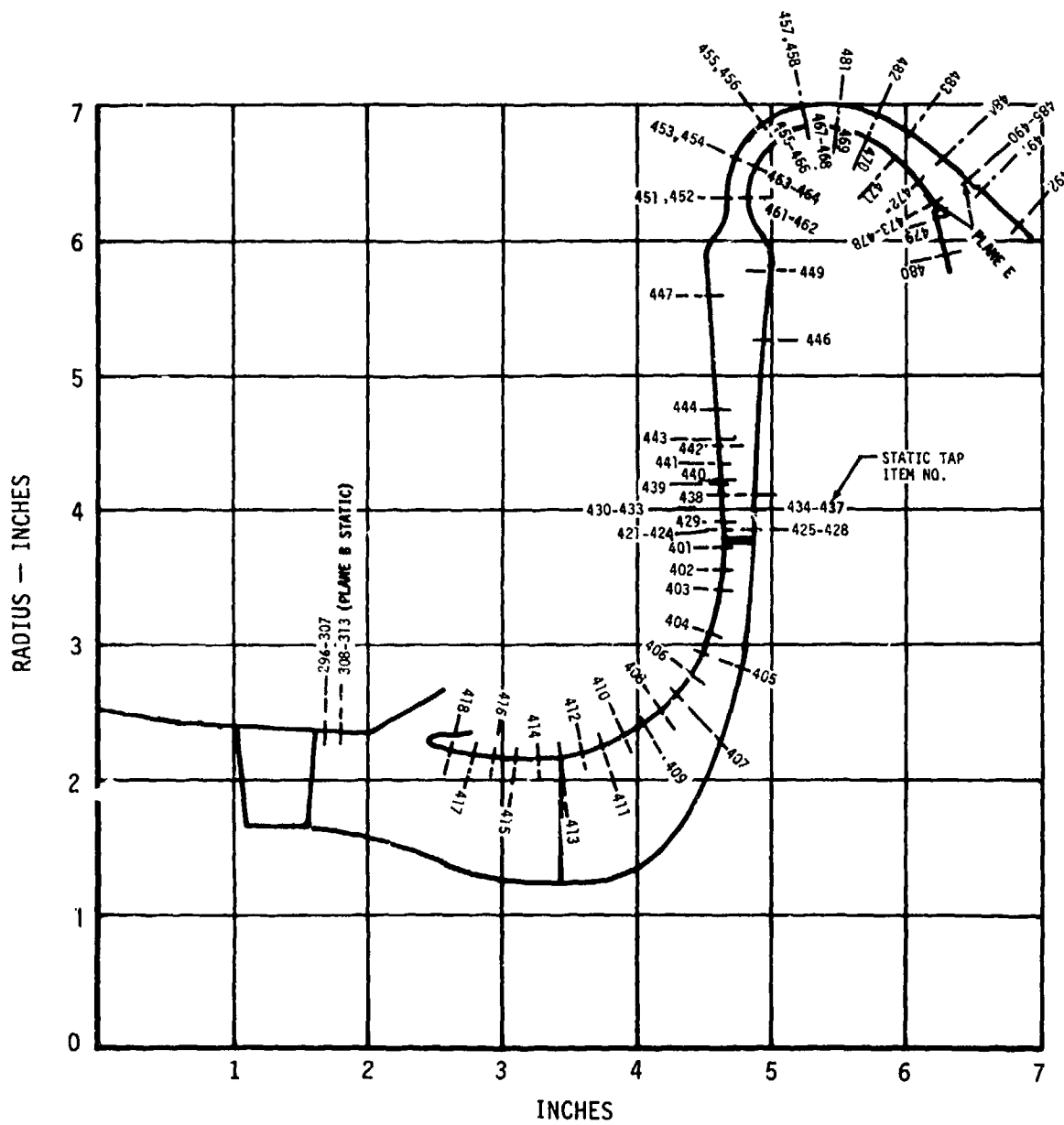
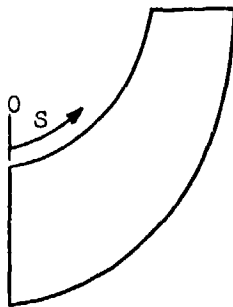


Figure 25. Centrifugal Static Pressures - CCV-I and FCV-I.

TABLE 9. CCV-I IMPELLER SHROUD STATICS

$$S_T = 2.185 \text{ in.}$$



Tap No.	S (in.)	$S/S_T \times 100\%$	Item No.
8	-1.64	-37.6%	418
9	-1.30	-29.8	417
10	-.99	-22.7	416
11	-.67	-15.3	415
12	-.33	-7.5	414
13 (L.E.)	0	0	413
14	.32	7.3	412
15	.65	14.9	411
16	1.99	22.7	410
17	1.32	30.2	409
18	1.65	37.8	408
19	1.97	45.0	407
20	2.34	53.5	406
21	2.68	61.3	405
22	3.00	68.6	404
23	3.65	83.5	403
24	3.97	90.9	402
25	4.28	98.0	401

#### Centrifugal Discharge (Plane E)

The total pressure and temperature rakes for Plane E are shown in Figures 26 and 27. These four-element rakes were equally spaced across the discharge passage and located  $120^\circ$  apart (see Figure 28).

The discharge total pressure was also measured with a 15-element wake rake that was traversed to various immersions. This rake design was similar to the rake shown in Figure 22.

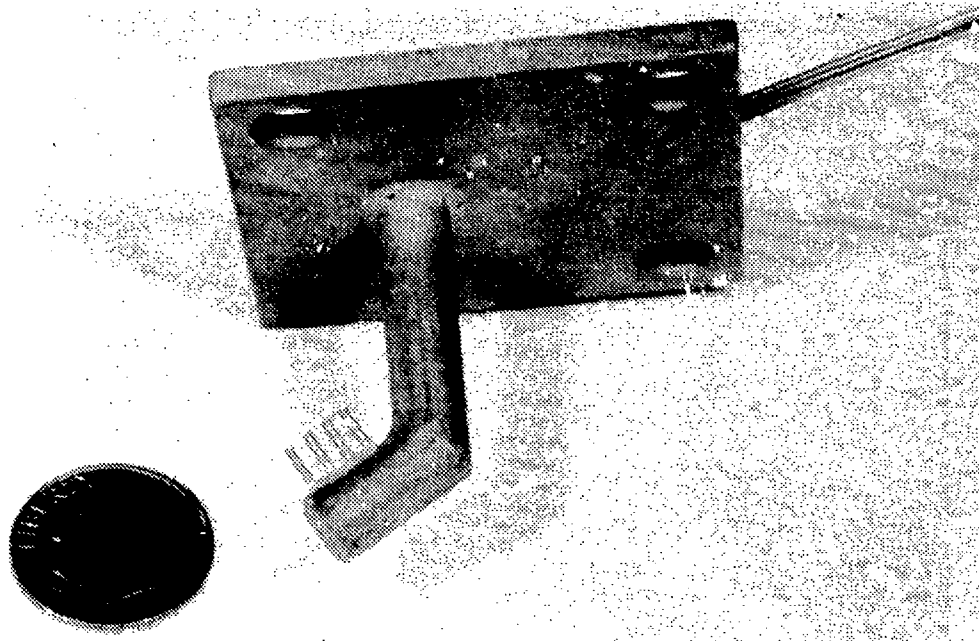


Figure 26. Plane E Total Pressure Rake.

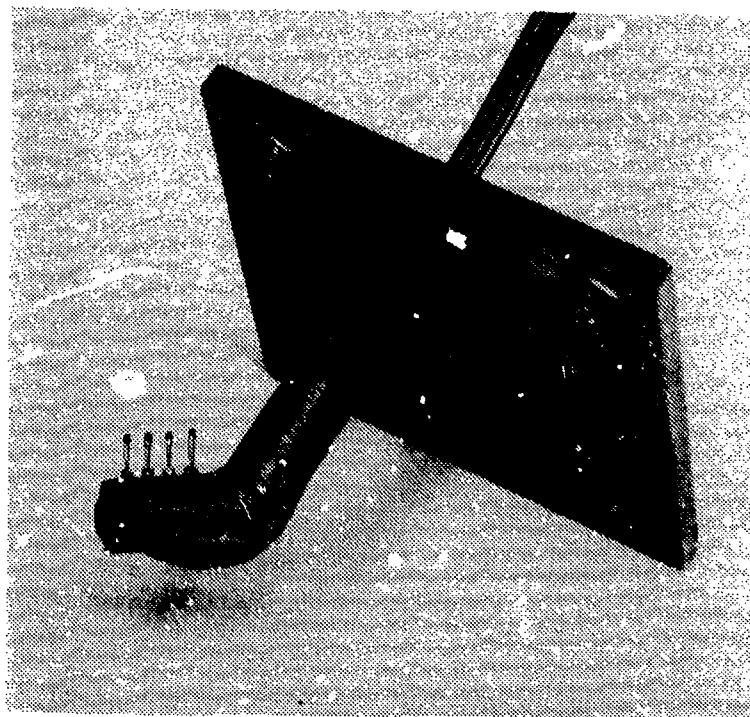


Figure 27. Plane E Total Temperature Rake.

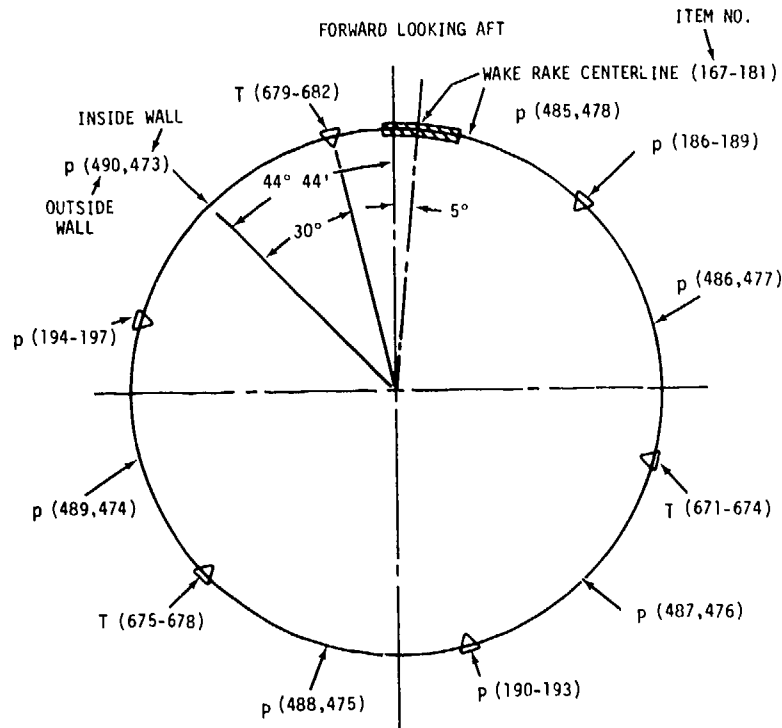


Figure 28. Plane E Instrumentation.

#### Axial Rotor Exit Traverse Probes

A miniature Cobra probe was made to measure rotor outlet total pressure, angle, and temperature. This probe had a nominal stem diameter of 0.094 in. and is shown in Figure 29. The probe was constructed using three pressure tubes of 0.022-in. OD x 0.005-in. wall and an unshielded Chromel-Alumel thermocouple made from 0.022-in.-diameter MgO tubing. Two probes were fabricated and calibrated from 0.2 to 0.8 Mach number at the design pitch angle of  $-15^\circ$ .

#### Vane-Mounted Thermocouples

Thermocouples were mounted in three Stage 1 stator vanes. The 47% immersion position was selected to approximate the mean streamline location. The thermocouple junction was mounted 0.005 in. off the vane near the pressure surface trailing edge.

#### Airflow Measurement

The compressor airflow was measured using a downstream choked venturi. A check on the compressor flow is made using the inlet bellmouth. A calibration of the inlet bellmouth was conducted during the blow tests,

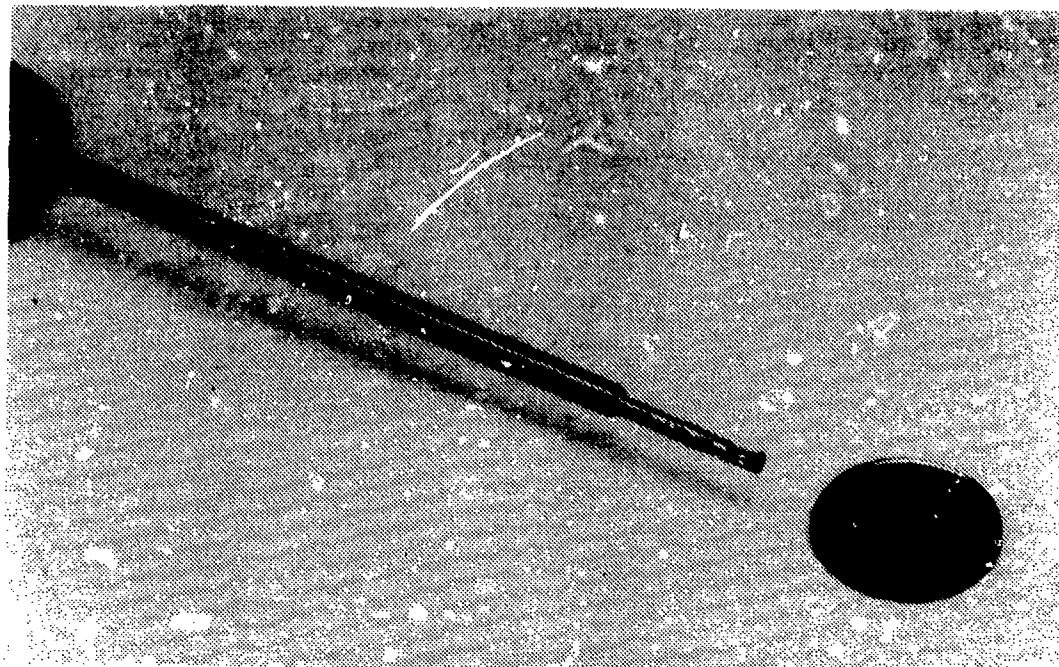


Figure 29. Cobra Probe.

and these results are shown in Figure 30. Compressor bleed airflows were determined using separate venturi measurements and were summed with the discharge venturi flow for the total compressor inlet airflow.

#### IGV BLOW TEST

##### Centrifugal IGV Blow Test

The inlet casing used for the centrifugal stage component test was tested to measure inlet guide vane losses and flow profile. The Plane C impeller inlet instrumentation that was used on the axial component test was also employed for this test. The Plane C instrumentation is discussed under "Centrifugal Impeller Inlet (Plane C)" (pg 57).

The static pressure instrumentation on the inlet casing was identical to centrifugal component test, since the same hardware was used. The axial compressor test dummy centrifugal shroud was also used, and the static taps are shown in Figure 24.

The inlet airflow was measured by a choked venturi mounted in the inlet supply line, since the test rig discharged to the atmosphere (see Figure 7). Inlet total temperature was determined using eight screen-mounted Chromel-Constantan thermocouples. The inlet total pressure was measured in the inlet plenum with four total pressure baskets.

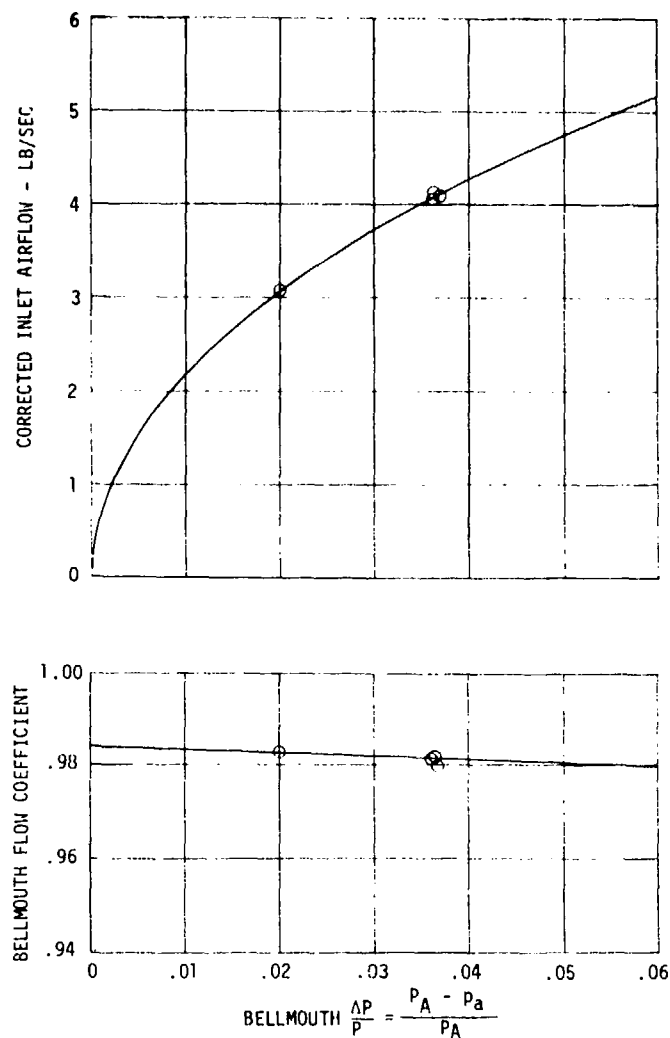


Figure 30. Bellmouth Airflow.

### Axial IGV Blow Test

The instrumentation required for the axial compressor test presented a more difficult problem because of the close proximity of the sensors to the guide vane and the wider range of angle variation to be measured (see Figure 21). The standard compressor casing was used so any rework could not interfere with future component tests. The rework limitation and angle variation discouraged the use of a large wake rake similar to the Plane C or E design, so it was decided to mount a low profile rake from an indexable centerbody which could sweep at least two vane pitches. The hardware is shown in Figure 8 where the one five-element rake measures total pressure and the opposite rake measures flow angle. The two rakes are coupled together via bevel gears to a common yawing

actuator. The entire centerbody assembly is piloted off the front frame and is indexed in the circumferential direction using a pair of remotely actuated push-pull screw jacks.

The casing static pressures were the same as the axial and combined compressor test because the same casing was used. The rotating centerbody had four inner wall static pressures at 40°, 100°, 220°, and 280° to sense the static pressure at similar angular settings from four vanes.

The inlet airflow, total pressure, and temperature measurements were identical to the setup for the Centrifugal IGV Blow Test.

#### FCV-II Second Stator Exit Traverse

A special test apparatus was designed to actuate a three-element Cobra probe in the radial and transverse directions. This probe was installed through one of the six bleed bosses and did not require any casing rework because the existing intercompressor bleed slot was adequate (see Figure 31). This positioned the probe axially about 1-1/2 chords downstream of the second stator vane. In the design of this traverse

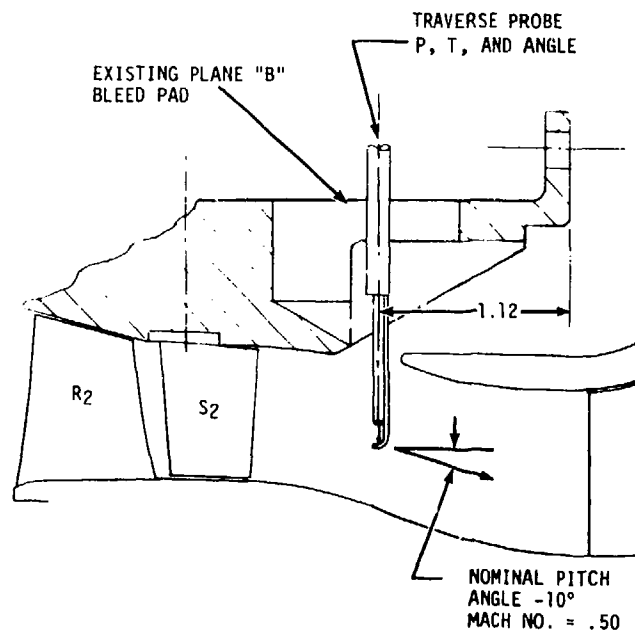


Figure 31. Axial Outlet Traverse Setup.

system, three modes of operation were considered (see Figure 32);

1. X-Y traverse.
2. Inverted R- $\theta$ .
3. R- $\theta$  traverse.

The X-Y traverse mode was selected because it offered the simplest actuation and sealing solution. A standard traverse probe and actuator were mounted on a movable shoe in a conventional fashion to achieve the radial travel and probe yawing capability. A second standard actuator was mounted to this shoe which travelled back and forth in the transverse direction. During a data reading the first actuator was fixed at a preset probe immersion while the second actuator travelled in the transverse direction to obtain the circumferential P, T, and angle data. Since the probe was at a fixed height from the compressor centerline, the immersion radius varied during the reading and must be considered in the analysis of the data. Since the travel requirement for this installation was only 0.90 inch, the immersion change was small. The R- $\theta$  traverse mode would permit constant radius data and would be a better choice for larger circumferential travels.

A calibrated 0.094-in.-diameter traverse probe was installed for the test. The probe design was identical to the axial rotor exit traverse probes.

#### BLADE AND VANE STRAIN GAGES

The Stage 1 and Stage 2 stator vanes were strain-gaged for both the axial and full compressor tests. The Stage 1 and Stage 2 rotor blades and the full impeller blades were strain-gaged for the combined compressor test. The axial compressor and centrifugal compressor inlet guide vanes were not instrumented.

#### Stator Vane Strain Gages

Figures 33 and 34 show the strain gage locations for the axial compressor and combined compressor tests, respectively. The gage locations for the axial compressor test were chosen to provide coverage of the calculated first five natural modes and estimated chordwise bending modes. The gage locations specified for the combined compressor test were selected from calculated data to give good coverage of the first four modes.

The 1/16-inch grid strain gages were cemented directly to the airfoil surface and the lead wires were sandwiched between layers of insulating silk which were cemented to the airfoil surface. This method of mounting provided a low profile to minimize aerodynamic losses. The strain gage lead wires were routed through a hole which was drilled through the center of the vane stem.

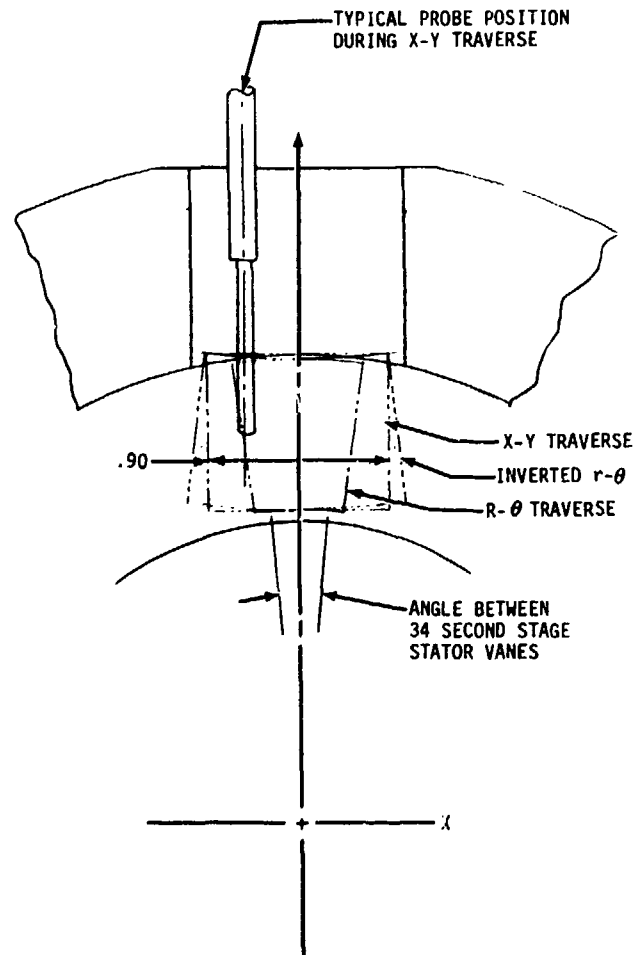
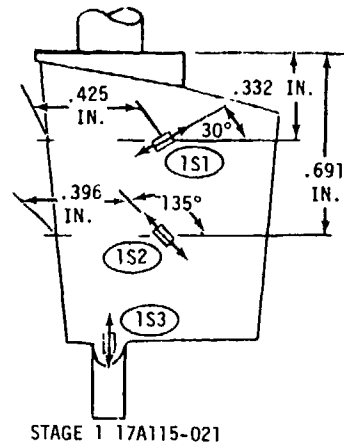


Figure 32. Axial Outlet Traverse Modes.

The Stage 1 and Stage 2 rotor blades and the full impeller vanes were instrumented for the FCV-I combined compressor test. The gage locations shown in Figure 35 were determined by stress distribution testing of a large-scale airfoil model. For this test, gages were mounted on the airfoils as shown in Figure 36. The Stage 1 blade sample was instrumented with 55 strain gages spaced at approximately 0.15 inch, the Stage 2 with 64 gages approximately 0.10 inch apart, and the impeller vane with 33 gages approximately 0.15 inch apart. The strain-gaged airfoils were vibrated at each of their natural modes and the stress distribution was recorded for each mode. From this data the strain gage locations were selected to give coverage of all modes through 35,000 Hz.



NOTES:

- 1) All gages to be located on concave side of airfoils.
- 2) One gage per vane (total six gages).
- 3) All gages to be 1/16 in. grid.
- 4) Gage 1S3 to be located at airfoil - spindle blend on thin section.
- 5) Gages 2S1 and 2S2 to be located close to airfoil trailing edge.
- 6) Strain gages and lead wire profile to be minimized for low aerodynamic loss.

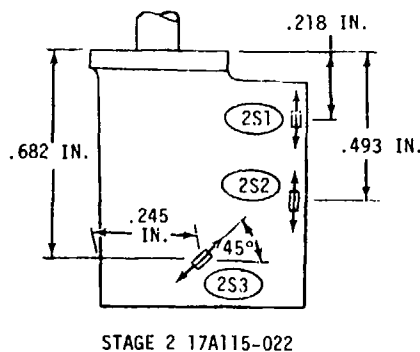
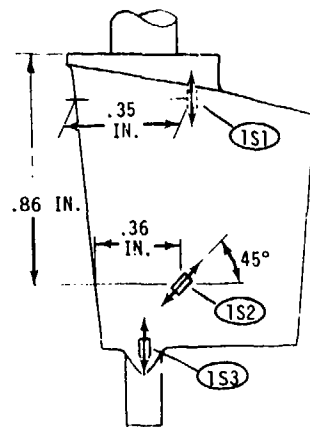


Figure 33. ACV Stator Strain Gage Locations.

The 12 strain gages were calibrated in the first mode to check linearity and sensitivity of stress versus tip amplitude. The scope limits or maximum allowable alternating stresses were determined from the stress distribution test results which correlate the maximum airfoil stress to the stress at the gage location for each of the natural modes.

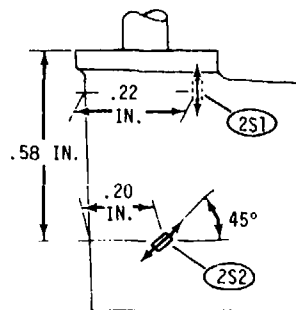
The rotor strain gages used for the full compressor test were cemented directly to the airfoil surface and used insulated lead wires cemented to the airfoil with a silk fabric covering. The lead wires were routed as shown in Figure 16. The leads were brought through 1/16-inch-diameter holes from the flow path side to the inside of the blisks and impeller where they were cemented and routed aft. Four 1/8-inch-diameter holes were used to carry the leads through the disk portion of the impeller. On the back side of the impeller, the leads were tack-welded with nichrome strips and routed into the plug which gathered the leads into a bundle at the rotor axis.



STAGE 1 17A115-021

NOTES:

- 1) Gages 1S1 and 2S1 to be located as close as possible to the fillet radius but not on it. Both of these gages to be on the convex side.
- 2) Gage 1S3 to be located on the thin section at the airfoil - spindle blend on the concave side.
- 3) Gages 1S2 and 2S2 to be located on the concave side.
- 4) One gage per vane (total 5 gages).
- 5) All gages to be 1/16 in. grid.
- 6) Strain gage and lead wire profile to be minimized for low aerodynamic loss.
- 7) Gages to be calibrated for stress vs amplitude in first two modes.



STAGE 2 17A115-022

Stage	Vane No.	Gage
1	1	1S1
1	5	1S2
1	10	1S3
2	10	2S1
2	1	2S2

Figure 34. FCV Stator Strain Gage Locations.

The lead wire bundle was supported in conduit tubes through the balance piston shaft and flexible coupling. This lead bundle passed through a 1/4-inch hole in the center of the high speed gearbox pinion gear and then on to the slip ring drive where the leads were attached to a rotating terminal board which plugged into the slip ring.

A 12-channel slip ring was used to transfer the strain gage signals from the rotor. This slip ring was mounted to the high speed gearbox through an isolation drive unit. This drive unit also served as a storage location for the diodes required to read out 12 strain gages with a 12-channel slip ring.

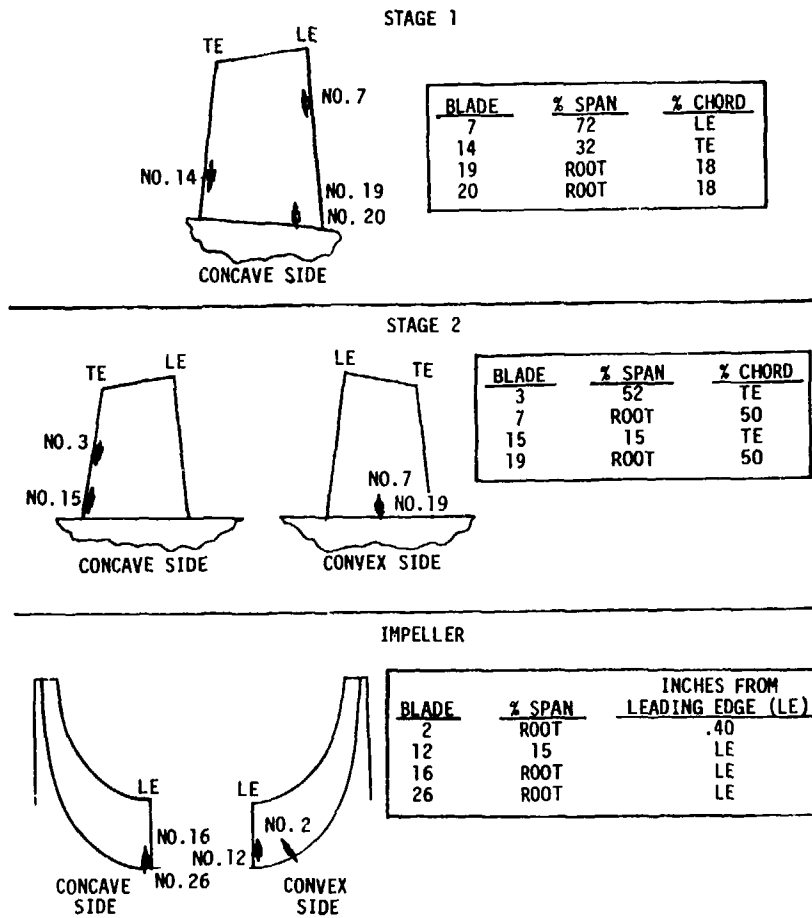


Figure 35. FCV Rotor Strain Gage Locations.

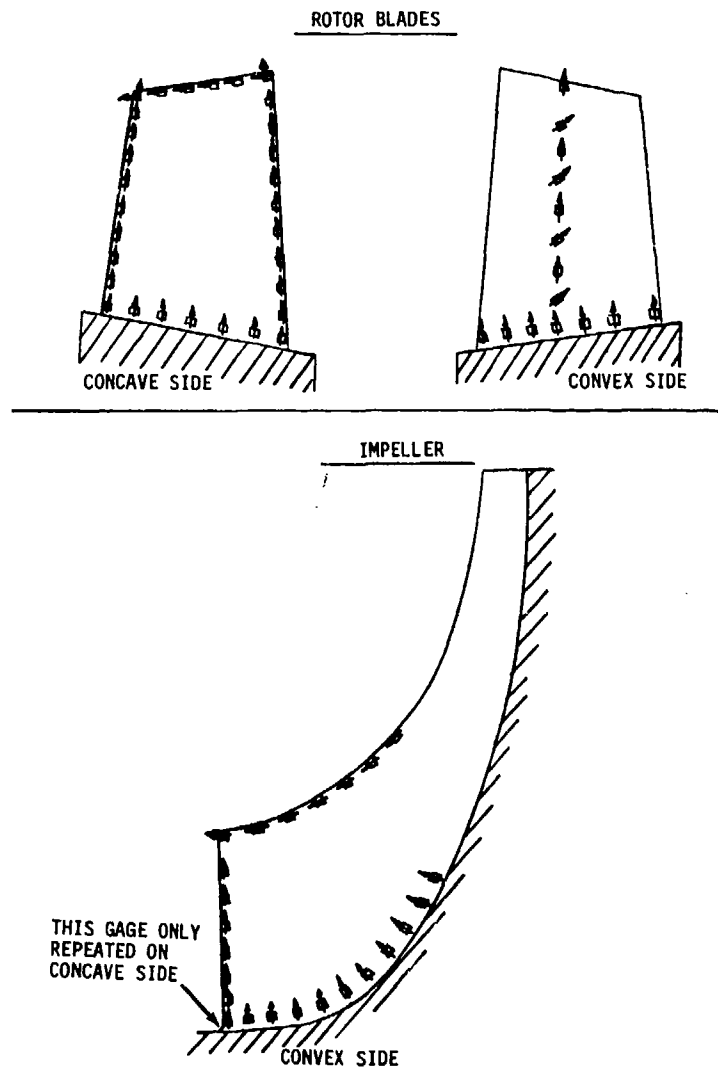


Figure 36. Strain Gage Locations - Stress Distribution.

## TEST EQUIPMENT AND PROCEDURE

The program consisted of tests conducted at both the Evendale and Lynn test facilities. Evendale tests included the axial and CCV-I centrifugal components and the static IGV blow tests. The Lynn facility testing included the combined compressors and subsequent centrifugal compressor tests. The Evendale and Lynn test equipment and support systems are described in this section.

### COMPRESSOR DRIVES

The Evendale axial and centrifugal component tests were carried out in the Aero Component Laboratory Cell A9E that is powered by a tandem pair of 350-horsepower variable speed induction motors (see Figure 37). These motors were provided with a variable frequency power supply from a variable RPM generator that was driven by a Dynamatic coupling from a 4500-hp constant speed motor. Compressor speed was varied by changing the generator RPM. The maximum speed of these motors is 20,000 rpm, so a 3.75:1 speed increaser gearbox was used for a speed capacity of 75,000 rpm. A flexible drive coupling was used to connect the gearbox to the compressor test vehicle.

The combined compressor tests were carried out in the Lynn Small Engine Compressor Test (SECT) facility. This facility was powered by a 15,000-hp steam turbine through a series of three-speed increaser gearboxes to a rated speed of 61,000 rpm.

### STATOR ACTUATION

#### Axial Test

The inlet guide vanes and Stage 1 vanes in the axial compressor test were actuated electrically. The two stages were equipped with a DC drive motor, screw jack actuator, motor control relay system, vane angle potentiometer, and analog function generator. A schematic diagram of the system for one stage is shown in Figure 38.

The control system provided automatic vane tracking as a function of speed but also had an override feature so the vane angles could be adjusted independently of speed. The vane angles were monitored on a panel meter which was used as the primary readout. A secondary readout was provided for the digital system to record vane angles on the data printout.

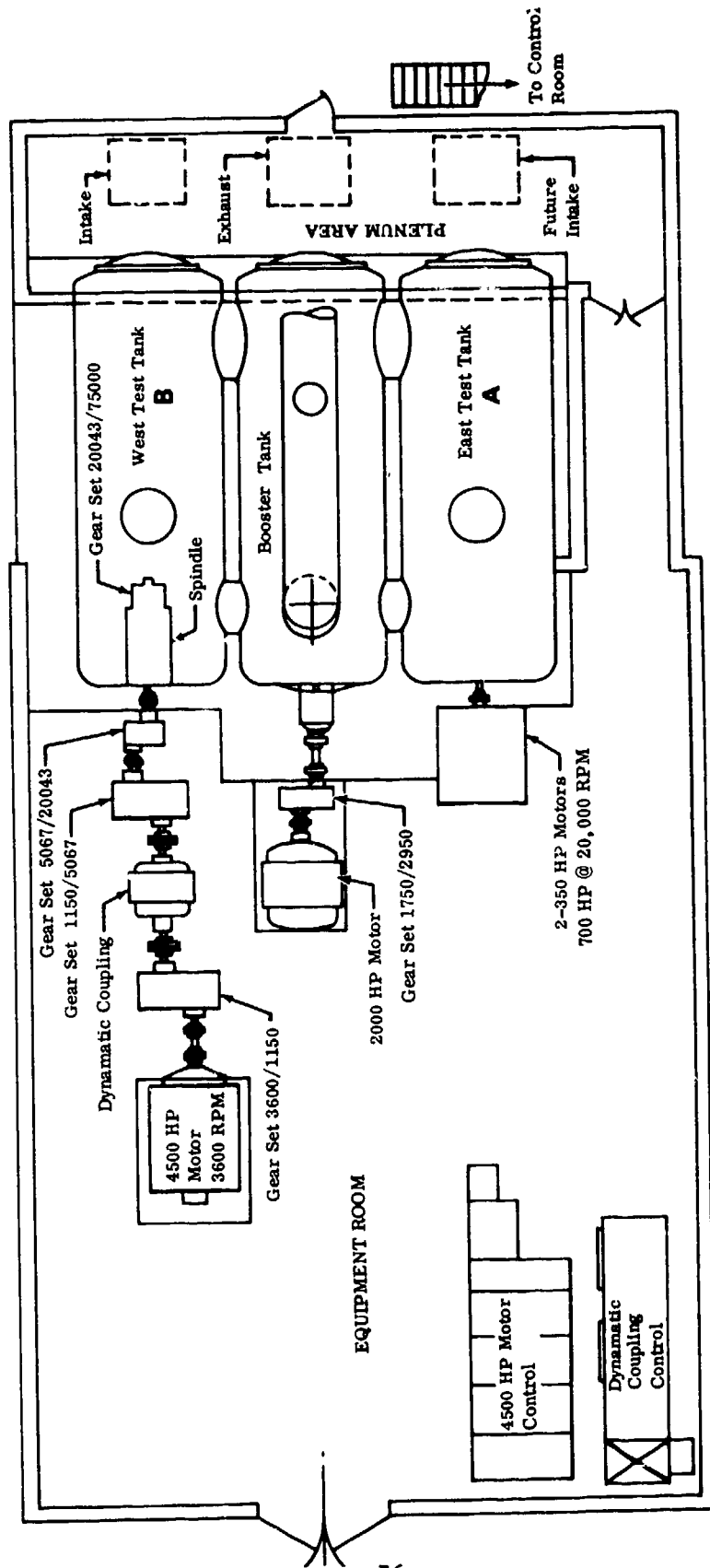


Figure 37. Aero Component Test Facility Layout - Cell A9.

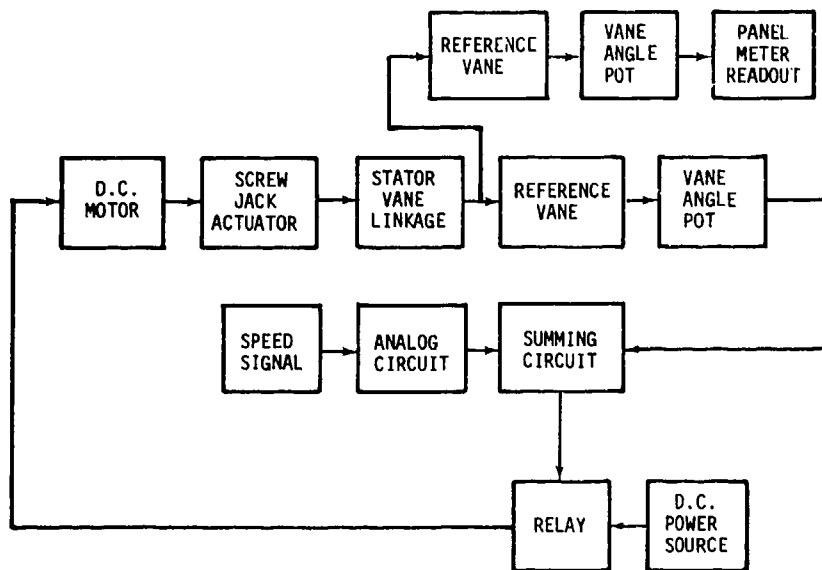


Figure 38. Stator Vane Actuation System Schematic.

At the start of each run the readout system was calibrated using a pin to locate the vane ring relative to the casing. During accels and decels, the system was operated in the automatic tracking mode. In setting up for a data point, an override adjustment was used to set the desired vane angles; power to the actuation motors was then switched off to prevent the vanes from moving while a data reading was being taken. To eliminate any hysteresis effects, the vanes were always set while going from an open to a closed vane angle whenever data points were set up.

#### Centrifugal Test

The inlet guide vanes used in the centrifugal compressor test, like the Stage 2 vanes in the axial and combined tests, were not remotely actuated. These vanes could be set at any one of seven positions where they were held by a close fitting pin inserted through the actuator ring and into a slot in the compressor casing.

#### Combined Test

The Lynn SECT facility used a hydraulic vane actuation system. The vane actuation rings were driven by hydraulic cylinders which receive commands from the vane console located in the control room. The hydraulic system was operated at 2100 psi pressure and the actuator pistons had an area of 0.147 square inch. Each stage was equipped with two potentiometers mounted on separate vane stems. These potentiometers provided the feedback signal to the controller indicating the vane position.

One of the potentiometers was the prime signal which was used to control the test; the other potentiometer was an alternate which was constantly compared to the prime to detect a malfunction in the system. If the prime and alternate signals disagreed by more than a preset amount, a warning indicator was triggered.

The control could be operated in several modes to provide stator angle tracking or fixed angle operation. For most of the FCV-I testing, the control was set up for automatic tracking of vane angle versus corrected speed for the schedule shown in Figure 39. At data point readings, the vanes were trimmed to the desired angle by a manual override mode of operation. For stress mapping purposes, several speed swings were made with the vanes offset several degrees from the nominal tracking schedule; also, manual angle adjustments were made from the nominal angle at constant speed.

#### LUBRICATION SYSTEMS

The lubrication system for the vehicle bearings and oil dampers was part of the facility installation. The basic facility lubrication systems were adapted for the specific test vehicle requirements.

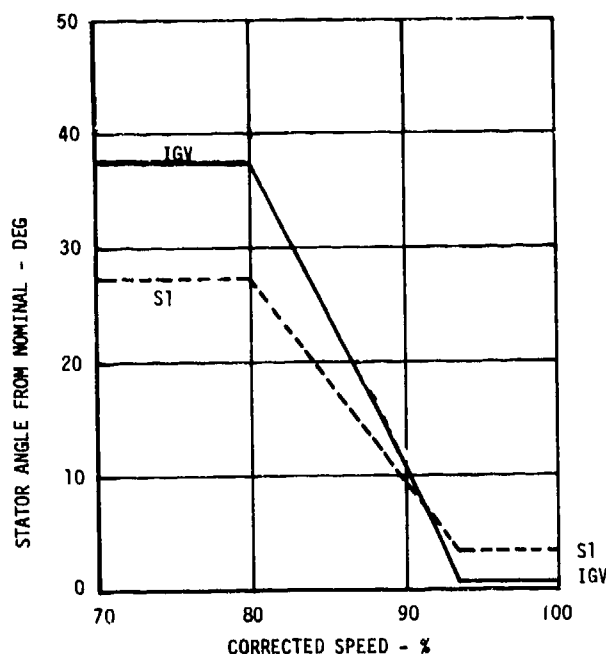


Figure 39. FCV-I Vane Tracking Schedule.

A MIL-L-7808 lubricant was used, and Table 10 indicates the test vehicle requirements.

TABLE 10. LUBRICATION REQUIREMENTS

Item	Pressure (psig)	Flow (gpm)	Oil Inlet Temperature (°F)
Forward Bearing	30-40	1	100-120
Forward Damper	30*	.1	100-120
Aft Bearing (Aft side)	30-40	.85	100-120
Aft Damper	75*	.1	100-120

\*Damper supply capacity pressure.

In addition to these supply pressures, the bearing temperature rise as determined from the oil supply and bearing outer race temperatures was to be less than 100°F for safe operation. The front and rear sumps were maintained below atmospheric pressure by ejectors in the facility lube systems.

The Evendale lubrication system was a permanent part of the facility. A heat exchanger was added to heat the supply oil to the 100°-120°F range. The Lynn SECT facility utilized a portable lube cart that provided the required pressures, flows, and temperature. Each bearing and damper supply line had separate regulation and filtration. In addition to the facility filters, a 10-micron filter was installed in each supply line.

#### THRUST BALANCE SYSTEM

The object of the thrust balance system is to maintain a constant forward thrust on the vehicle rotor for all speeds and operating conditions. For optimum bearing operation the thrust load should be held between 150 and 250 pounds. Instantaneous load increases or decreases are tolerable; however, operation with thrust in the aft direction must be avoided.

In both the Evendale and Lynn facilities, the rotor thrust load was measured by the load cell output and adjusted by changing the pressure in the balance piston cavity.

### Evendale Test Facility

The Evendale test facility used an analog computer circuit to effect automatic thrust load control. The load cell signal was inputted to the analog circuit where it was compared to the desired reference level, thus generating an error signal. This error signal was used to control an air-operated valve which regulated airflow into the balance piston cavity. Balance piston air was supplied from a shop air line and exhausted from the balance piston cavity into the atmospheric vent cavity.

During the initial test runs, the analog computer circuit was not used because the load cell output was questionable. For these tests the balance piston control valve was adjusted manually. Balance piston pressure levels were calculated from pressure-area measurements made in the vehicle.

For the axial compressor test, the load cell was wired to provide two output signals. One of these signals was used for the thrust control system while the second signal was monitored on the Sanborn trace recorder. For the centrifugal compressor test, the load cell was wired to provide three output signals. One of these signals was monitored on a strip chart recorder while all three signals were used for the thrust controller.

### Lynn Test Facility

The Lynn test facility utilized a feedback control system to regulate the rotor thrust. This system is depicted schematically in Figure 40 and operates as described below.

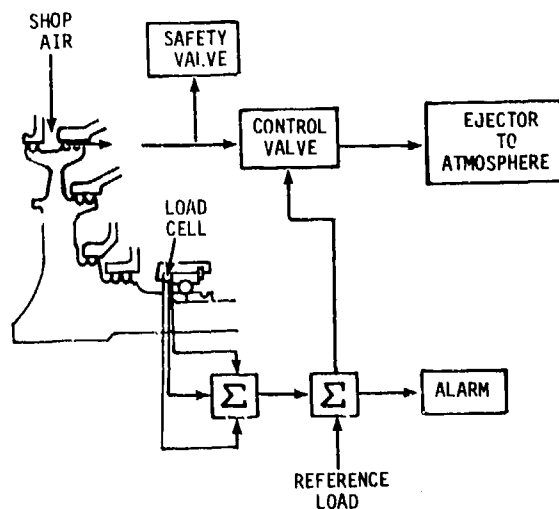


Figure 40. Lynn Thrust Balance System Schematic.

The rotor thrust was also controlled by regulating the air pressure in the balance piston cavity. Air was supplied to this cavity from the compressor discharge seal pressurization cavity through the outer balance piston seal, and was regulated by a control valve in the discharge line from the balance piston cavity. This control valve was an air-operated gate valve which was regulated by an electronic controller. The downstream side of the control valve was connected to an ejector to get additional pressure range. The electronic controller takes the three load cell outputs, sums the level, and compares it to the desired reference load. If the rotor load was lower than the reference, the control valve closed, thus increasing the balance piston pressure; conversely, the valve opened if the rotor load was too high. The electronic controller also triggered an alarm system when the rotor thrust deviated by more than 50 pounds from the reference level.

In the event of a control valve failure, the valve will close, thus raising the balance piston pressure. To prevent serious bearing overload, a relief valve was installed in the air line between the balance piston cavity and the control valve.

The individual load cell outputs were monitored on a strip chart trace recorder, and the sum of the load cell readings was digitally displayed at the rotor console.

#### COMPRESSOR BLEED CONTROL

Three different compressor bleeds are controlled for the various component tests. The axial component test evaluated axial discharge bleed (Plane B), since it affected the centrifugal stage inlet conditions. The centrifugal and combined component tests required bleed from the axial discharge (Plane B) and from both the forward and aft sides of the impeller outlet (vaneless bleed).

The Plane B system was designed for a nominal compressor inlet corrected airflow of 0.23 lb/sec at 30% speed; this design point represented the most severe case. The downstream condition for the bleed discharge was atmospheric, so the test apparatus was installed to a vacuum line to overcome the piping, valving, and venturi pressure losses. For the axial component test the bleed airflow was regulated with a remotely actuated valve that connected with the main vacuum line. The combined compressor control valve required additional protection to automatically open the valve to 100% when the compressor speed went below 70% corrected speed. This was necessary to avoid the possibility of stalling the axial compressor in the event of an emergency shutdown. When testing below 70% speed, the operator could override this automatic control to provide any desired setting. The bleed airflow was measured with a 1.5-inch orifice plate in the SECT facility, and test results of 0.25 lb/sec at 30% corrected speed were observed.

The forward and aft vaneless space bleed systems were sized for 2% bleed airflow from the forward wall and 1% bleed airflow from the aft wall. These flows represented typical engine requirements where the 2% forward wall bleed would be used for high temperature turbine nozzle cooling and the 1% aft wall bleed for internal sump and seal pressurization. This bleed improved the diffuser static pressure recovery. There was sufficient pressure developed in the machine at the impeller discharge to throttle these bleed lines to atmosphere. The forward and aft bleeds were measured in the SECT facility using 0.9- and 0.7-inch-diameter orifice plates respectively. The system capacity was more than adequate because respective flows of 10.5% and 22.8% for the forward and aft bleeds were found to pass at the design airflow in the combined compressor tests.

The various bleed airflows were monitored on an analog computer readout during the test as well as being printed out in the data reduction program. The analog display was useful in setting data points.

#### INLET TEMPERATURE AND PRESSURE CONTROL SYSTEM

The combined compressor tests were conducted at high speeds using reduced inlet temperature and pressure. The Lynn SECT facility provided the refrigerated air at the reduced inlet conditions via an expansion turbine in the air inlet supply system. This turbine was provided high-pressure dried air from the nearby air station and was loaded using a synchronous generator that supplied power to the plant grid. Since the expansion turbine was in series with the compressor, the variation in air supply regulated both compressor inlet temperature and pressure. A schematic of the air supply system is shown in Figure 41. The supply pressure was varied with valve V25, and valves V26 and V28 were usually closed. Valve V28 can be used to bypass supply air for raising the supply temperature and pressure. Positive pressure or ram conditions are avoided by the protective atmosphere vent valve VC5. The valve VC4 was inactive and open during the test.

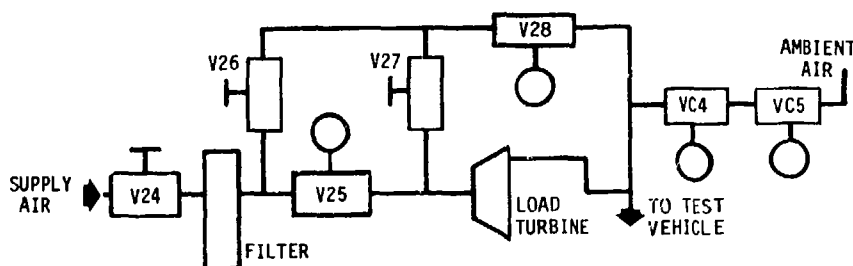


Figure 41. Air Refrigeration System Schematic.

The test procedure used for starting up the refrigeration system was as follows:

1. Started vehicle to about 50,000 rpm with atmospheric air supplied through the vent valve VC5. Valve VC25 was closed and V28 was 100% open.
2. Valve V25 was gradually opened while VC5 was closed to maintain atmospheric inlet pressure. Valve V28 was held at 100% open.
3. When the atmospheric vent valve VC5 had been completely closed, the refrigeration bypass valve V28 was gradually closed while the supply valve was opened to maintain a slightly subatmospheric pressure.
4. When the bypass valve V28 was completely closed, further control for inlet pressure was set by valve V25 and the air station supply.
5. Changes in compressor speed were made gradually to reach the 20 in. hg absolute inlet pressure at 100% corrected speed. Slower speeds were tested at higher inlet pressures while maintaining a near-constant supply temperature to minimize the stabilization time.

During the FCV-I test a minimum temperature of 399°R was reached at 100% corrected speed with an inlet pressure of 20 in. hg absolute.

#### DATA ACQUISITION SYSTEMS

The acquisition of test data was accomplished using a digital recording system for the bulk of the pressure and temperature data and various direct readouts in the test cell control room. The digital recording system used scanning valves for the various pressures and scanning switches for the various temperatures. The rotary scanning valves, typically, had 11 to 22 pressure lines connected to a common pressure transducer. On each data reading, the reference pressures were also logged to check the transducer calibration. The various thermocouple signals were recorded through scanning switches in the digital recording system. The pressure and temperature signals were amplified and stored in an on-line computer system or punched paper tape. An on-line computer system was used for the Evendale axial and centrifugal component tests. The data printout for the on-line computer consisted of a performance summary from a remote terminal in the test cell control room and full printout of results at the computer site. The blow tests and Lynn component tests used an off-line computer with a punched paper tape. The punched paper tape system was processed in the test cell control room using a remote data terminal. The time for the logging on the digital recording system varied with the total number of parameters, but was usually completed in 2 to 3 minutes.

Operational data was also obtained during the test using various continuous monitors.

Analog computer display  
Stress and vibration displays  
Operational parameters

An analog computer was used to display compressor airflow and pressure ratio on an X-Y recorder. This provided a record of the stall point, and aided in the selection of a throttle valve setting for equally spacing data points along a speed line.

The stress and vibration monitors were displayed on strip chart recorders and oscilloscopes and recorded for playback on magnetic tape.

Compressor speed, bearing thrust load, vane angle, and throttle valve setting were monitored on a digital display located on the control console. These parameters were also connected to a strip chart recorder. Operational pressures and temperatures were monitored on control room displays and recorded with each test point.

The strip chart records and magnetic tapes were very useful in analyzing the axial rotor blade failure and thrust bearing problem on the axial component test. The playback of the magnetic tapes of FCV-I rotor strain gage signals was essential because of the high rate at which this data is obtained during the test. On-line monitoring of the rotor strain gage signals was primarily to avoid regions of excessive stress, and quantitative stress values were obtained on playback.

## COMPRESSOR DATA REDUCTION

### STAGE PERFORMANCE

The reduction of the test data for the overall performance is presented for a standard day (59°F, 14.696 psia). The inlet corrected airflow into the axial compressor was based on the inlet plenum total pressure ( $P_A$ ) and temperature ( $T_A$ ):

$$(W_c)_A = W\sqrt{T_A/518.7} / (P_A/14.696) \quad (2)$$

In the case of the centrifugal compressor, the total pressure ( $P_B$ ) and total temperature ( $T_B$ ) conditions were used for corrected airflow:

$$(W_c)_B = W\sqrt{T_B/518.7} / (P_B/14.696) \quad (3)$$

The stage pressure ratio was based on the measured inlet and exit total pressures:

1. Axial stage pressure ratio =  $P_B/P_A$
2. Centrifugal stage pressure ratio =  $P_E/P_B$
3. Overall pressure ratio =  $P_E/P_A$

The adiabatic efficiency was based on the enthalpy rise as determined from the measured temperatures and pressures and the real gas properties of the air, including the effects of humidity:

$$\eta = (\text{Isentropic Enthalpy Rise}) / (\text{Actual Enthalpy Rise}) \quad (4)$$

For high pressure ratio compressors, a variable specific heat was important in calculating the stage efficiency. This was especially important for the centrifugal stage compressor.

The compressor corrected speed ( $N_c$ ) was determined from the measured RPM ( $N_g$ ) and the inlet total temperature:

1. Axial or Axial-Centrifugal Compressor  $(N_c)_A = N_g\sqrt{T_A/518.7}$
2. Centrifugal Compressor  $(N_{CENT}) = N_g/\sqrt{T_B/518.7}$

The corrected airflow and speed data were normalized to design point conditions for the axial and centrifugal stages. The design airflow and speed for the axial compressor were 5.0 lb/sec and 60,400 rpm, and for the centrifugal stage were 2.34 lb/sec and 51,800 rpm.

### Centrifugal Stage Calculations

Performance of the impeller and diffuser was calculated using the measured plenum inlet, impeller exit static pressure, and the diffuser exit conditions. In the case of a centrifugal stage test, the total pressure loss of the inlet guide vanes was deducted from the inlet plenum total pressure in order to determine the total pressure at the impeller inlet (Plane C). This was necessary because the IGV loss would not be present when the stage operated with the axial compressor. These inlet guide vanes were used only to simulate the swirl exiting from the axial compressor.

The impeller inlet conditions were calculated at the mean inlet diameter using the air angle determined from the IGV blow test, measured inlet airflow, total pressure ( $P_C$ ), wheel speed, annulus area, and a blockage factor of 0.97. These data, coupled with the continuity equation, established the inlet velocities and flow angles.

The impeller exit total pressure was estimated using the measured temperature rise, wheel speed, airflow, tip static pressure, annulus area, and a blockage factor of 0.90. This total pressure was used to calculate the impeller pressure ratio and efficiency as well as to determine the inlet conditions into the diffuser (total pressure, inlet Mach number, and angle). The impeller slip factor ( $\sigma$ ) included the shroud heating and windage which are part of the stage temperature rise but it does not include the bulk of the backface windage:

$$\sigma = (Vu)_B / U_B \quad (5)$$

The static pressure recovery and total pressure loss were calculated for the diffuser as follows:

$$C_P = (p_E - p_D) / (P_D - p_D) \quad (6)$$

where  $C_P$  = static pressure recovery coefficient

$$\omega_d = (P_D - p_E) / (P_D - p_D) \quad (7)$$

where  $\omega_d$  = total pressure loss coefficient

### TRAVERSE DATA

Traverse test data were obtained in the circumferential direction behind the axial compressor inlet guide vanes and Stage 2 stator vanes. These data were mass-averaged over two blade pitches in the circumferential direction before making a second integration in the radial direction. At each radial immersion, mass-averaged values were integrated for mass flux, total and static pressure, total temperature, Mach number, velocity, and flow angle. The integrated results in the

radial direction were calculated to determine the overall values of pressure ratio, temperature ratio, efficiency and airflow. The local values of static pressure were determined using the wall static pressure and the design variation of static pressure ratio across the annulus. The inlet total temperature was used for the local total temperature in reducing the axial inlet guide vane blow test data. The Stage 2 stator exit traverse total temperature was determined using the measured temperature, the calibration data for the probe recovery factor, and the local Mach number determined from the calculated local static pressure and the measured total pressure. A simple straight-line method of integration was used, since a more precise method was not warranted and could introduce instabilities. The mass flux term ( $\rho VR$ ) was computed at each point using the expression

$$\rho VR = (\sqrt{\gamma g_0 / RT_1}) \times p_1 \times R_1 \times M_1 \times [1 + (\gamma - 1)(M_1)^2 / 2]^{1/2} \quad (8)$$

This value of mass flux was then integrated in the circumferential direction:

$$\overline{\rho VR} = \sum_{i=2}^n (1/2) [(\rho VR)_i + (\rho VR)_{i-1}] [\theta_i - \theta_{i-1}] \quad (9)$$

The mass-averaged values of total pressure were computed using the expression

$$\overline{P}_1 = \left\{ \sum_{i=2}^n (1/2) [(\rho VR)_i \times (P_1)_i + (\rho VR)_{i-1} \times (P_1)_{i-1}] [\theta_i - \theta_{i-1}] \right\} / \overline{\rho VR} \quad (10)$$

The mass-averaged values of total temperature, radius, static pressure, and angular momentum ( $rC_\theta$ ) were computed in the same fashion as the total pressure. The average air outlet angle was calculated using the mass-averaged angular momentum ( $rC_\theta$ ), radius, and the velocity. The mass-averaged total velocity was determined from the values of static and total pressure and total temperature.

The radial traverse data were reduced using the measured total pressure, flow angle, and temperature. The static pressure was calculated using the measured wall static pressure and the design variation across the annulus. The probe recovery factors were determined from calibration test results.

## TEST RESULTS

### AXIAL COMPRESSOR TEST (ACV)

#### Summary of Test Runs

The axial compressor vehicle was operated for a total of 48 hours 10 minutes during eight separate runs. An approximate breakdown of time at various speeds for each of these runs is presented in Table 11, and the stalls experienced during this testing are listed in Table 12. Brief descriptions of the major events of each run follow.

#### Run No. 1 - 4/28/72 and 4/29/72

Mechanical checkout to 80% speed (49,500 rpm maximum physical speed) with wide-open throttle valve. Vanes were locked in the closed position for all of this testing. No mechanical problems were indicated, and instrumentation and systems to be debugged were identified prior to performance running.

#### Run No. 2 - 5/4/72

Completed mechanical checkout to 100% speed (61,000 rpm maximum physical speed) with wide-open throttle valve. Checked out vane actuation system and no mechanical problems were indicated.

#### Run No. 3 - 5/4/72 and 5/5/72

Obtained performance data on the nominal vane schedule up to 100% speed and stator optimization at 85% speed.

#### Run No. 4 - 5/8/72

Investigated bleed flow effects at 70% and stator optimization at 95% speed.

#### Run No. 5 - 5/9/72

Investigated stator optimization at 100%. During this 100% speed operation the aft bearing housing strain gage signals showed signs of distress. A slight increase in the aft bearing temperature, coupled with these erratic stress readings, dictated that the vehicle should be shut down for further investigation.

TABLE 11. AXIAL COMPRESSOR VEHICLE RUN TIME SUMMARY

% Speed	Run Number								Total	%
	1	2	3	4	5	6	7	8		
70	:10	:35	-	3:20	1:00	1:30	:30	:30	7:35	15.8
80	:10	:30	1:15	-	-	-	:10	-	2:05	4.3
85	-	-	7:00	-	1:25	2:00	:25	1:20	12:10	25.2
90	-	:15	1:00	-	-	-	-	:15	1:30	3.1
95	-	:15	1:05	5:20	:45	-	-	2:45	10:10	21.1
100	-	:05	:35	-	4:20	-	-	1:35	6:35	13.7
Other*	2:10	:35	:45	:50	:10	1:55	:05	1:35	8:05	16.8
Total	2:30	2:15	11:40	9:30	7:40	5:25	1:10	8:00	48:10	100.0
%	5.2	4.7	24.2	19.7	15.9	11.2	2.5	16.6	100.0	
Max Physical Speed (rpm)	49,500	61,000	60,800	58,230	60,570	52,220	52,050	61,450		

\*Includes time at speeds below 70% and time in accels and decels not included in speeds shown.

TABLE 12. AXIAL COMPRESSOR VEHICLE STALL SUMMARY

Stall No.	% Speed	Vane Angle		Run No.
		IGV	IS	
1	80	43	32.5	3
2	90	20.4	16.2	3
3	95	8.2	7.4	3
4	85	31	24.5	3
5	85	31	24.5	3
6	85	26	21	3
7	85	26	16	3
8	85	30	21	3
9	85	21	21	3
10	85	13	0	3
11	70	45	35.4	4
12	70	45	35	4
13	70	45	35	4
14	95	10	9.1	4
15	95	10	0	4
16	95	10	5	4
17	95	6	5	4
18	95	6	0	4
19	95	14	9	4
20	95	14	13	4
21	95	0	0	4
22	100	-2	0	5
23	100	0	5	5
24	95	3	7	8
25	95	14	6	8
26	100	3	5	8

Run No. 6 - 5/11/72

For this run, chip detectors were installed in the sump scavenge lines. The vehicle was operated up to 85% and shut down when the aft bearing housing strain gages and vibration pickups showed significant activity. The aft sump chip detector showed some pickup.

Run No. 7 - 6/6/72

A short run was conducted to check out the facility drive motor.

Run No. 8 - 6/7/72

Investigated stator optimization at 95% and 100% speed. While operating at 100% speed (61,050 rpm) the Stage 1 rotor blades failed, terminating the axial compressor test.

#### Mechanical Performance

The overall operation of the axial compressor vehicle was very smooth. Maximum radial bearing squirrel cage motion was 0.0005 inch at the forward bearing and 0.0008 inch at the aft bearing. The proximity probe on the forward end of the flexible coupling indicated peak runout of 0.005 inch, of which 0.002 inch was base runout at low speed.

The peak frame vibrations occurred at 100% speed but were less than 0.4 inch per second average velocity which is equivalent to 10 g's peak acceleration. No significant rotor or stator criticals were observed during transient speed operation.

The bearing temperatures and lube oil supply and scavenge temperatures were monitored throughout the test and compared to the maximum allowable temperature values shown in Figure 42. The temperature limits were established from a calculated point where the internal bearing clearance was zero at the maximum bearing design speed (66,000 rpm) and load. The bearing thermocouples were quick to respond to speed changes, and the aft bearing temperature also responded to thrust load changes.

Load cell performance prior to the bearing failure indicated that it was responsive to load changes. The load indicated on the strip chart showed variations from 150 to 350 pounds. These loads were later verified by thrust calculations using actual pressure data. This was surprising in view of the fact that the bench calibration and calibration recheck after installation in the test vehicle did not correspond. This difference in calibration was the prime reason for the load cell reading to be questioned and not used in the automatic thrust control system.

After the bearing failure, the load cell was recalibrated, both on the bench and after vehicle installation, with good agreement. However, during the next run the load cell showed poor response to load changes. At the time of the compressor blade failure, the load cell did register a high thrust load shift, indicating that it was still functioning.

The stator vane control system provided tracking within 2° of the desired schedule. This schedule was set up as a function of physical speed only, so there was some tracking error due to the temperature correction. However, all data was taken with the vanes trimmed to the corrected speed schedule.

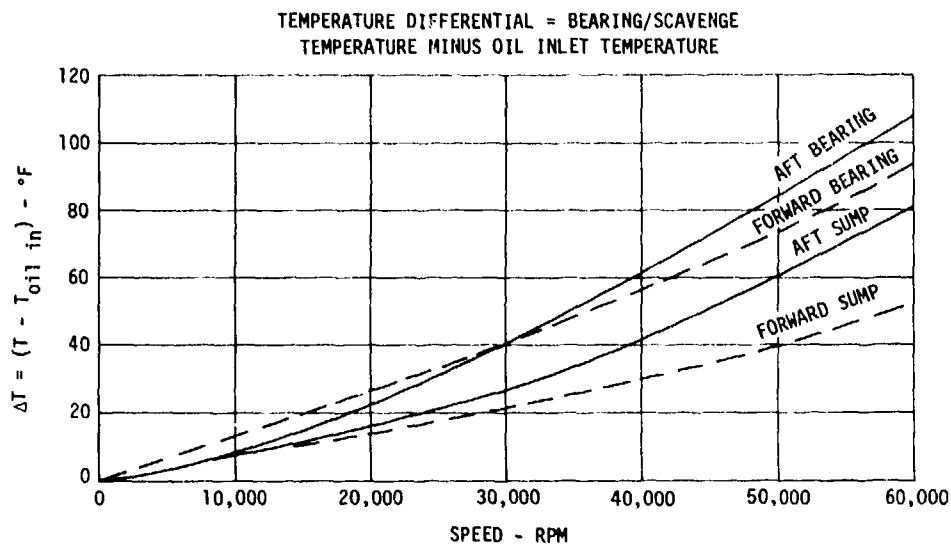


Figure 42. Maximum Allowable Bearing and Sump Temperature Differential.

The stator vane strain gages showed very little activity throughout the test, with stresses never exceeding 8,000 psi. Three of the six gages were lost very early in the test due to lead wire damage at the vane spindle. The three operational gages were the two trailing edge gages on Stage 2 and the inner spindle gage on Stage 1. Because of this low response the gage positions were changed for the subsequent FCV-I test.

The stator vane strain gages provided a good stall indicator. At stall, the stress signal went completely off the oscilloscope, which is typical of a sudden DC shift probably caused by the rapid temperature change in the air passing over the gage. In addition, the X-Y plotter displaying the instantaneous flow and pressure ratio indicated stalls by a sudden drop in pressure ratio.

The microphone located at the compressor inlet was also a good stall indicator with a general level increase at the point of stall. The sound picked up by this microphone was predominantly the passing frequency of the Stage 1 blades (20 times the compressor speed); however, at one point in the test while throttling at 85% speed, a 2000 Hz frequency was noted on the microphone. This was identified as a possible first flex response of the first rotor blades, and investigation of that aerodynamic region was abandoned.

The general operation of the facility and related systems was adequate; however, some tripouts were experienced with the electric drive system. A repair to a cooling fan motor corrected that situation. Of particular value was the rapid turnaround in reduced data from the on-line data

acquisition system (about 20 seconds) for aerodynamic performance during the stator optimization experiment.

#### Bench Frequency Testing

Blades: After the blisks were tip ground, each of the airfoils was checked to determine the first mode frequency, and one airfoil from each stage was checked for all modes up to 30,000 Hz. Campbell diagram plots of these frequencies are presented in Figures 43 through 45 for Stages 1 and 2. The first mode is depicted as a frequency band between the minimum and maximum measured frequencies and is corrected for speed effects using a calculated correction factor.

Vanes: One vane from each of three vane stages was frequency tested. For these tests the vane spindles were assembled in a holding fixture with the same hardware used in the stator assembly. The inner spindles of the IGV and Stage 1 vane were also restrained to simulate the compressor configuration. The observed frequencies are plotted on Campbell diagrams in Figures 46 through 48.

Rotor Assembly: As a check on the calculated rotor dynamics, the rotor assembly was vibrated to determine the frequency of the first bending mode. The assembled rotor (including the compressor rotor, balance piston and spline adapter coupling) was supported in V-blocks on rubber pads to simulate a free-free mounting. The support points were at the two bearing locations, but the bearings were not part of the rotor assembly.

The first bending critical was observed at 1778 Hz (106,680 rpm). The calculated dynamic analysis for the same rotor configuration indicated the free-free bending mode to be at 1735 Hz (104,102 rpm). This good agreement between calculation and static test confirmed the analysis of the vehicle configuration.

#### Thrust Bearing Failure

Summary of Events up to Failure: The axial compressor vehicle was run a total of 39 hours and attained a maximum speed of 61,000 rpm. For the majority of this testing, vehicle operational characteristics were excellent, as determined by vibration amplitudes and bearing temperatures.

The bearing support squirrel cage strain gages indicated rotor radial deflections of 0.0005 inch at the forward bearing and 0.0008 inch at the aft bearing which are well within the 0.003-in. snubber gap of the bearing supports. The bearing temperatures, which are monitored by thermocouples mounted in the bearing housings and touching the outer race outside diameters, were constant at steady state operating conditions and showed good response to changes in speed and bearing load.

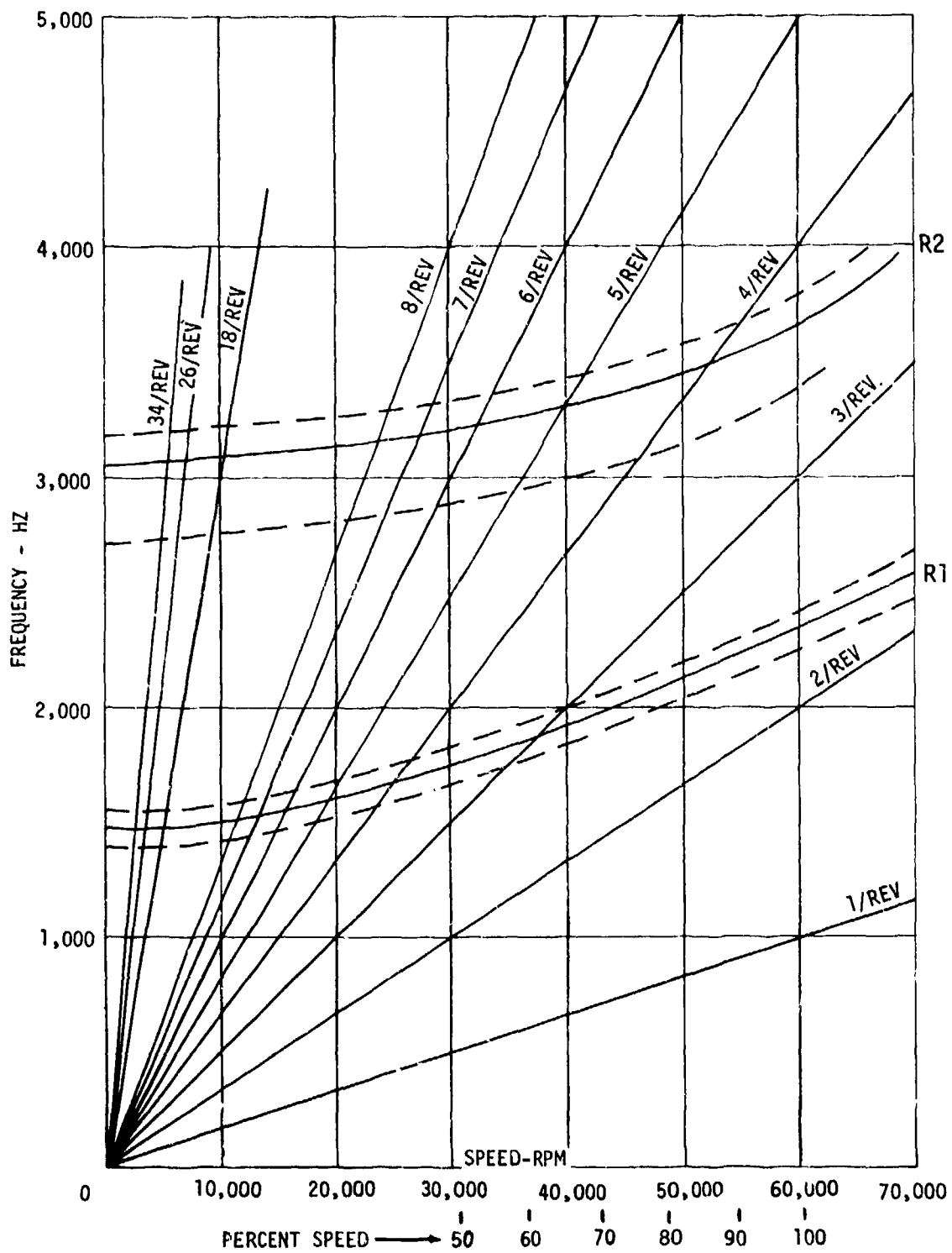


Figure 43. Campbell Diagram for ACV Stage 1 and 2 Blades - 1st Mode.

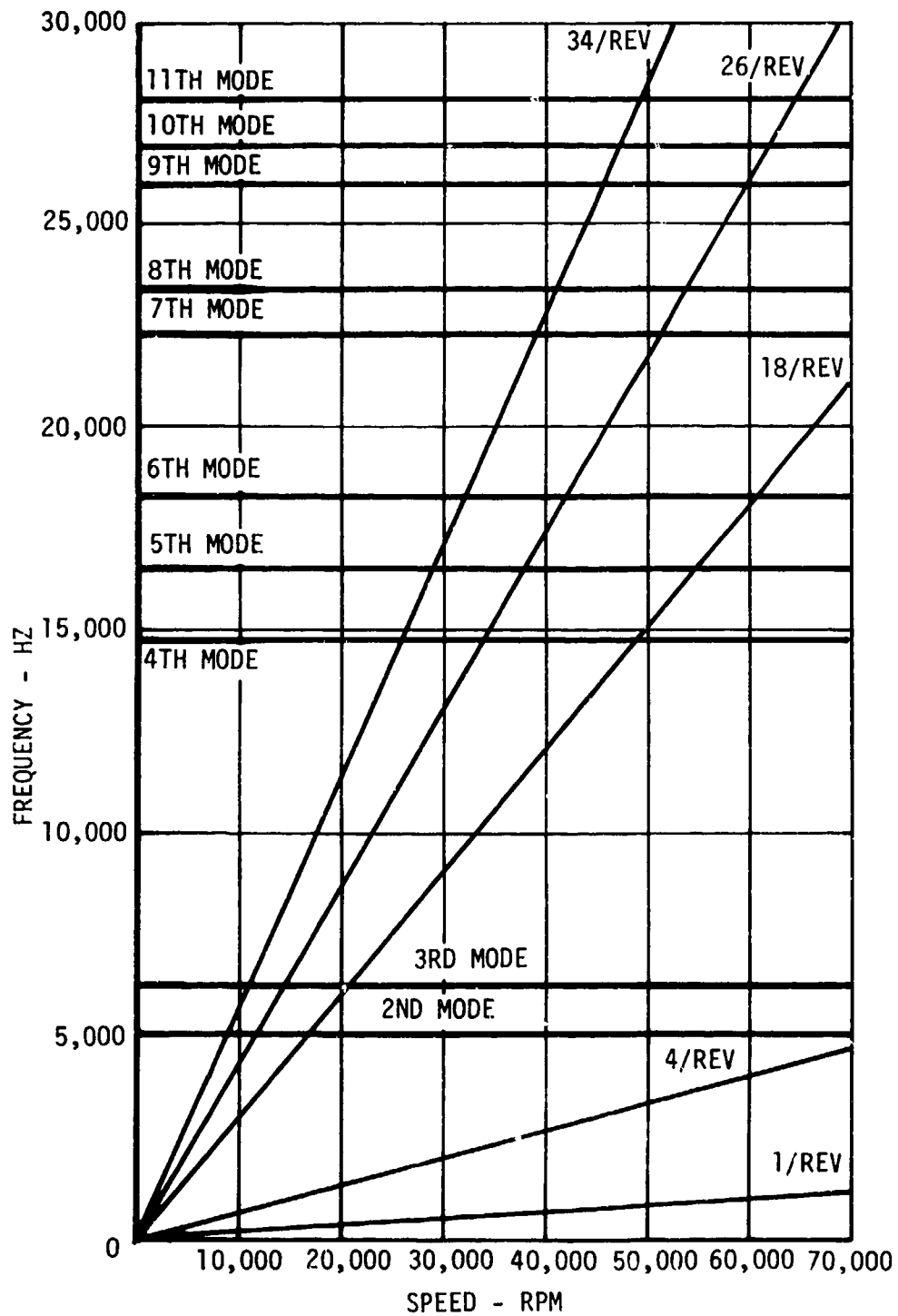


Figure 44. Campbell Diagram for ACV Stage 1 Blades - Higher Modes.

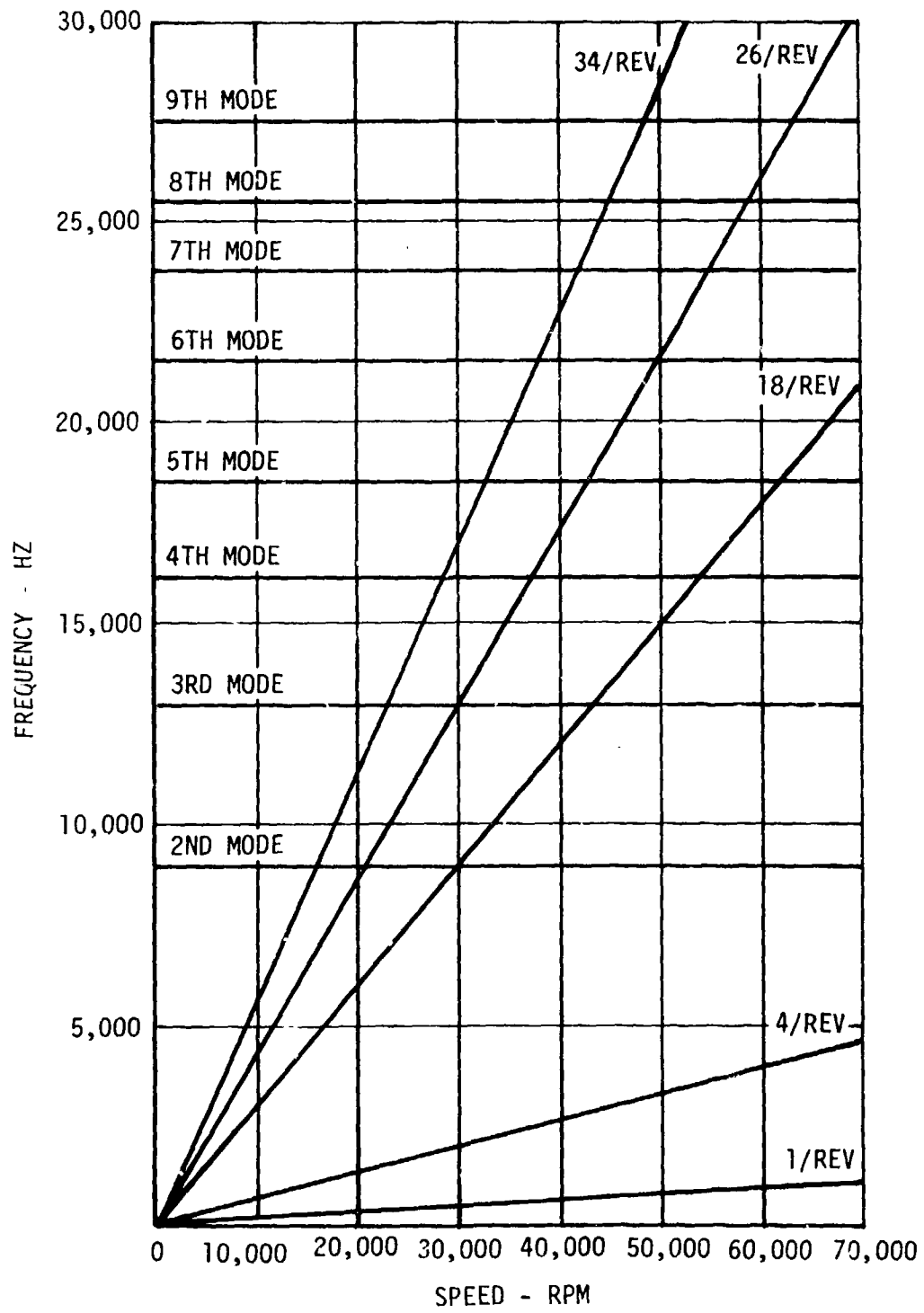


Figure 45. Campbell Diagram for ACV Stage 2 Blades - Higher Modes.

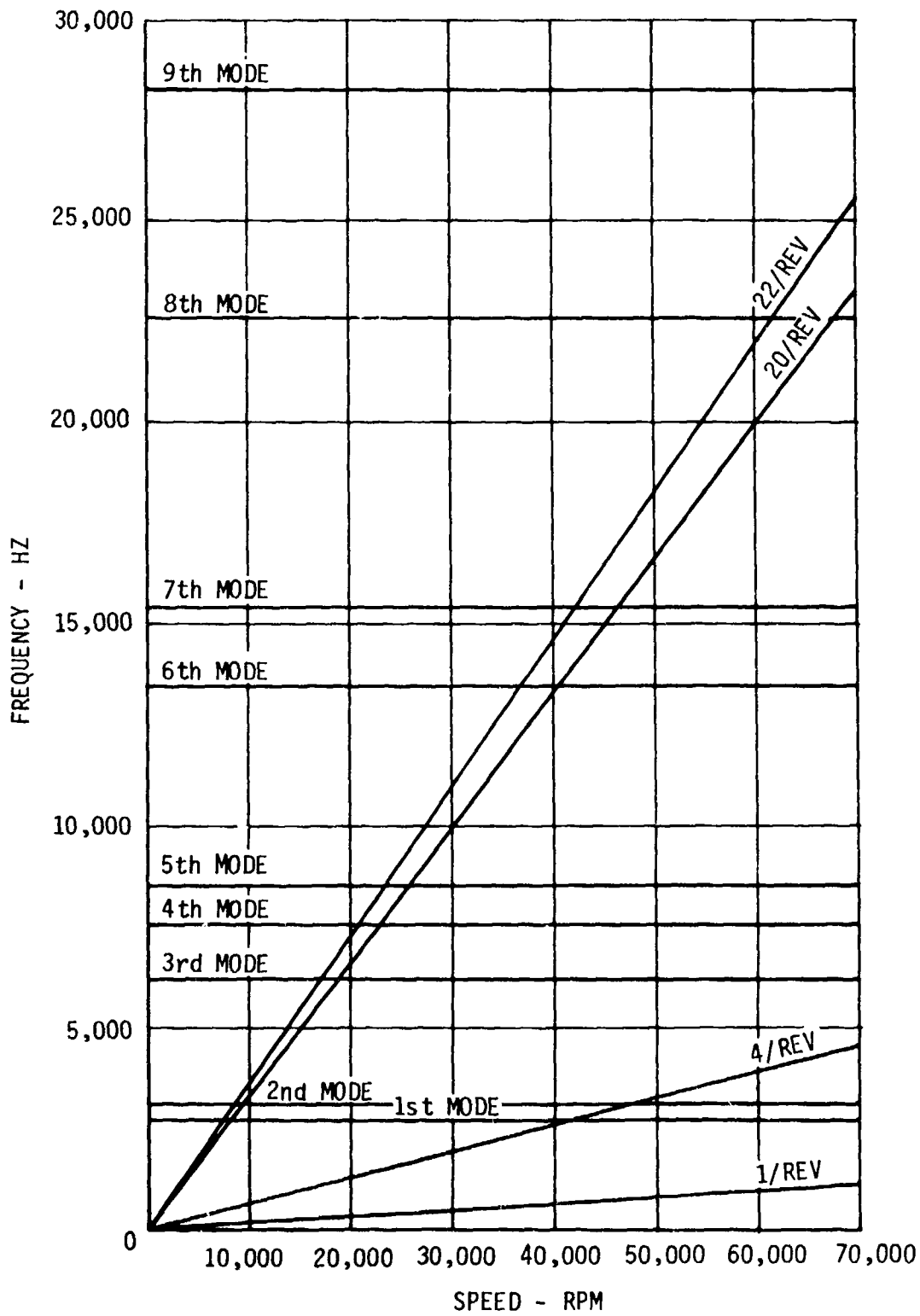


Figure 46. Campbell Diagram for IGV.

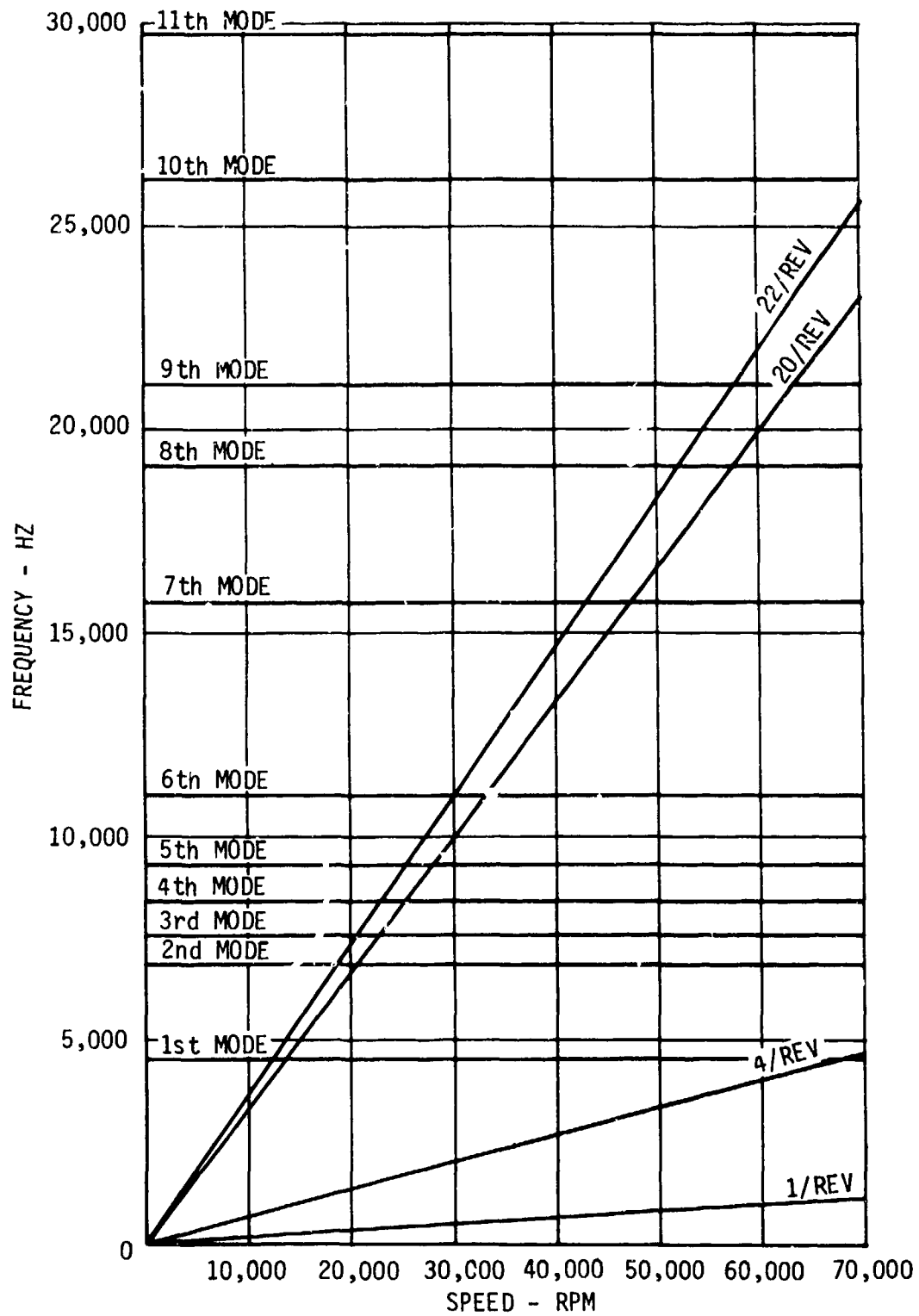


Figure 47. Campbell Diagram for Stage 1 Vane.

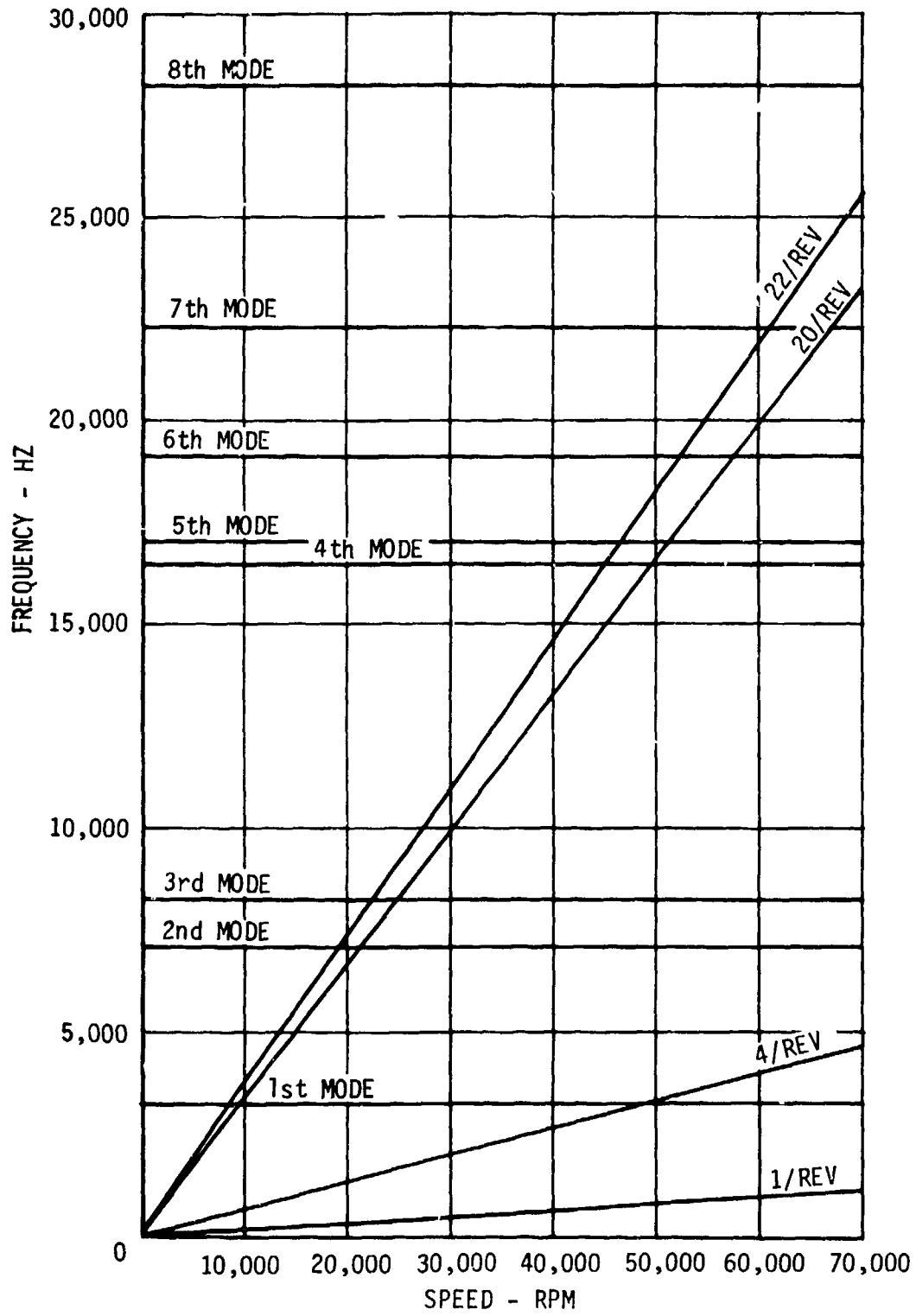


Figure 48. Campbell Diagram for Stage 2 Vane.

Rotor thrust, which is controlled by varying the balance piston air pressure and monitored by a load cell located in the aft bearing housing, was varied between 175 and 350 pounds forward load with the majority of operation at 250 pounds.

After 33.5 hours of operation, the vehicle was shut down when the aft bearing strain gages showed an increase in noise level, and a 5°F temperature rise was noted on the aft bearing. At this time chip detectors were installed in the lube scavenge system and testing was resumed (Run 6). After an additional 3.2 hours of operation at 50% and 70% speed, the chip detectors were inspected and found to be clean. Testing was resumed at 85% speed, and after about 1.5 hours the noise on the aft bearing housing strain gages had increased significantly and the 1/rev portion of the signal had increased from 0.0002-in. radial deflection to 0.0005 inch. A comparison of the bearing noise level can be seen in the spectral analysis of the aft bearing strain gage stress signal shown in Figure 49 after 8-1/3 hours of vehicle operation and in Figure 50 after 38-1/2 hours (note scale change between figures). Testing continued for 0.5 hour, at which time the aft bearing 1/rev deflection was up to 0.0012 inch, the thrust load cell readout became erratic and the vehicle was shut down.

An inspection showed that the aft bearing sump chip detector contained M50 bearing material while the forward bearing sump chip detector was clean. The aft bearing was removed and found to have failed.

#### Thrust Bearing Failure

Failure Investigation: The thrust bearing was removed from the test vehicle and inspected by General Electric and MRC bearing specialists. The bearing was found to have failed at the aft inner race and balls, and it suffered some cage socket damage (see Figures 51 through 53). There was no perceptible damage to the outer race or the forward half of the inner race. A check of the aft oil jets (see Figure 54) revealed that one of the two jets was hitting the cage and had an undesirable fan shape spray pattern. This poor pattern and orientation would allow the inner race to run hotter, thereby reducing the bearing contact angle and thrust load capability.

The following bearing specifications were reviewed:

1. ABEC-7.
2. M50 Material for races and balls.
3. Outer land riding, silver-plated steel cage.
4. Split inner race.

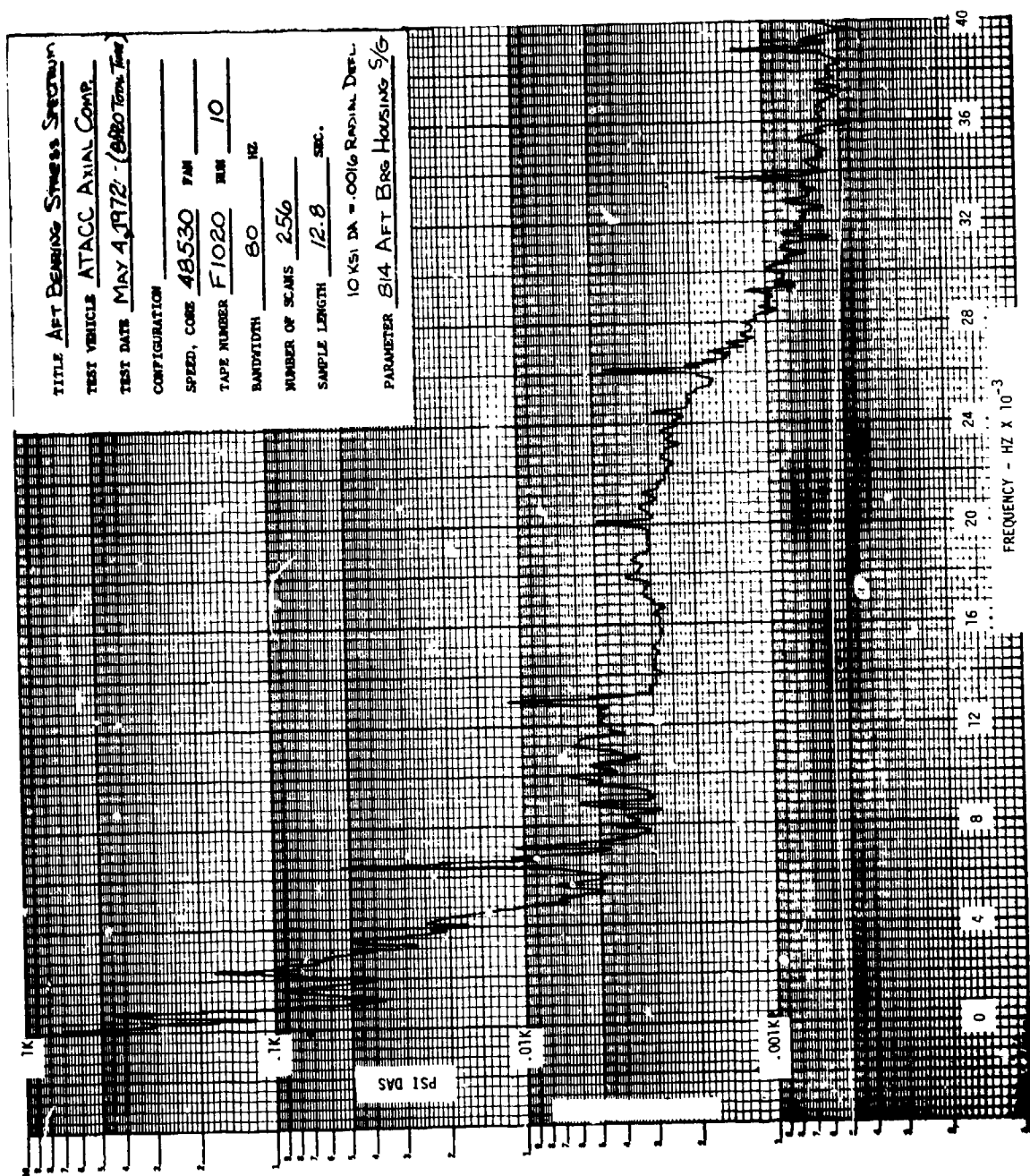


Figure 49. Aft Bearing Stress Spectrum - 8-1/3 Hours Total Time.

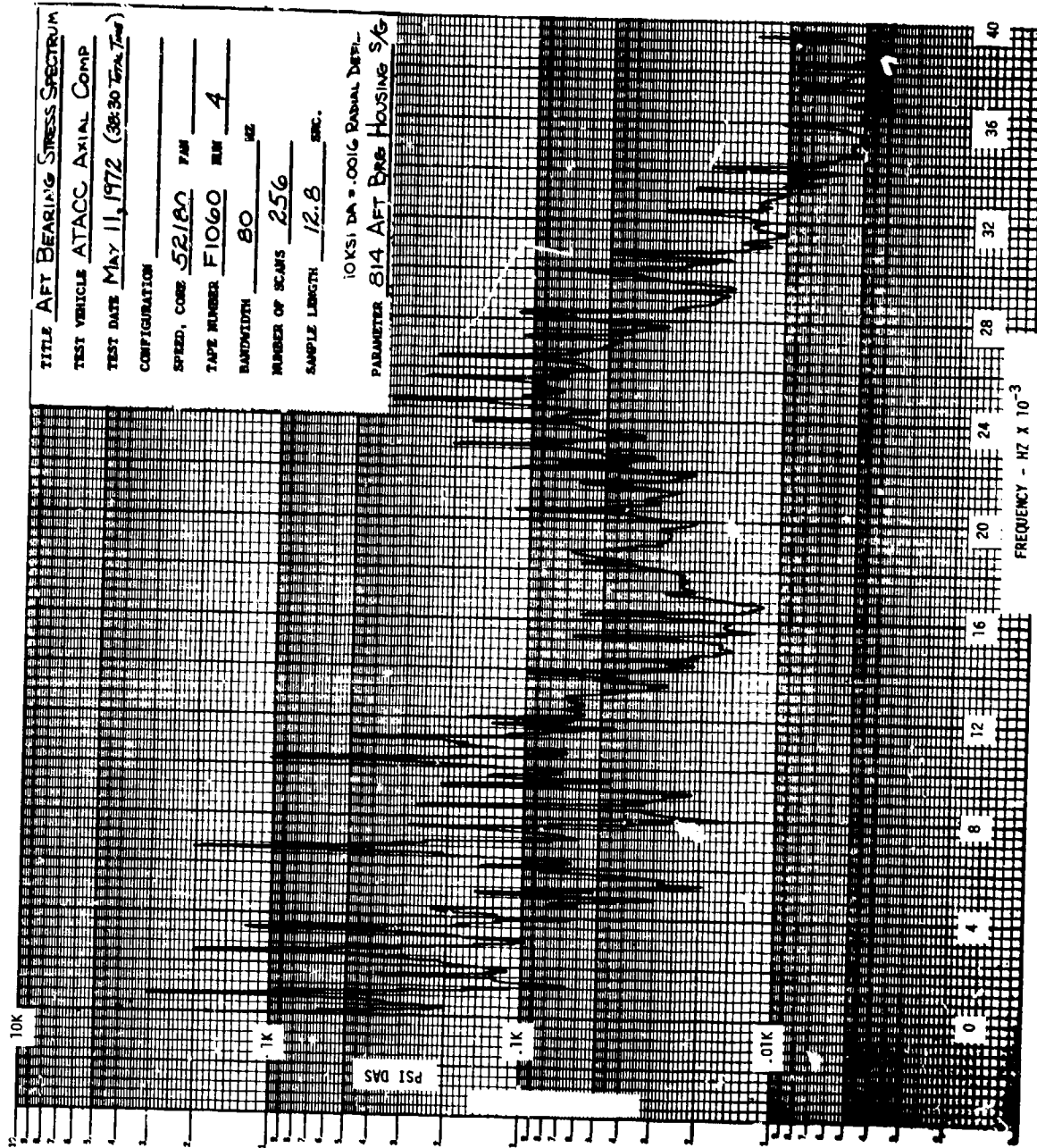


Figure 50. Aft Bearing Stress Spectrum - 38-1/2 Hours Total Time.

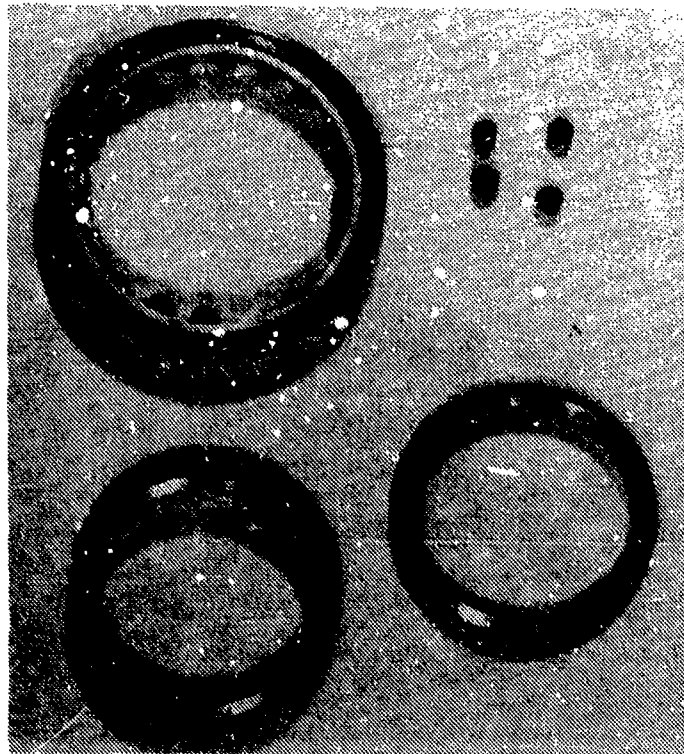


Figure 51. Failed Thrust Bearing.



Figure 52. Closeup of Bearing Inner Race Damage.



Figure 53. Closeup of Ball and Cage Damage.

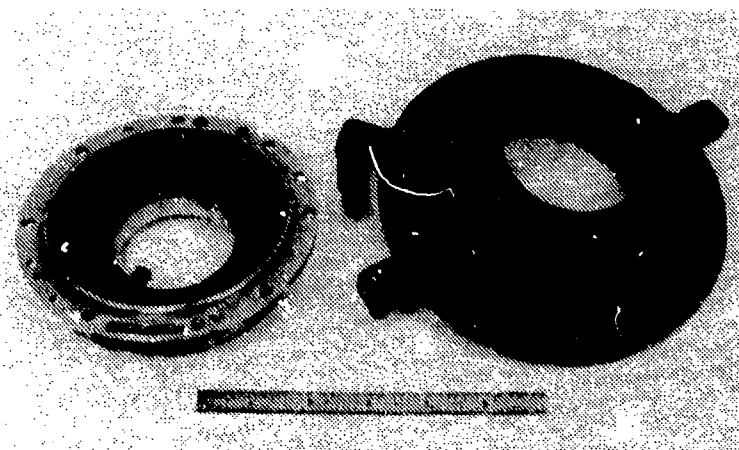


Figure 54. Aft Bearing Housing and Lube Jets.

5. 61,000 rpm operating speed, 66,000 rpm maximum speed.
6. 400-hour life at 100-lb thrust load.
7. 3000-lb transient thrust load.

An analysis of this design using the GE RECAP computer program showed a calculated  $B_{10}$  bearing life of 354 hours at 150-lb thrust and 140 hours at 300-lb thrust load. The assumed radial load was 100 lb. Actual thrust loads during the test were computed using measured pressures and revealed a 250- to 300-lb load during the high-speed operation. The measured load cell thrust level during the test was inconclusive because of the unreliable and erratic operation of the thrust load cell.

Conclusions: The investigation concluded that the bearing failed from excessive thrust load which was accelerated by the poor lube jet spray pattern and orientation. The low bearing design contact angle of  $15^\circ$  had little margin for poor cooling or overloads.

Recovery Plans and Preventative Action: The lubrication jet was repaired by plugging and redrilling. A check of the repaired jet showed proper orientation and spray pattern. Continued operation during the axial test was carried out at reduced axial thrust loads (100-150 lb). No further problems were detected over the remainder of the axial stage test.

For subsequent tests, the thrust bearing inner races were reworked to increase the contact angle from  $15^\circ$  to  $20^\circ$ . This was accomplished by changing the race curvature of 0.520 inch to a value of 0.515 inch on the outer race and 0.525 inch on the inner race. The calculated  $B_{10}$  life for this design was 427 hours for 200 lb of thrust load at 61,000 rpm.

#### Rotor Blade Failure

Summary of Events up to Failure: Axial compressor testing was terminated 6/8/72 when the compressor failed during operation at 100% corrected speed, resulting in extensive damage to all blading.

During the final run, the compressor map at 95% and 100% speeds was being determined. Two speed lines at 95% and one at 100% (including stall points) had been completed. The 100% speed line with the IGV set  $4^\circ$  open and the Stage 1 vane  $5^\circ$  closed was being investigated when the failure occurred. At the time of failure the compressor was being stabilized for a data reading at 61,050 rpm. The only change being made was adjustment of the CDP seal pressurization air for zero leakage.

When the failure occurred the compressor went up in speed to a point where the facility drive motors were shut down by the automatic over-speed trip-out system. Strip chart trace recordings of the event indicated a 3500-rpm speed increase in 3 seconds and a coast down to zero speed in 78 seconds after the failure. The trace from the X-Y recorder of pressure ratio versus flow indicated an immediate drop in pressure ratio, as did the strip chart trace.

Failure Investigation: Inspection of the vehicle after the failure and during teardown revealed the following:

1. The IGV's and Stage 1 stators were completely closed (beyond the actuator system travel) (see Figure 55). The IGV levers were pulled out of the actuator ring (see Figure 56). The Stage 1 levers appeared to be in the normal closed position but the levers were twisted on the vane spindles.
2. All parts of the inlet protection screen, bellmouth, and bullet-nose were in position. Debris from the compressor was lying in the bellmouth and screen.
3. The drive motors were disconnected from the vehicle due to a shear pin failure between the motors and drive. (Review of the speed signal indicates this failure probably occurred when the compressor stopped.)
4. The compressor could not be rotated.
5. The aft bearing had failed.
6. The rotor was 0.040 in. forward of the buildup position with evidence indicating it had moved 0.082 in. forward of the buildup position.
7. With the exception of the airfoils, all of the compressor and vehicle hardware was located.
8. Airfoil damage was as follows:

Stage 1 rotor blades were all broken off near the root. No large pieces of these blades were found (see Figure 57).

Stage 2 rotor blades showed heavy damage with evidence of fatigue failure at the trailing edge tip corners (see Figure 57).



Figure 55. Front View of Failed Compressor.

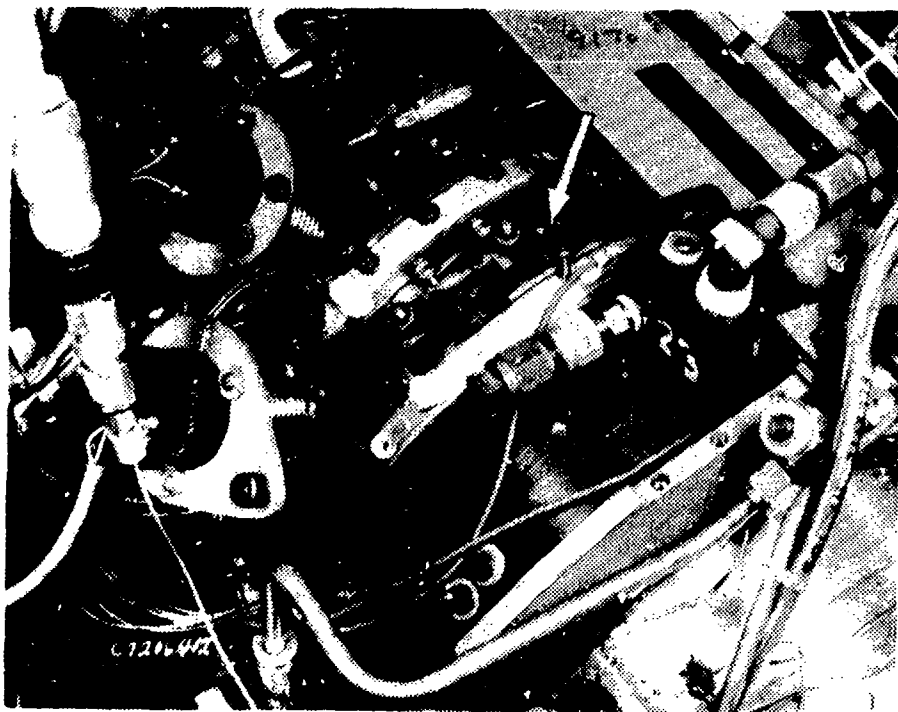


Figure 56. Outer Casing View Showing Damaged IGV Levers.

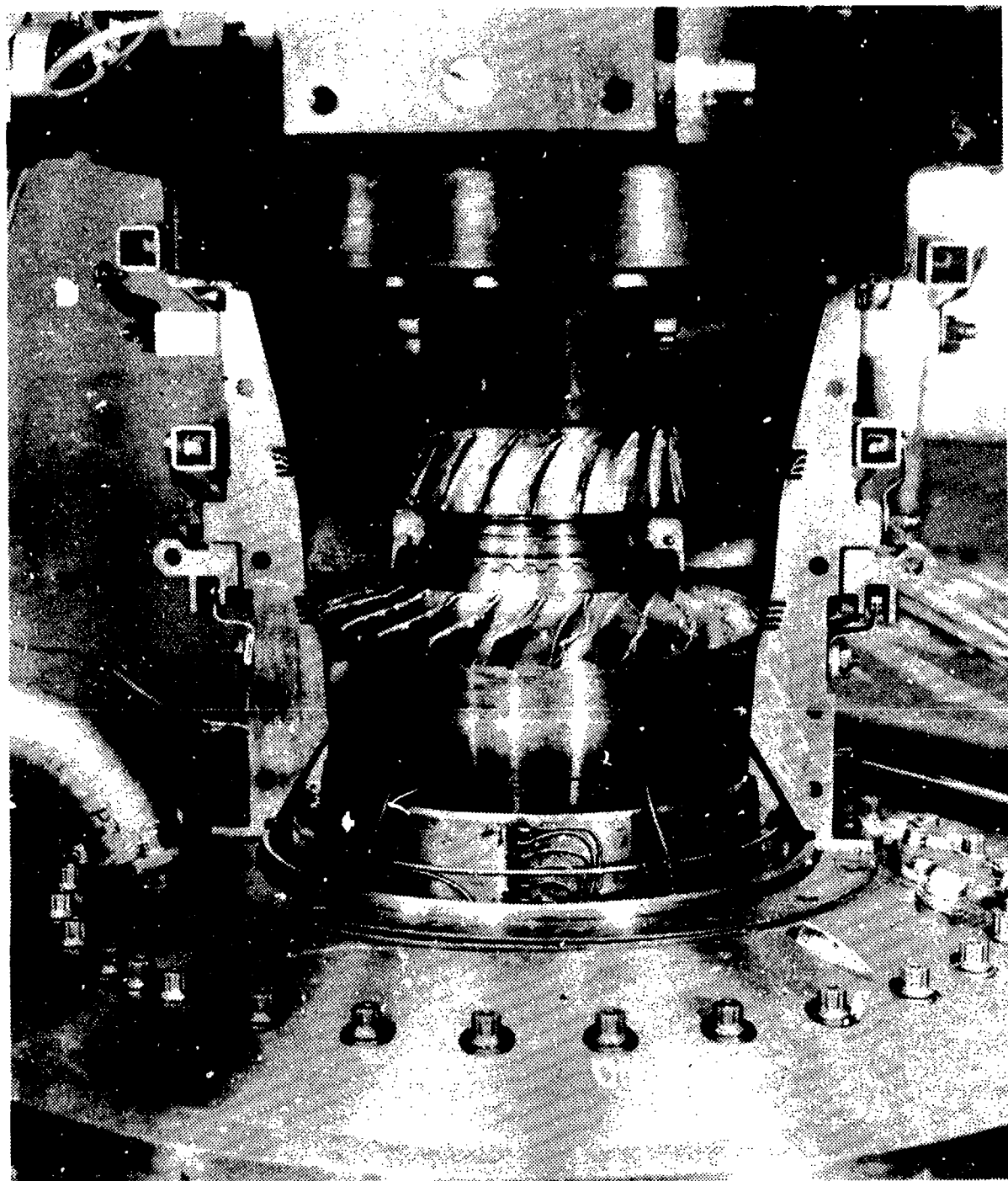


Figure 57. Damaged Rotor and Casing Hardware.

IGV's were bent and some torn by debris coming forward (see Figures 58 and 59).

Stage 1 vanes were nicked and torn at the leading and trailing edges (see Figures 58 and 59).

Stage 2 vanes were nicked at the leading edge with evidence of tip rub on the rotor (see Figures 58 and 59).

Four possible causes of failure were identified:

1. Stage 1 blade failure was caused by high stress throttling to stall or stall stresses which would produce a fatigue failure in the first flexural mode.
2. Stage 1 blade plate mode failure excited by the IGV or Stage 1 vane passing frequency stimulus. This type of failure could result in loss of a portion of the blade, causing subsequent additional damage.
3. Stage 1 blade root tensile failure caused by high end-effect stress coupled with low material properties.
4. Stage 2 blade trailing edge tip fatigue failure, causing subsequent additional damage.

Investigation conducted immediately after the failure and during disassembly of the vehicle ruled out the possibility of foreign object damage, facility malfunction or bearing failure as the cause. The major thrust of the failure investigation had been toward stress determination and material properties of the rotor stages.

In order to determine the cause of the failure, a detailed work plan was established to carry out the following tasks:

1. Fractographic analysis.
2. Material analysis:
  - a. Micro analysis.
  - b. Tensile tests.
  - c. Fatigue tests of blisk blades.
  - d. Chemical analysis.
3. Stress analysis:
  - a. Stage 1 blade root stress.
  - b. Review of potential stall stress levels.

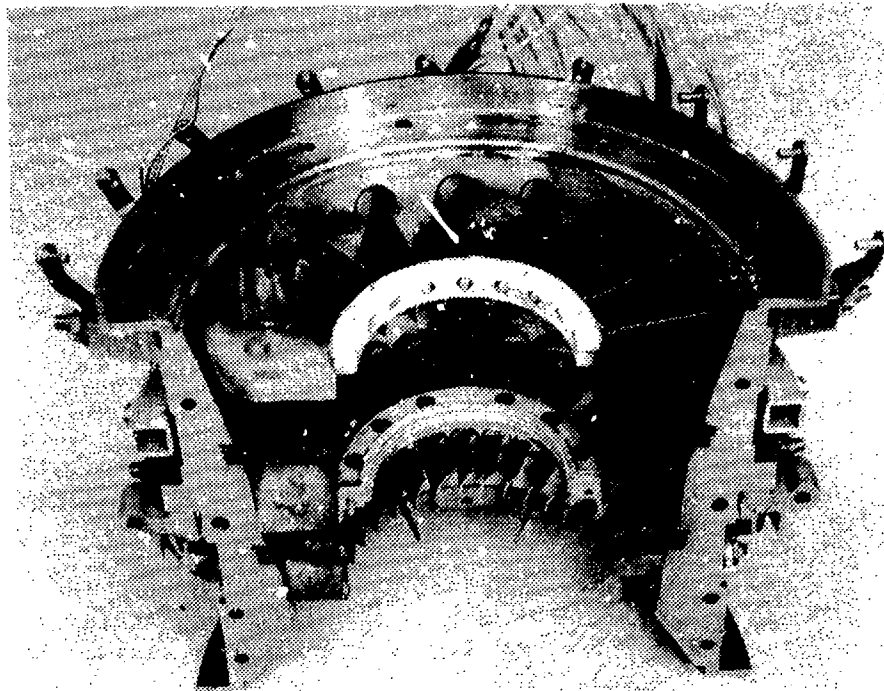


Figure 58. Stator Casing Half (FLA).

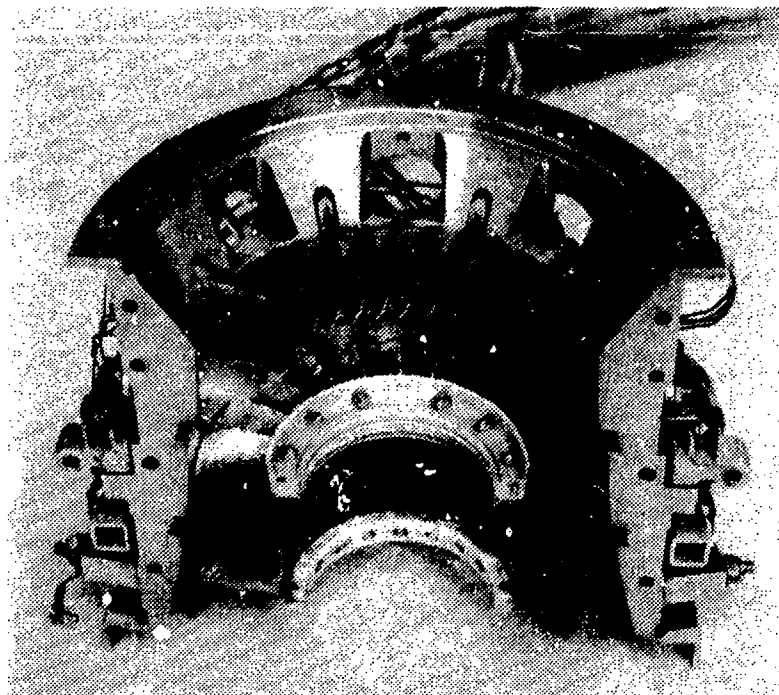


Figure 59. Stator Casing Half (ALF).

- c. Passing frequency excitation.
- d. Stage 2 blade mode shapes.
- e. Residual stress measurement.

4. Conclusions: The results of the fractographic and material analysis are summarized in the following discussion.

Fractographic Analysis: A fractographic analysis was carried out using a scanning electron microscope (SEM) and a replication technique with a conventional electron microscope. This analysis examined the fractured surface of the Stage 1 root and the Stage 2 tip corner.

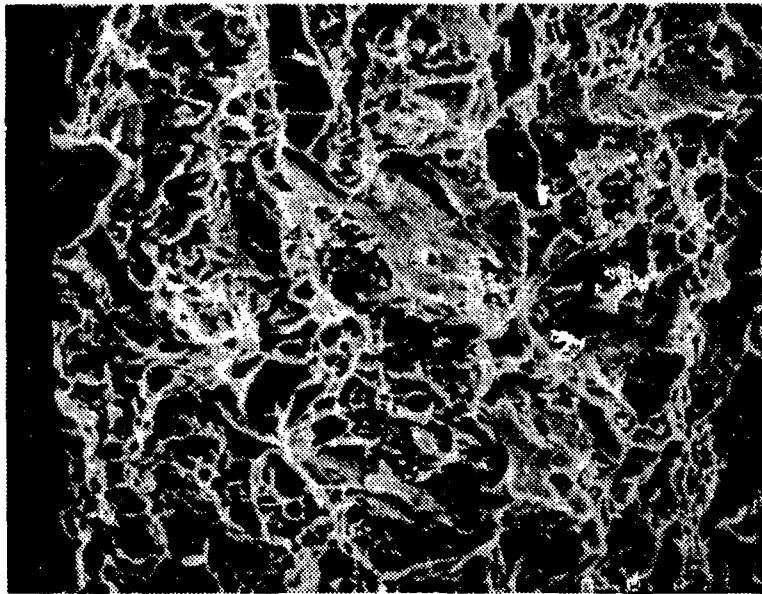
The SEM examination of the Stage 1 fractures revealed only tensile dimpling and quasi-cleavage, and no evidence of fatigue (see Figure 60). Since fatigue was suspected as the most probable cause of failure, a replication technique was carried out for some suspicious areas. The replication method found fatigue striations emanating from subsurface inclusions. One inclusion site was quite large (0.008 in. x 0.015 in.); however, other inclusion sites were of normal size for the AM355 material. The fatigue striation count was 100,000-240,000 lines per inch and is indicative of high cycle fatigue. See Figure 61 for typical results. It was apparent that the mean stress was high because only a small fatigue area was generated before tensile separation occurred.

A chemical analysis of the inclusion was made using the electron diffraction analysis method. The inclusions were identified as manganese sulfide.

The investigation of the Stage 2 tip corner fracture revealed fatigue beachmarks that were visible microscopically. The SEM analysis of the No. 3 blade tip corner could not confirm the fatigue evident from the microscopic examination, and it was possible that the surface was damaged by rubbing prior to fracture, so another blade was selected for SEM analysis. The No. 12 blade was selected for its clear beachmarks. It showed that the fracture initiated from the trailing edge convex side and propagated to the concave side to fracture at the tip corner. Striation counts were not possible because of rubbing damage to the fracture surface.

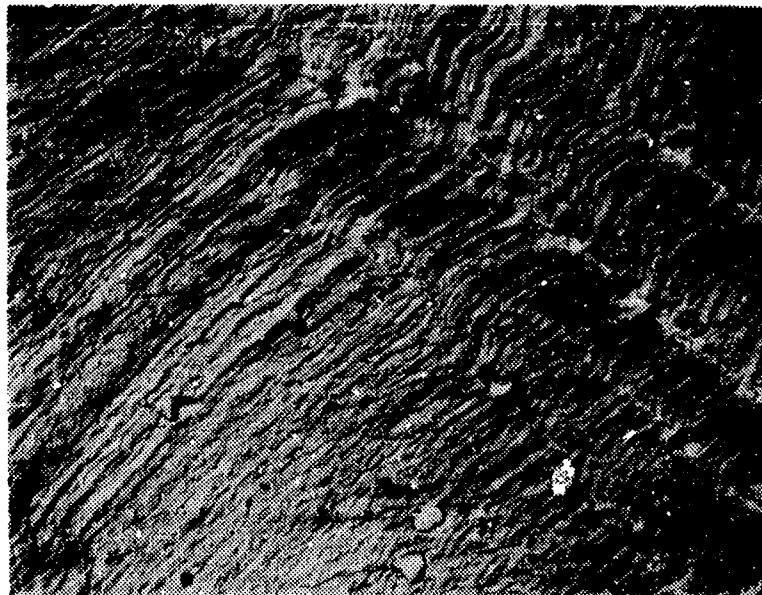
The Stage 2 trailing edge tip corner fractures were not necessarily secondary damage from the Stage 1 blade failure. They may have failed from a high order plate mode, so possible passing frequencies were reviewed and a check was made for possible Stage 2 mode shapes.

Material Analysis: A group of micro samples were taken from the Stage 1 and 2 blisks to determine chemistry, hardness and grain structure. The chemistry and hardness met the AM355 specification requirements. The structure had ferrite stringers and sulfide inclusions, but they were within the material specifications.



Remarks: View of typical tensile dimpling and quasi-cleavage in tensile fracture area.

Figure 60. SEM Examination of Stage 1 Blade Stub - 1000 X Magnification.



Remarks: Fatigue striations present 0.004 in. from surface origin of LCF crack. Striation density is approximately 180,000 lines/in.

Figure 61. Fatigue Striations in A286 Material - 5000 X Magnification.

Small tensile specimens were cut from the failed Stage 1 blisk to determine the tensile strength and ductility properties of the material. Four radial specimens and two axial specimens were tested. As shown in Table 13, only the elongation of the radial specimens is slightly below specification.

TABLE 13. TENSILE SPECIMENS			
	Tensile Strength (psi)	Elongation (%)	Reduction In Area (%)
Average of 4 Radial Specimens	173,000	11.8	29.7
Average of 2 Axial Specimens	171,800	15.2	49.9
Specification (Minimum)	165,000	12	25

The forging used for the Stage 1 blisk was accepted with a discrepancy in material properties in the transverse (radial) direction. The reported properties were 161,000 psi tensile strength, 8% elongation, and 8% reduction in area. The sample used to determine these properties was taken from the central portion at one end of the pancake forging where less material working would be introduced in the forging process, thus resulting in lower properties. A macroetch of the failed rotor disks indicated essentially axial grain flow, hence little upset in the forging process.

An AM355 blisk sample was fatigue tested in the first flex mode. This blisk was manufactured by the same vendor, using the same process as the axial-centrifugal compressor blisks. The results of this test were compared to fatigue tests of blade samples machined from AM355 bar stock, and design book data for AM355 material properties. The fatigue testing was controlled by adjusting the blade vibratory tip amplitude for each data point. A correlation of stress versus tip amplitude was obtained from one strain-gaged blade. The average failure tip amplitude for the bar stock blades was 0.1017-in. double amplitude and for the blisk blades 0.0750-in. double amplitude. These amplitudes corresponded to stresses of 81,500 psi and 60,000 psi respectively, as compared to a minimum value of 68,000 psi quoted by the design book. The actual stress level could be slightly higher if the strain gage was not located exactly on the high stress point. However, relative fatigue strengths obtained directly from the tip amplitude values should be valid, and indicated that the blisk blades are significantly weaker than the blades machined from bar stock.

The chemical analysis of the AM355 material was determined spectrographically. The results are shown in Table 14.

TABLE 14. AM355 CHEMICAL ANALYSIS						
Element	Mn	Si	Cr	Ni	Mo	C
Stage 1	1.2	.39	15.5	4.3	3.05	Not determined
Stage 2	1.2	.42	16.0	4.25	3.25	Not determined
Specification	.5/1.25	.5 max.	15/16	4/5	2.5/3.25	.10/.15

These analyses confirm that both blisks were made from the same heat of material and met the General Electric material specification.

Stress Analysis: The Stage 1 blade root stress distribution was recalculated using a three-dimensional irregular structural element stress and deflection computer program. A peak stress of 107,000 psi was calculated at 30% chord on the concave surface for centrifugal loading. The estimated peak stress immediately above the root fillet was 128,500 psi. This peak stress included the gas loading forces and a stress concentration factor for change in cross-section at the blade root. From a Goodman diagram, the allowable alternating stress for minimum material was 26,000 psi.

Strain gage data recorded on a similar axial compressor was reviewed to determine if regions of high vibratory stress could be identified. Areas of interest included a Stage 1 blade separated flow condition at approximately 85% speed and also stress levels during high speed stalls.

The separated flow stresses peaked at 12,500 psi which at 85% speed is not sufficient to produce failure. It is possible that this stress could be higher in the axial compressor due to different vane schedules.

A review of the test history indicated that operation in the 85% speed region was accomplished early in the test plan. Because of the extensive testing at higher speeds that occurred after this 85% speed, stresses at 85% speed were not a probable cause of the failure.

The maximum speed stall observed during stress coverage of this similar compressor was at 90% speed. At the moment of stall the stress peaked at 7500 psi. Once again, this stress was not high enough to produce failure; however, as speed was increased the magnitude of the stall stress would increase due to the higher blade loading. It was possible that the 11 stalls at 95% speed and 3 at 100% speed were of high enough level to initiate the failure.

A similar Stage 2 blisk was tested to determine mode shapes that would be sensitive to trailing edge tip cracking. This test indicated that the 6th and 9th modes have nodal lines across the trailing edge tip. These modes occurred at 21,600 Hz and 27,500 Hz in the Stage 2 blade. Neither of these modes was coincident with a per-rev excitation at the failure speed. Possible excitation of the 7th mode could occur at 55,000 rpm (approximately 90% speed) by the 26 Stage 1 vanes.

The residual surface stresses were measured for a similar AM355 blisk by using an X-ray diffraction method. The results showed a 112,000 psi residual compressive stress. This residual surface stress may account for the subsurface fatigue origins.

Conclusions: The Stage 1 blade failure was fatigue resulting from excessive vibratory stress at high speed. The mechanism which produced the high vibratory stress was probably high speed stall or throttling to stall at high speed. The AM355 material was below average in properties but not below the material minimum requirements.

The Stage 2 trailing edge tip corner had failed from fatigue, but it was not clear if the fatigue was a result of the Stage 1 blade failure. Evaluation of possible plate modes did not reveal any coincident per-rev excitation at the failure speed.

#### Aerodynamic Test Results from Axial Compressor Test (ACV)

The performance map of the axial compressor was obtained for the predicted nominal as well as other stator schedules for the purpose of performance optimization. The stage characteristics and effectivities of the stages were computed from the test data. Also included in the test results are the casing static pressure data and the intercompressor duct profile data.

#### Nominal Stator Schedule Performance

The performance map of the axial compressor operating with the nominal stator schedule is shown in Figure 62. It may be observed that at 100% corrected speed, the predicted stall pressure ratio was not attained, although the operating line pressure ratio was reached at approximately 3% higher flow. The peak efficiency at 100% speed for the nominal schedule was 78.5%, which is approximately 4-1/2 points lower than the objective. At lower corrected speeds, the efficiency gap increases, as may be seen from the map in Figure 62.

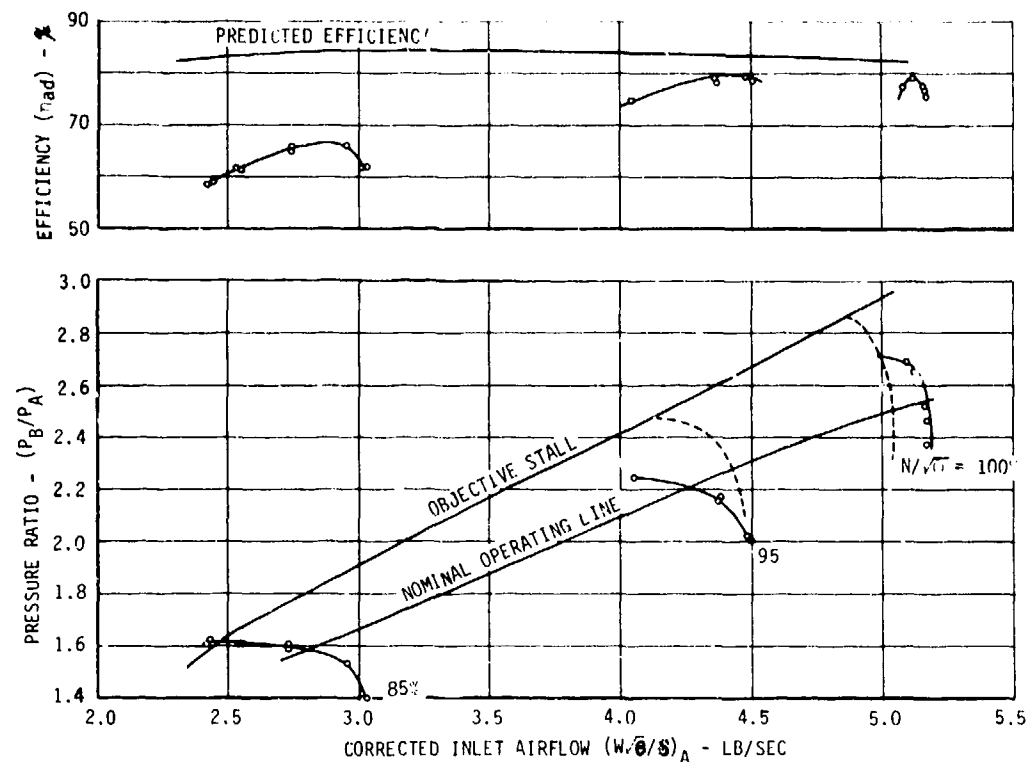
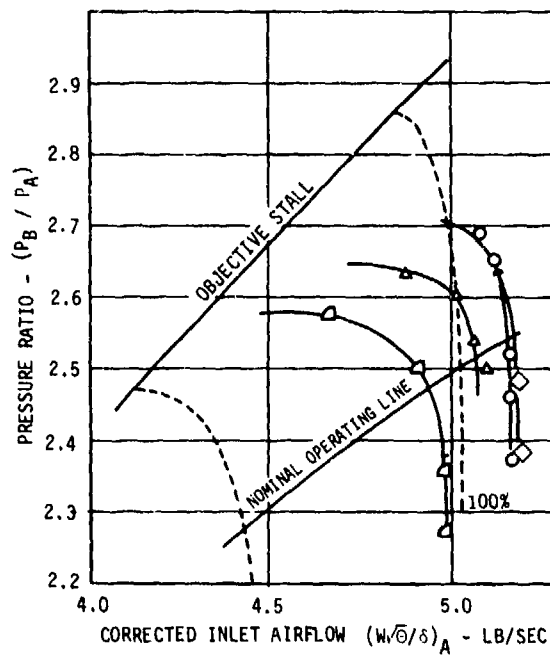
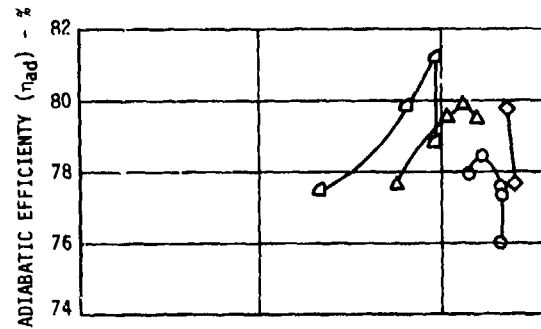


Figure 62. ACV-I Axial Compressor Performance Nominal Stator Schedule.

#### Variable Stator Schedule Performance

The compressor performance for different IGV and Stage 1 stator settings was plotted in Figures 63 through 66. It was clear that a marked improvement in efficiency was achieved. At 100% corrected speed, the optimum closure was for IGV 3° closed and S1 5° closed. At 95% speed, the optimum efficiency was achieved at an IGV and an S1 setting of 3° and 7° closed respectively. At lower speeds it appears that the most efficient range of the compressor was close to the 100% corrected speed design setting. With the optimized closures, the efficiency of the compressor was within 2 percentage points of the predicted efficiency at design speed. This tendency appeared to persist at lower speeds although sufficient data was not taken to optimize stator schedule below 85% corrected speed.

Because of the flow-speed characteristics of the compressor, the optimum axial compressor schedule could not be used. Therefore, an optimized stator schedule was derived from the axial and centrifugal compressor performance considerations (see Figure 67). This modified schedule shown in Figure 68 was used during the subsequent combined compressor test FCV-I.



STATOR SCHEDULE

KEY	IGV	S1
○	-2	0
△	0	5
□	3	5
◇	-4	5

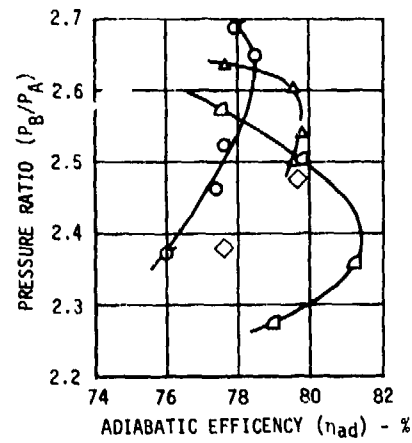


Figure 63. Axial Compressor Performance - 100% Speed, VG Optimization.

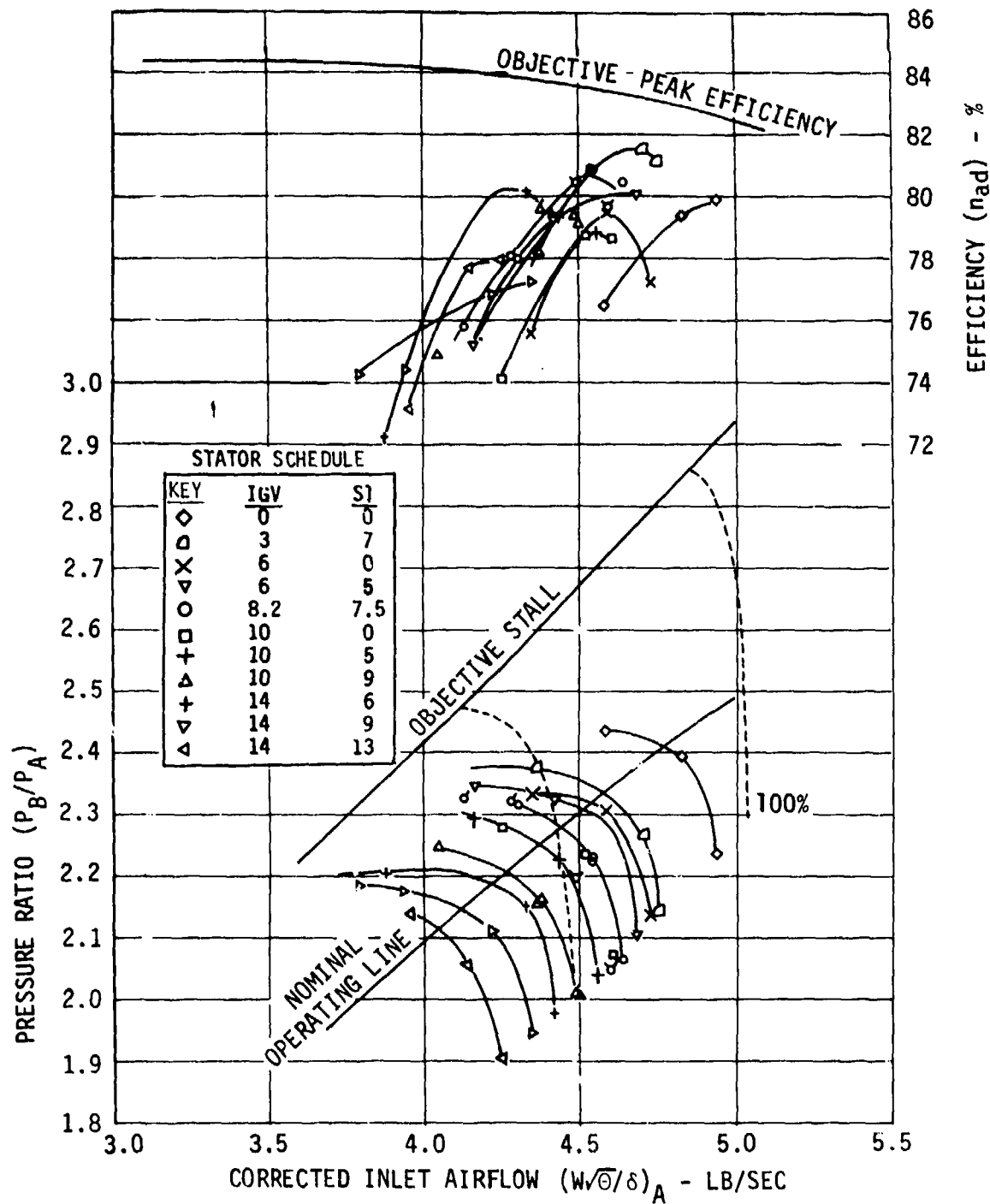


Figure 64. Axial Compressor Performance - 95% Speed, VG Optimization.

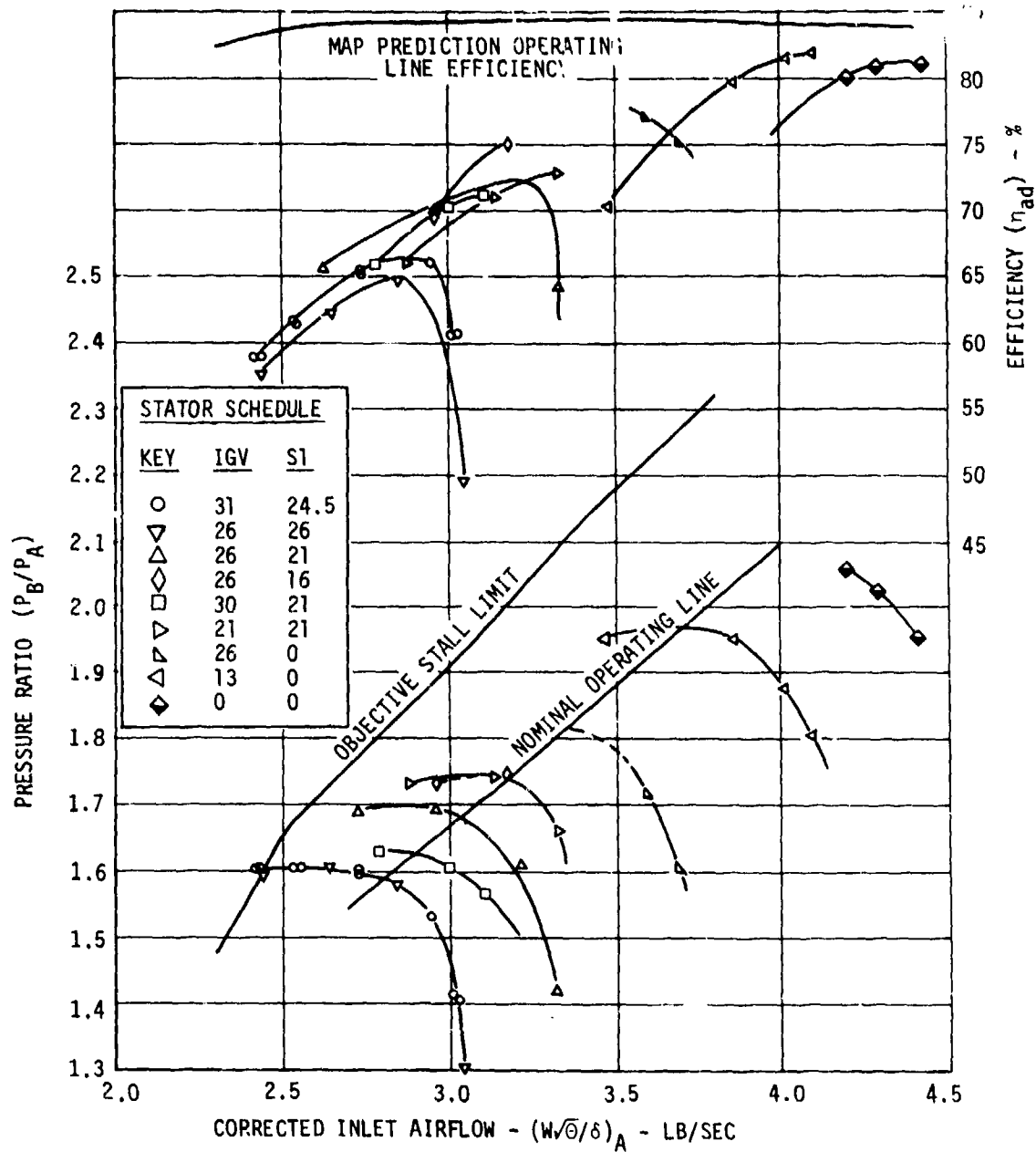


Figure 65. Axial Compressor Performance - 85% Speed, VG Optimization.

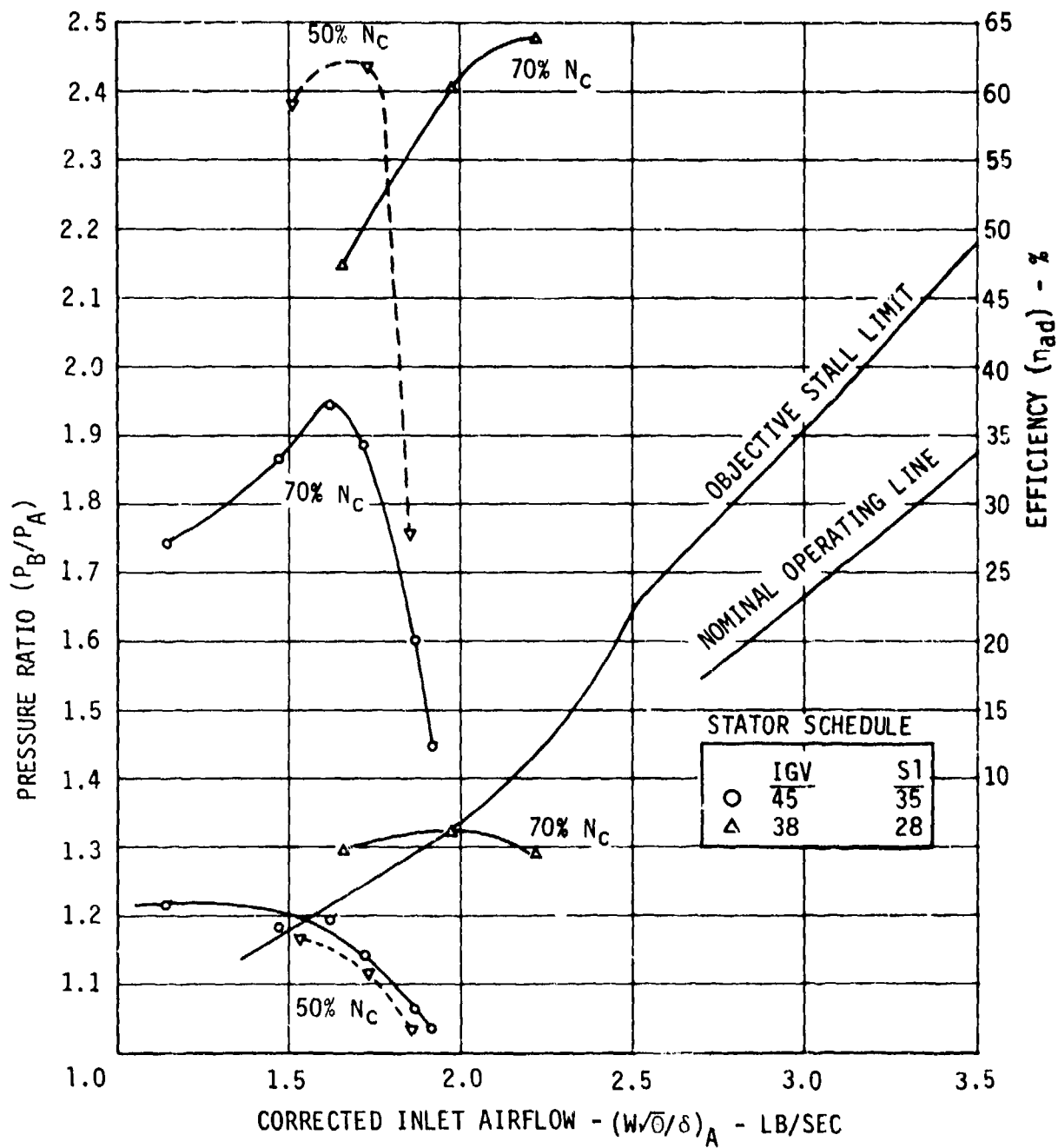


Figure 66. Axial Compressor Performance - Low Speed.

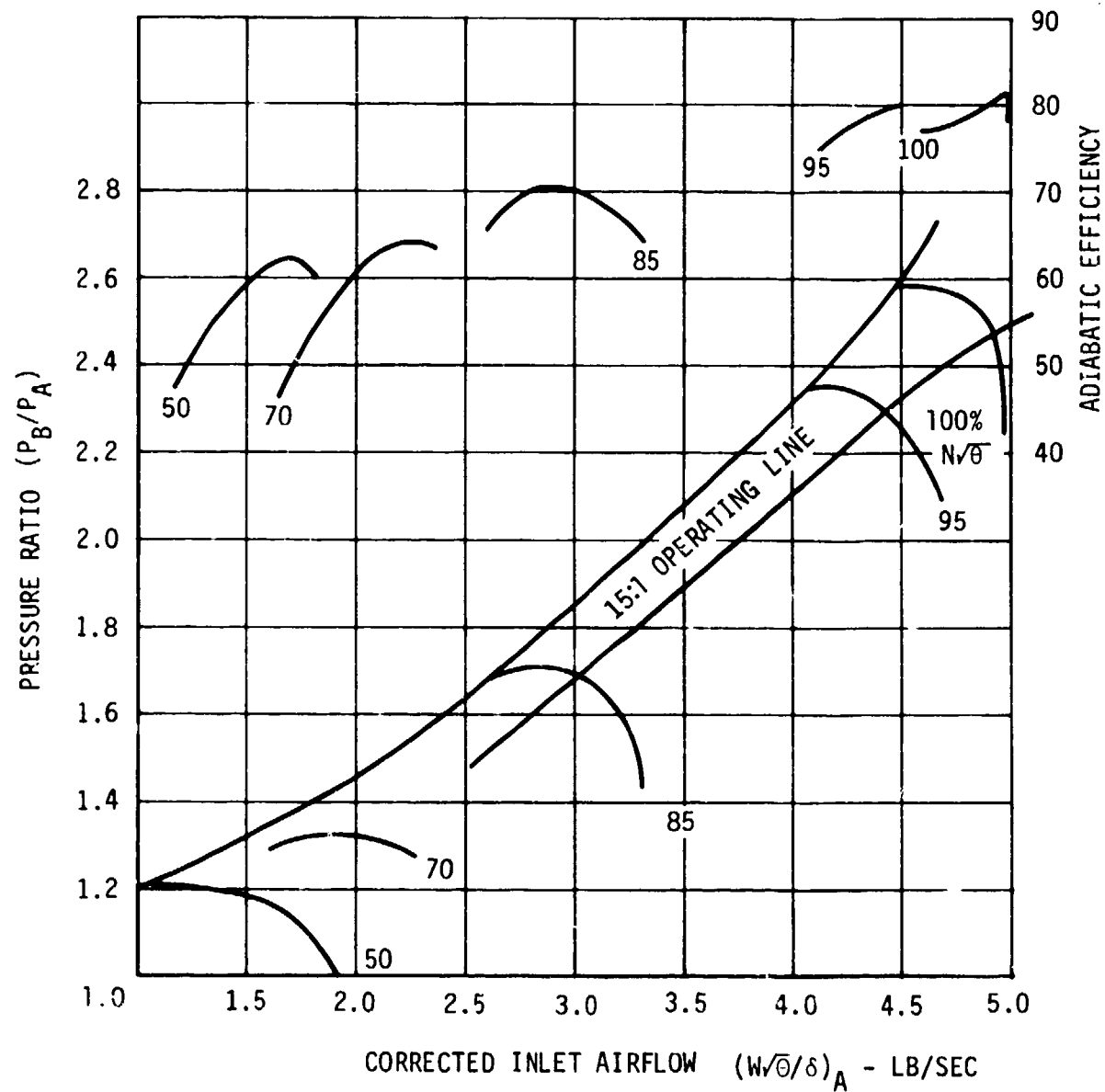


Figure 67. Axial Compressor Performance - Optimum Stator Schedule.

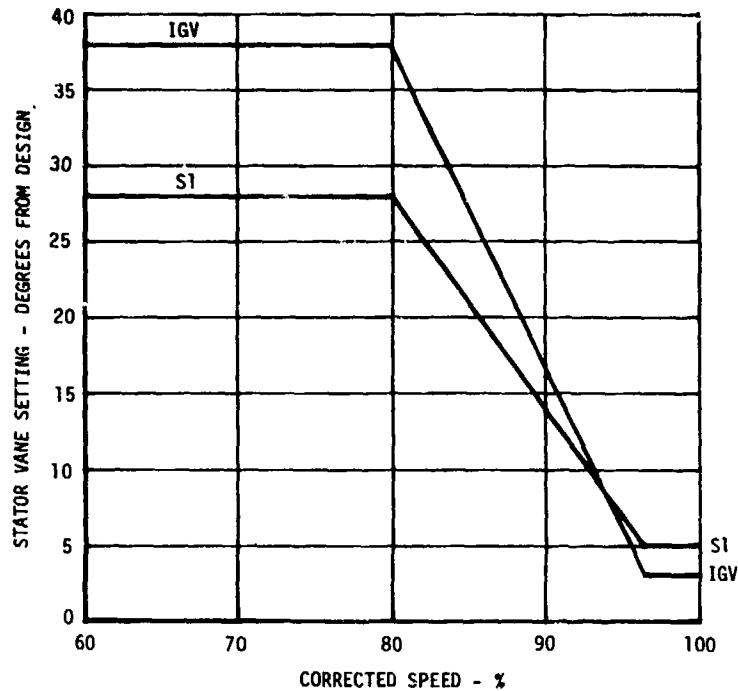


Figure 68. FCV-I Stator Schedule A.

### Effectivities

The stall performance of an axial compressor stage has been related to a stall aspect ratio parameter (SARP) and the effective static pressure rise coefficient ( $\Delta p/q$ ) at stall. The SARP is defined as a function of aspect ratio ( $c/h$ ), solidity ( $\sigma$ ), and outlet air angle ( $\beta_2$ ):

$$\text{SARP} = \sqrt{(c/h) \times (\sigma / \cos \beta_2)} \quad (11)$$

The ratio of the effective static pressure rise, averaged over the stage, to the effective static pressure rise coefficient at stall is defined as the stage effectivity:

$$\text{Effectivity} = (\Delta p/q) / (\Delta p/q)_{\text{stall}} \quad (12)$$

The effectivity is used as a measure of the potential of the stage to produce a static pressure rise. At the design point, the effectivity is less than unity and is equal to unity at stall for the limiting stage.

The effectivity was calculated for each axial stage using test results obtained at 100%, 95%, and 85% corrected speed. These results for the optimized stator schedule are shown in Figures 69 through 71. At 100% corrected speed, the first stage effectivity is close to the design value at the design pressure ratio of 2.5:1 but the second stage is somewhat below the design intent (see Figure 69). Further throttling

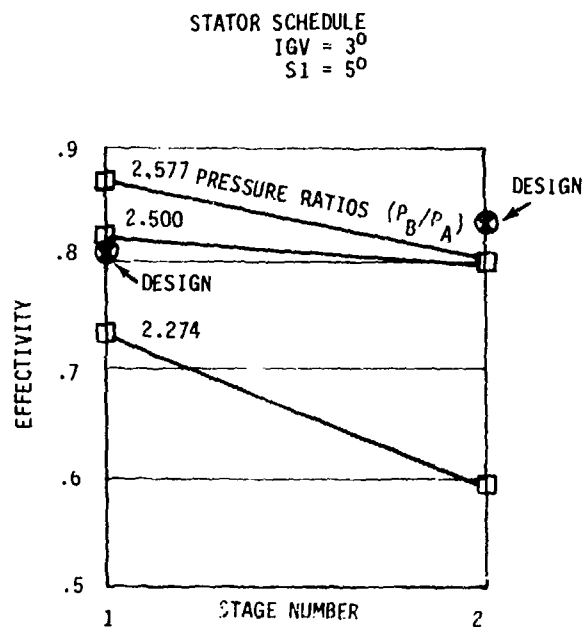


Figure 69. Axial Compressor Effectivity - 100% Speed.

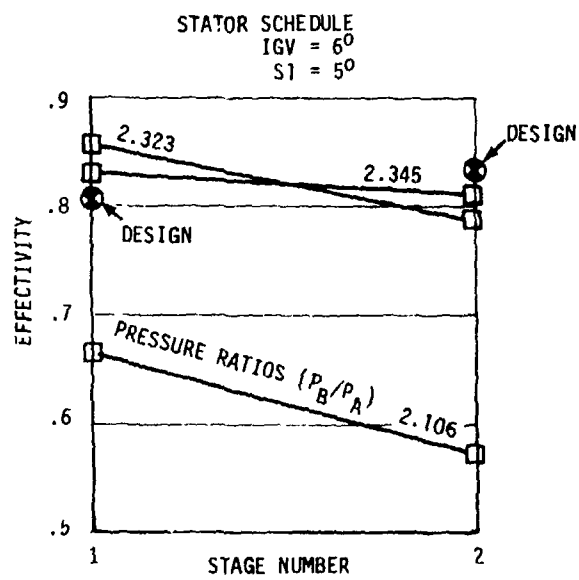


Figure 70. Axial Compressor Effectivity - 95% Speed.

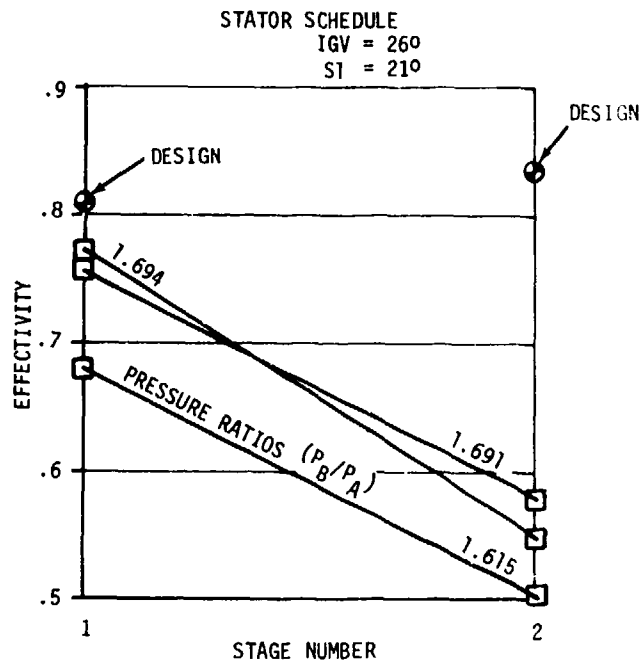


Figure 71. Axial Compressor Effectivity - 85% Speed.

at 100% speed to a 2.577:1 pressure ratio raises the first stage effectivity while the second stage effectivity remains below the design intent. This trend would indicate that the first stage outlet flow profile is inhibiting the second stage static pressure rise. The results for 95% and 85% corrected speed indicate a drop in second stage effectivity as the axial compressor is throttled toward stall (see Figures 70 and 71). This is another indication of an adverse flow profile from the first axial stage. The low absolute levels of effectivity at 85% corrected speed are a result of the large amount of closure of the variable stators.

#### Stage Characteristics

The stage characteristics of pressure coefficient, flow coefficient, and stage efficiency were calculated from the measured wall static pressures, total temperatures, and airflow. The actual characteristics are calculated using the following expressions:

Work coefficient

$$\psi = (T_2 - T_1) (2g_o J C_p / U_1^2) \quad (13)$$

Pressure coefficient

$$\psi' = T_1 - \left[ \left( P_2/P_1 \right)^{\frac{\gamma-1}{\gamma}} - 1 \right] \times (2g_o J C_p / U_1^2) \quad (14)$$

Flow coefficient

$$\phi = V_{Z1} / U_1 \quad (15)$$

where  $V_{Z1}$  is the axial velocity calculated at the design stator setting

$U_1$  is the wheel speed at the inlet pitch line

therefore, the stage efficiency ( $\eta$ ) is

$$\eta = \psi' / \psi \quad (16)$$

The characteristics are normalized to correct for variable stator operation using the following expressions:

$$\phi_N = \frac{1}{1/\phi + \tan \beta_1 - \tan (\beta_1 + \Delta\beta)} \quad (17)$$

where  $\beta_1$  = design exit flow angle (previous stator)

$\Delta\beta$  = change in stagger (previous stator)

$$\psi_N = \psi \cdot (\phi_N / \phi) \quad (18)$$

$$\psi'_N = \eta \cdot \psi_N \quad (19)$$

The stage characteristics calculated from the ACV test data were plotted in Figures 72 through 74 for both stages at 100%, 95%, and 85% corrected speed. All of the various stator schedules were included since normalized values of work coefficient and flow coefficient were plotted.

These results at 100% corrected speed indicate that the work input of the first stage was higher than design and the efficiency was about four points low (see Figure 72). The second stage results indicate that the work input was a little below the design intent, but the efficiency was at the design objective level. These results identify a deficiency in the first axial stage which was also apparent in the effectivity results. The fact that the second stage work input is somewhat low may be due to the flow profile from the first stage. The test results at 95% and 85% corrected speed show a similar trend (see Figures 73 and 74). The wider scatter of test data at 85% corrected speed is a result of the large variation in stator settings which were tested. The range of vane angles at 95% and 100% corrected speed was less than at 85% corrected

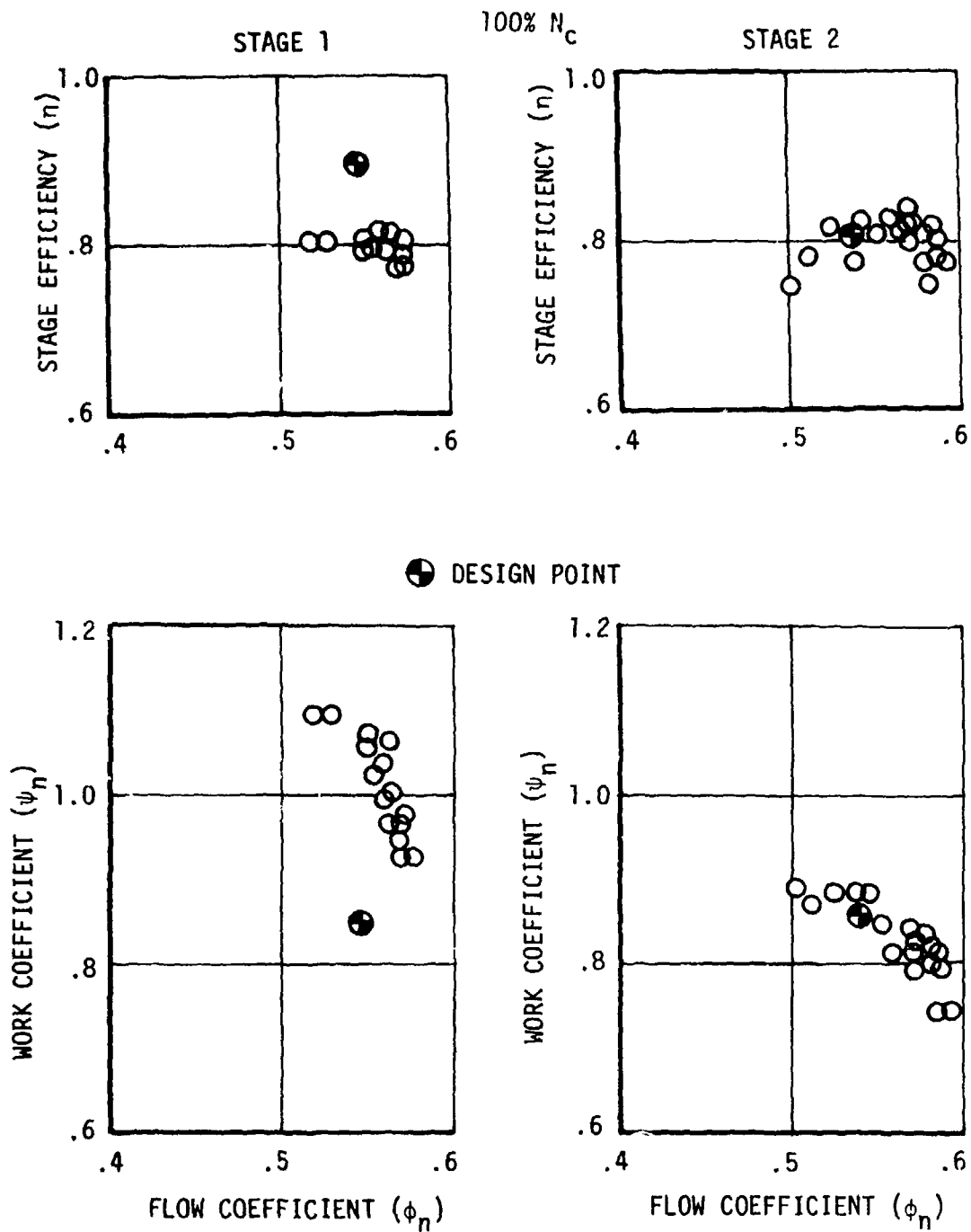


Figure 72. Axial Compressor Normalized Stage Characteristics - 100% Corrected Speed.

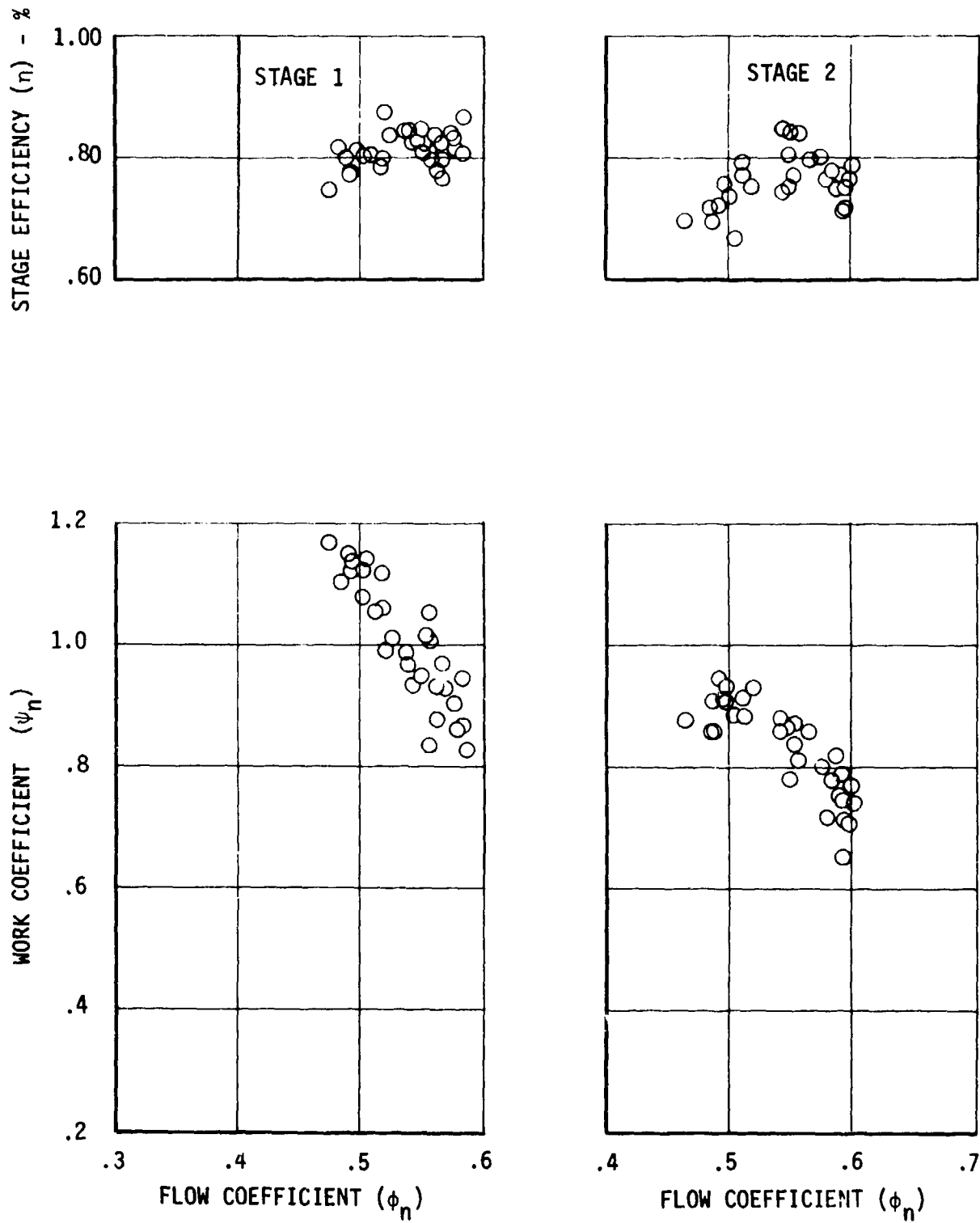
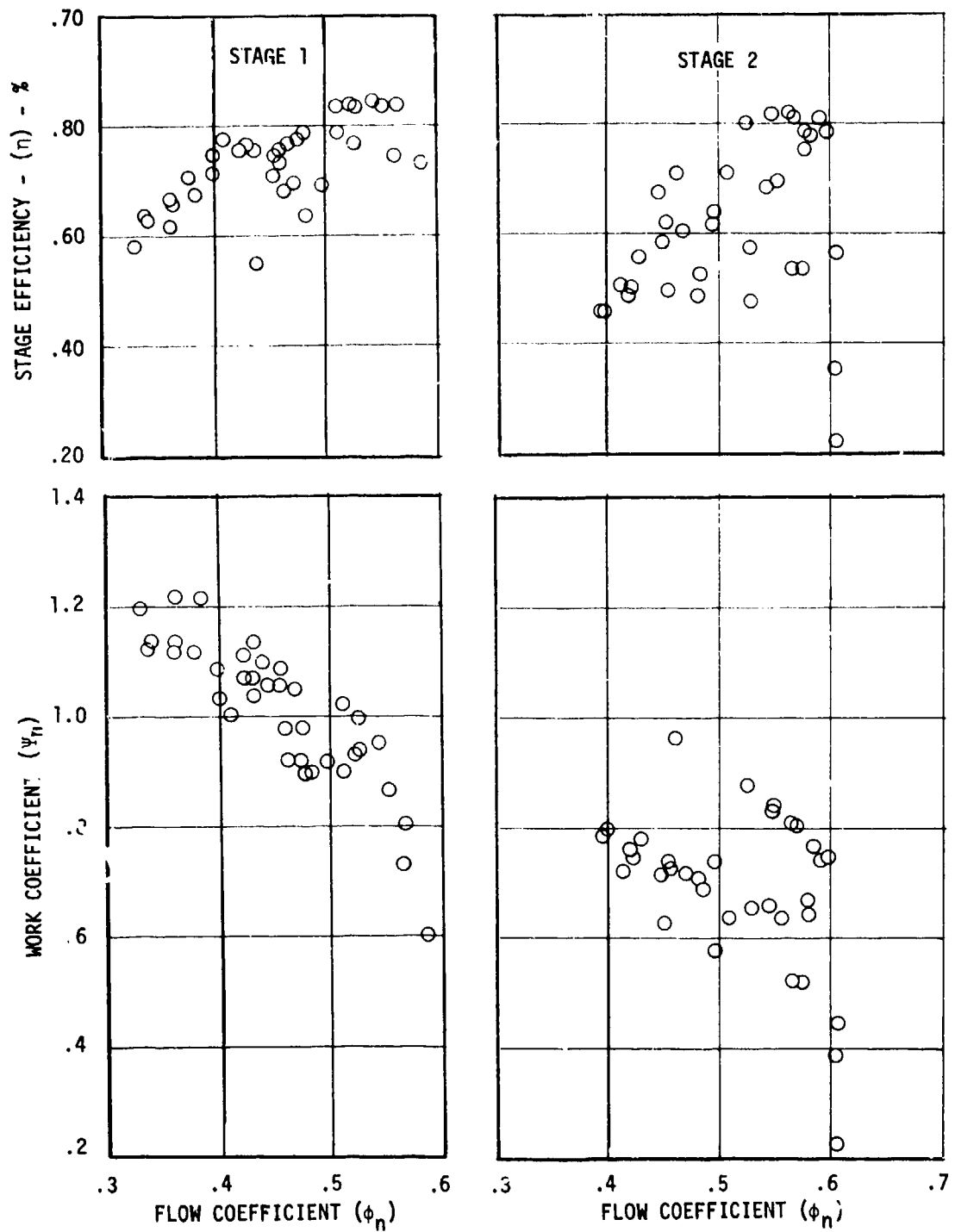


Figure 73. Axial Compressor Normalized Stage Characteristics - 95% Corrected Speed.



speed, and the data tended to group closer using this simplified normalizing procedure.

#### Casing Static Pressure Distribution

The casing static pressure distribution is based on the static pressure change across the blade row, which is negative for an inlet guide vane and positive for rotors and stators. Static pressure data at 100% corrected speed and 2.5:1 overall total pressure ratio are plotted in Figure 75. These results indicate good agreement with the design intent.

#### Intercompressor Duct Flow

Figures 76 through 78 show the radial flow distribution at the centrifugal compressor inlet (Plane C) measured during the traverse test for 100% and 95% corrected speed. The total temperature traverse test data is shown in Figure 76 along with the design objective radial temperature profile. The test data temperature level is higher even though the pressure ratio was 2.46:1 versus the design value of 2.5:1. The general shape of the temperature profile is similar to the design intent. A review of the stage characteristics shown in Figure 72 reveals that this higher work input is occurring in the first stage axial rotor.

The 100% corrected speed total pressure and angle traverse test data are shown in Figure 77 along with the design intent. The total pressure in the outer third of the annulus indicates a below-objective level; hence, a region of low efficiency. The angle data are peculiar because of the low swirl at the casing and high swirl at the hub. The high level of hub swirl was a concern since it may have been generated by the drag of the rotating hub wall or by separation in the stage two stator. Another possibility for this angle variation would be bias of the traverse results caused by a stator vane wake, since only one radial location was surveyed. The total pressure and flow angle test data at 95% corrected speed are shown in Figure 78, where a similar total pressure and angle variations were observed.

#### Axial-Centrifugal Compressor Considerations

The axial compressor test demonstrated a wide range in flow-speed characteristics by use of the variable stators (see Figures 63, 64, and 65). The efficiency of the axial compressor was about 2 points below the objective level, but since the axial compressor produced about 25% of the overall enthalpy rise, it only influenced the overall axial-centrifugal efficiency by 1/2 point. The flow-speed characteristic was adequate for matching with the objective centrifugal stage. It was judged not worthwhile to redesign the axial compressor for a higher efficiency because of the uncertainties this would introduce in the matching with the centrifugal compressor relative to the small potential gain in overall efficiency. Of greater interest were matching effects and vibratory stress data on the axial compressor blades over the range of operation contemplated for the

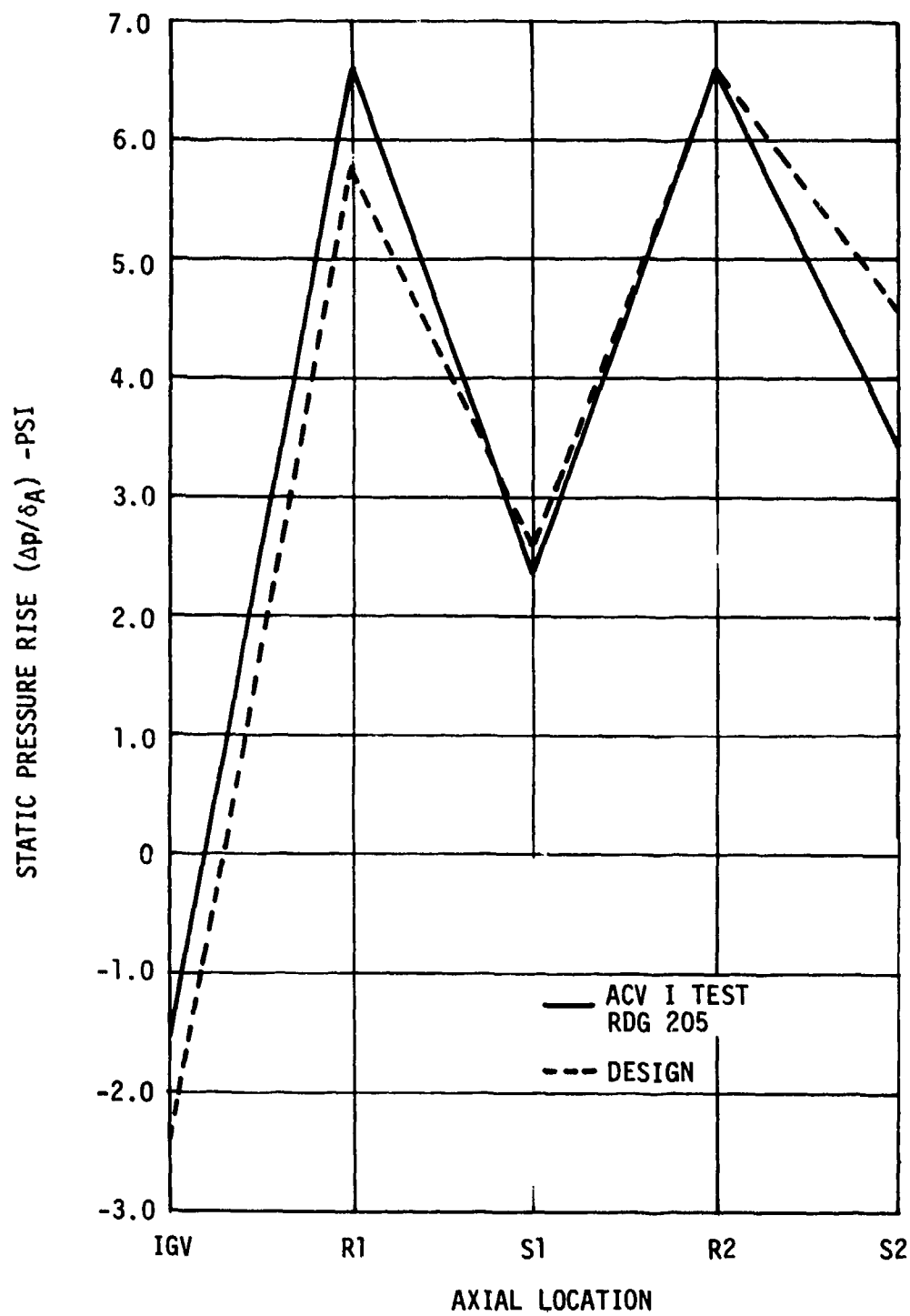


Figure 75. Axial Compressor Static Pressure Distribution - 100% Corrected Speed.

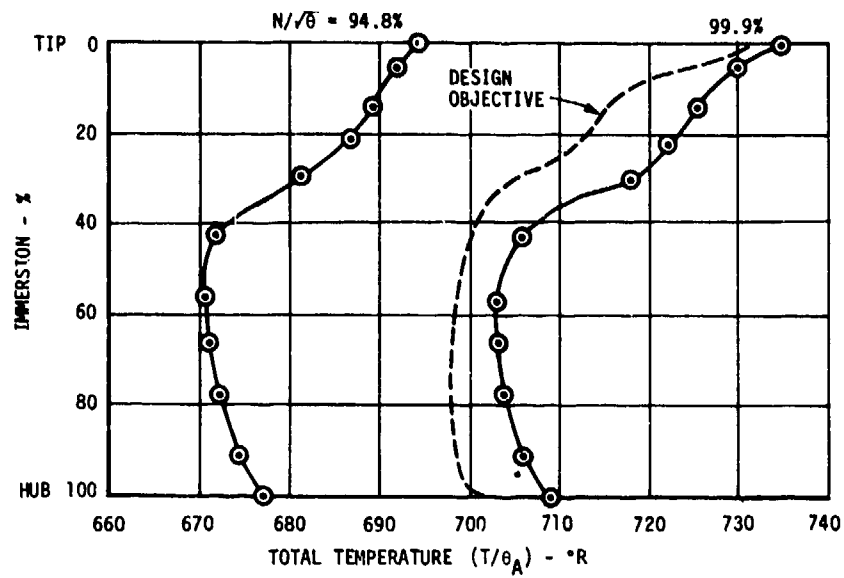


Figure 76. ACV-I Plane C Traverse Data.

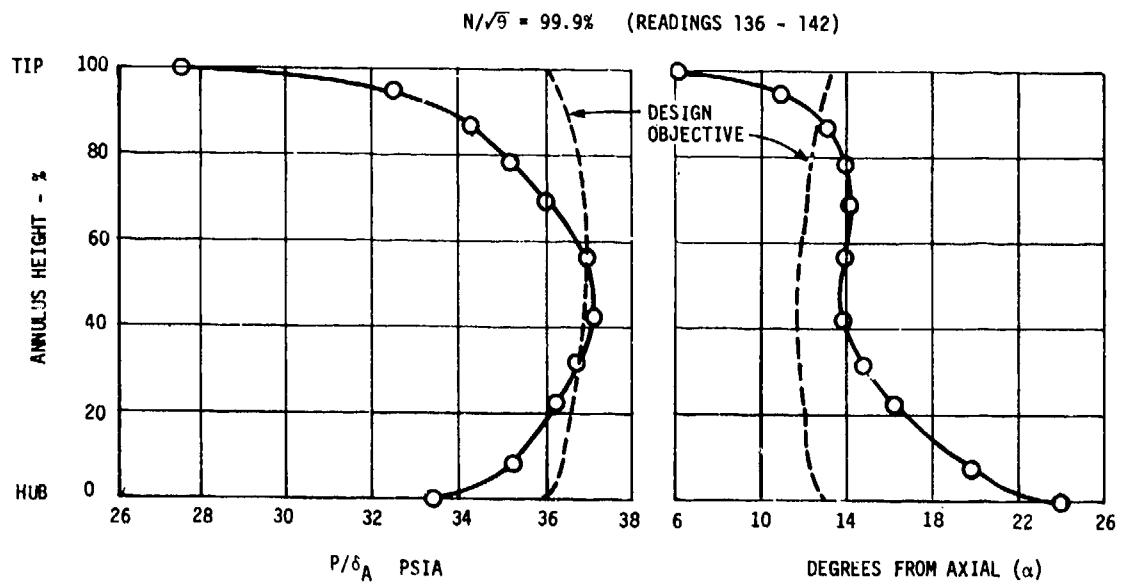


Figure 77. ACV-I Plane C Traverse Data.

$N/\sqrt{\theta} = 94.8\%$  (READINGS 128 - 132)

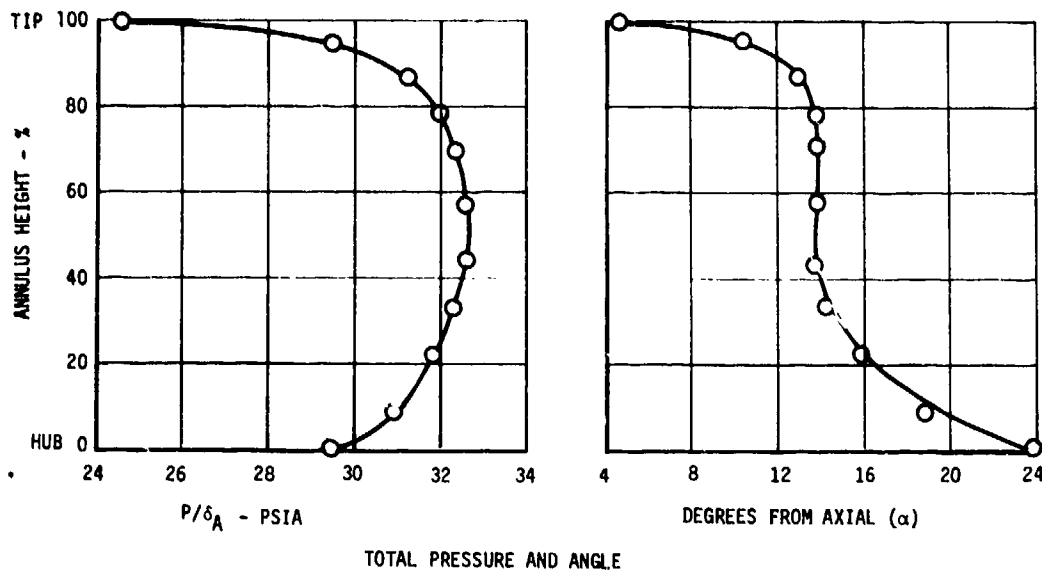


Figure 78. ACV-I Plane C Traverse Data.

axial-centrifugal component test. For these reasons, it was decided to use this aero design of the axial compressor for the FCV-1 axial-centrifugal component tests.

#### CENTRIFUGAL IGV BLOW TEST

##### Summary

The test was performed in two runs on 11 and 14 November 1972 in the Evendale Aero Component Laboratory Test Cell A8W. Test data was obtained using the standard shroud and casing instrumentation plus the 15-element Plane C wake rake and the 3-parameter Cobra probe used in the ACV test. Test data were obtained at the following conditions:

1. Nominal IGV setting at airflows of 2.34, 2.06, and 1.5 lb/sec.
2.  $-5^\circ$  IGV setting at airflows of 2.34 and 1.5 lb/sec.
3.  $+5^\circ$  IGV setting at airflows of 2.34 and 1.5 lb/sec.
4.  $-10^\circ$  IGV setting at airflow of 2.37 lb/sec.

The test data for each condition obtained wake rake readings at seven immersions (5%, 10%, 30%, 50%, 70%, 90%, and 92% from tip) and a Plane C Cobra probe traverse for angle, total pressure, and temperature. The principal function of the Cobra probe was angle, since total pressure was derived from the wake rake survey. There were no problems on this test, and all planned test data were obtained. A total of 68 full data points were logged during the test.

### Aerodynamic Test Results

The inlet guide vane for the centrifugal component vehicle was tested over a representative range of flows and stagger settings to determine its loss characteristic. The test consisted of selecting values of airflow and inlet guide vane stagger that would encompass the range contemplated for the CCV component test. At each test condition, a traverse was made for angle and total pressure at a plane that corresponded with the leading edge of the impeller (see Figures 79 through 86).

The test procedure was to set the design airflow (2.34 lb/sec) and design inlet guide vane stagger and then radially traverse in succession the Cobra and wake rake. Perturbations in inlet guide vane setting of  $-10^\circ$ ,  $-5^\circ$ , and  $+5^\circ$  from nominal were also made. Then, at the nominal inlet guide vane setting, airflows of 2.0 and 1.5 lb/sec were checked. The wake rake traverse was weight-averaged in the tangential direction to give an average total pressure for each immersion and then integrated in the radial direction to give a total pressure recovery coefficient for the test configuration.

In Figures 80, 82, 84, and 86, the results are plotted for varying the inlet guide vane stagger from  $+5^\circ$  to  $-10^\circ$ , in increments of  $5^\circ$ , at design airflow. In Figures 81, 83, and 85, similar data at stagger settings of  $+5^\circ$  and  $-5^\circ$  are shown for a nominal airflow of 1.5 lb/sec. A kink was observed in the angle traverse data near 15% annulus height for the nominal IGV setting at 2.08 lb/sec airflow (see Figure 80). This angle variation was not evident in the data for higher and lower airflows for the nominal vane setting, and it is attributed to an IGV wake influencing the Cobra probe. A similar variation was observed near the casing for the  $-5^\circ$  IGV setting at 2.36 lb/sec airflow (see Figure 82).

The profiles at nominal stagger and an airflow of 2.08 lb/sec are presented in Figure 80. Figures 79 through 81 demonstrate respectively, the effect of reducing airflow at nominal inlet guide vane setting.

### Aerodynamic Analyses

The results of weight-averaging the profiles to determine a total pressure recovery coefficient for the configuration are shown in Figure 87. It is apparent that the nominal stagger condition represents

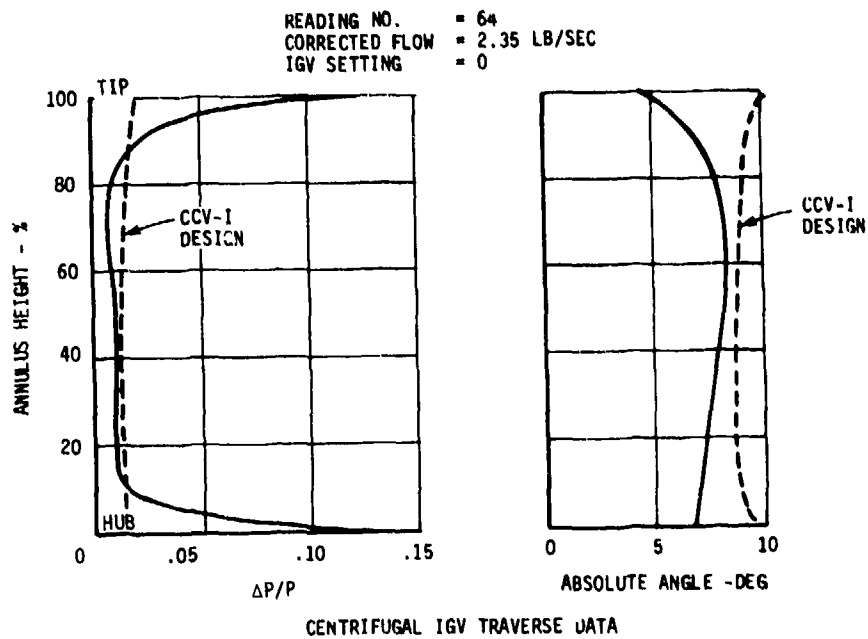


Figure 79. Total  $\Delta P/P$  and Absolute Angle vs Annulus Height.

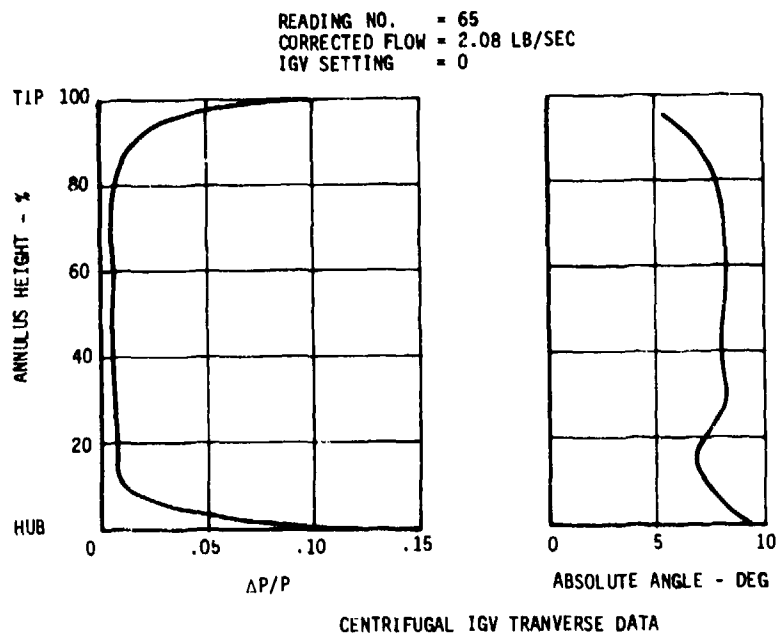


Figure 80. Total  $\Delta P/P$  and Absolute Angle vs Annulus Height.

READING NO. = 66  
 CORRECTED FLOW = 1.52 LB/SEC  
 IGV SETTING = 0

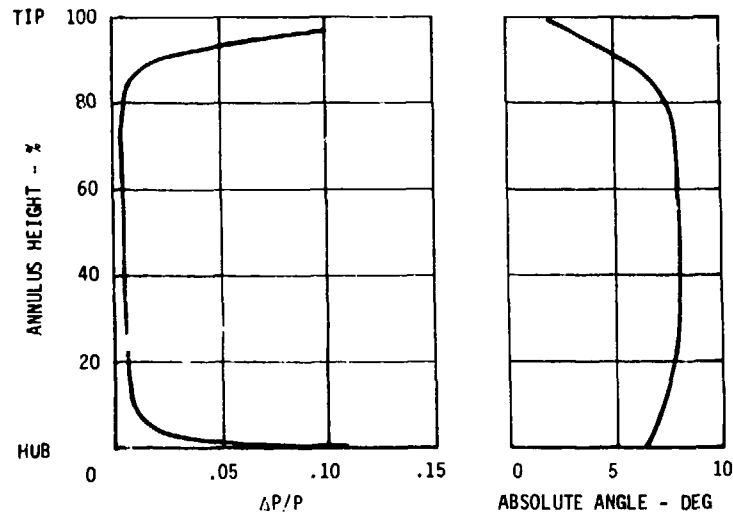


Figure 81. Total  $\Delta P/P$  and Absolute Angle vs Annulus Height.

READING NO. = 68  
 CORRECTED FLOW = 2.36 LB/SEC  
 IGV SETTING = -5

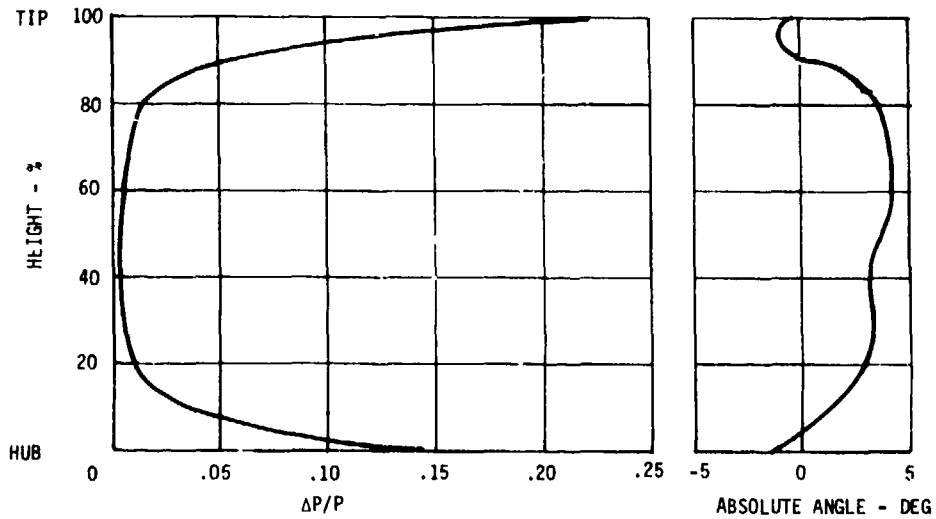


Figure 82. Total  $\Delta P/P$  and Absolute Angle vs Annulus Height.

READING NO. = 67  
CORRECTED FLOW = 1.52 LB/SEC  
IGV SETTING = -5

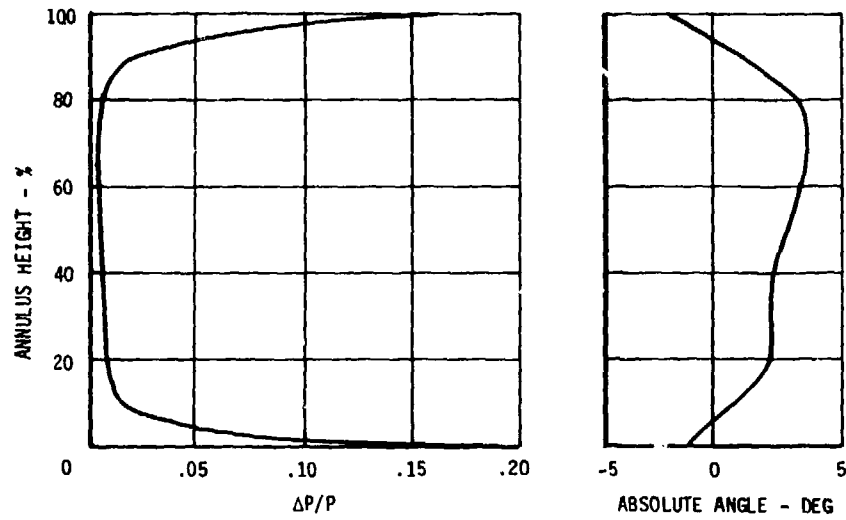


Figure 83. Total  $\Delta P/P$  and Absolute Angle vs Annulus Height.

READING NO. = 43  
CORRECTED FLOW = 2.34 LB/SEC  
IGV SETTING = +5

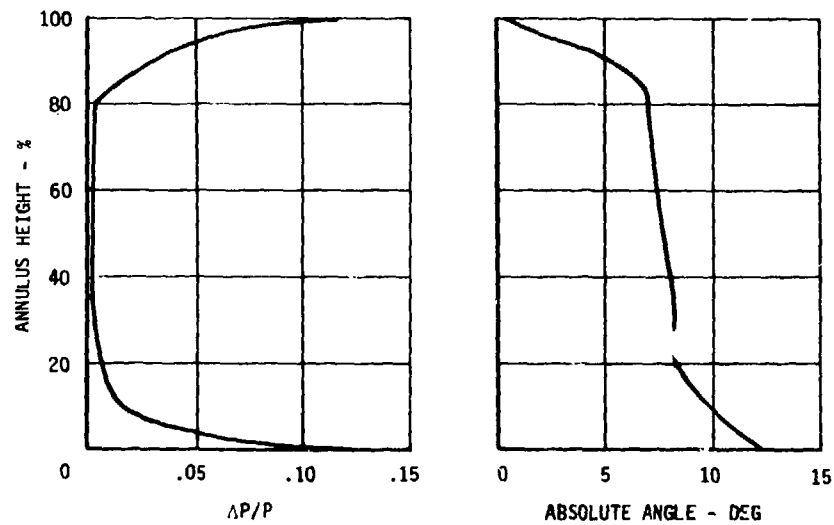


Figure 84. Total  $\Delta P/P$  and Absolute Angle vs Annulus Height.

READING NO. = 50  
CORRECTED = 1.51 LB/SEC  
IGV SETTING = +5

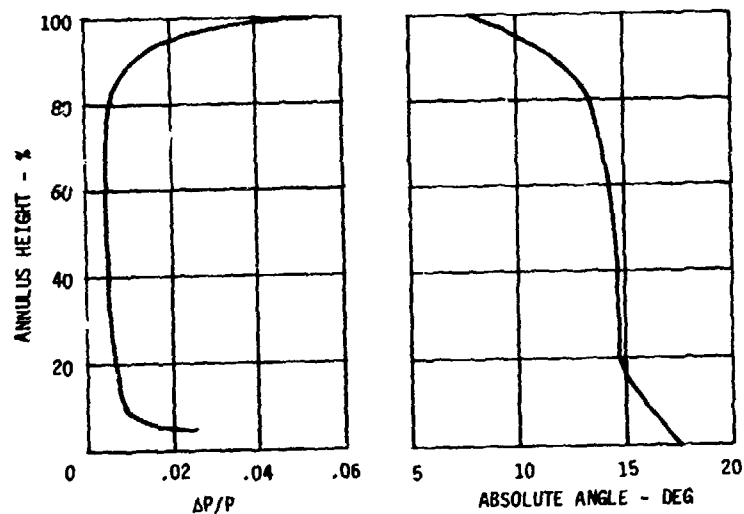


Figure 85. Total  $\Delta P/P$  and Absolute Angle vs Annulus Height.

READING NO. = 57  
CORRECTED FLOW = 2.36 LB/SEC  
IGV SETTING = -10

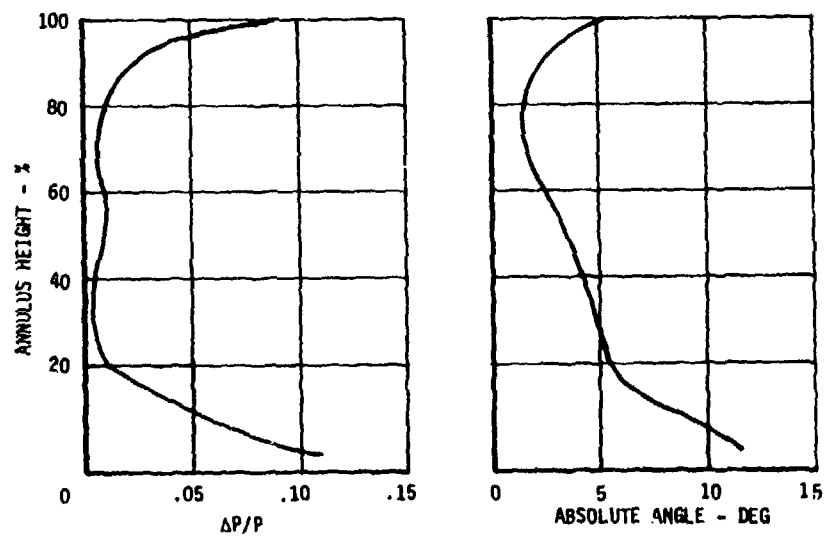


Figure 86. Total  $\Delta P/P$  and Absolute Angle vs Annulus Height.

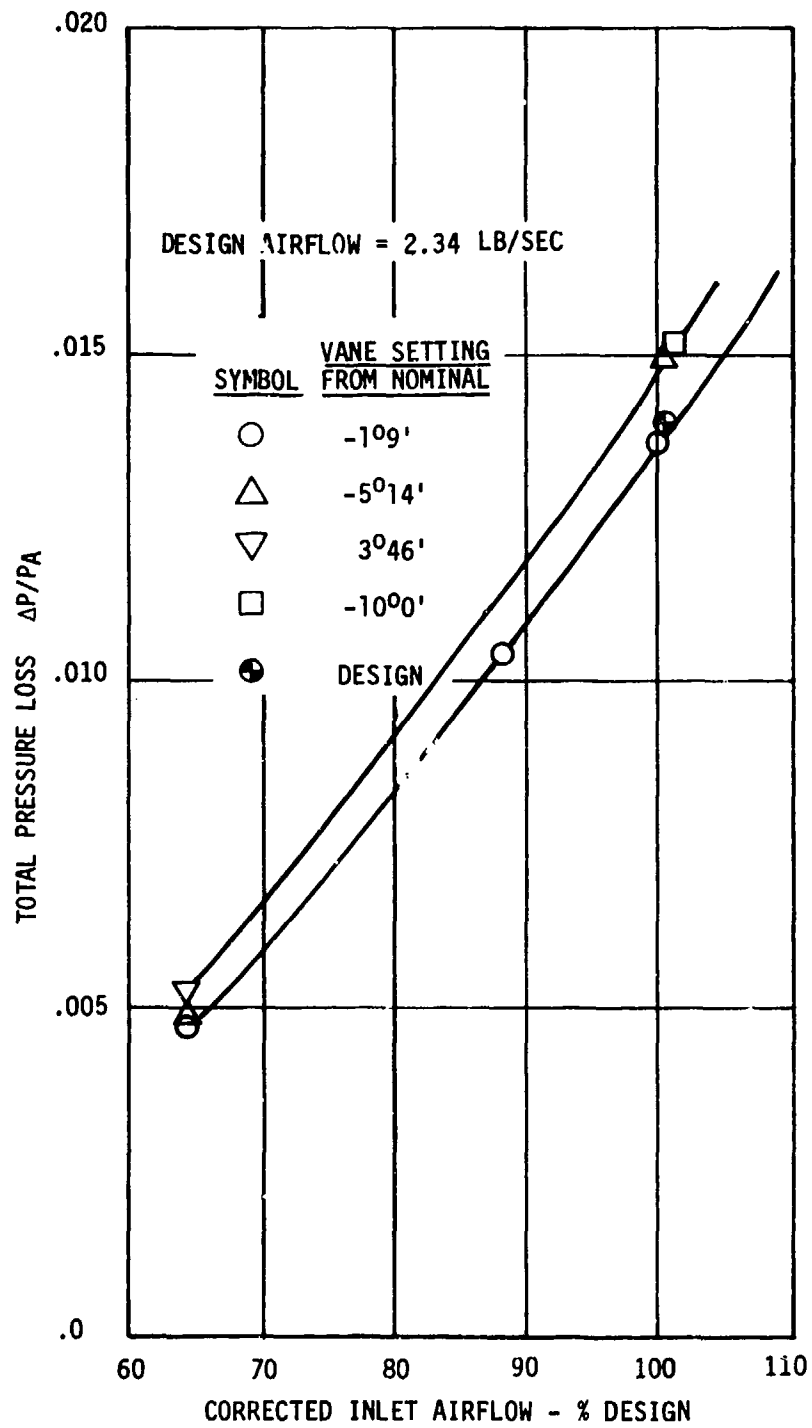


Figure 87. Total Pressure Recovery Factor vs Corrected Inlet Flow.

the minimum loss condition and that perturbation on either side of this setting results in increased loss. The design point total pressure loss was 0.014, and this is close to the measured loss of 0.136 at the design airflow and vane setting. A comparison of the measured and design total pressure loss across the annulus is shown in Figure 79. The measured losses were higher near the inner and outer walls and lower at 10% to 88% of the annulus height. Also, the measured air angles were lower than the design values near the casing and to a lesser extent near the hub (see Figure 79). A data match was carried out to calculate the wall static pressure using the measured airflow, total temperature, angle, total pressure, and design blockage. The calculated wall static pressure from the data match is shown in Figure 88 along with the measured wall static pressure data. Some deviation in the profile was apparent as the flow approached the measuring station. This indicated incipient separation downstream of the traversing station due to the diffusion required to bring the static pressure to ambient. This situation would not prevail if an impeller were present. The total pressure traverse data indicated that the region of high loss does not convect very far into the flow during this blow test. In an actual component test, the presence of the impeller will alter these downstream conditions so the separation observed in the outer 10% of the flow path should not occur and the predicted and measured wall static pressures should agree. This departure of the flow from the design intent, because of the higher blockage in the plane of the traverse, is the reason the air angles are lower during the test.

The intercompressor duct employed during the blow test was somewhat different in contour from the configuration employed in the centrifugal component vehicle. The blow test duct had a hub radius at Plane C of 1.34 inches versus a value of 1.25 inches used in the CCV-I component test. The blow test duct had been configured for another impeller design than was actually used for the CCV-I component test. To explore the compatibility of the measured angles presented in Figure 79 or with those required by the design, a "data match" was undertaken using the aerodynamic design program. The results of this "data match" were plotted in Figure 89 for the measured and deduced angles at the traverse plane and inlet guide vane exit. The deduced angles were compared with design intent, and a general underturning of the flow over the entire span was indicated. This was especially true at the outer wall, where the magnitude of the underturning was in the order of  $6.5^\circ$ . The difference in inducer relative angle due to this underturning was small. The main objective of the test - to establish total pressure recovery characteristics - was fully met.

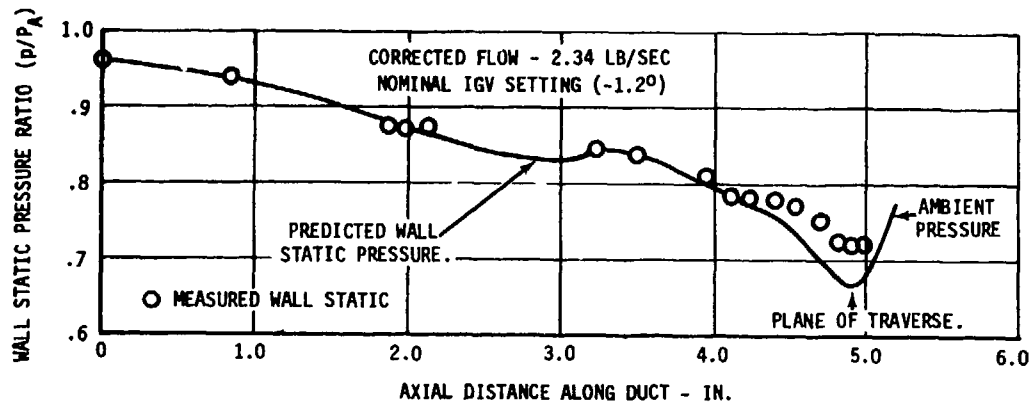


Figure 88. Wall Static Pressure Ratio vs Axial Distance Along Duct.

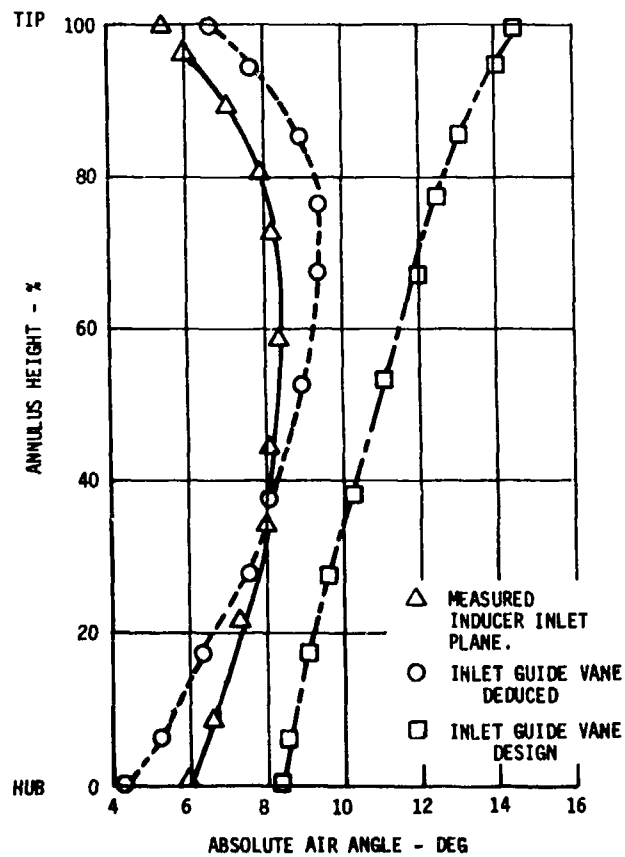


Figure 89. Angle Data Match for Block I Duct.

## AXIAL IGV BLOW TEST

### Aerodynamic Test Results

The axial IGV test was also performed in Cell A8W of the Evendale Aero Component Laboratory using the repaired axial compressor casing and IGV's. The test was completed in two runs on 14 and 17 December 1972.

The test was run for an airflow of 3.08 lb/sec at a vane setting angle of  $20.6^\circ$  and for an airflow of 4.1 lb/sec at vane setting angles of  $-1^\circ 8'$ ,  $10^\circ$  and  $-6.5^\circ$ . Vane angles were set using the preset pin locations that were used for the vane angle bombsight checks. This pin was installed through a precision hole in the vane actuator ring and into slots machined in the compressor casing. The vane ring was then locked in place with a tierod.

Data were gathered for each setting at 21 locations spaced at  $2^\circ$  intervals of the centerbody instrumentation from an initial set point between vane wakes. Some additional points were also recorded to define the wake trough. At each circumferential location the five angle sensors were nulled separately and a full data log was then recorded at an average rake angle setting for total and static pressure data. A total of 99 full data points were recorded during this test. Some problems were encountered with internal choking in the test setup downstream of the measurement station. This choking occurred near the minimum casing diameter and centerbody used for the rakes, and it restricted the maximum airflow to 4.1 lb/sec. Special casing hardware should be considered on future blow tests of this type. The flow levels that were achieved for this test were deemed adequate to define the IGV performance.

Figures 90 through 100 show circumferential distribution of air angles and total pressure loss coefficient based on exit dynamic head, for various immersions and IGV closure settings. In addition, plots were prepared for spanwise distribution of air angle and total pressure loss as well as measured angle relationship with the IGV setting for tip, mean and hub streamlines.

Contours of outlet flow angle were plotted in Figures 101 and 102 for the test results at  $-1^\circ 8'$  and  $10^\circ$ , respectively. The contour plot of vane total pressure drop is shown in Figure 102 for the  $-1^\circ 8'$  data set. The vane wakes were readily observed on these contour charts. The warp in the trough of high pressure drop shown in Figure 103 approximated the twist of the trailing edge of the inlet guide vane.

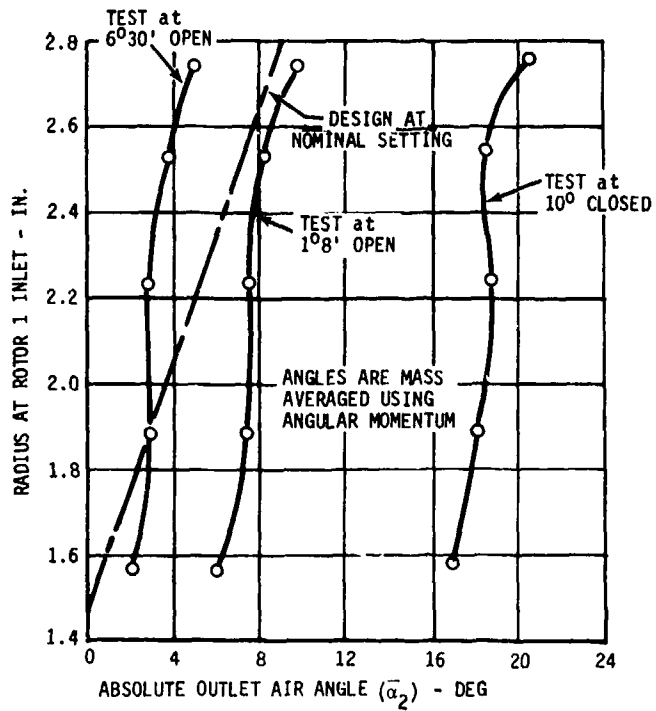


Figure 90. Absolute Air Angle at Rotor 1 Inlet.

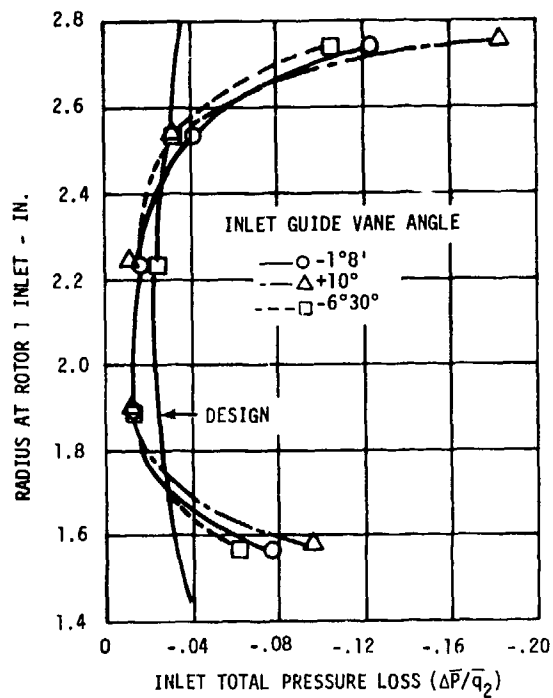


Figure 1. Inlet to First Rotor Pressure Loss.

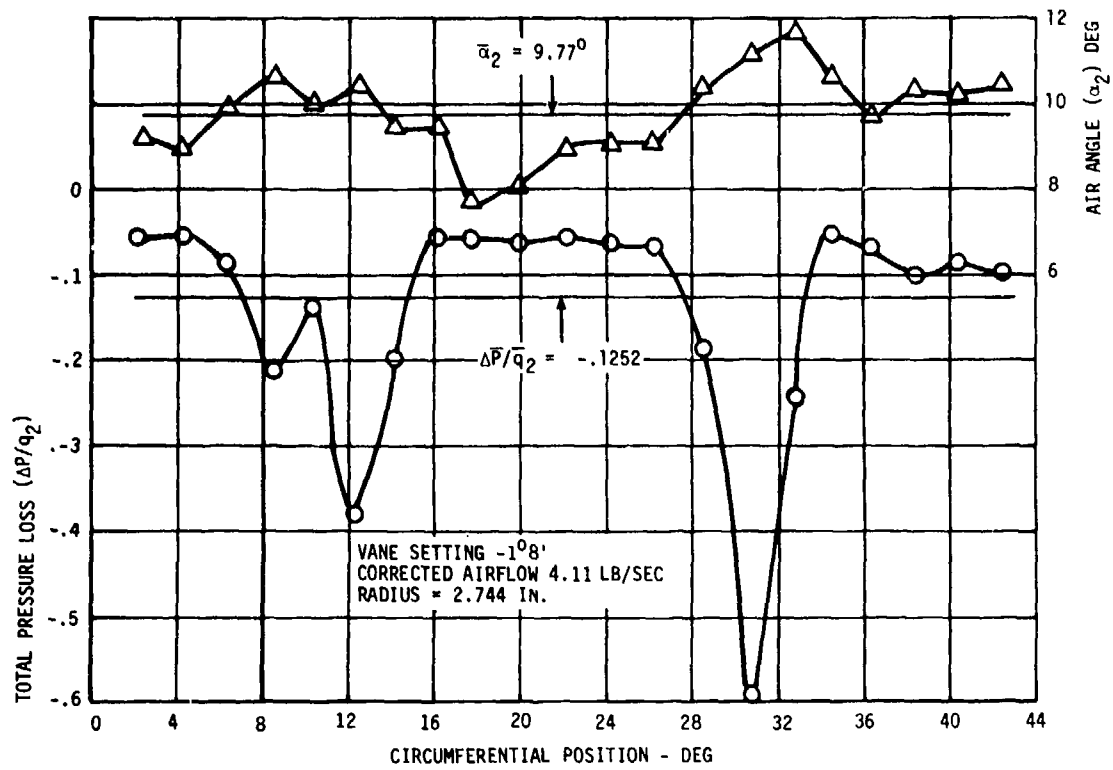


Figure 92. Axial IGV Blow Test - 4.5% Immersion.

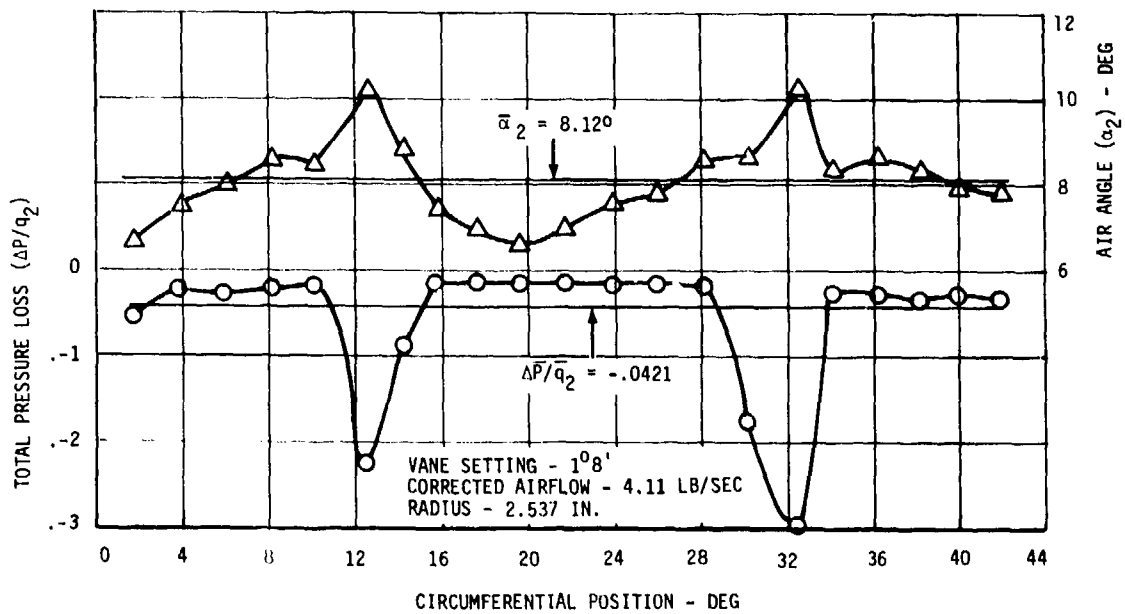


Figure 93. Axial IGV Blow Test - 19.7% Immersion.

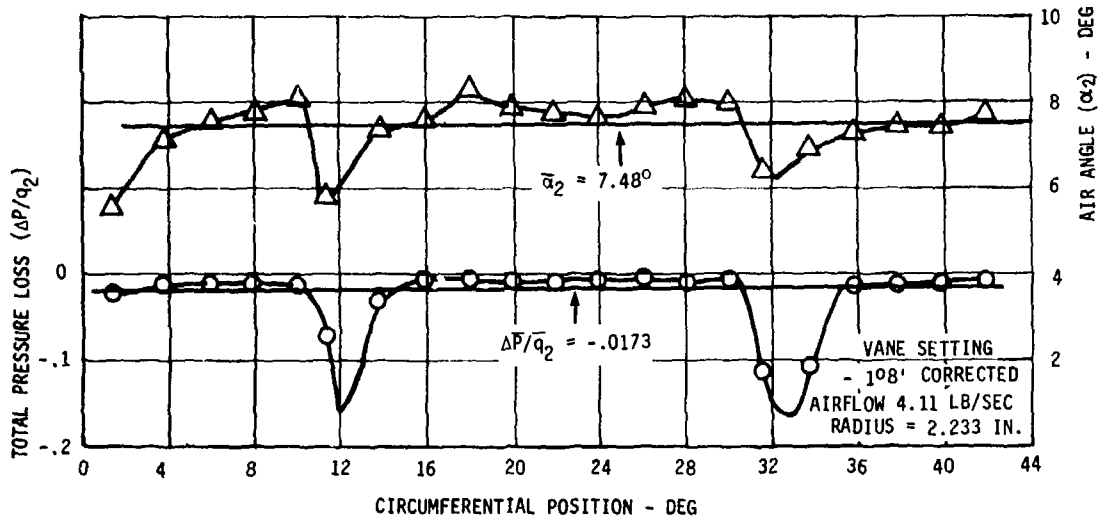


Figure 94. Axial IGV Blow Test - 42.0% Immersion.

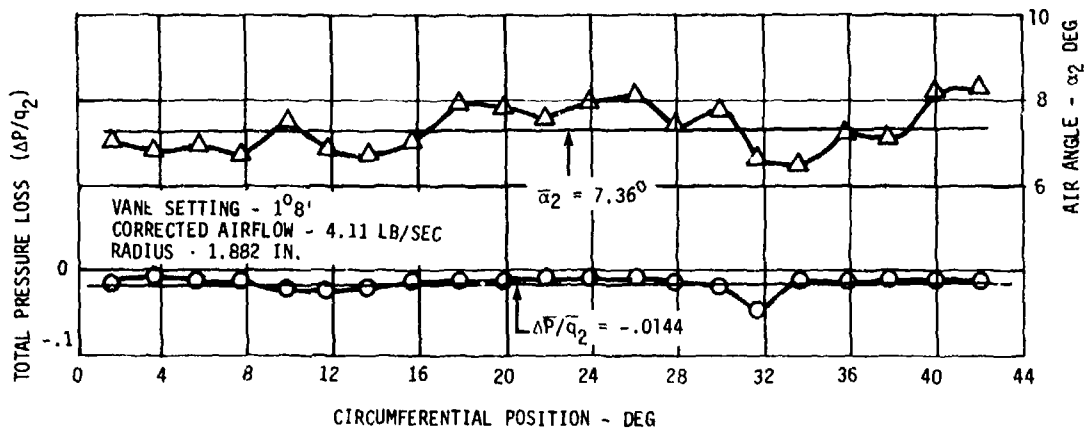


Figure 95. Axial IGV Blow Test - 67.8% Immersion.

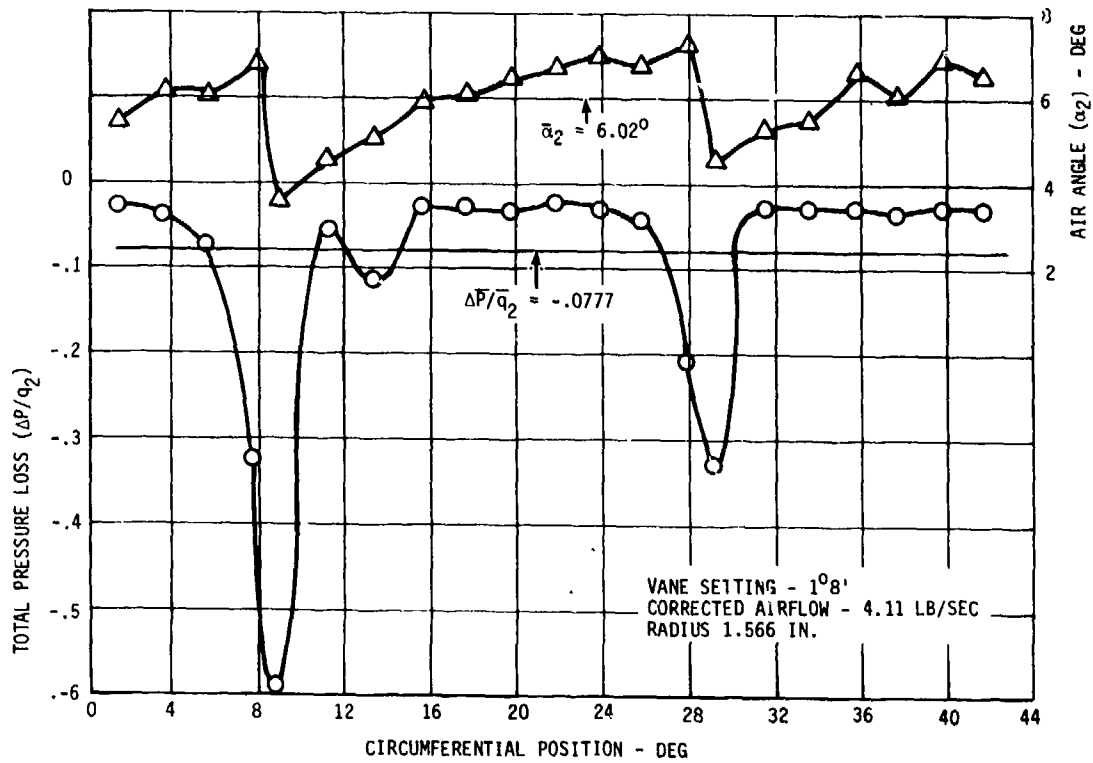


Figure 96. Axial IGV Blow Test - 91.0% Immersion.

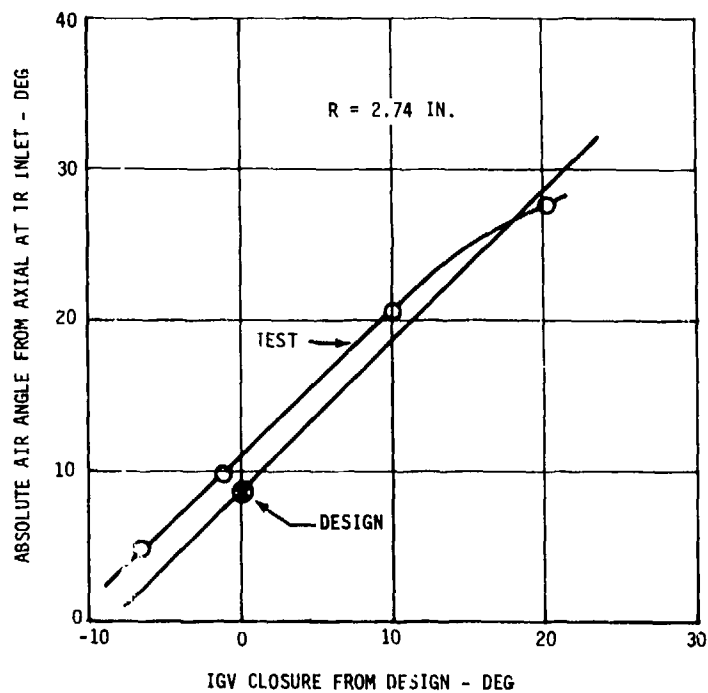


Figure 97. Rotor 1 Inlet Air Angle - Tip.

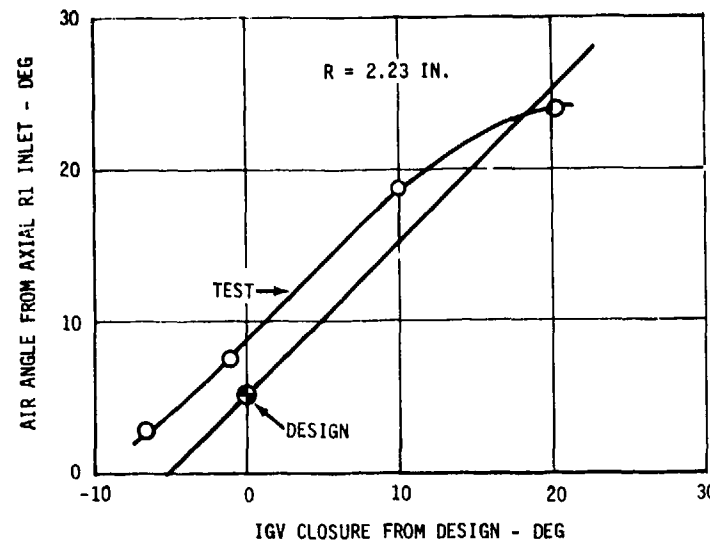


Figure 98. Rotor 1 Inlet Air Angle - Pitch.

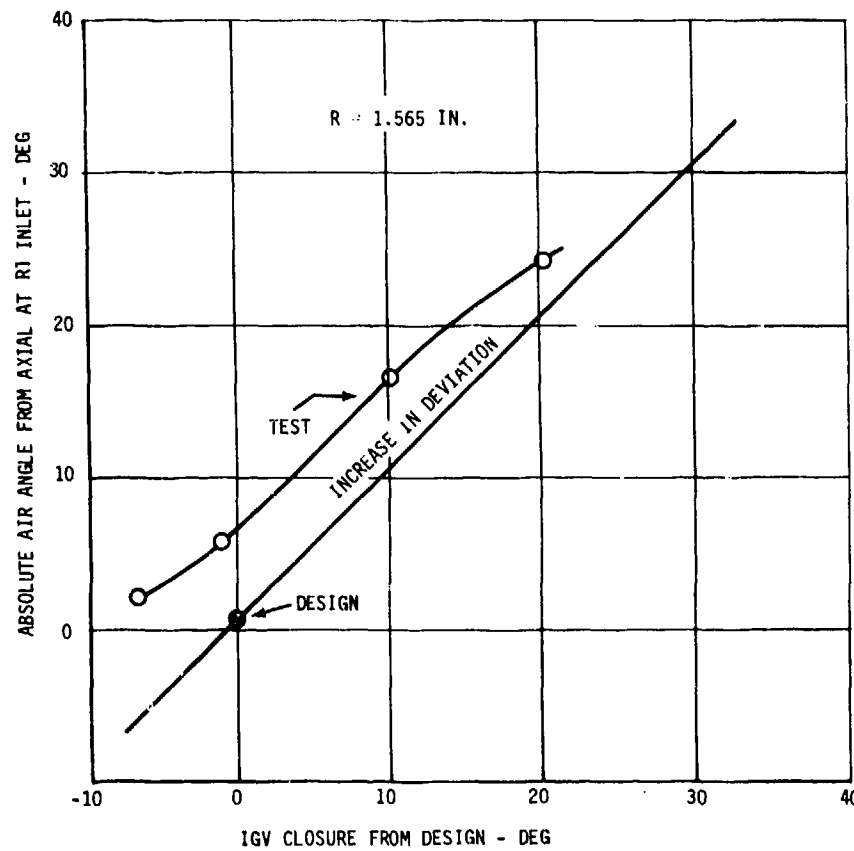


Figure 99. Rotor 1 Inlet Air Angle - Hub.

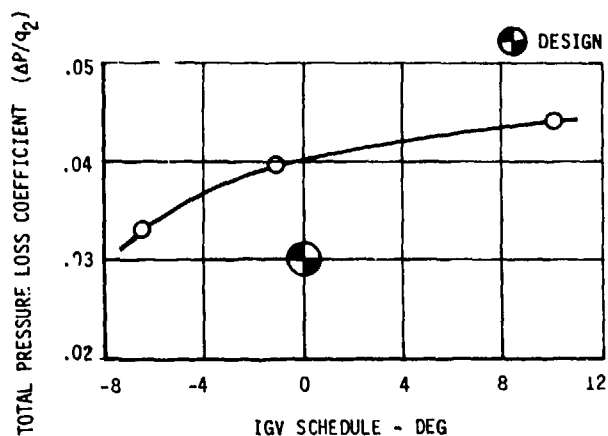


Figure 100. Axial IGV Total Pressure Loss.

#### Aerodynamic Analysis

The data obtained during the IGV blow test showed approximately  $6^\circ$  overturning at the hub, decreasing to  $2^\circ$  at the tip. This phenomenon was similar at all IGV settings, as may be observed from Figure 90. Consequently, an analysis was undertaken to determine its cause. This analysis was directed at determining the secondary flow effects from the variable circulation required by the design across the blade span. Secondary flow considerations from the prescribed outlet swirl distribution will tend to overturn the flow near the hub and underturn the flow near the tip. The presence of inlet boundary layers will further underturn the flow near the tip. At the hub, the inlet boundary layer will tend to offset the secondary flow from radially increasing circulation; however, the boundary layer effects are localized near the annular walls. The amount of turning from secondary flow was calculated to be  $2^\circ$  of underturning at the tip and  $1^\circ$  of overturning at the hub. This secondary flow effect could not provide a satisfactory explanation for the amount of measured hub overturning. A conclusion was reached that the hub probe could have given biased readings throughout the test.

Other factors that could account for some of the observed angle variation are the modification to the 63 Series vanes to permit anti-icing along with the very low cambers required near the hub of this design. Cascade data on this type of airfoil would be useful in understanding the observed angle variations. The angle variations from design would not explain the higher observed loading on the stage 1 rotor shown in Figure 75 since the change in inlet angular momentum is in the opposite direction and the change in the inlet relative air angle is small.

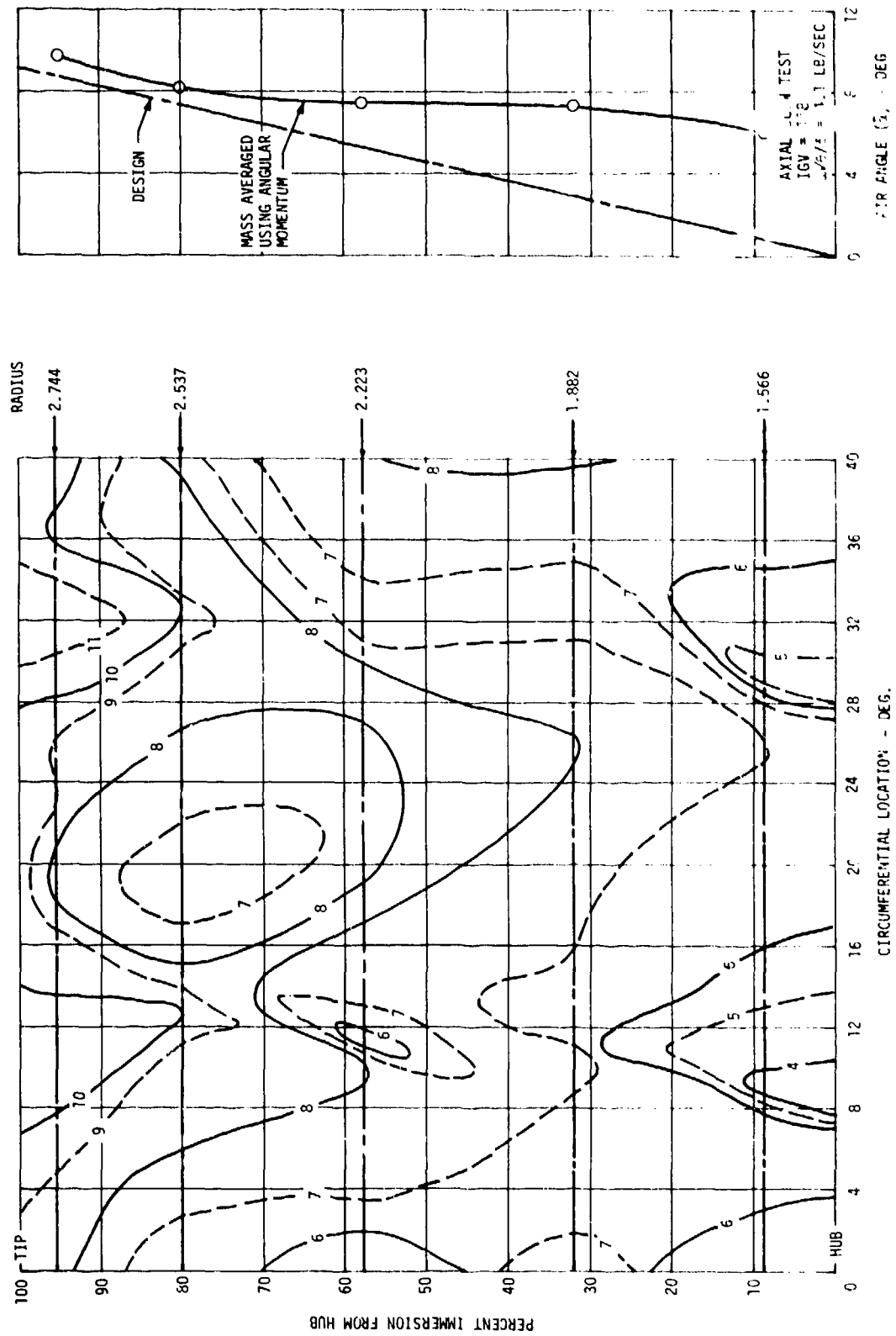


Figure 101. Axial Blow Test - Outlet Angle Contours.

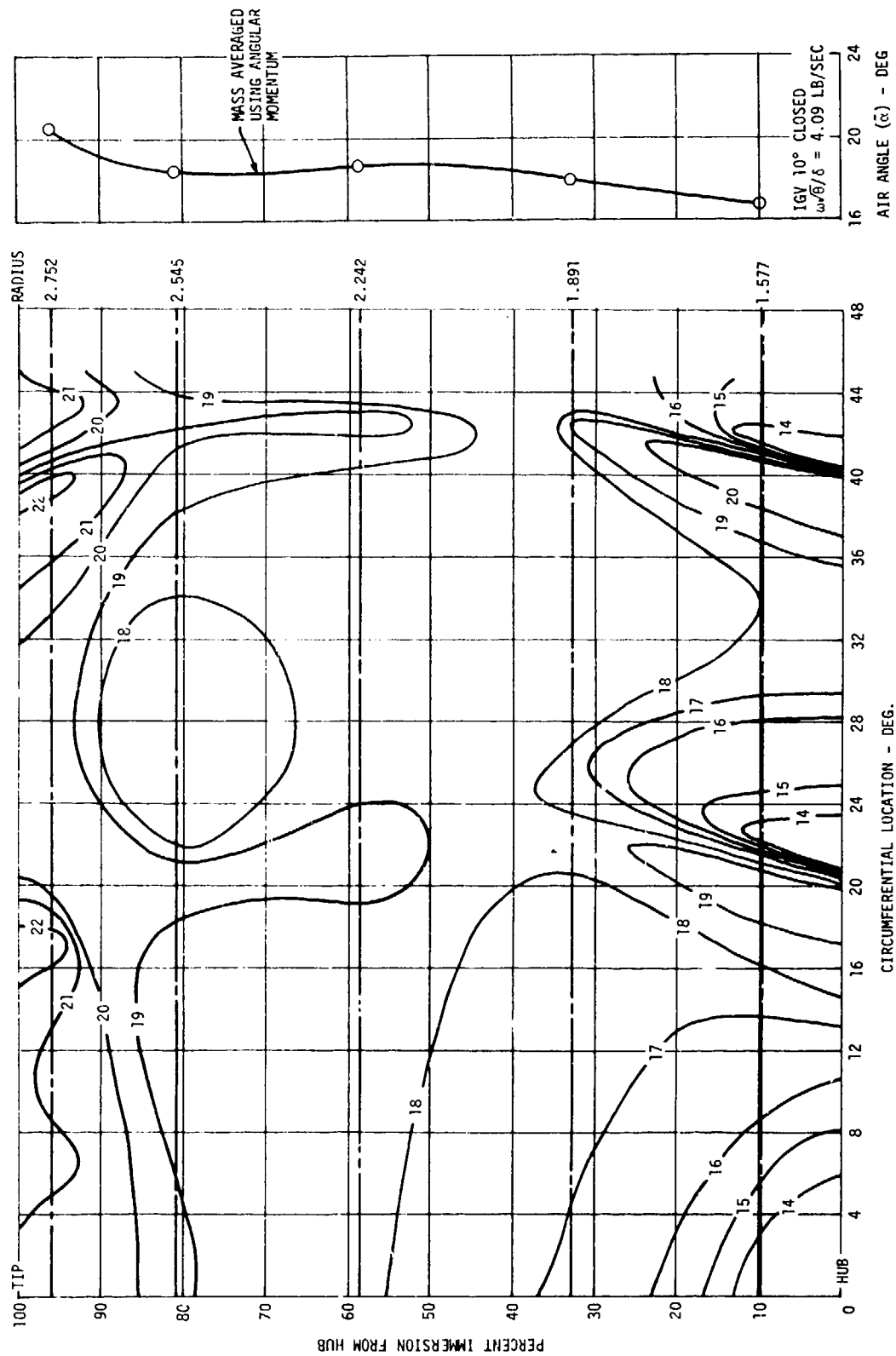


Figure 102. IGV Blow Test - Outlet Angle Contours.

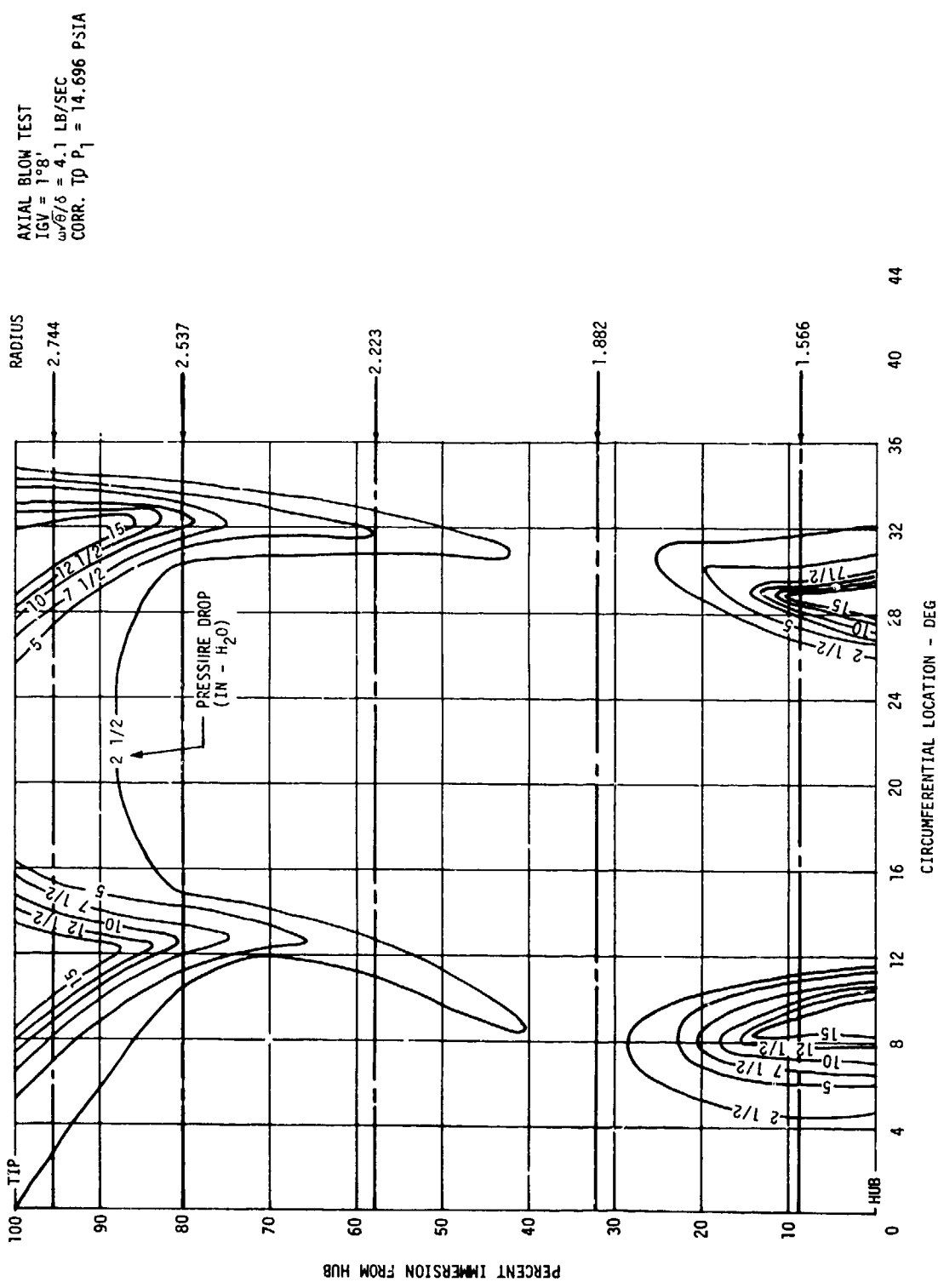


Figure 103. IGV Blow Test - Pressure Loss Contours.

The data obtained regarding the total pressure loss across the IGV, on the other hand, was very satisfactory. Figures 92 through 96 show the circumferential distribution of total pressure loss coefficient and flow angle at various immersions for  $-1^{\circ}8'$  vane closure settings. Figure 100 shows the integrated loss coefficient as a function of IGV closure. At the nominal IGV setting, the total pressure loss is 0.04. This is slightly higher than the assumed design value of 0.03, but this increase in loss represents a negligible loss of efficiency at the 2.5:1 design pressure ratio.

### CENTRIFUGAL COMPRESSOR TEST (CCV-I)

#### Summary

The centrifugal compressor vehicle was operated for a total of 23 hours 10 minutes. An approximate breakdown of time at various speeds is presented in Table 15. Five stalls were observed on this vehicle: one each at 50%, 75%, and 85% speed and two at 90% speed.

The testing was accomplished in two runs; the first run on April 17 and 18, 1973 accumulated 10 hours of operation and the second run on April 18 and 19, 1973 logged 13 hours. A maximum physical speed of 53,400 rpm was reached with no major mechanical problems arising throughout the test.

TABLE 15. CENTRIFUGAL COMPRESSOR VEHICLE TIME SUMMARY		
Speed (%)		Time (hr:min)
Less Than	75	6:50
	75	2:41
	85	4:02
	90	2:35
	95	4:29
	100	<u>2:33</u>
Total		23:10

The initial run tested up to full corrected speed and obtained 33 data readings. These data were at the nominal IGV position and included partial speed line mapping at 75%, 85%, 95%, and 100% corrected speed. Vaneless space bleed and Plane B (centrifugal inlet) bleed effects were evaluated. The second test run evaluated the  $+5^{\circ}$  vane positions at 90%, 95% and 100% corrected speed and completed the speed line mapping for the nominal vane position. The Plane E wake rake data (centrifugal discharge) was also obtained for the nominal vane setting at 90%, 95%, and 100% corrected speed.

There were indications from the impeller touch probes of incipient shroud rubbing at high RPM's, so stalls at 95% and 100% corrected speed were avoided.

### Mechanical Performance

The centrifugal component test was completed with no major mechanical problems; and like the axial component test, it had a very smooth operation. The maximum peak-to-peak bearing squirrel cage motion was 0.0008 in. on the forward bearing and 0.0010 in. on the aft bearing. The proximity probe on the forward end of the flexible coupling indicated a maximum run-out of 0.002 in. The peak frame vibration occurred at 100% speed, but it was less than 0.5 in. per second average velocity which was equivalent to 11 g's peak acceleration.

The load cell hook up was changed from the previous ACV test. The ACV test used 16 strain gages to make up 2 bridge circuits of 8 gages each. This was modified for the CCV-I test and all subsequent tests where 12 strain gages were used to make up 3 bridge circuits. A schematic of these circuits are shown in Figure 104. The ACV test had one active gage on each of the three support posts of the load ring. This hookup provided an automatic averaging of the load in the three posts but it had erratic signals during that component test. The arrangement for the CCV-I and subsequent tests used two active gages on the same post for each bridge and measured the load of one post. The total load was obtained by summing the three readings. The three bridge circuits did not have the erratic signals observed on the ACV test and provided a reliable measure of the bearing thrust load. The three load cell outputs were summed and used as feedback for the thrust controller. In addition, each of the three outputs was monitored on a digital voltmeter and periodic thrust calculations were made using the vehicle pressures. While each of the three load cell outputs did not follow the same pattern, the sum of the three showed consistency with the calculated load.

In order to produce sufficient forward thrust at lower pressure operating points, the vent cavity discharge was capped. The aft bearing seal air pressure was also increased to prevent vent cavity air from bleeding into the aft sump.

The impeller shroud touch probes indicated several contacts during transient speed increases and during stalls. To minimize risk of a shroud rub, all speed increases were made very slowly and the high speed stalls were deleted from the test plan. Examination of the shroud at teardown after the test indicated very light rubbing toward the impeller discharge with the touch probes worn flush to the shroud surface.

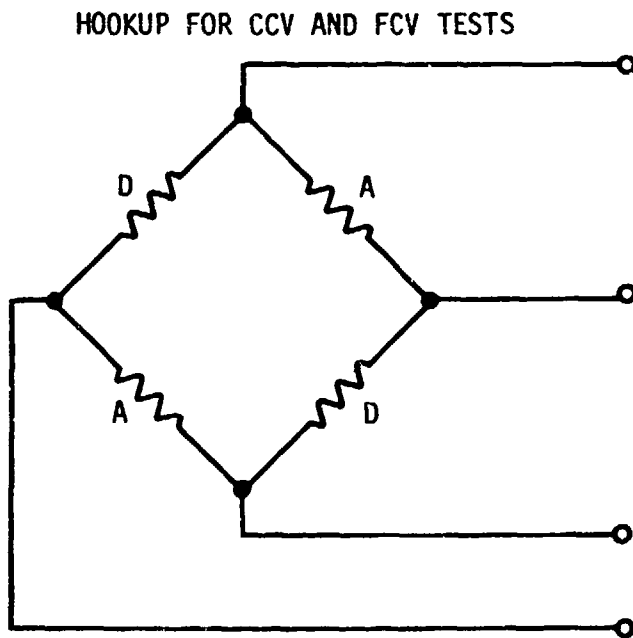
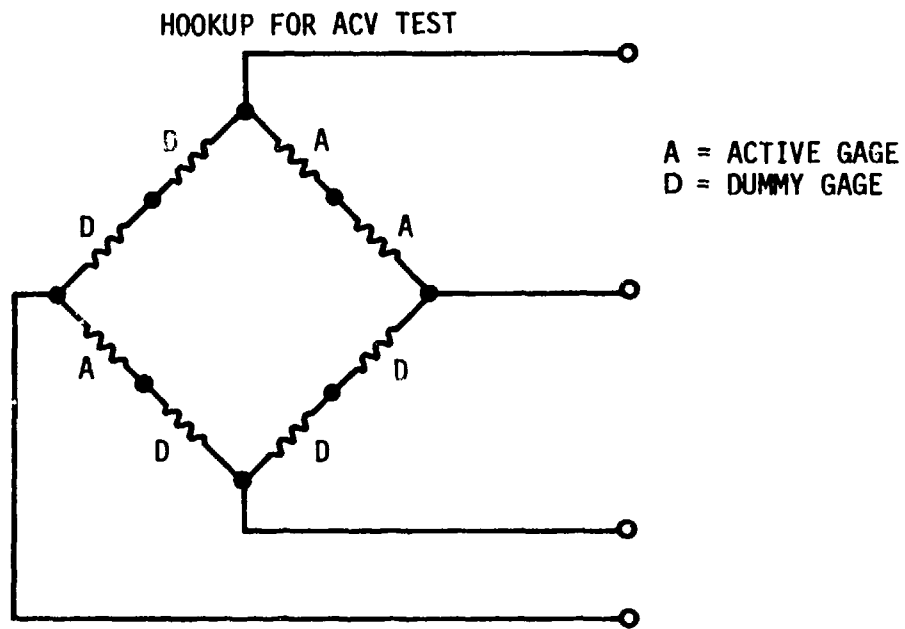


Figure 104. Load Cell Strain Gage Wiring.

### Bench Frequency Testing

Impeller: All of the impeller vanes were frequency checked for the first natural mode, and one full blade was checked for all modes up to 30,000 Hz. The first mode measured frequency band and its relationship to a four per rev stimulus was plotted in Figure 105.

Inlet Guide Vanes: Two centrifugal compressor inlet guide vanes were tested to determine natural frequencies and mode shapes. For this test the vanes were mounted in a support block using the same spindle hardware used in the compressor assembly. The vanes were excited using an electromagnetic driver and the nodal lines traced out with a hand-held pickup. The nodal patterns were sketched in Figure 106, and the natural frequencies were plotted in a Campbell diagram in Figure 107.

### Assemble Test Results

The overall performance map at nominal inlet guide vane setting was plotted in Figure 108 for a corrected speed range from 85% to 100%  $N_C$ .

The compressor was throttled from deep choke to stall at 50%, 75%, 85%, and 90% corrected speed. Elsewhere, throttling was terminated within the stall boundary. At 100% corrected speed the maximum pressure ratio recorded was 6.09:1 for the IGV's 5° open, a corrected flow of 97.5% of design and an overall efficiency of 0.736 (see Figure 106).

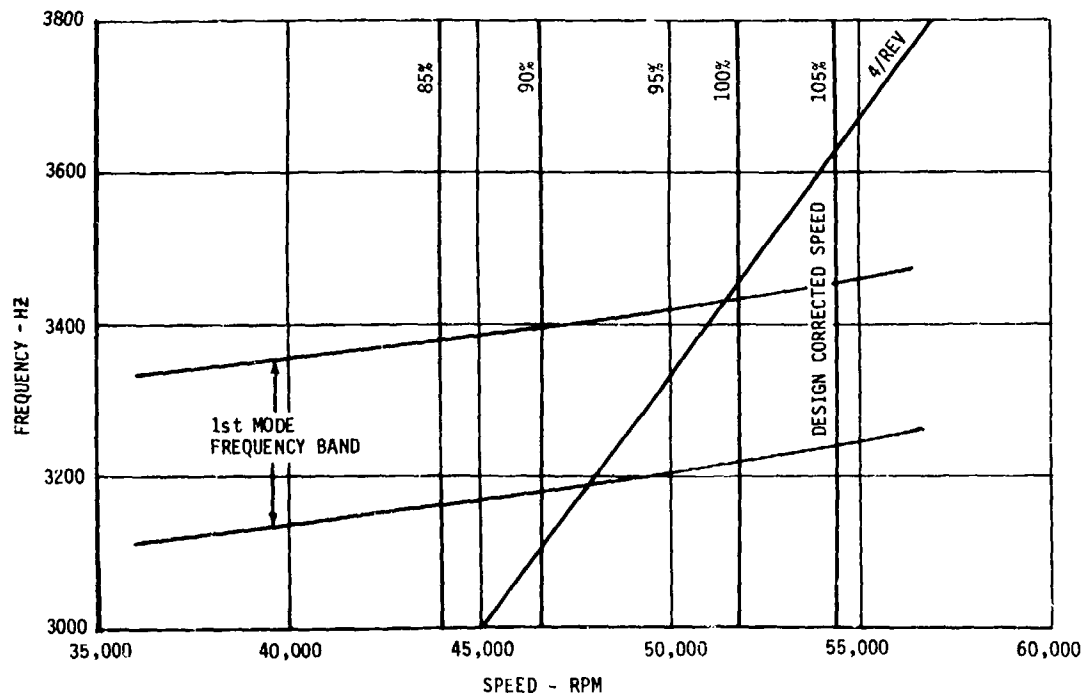
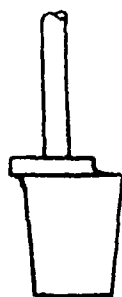
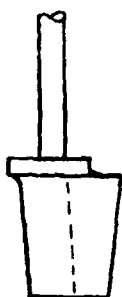


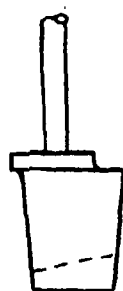
Figure 105. Campbell Diagram for Impeller Vane.



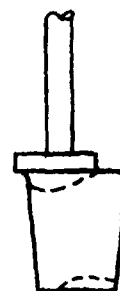
2702 HZ  
2713 HZ



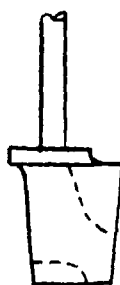
6911 HZ  
7056 HZ



11049 HZ  
11156 HZ



14422 HZ  
14629 HZ



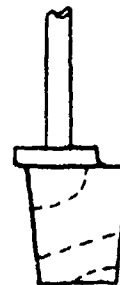
16260 HZ  
16790 HZ



21728 HZ  
22316 HZ



24915 HZ  
26047 HZ



35863 HZ  
38894 HZ

Figure 106. Centrifugal Compressor Inlet Guide Vane Nodal Patterns and Natural Frequencies.

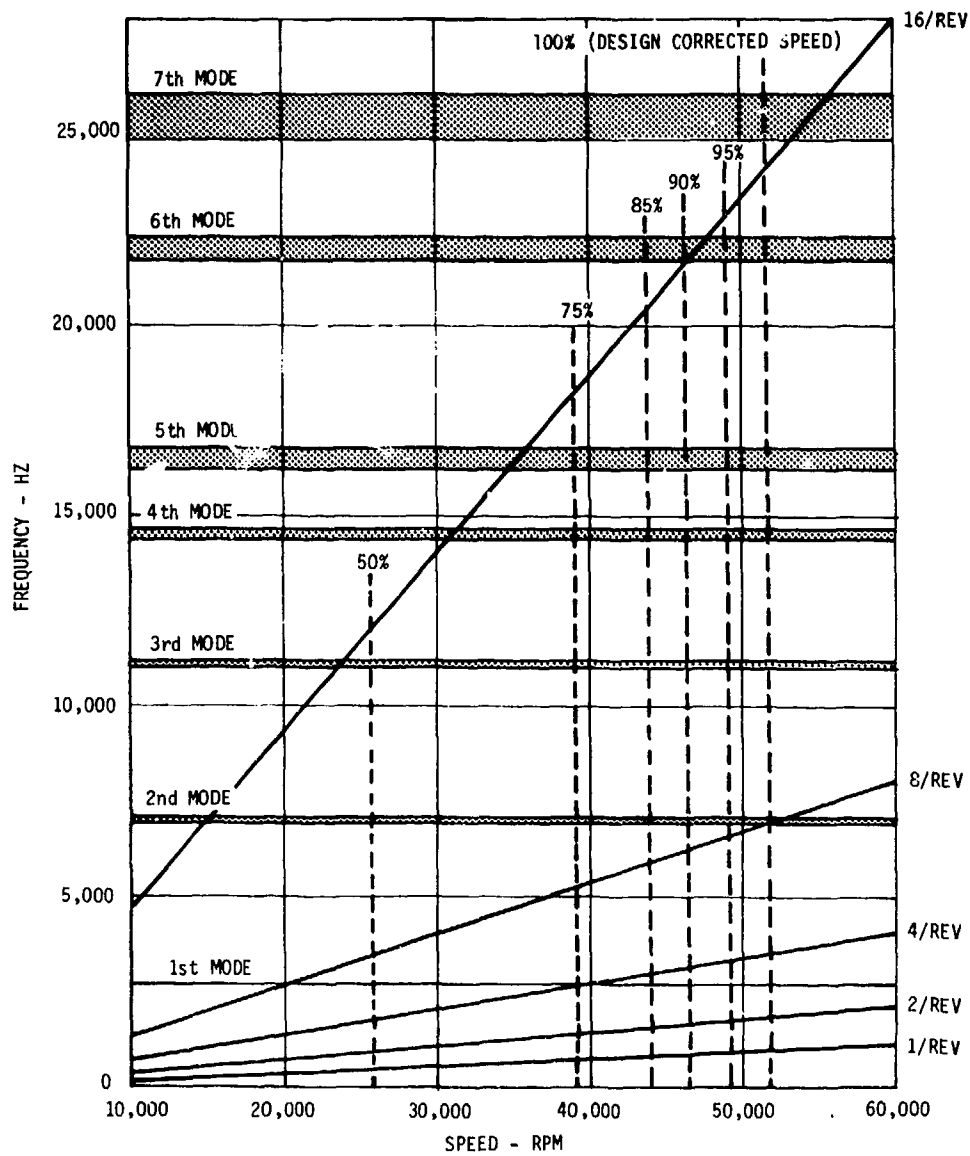


Figure 107. Campbell Diagram for Centrifugal Compressor Inlet Guide Vane.

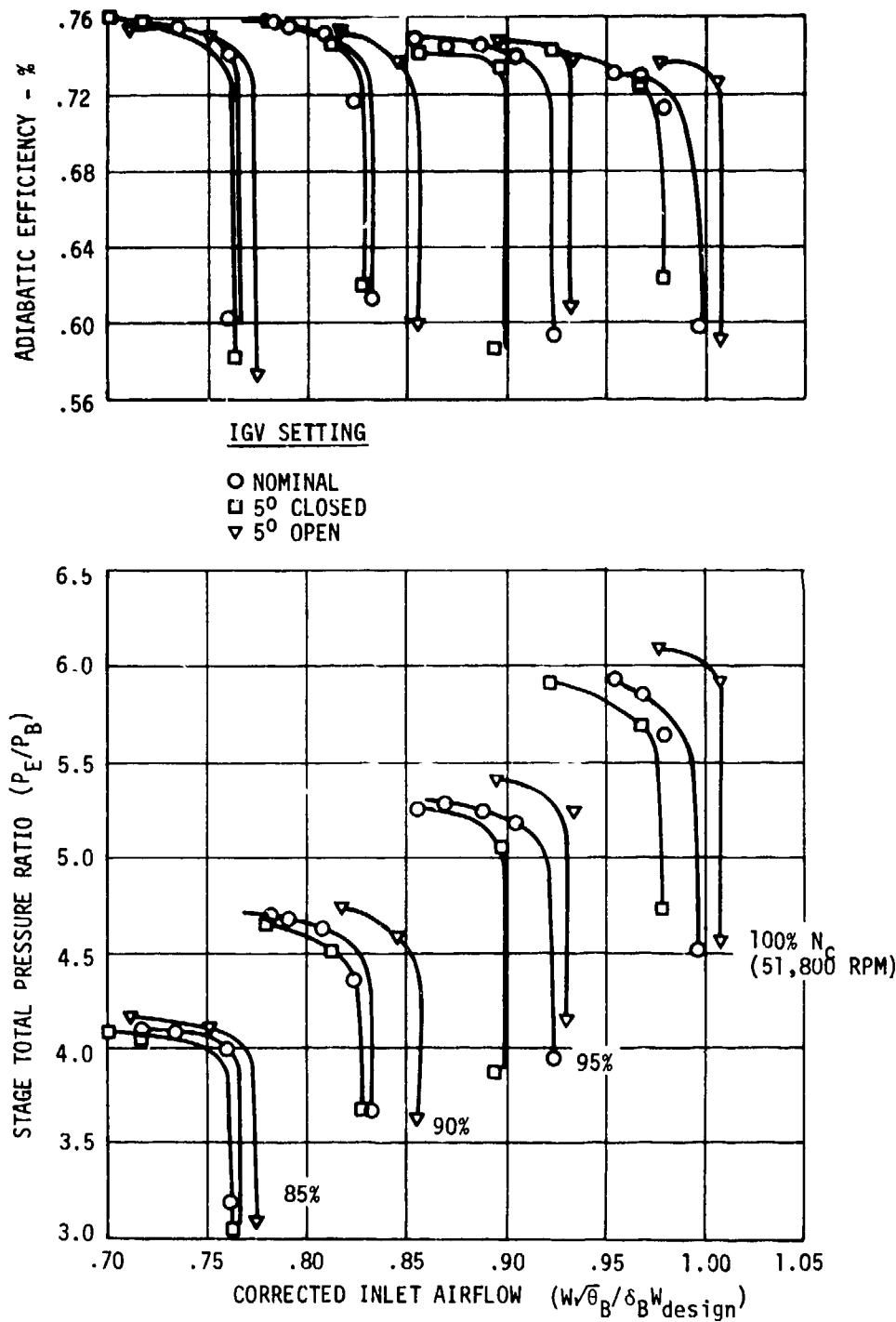


Figure 108. Centrifugal Compressor Performance Map for Various IGV Settings.

Figure 109 shows a plot of choke flow versus corrected speed for nominal inlet guide vane setting.

A plot of shroud static pressure versus meridional distance was prepared in Figure 110 for 100% speed showing the effect of throttling from choke toward stall. It can be noted that at choke condition there was dip in the profile in the inducer. This was due to the high-velocity negative-incidence flow in the inducer. As the compressor was throttled and the inducer was on a more positive incidence, a higher degree of diffusion and consequent rise in static pressure occurred. In the outer region of the impeller, the gradient of static pressure was determined by the strength of the rotating gravitational field which was largely independent of flow. Therefore, the profiles were predominantly parallel in the outer region, and changes in static pressure were confined to the inducer.

The inlet guide vanes at the nominal setting imparted prewhirl to the flow in the direction of rotation. The effect of closing the inlet guide vanes increased the moment of momentum of the flow in the negative direction. This unloaded the impeller. The converse is true of opening the inlet guide vanes. Figure 111 demonstrates this effect, where the pressure distribution was plotted for nominal and  $+5^\circ$  settings of the inlet guide vanes at 100% corrected speed.

The gradient in static pressure for a centrifugal force field can be shown to be primarily a function of radius and the square of the angular velocity. Therefore, the slope of the shroud static pressure profile should increase with both radius and corrected speed. This was clearly seen in Figure 112 where the pressure is plotted for increasing corrected speed at flows corresponding to an approximate operating line.

The performance map for the impeller at nominal inlet guide vane setting is shown in Figure 113. At 100% corrected speed, the maximum recorded impeller pressure ratio was 7.27 with a corrected flow of 99.9% of design and an impeller efficiency of .847.

For a centrifugal compressor, an intimate relationship exists between the internal flow structure in the impeller and the transfer of energy to the fluid. This relationship is usually expressed as a global value of "slip-factor". "Slip-factor" and impeller efficiency are not independent but represent two aspects of the same phenomenon, the ability of the impeller to impart energy to the fluid. Figure 114 shows a plot of the deduced slip-factor for the tested range of the impeller.

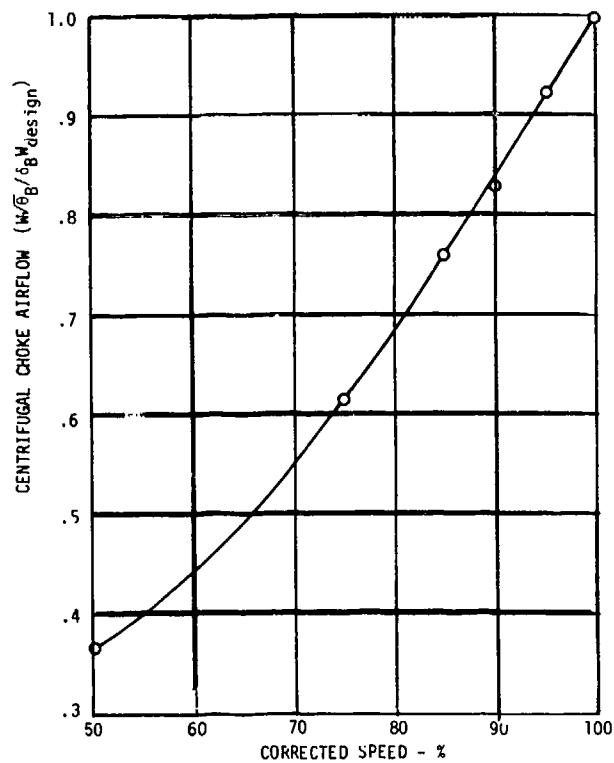


Figure 109. Centrifugal Compressor Choke Flow vs Corrected Speed - Nominal IGV Setting.

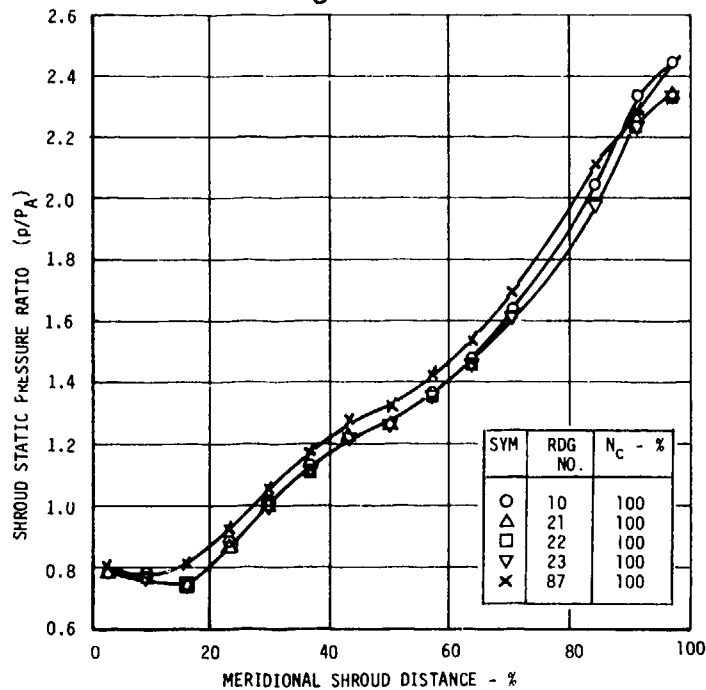


Figure 110. Shroud Normalized Static Pressure vs Meridional Distance - 100% Speed (Throttle).

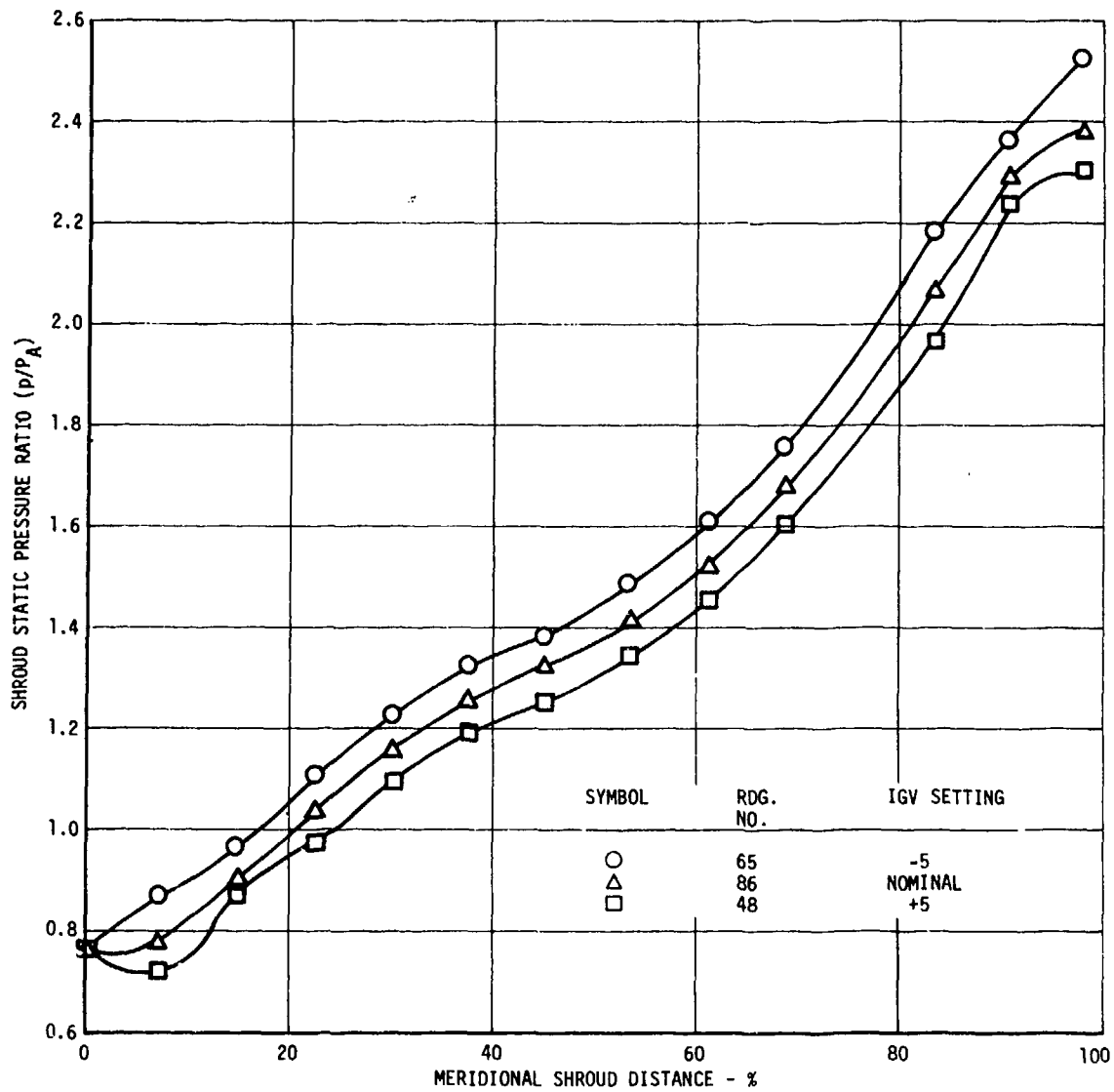


Figure 111. Shroud Normalized Static Pressure vs Meridional Distance - 100% Speed (Effect of IGV).

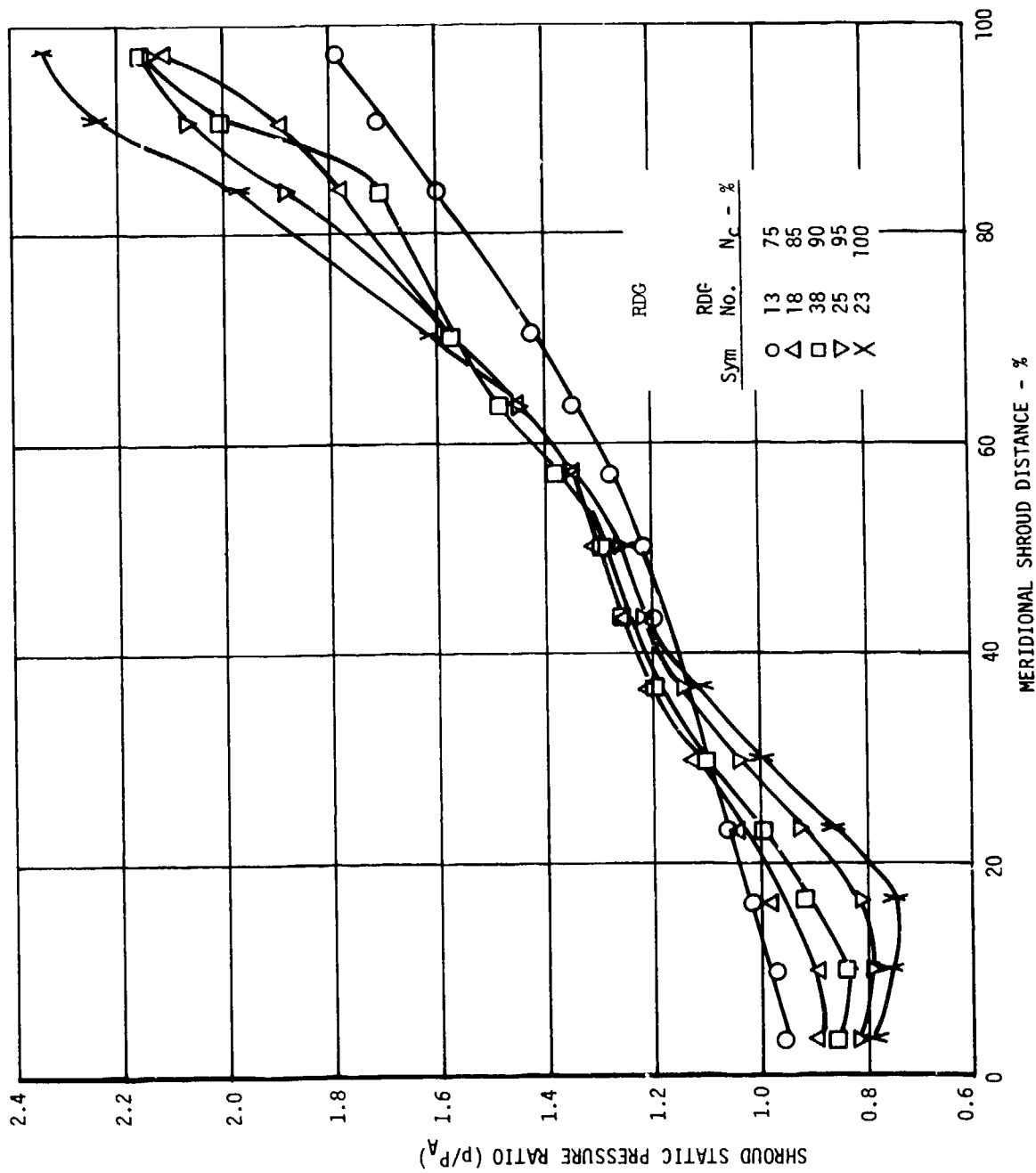


Figure 112. Shroud Normalized Static Pressure vs Meridional Shroud Distance Along Operating Line.

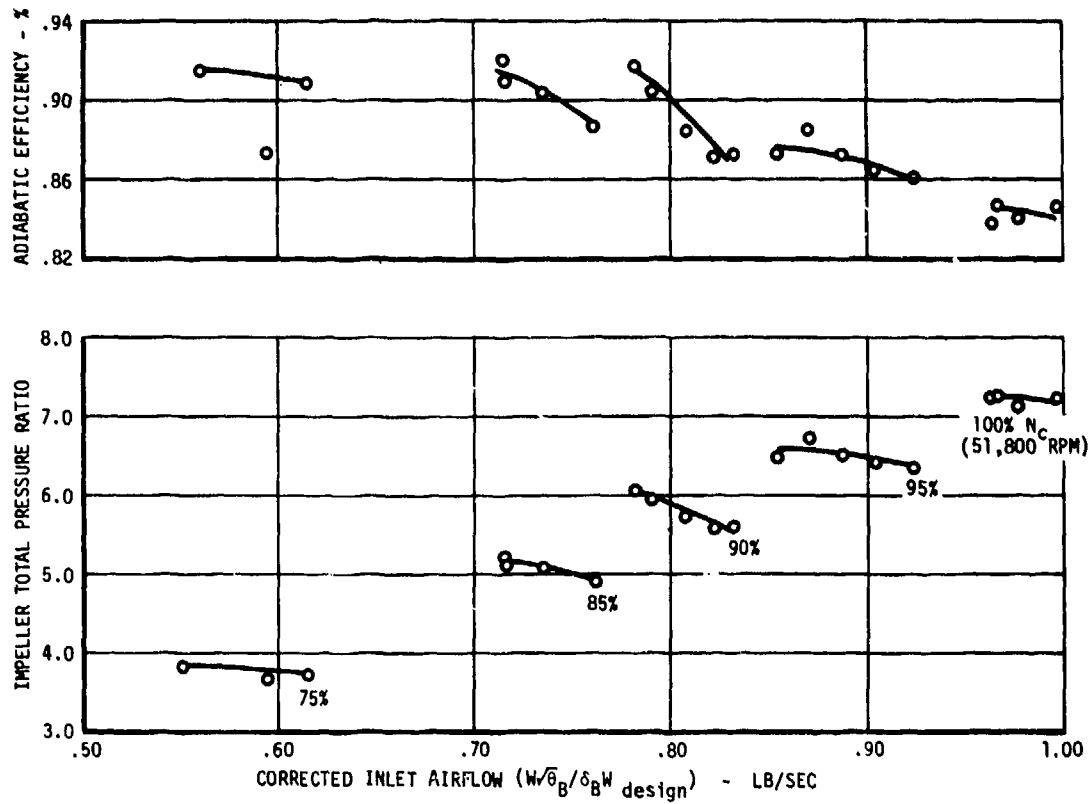


Figure 113. Impeller Performance for Nominal IGV Settings.

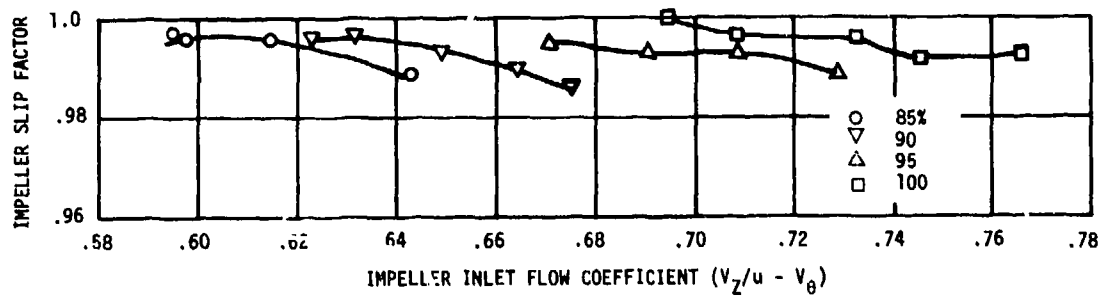


Figure 114. Impeller Slip Factor.

Figure 115 shows the normalized static pressure versus axial distance along the diffuser. The plot is continued along the center of the passage in the deswirl vanes and through the exit annular diffuser. The data shown represents conditions at the maximum pressure ratio tested for 100% corrected speed and nominal setting on the inlet guide vane. The quasi-vaneless region manifests the normal characteristics of a conserved supersonic source vortex. At approximately 0.8 inch along the pipe, an oblique shock interaction causes a rise in pressure followed by a supersonic expansion up to the pipe inlet lip. A strong normal shock, with a consequent sharp rise in pressure, is located just ahead of the inlet lip. After the normal shock the fluid diffuses with the usual profile for a conical diffuser.

Figure 116 shows the effect of throttling the diffuser from deep choke to maximum pressure ratio at 100% corrected speed. It may be noted that in the deep choke condition, strong shock interactions are occurring within the conical diffuser.

Figure 117 shows a composite plot of static pressure recovery and total pressure loss coefficient versus impeller exit absolute air angle for various corrected speeds. The loss coefficient shows the usual abrupt rise as the absolute air angle is reduced. This abrupt rise corresponds to choked flow.

A wake survey at the exit of two adjacent deswirl passages at four immersions is shown in Figure 118. This data was weight averaged by a finite increment technique to give a discharge blockage coefficient of 0.8357 at 100% corrected speed. The blockage coefficient is defined as the effective flow area divided by the actual flow area. The calculation proceeds as follows:

Mass Average Total Pressure	85.065 lb/in. <sup>2</sup>
Mean Static Pressure	84.1 lb/in. <sup>2</sup>
Total/Static Pressure Ratio	1.014
Mass Average Total Temperature	1008.2°R
Airflow	2.19 lb/sec
Flow Function $W\sqrt{T}/AP$	0.1158
Effective Area	7.0592 in. <sup>2</sup>
Absolute Air Angle	16.0°
Actual Area	8.4470 in. <sup>2</sup>
Blockage Coefficient	0.8357

The outlet Mach number is shown in Figure 119 for the various speed lines at 85%, 90%, 95%, and 100% corrected speed and nominal IGV setting.

Figure 120 shows the effect of bleeding at the exit of the impeller. The removal of approximately 1.5% of the low momentum air from either side of the impeller tip shows an increase in efficiency. Bleeding the forward side is more effective than bleeding the aft side. The latter shows

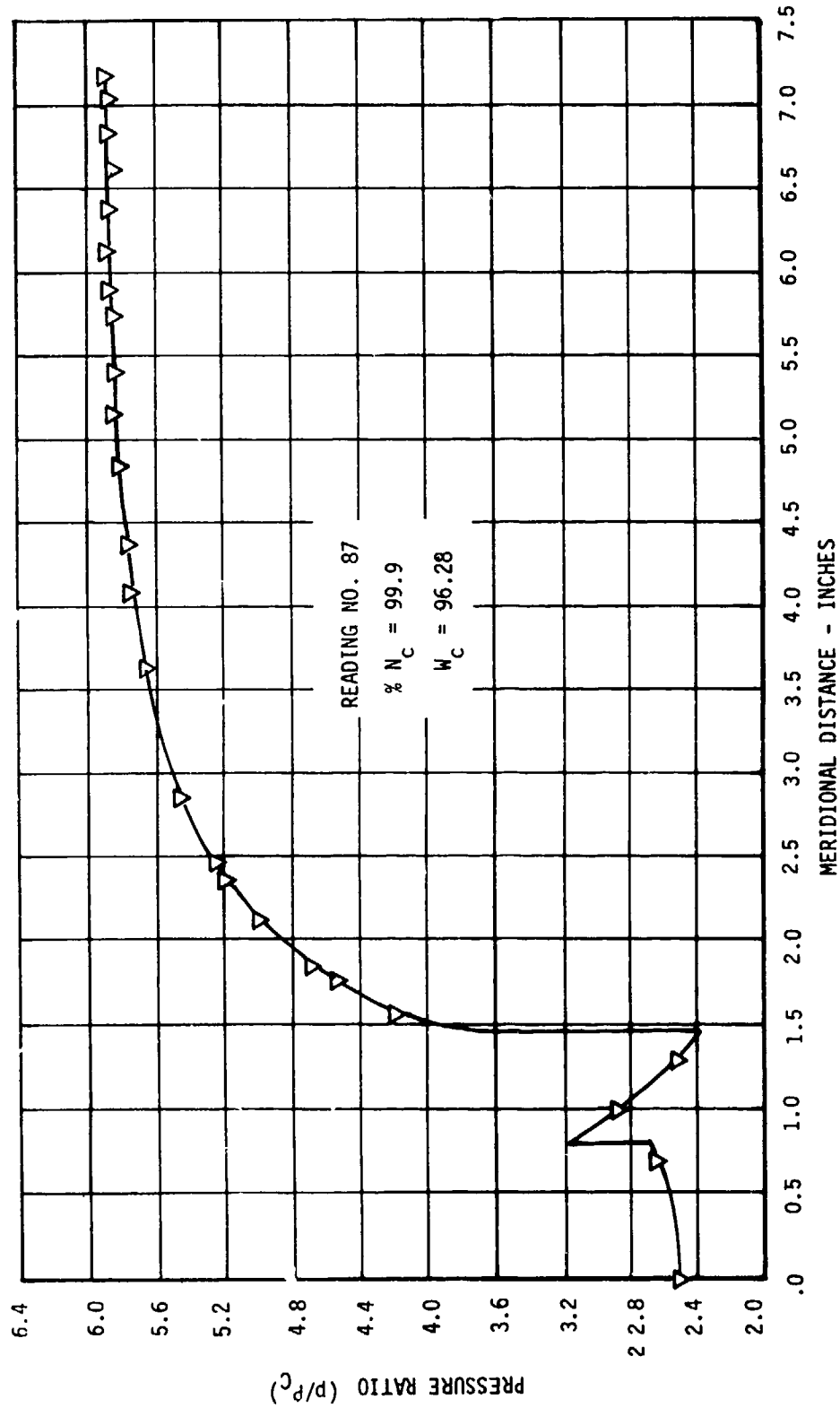
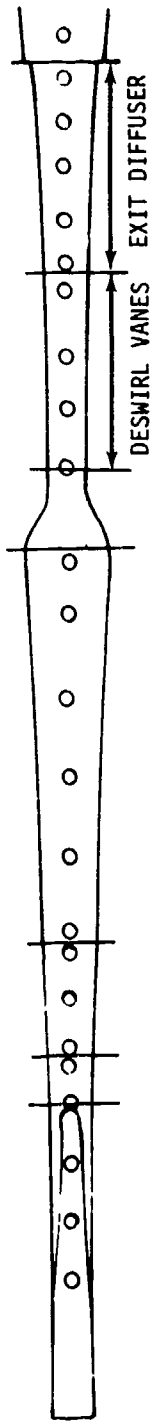


Figure 115. Diffuser Static Pressure - 100% Speed Nominal IGV.

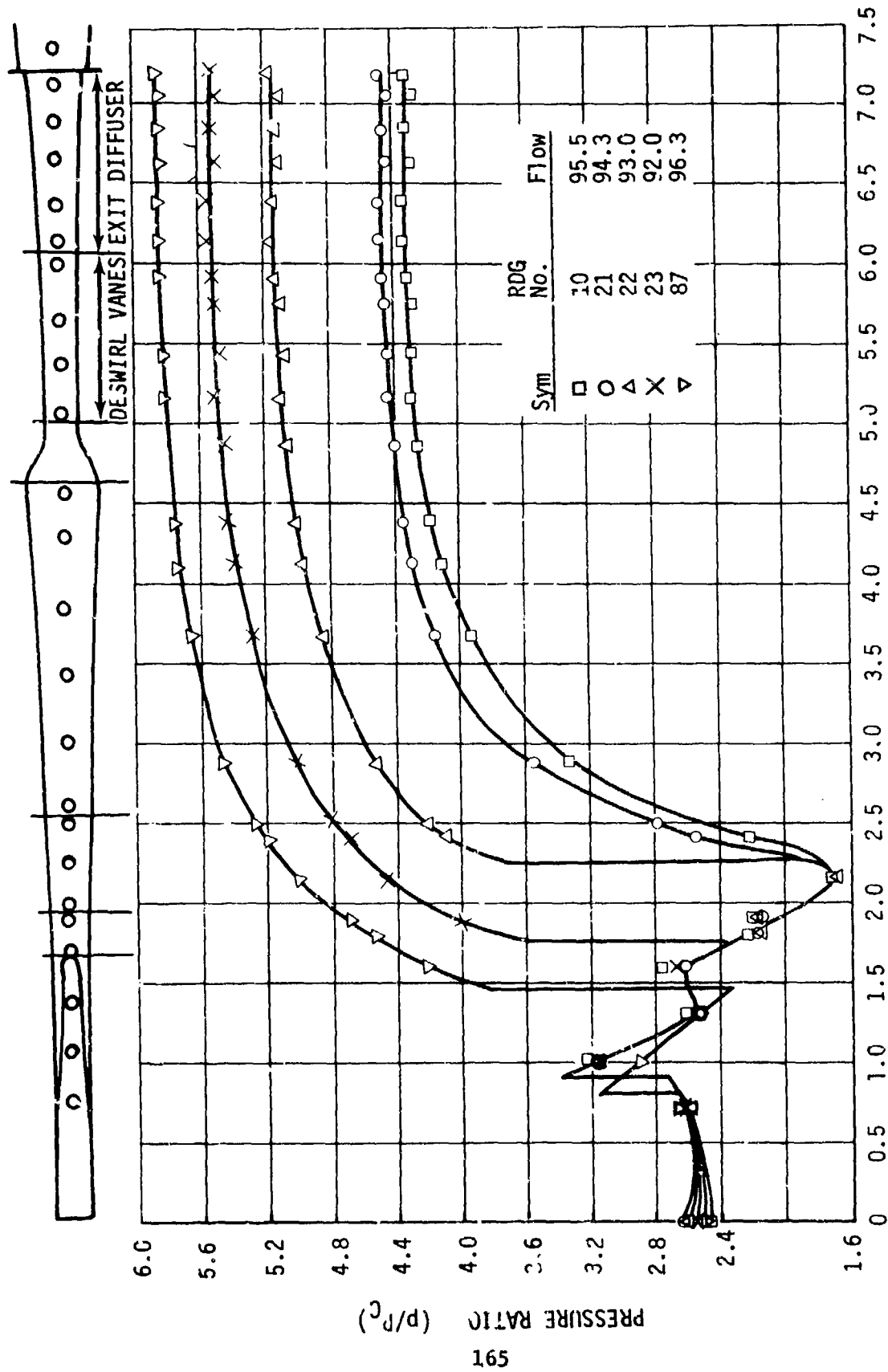


Figure 116. Diffuser Static Pressure - 100% Speed Nominal IGV Effect of Throttle.

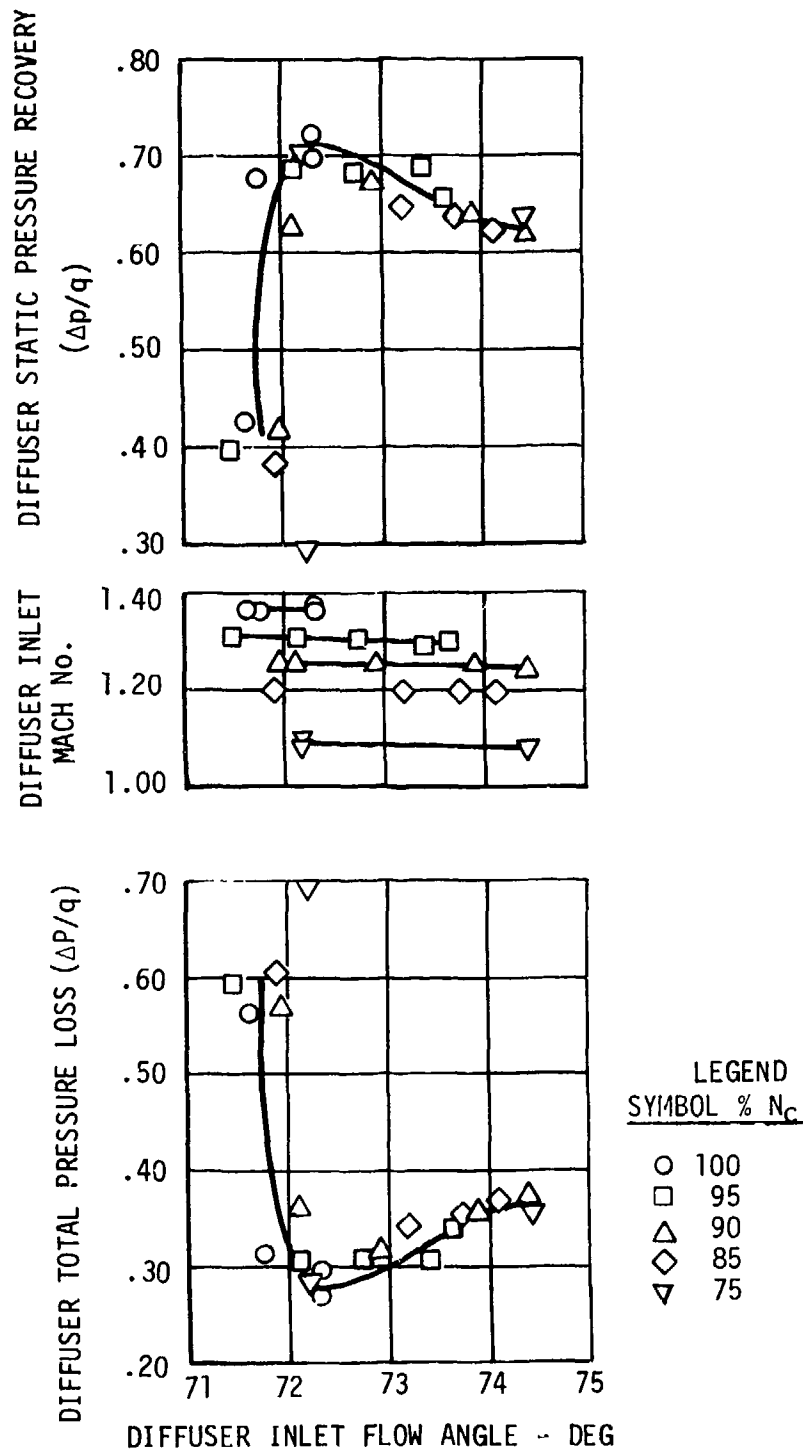


Figure 117. Diffuser Pressure Recovery and Loss Coefficient vs Absolute Air Angle.

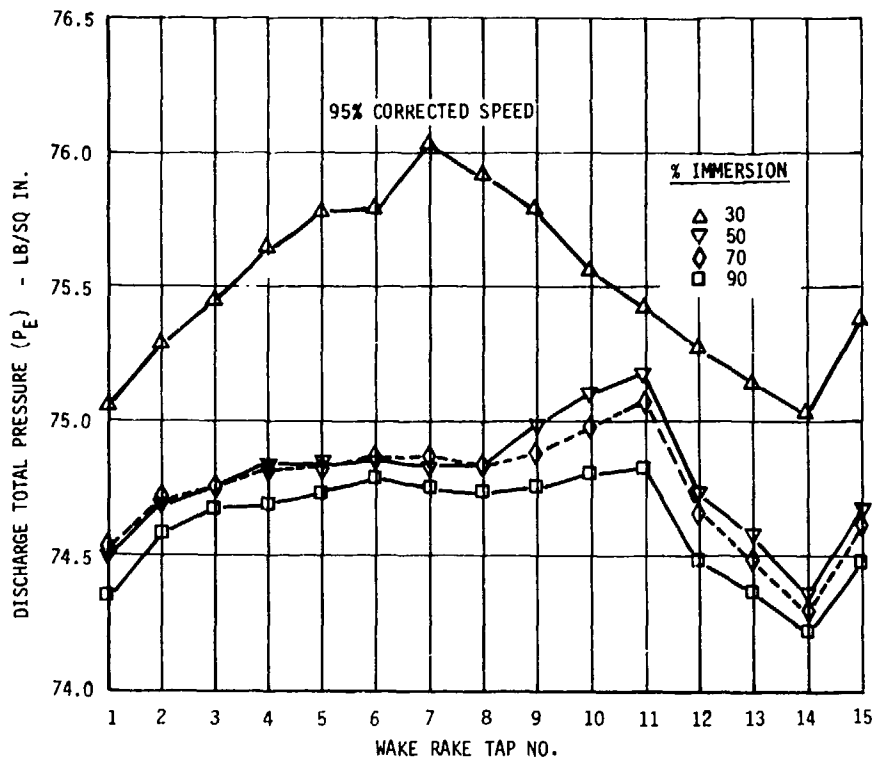


Figure 118. Deswirler Wake Survey.

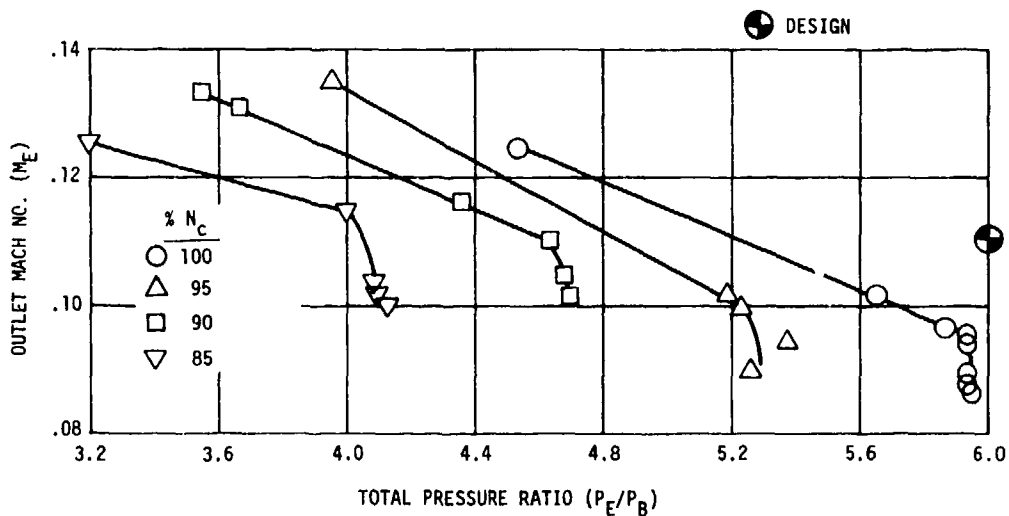


Figure 119. CCV-I Plane E Mach No. - Nominal IGV, No Bleed.

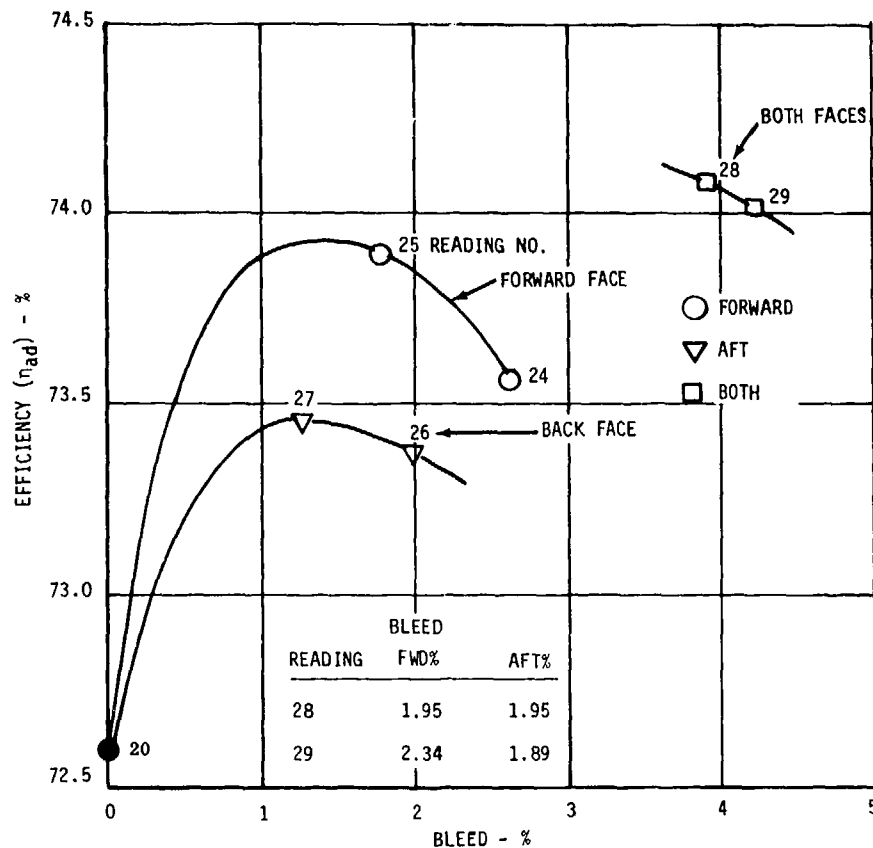


Figure 120. Impeller Exit Bleed.

0.85 points gain in efficiency, and the former 1.3 points. The effect does not appear cumulative. Bleeding approximately 2.0% flow from both sides simultaneously shows 1.5 points gain in efficiency.

The effect of bleeding the intercompressor duct ahead of the impeller, Plane B, at part speed is shown in Figure 121. A nominal bleed flow of 10% was removed. Little effect was seen on efficiency, but there was a small change in choke flow.

The principal data taken during the test program are tabulated in the appendix.

#### Analysis of Results

The operation of the test vehicle at high speeds indicated essentially zero clearance between the impeller blades and the stationary shroud. This region of close clearance was near the impeller exit where the shroud contour is near vertical. There was adequate clearance at the impeller inlet, so an increase in clearance to the design value of 0.005 in. could be accomplished by shimming the diffuser-shroud assembly

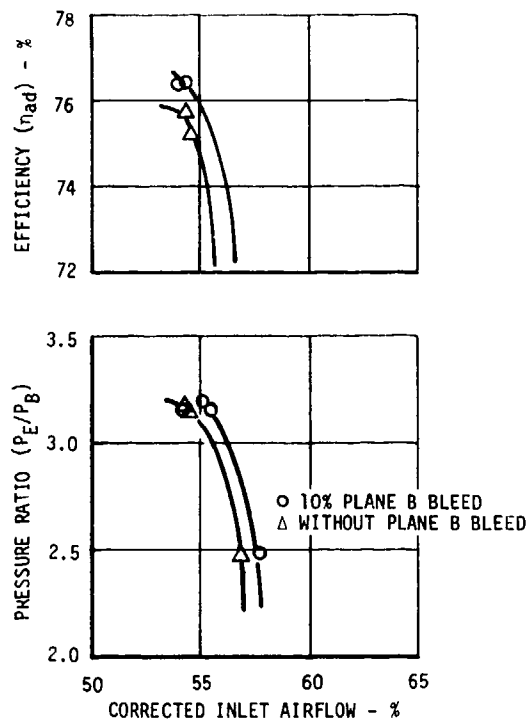


Figure 121. Intercompressor Duct Bleed.

forward. This additional cold shim thickness would be incorporated in all future builds of the centrifugal or combined compressor.

A comparison of the design and measured compressor performance is shown in Table 16 for IGV settings of  $-5^\circ$  and nominal. At  $-5^\circ$ , the overall stage pressure ratio was 6.089 versus the objective level of 6.033 except at a lower level of efficiency. The measured enthalpy rise was higher than predicted and was the reason the stage achieved the overall pressure ratio at the lower efficiency level. The impeller inlet Mach number was close to the design level, but the inlet relative flow angle was greater because of the lower airflow measured during the component test. The measured airflows were lower than design because the lower impeller efficiency required a larger diffuser throat area to pass the design airflow and because the design has 3% vaneless space bleed implied in the objective levels. The higher impeller slip factors near unity reflected this higher enthalpy rise. The impeller slip factor is calculated from the measured temperature rise, static pressure, and speed for a blockage coefficient of 0.9, and it is not a direct measure of the outlet tangential velocity. The calculation does not discriminate between Euler work and such things as frictional heating along the shroud. The source of this higher enthalpy rise was considered paramount in determining the cause of the lower impeller efficiency. During the test, the Plane B bleed was opened to maximum flow to see if there were significant leakage or heat transfer ahead of

TABLE 16. COMPARISON OF DESIGN AND MEASURED PERFORMANCE

Item	Reading 65	Reading 87	Design Point
<u>OVERALL</u>			
IGV Setting - degrees from nominal	-5°	0°	0°
Inlet Total Pressure - psia	14.283	14.305	36.538
Inlet Total Temperature - °R	533.58	534.43	704.85
Exit Total Pressure - psia	86.76	84.62	220.44
Exit Static Pressure - psia	86.26	84.10	218.57
Exit Total Temperature - °R	1013.7	1010.1	1265.69
Corrected Inlet Airflow - lb/sec	2.281	2.232	2.34
Actual Airflow - lb/sec	2.186	2.140	5.0
Corrected Speed - rpm	51787	51746	51800
Actual Speed - rpm	52524	52524	60400
Adiabatic Efficiency (total-to-total)	.736	.731	.810
Adiabatic Efficiency (total-to-static)	.733	.727	.805
Pressure Ratio (total-to-total)	6.089	5.928	6.033
Pressure Ratio (total-to-static)	6.054	5.891	5.982
<u>IMPELLER</u>			
Inlet Mach No. (r = 1.77 in.)	.816	.777	.783
Inlet Relative Flow Angle (r = 1.77 in.)	56.1	55.2	52.3
Pressure Ratio (total-to-total)	7.713	7.222	6.850
Adiabatic Efficiency (total-to-total)	.865	.838	.8838
Corrected Enthalpy Rise - Btu/lb	114.4	113.2	102.6
Temperature Ratio	1.900	1.890	1.796
Impeller Slip Factor ( $C_{\theta 2}/U_2$ )	.998	1.001	.91
Impeller Wheel Speed - ft/sec	1732.6	1732.6	1992.2
<u>DIFFUSER</u>			
Inlet Mach Number	1.354	1.370	1.265
Inlet Flow Angle - deg	73.19	72.32	71.65
Total Pressure Loss ( $\Delta P/q_c$ )	.320	.270	.193
Static Pressure Recovery ( $\Delta p/q_c$ )	.673	.723	.795
Exit Mach Number	.092	.094	.112

the impeller inlet. This bleed would purge the bleed cavity and reduce shroud heat transfer. The Plane B bleed did not change the measured slip factor, so this possible cause was eliminated from further consideration. Another cause of high work input could be local recirculation in the impeller tip region from separation on the diffuser inlet walls. The impeller tip bleed was used to evaluate possible recirculation effects by opening the forward and aft bleed. It was felt that this bleed would remove a significant portion of any recirculating flow. These results are shown in Figure 122 for the test data at 95% corrected speed. Forward bleed reduced the slip factor one point and aft bleed 1/2 point. The effect was not cumulative, since activating both bleeds lowered the measured slip factor one point. This small change in slip factor was not surprising, since the impeller temperature rise is typically higher near the shroud due to frictional effects. The higher slip factor was about 8 points higher than design, and since bleed could affect the measured slip factor by only one point, recirculation was not deemed a major problem. The measured exit temperature profile was also very uniform, so the impeller exit total temperature profile was probably reasonably uniform.

A "data match" was carried out to evaluate the generation of entropy and energy rise through the impeller. A reading near the design airflow at 100% corrected speed was selected for this analysis. The measured and calculated static pressure rise from the "data match" are shown in Figure 123. The calculated enthalpy rise and entropy rise are shown in Figures 124 and 125 respectively. Figure 125 indicates that 68% of the impeller entropy rise is generated between 50% and 100% of the meridional shroud distance. This implies a nominal loss level in the inducer portion, but separation or some other loss mechanism is present in the outer portion of the impeller. This separation could be triggered by the prior flow process and not by a local condition at the 50% meridional distance. An impeller investigation was initiated as part of a related centrifugal compressor program in order to understand more fully this basic loss generation. This program is discussed in the "Related Centrifugal Program" section.

The diffuser losses were higher than design as evidenced in Table 16, but this could be related to a poor impeller exit flow quality rather than a basic design problem within the diffuser. The higher diffuser losses were between the impeller exit and the diffuser throat. It was judged more important to raise the level of impeller efficiency before considering redesign of the diffuser. The diffuser exit cone and deswirl vanes were consistent with other designs and did not indicate any high loss regions. The quality of the flow at the diffuser discharge (Plane E) was good since the outlet Mach number and blockage level were lower than the design intent. The outlet Mach number was 0.09 versus the design value of 0.112 (see Figure 119).

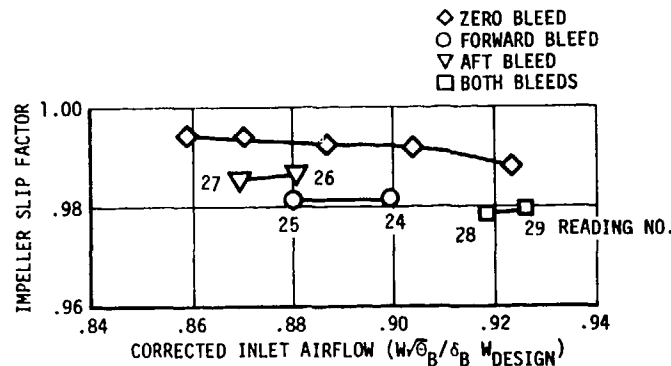


Figure 122. Effect of Impeller Exit Bleed on Slip Factor.

Matching studies were conducted using the test data from the ACV and CCV-I component tests in order to determine the combined compressor performance. These results are shown in Figure 126 for the optimized stator schedule shown in Figure 68. The data for the nominal IGV setting from the CCV-I test were used for the results without impeller exit bleed. The data with 3% impeller exit bleed was obtained by scaling the basic map by 1.03 and by using a 1.5-point efficiency addend. The stall limit for the combined compressor was determined to occur almost exclusively in the centrifugal stage since its stall limit occurred before the axial stage stalled. The only exception was at 70% corrected speed without impeller exit bleed where the axial stage stalled first with this smaller flow capacity centrifugal stage. It appeared that the basic matching effects of operating the centrifugal stage behind the axial compressor could be demonstrated using the ACV and CCV-I designs. Therefore, the combined compressor test would be carried out to define the matching effects concurrent with a program to raise the efficiency level of the centrifugal stage. The flow capacity of the centrifugal stage appeared adequate, and a higher flow capacity stage was not desirable because it reduced the stall margin of the combined compressor. Therefore, it was decided not to rework the diffuser to a larger throat area until more data on matching effects were available from the FCV-I component test.

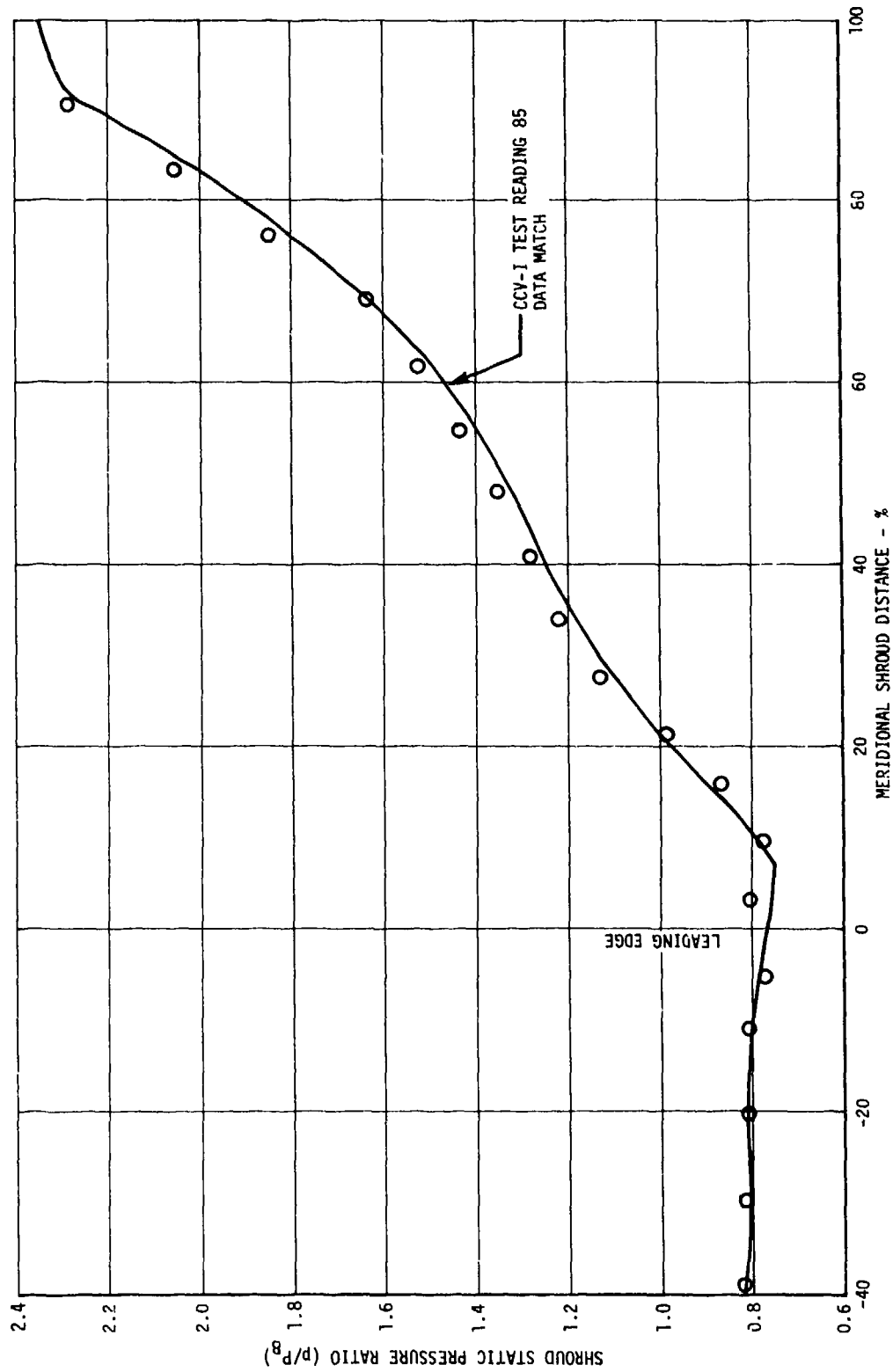


Figure 123. Calculated and Measured Wall Static Pressure Ratio.

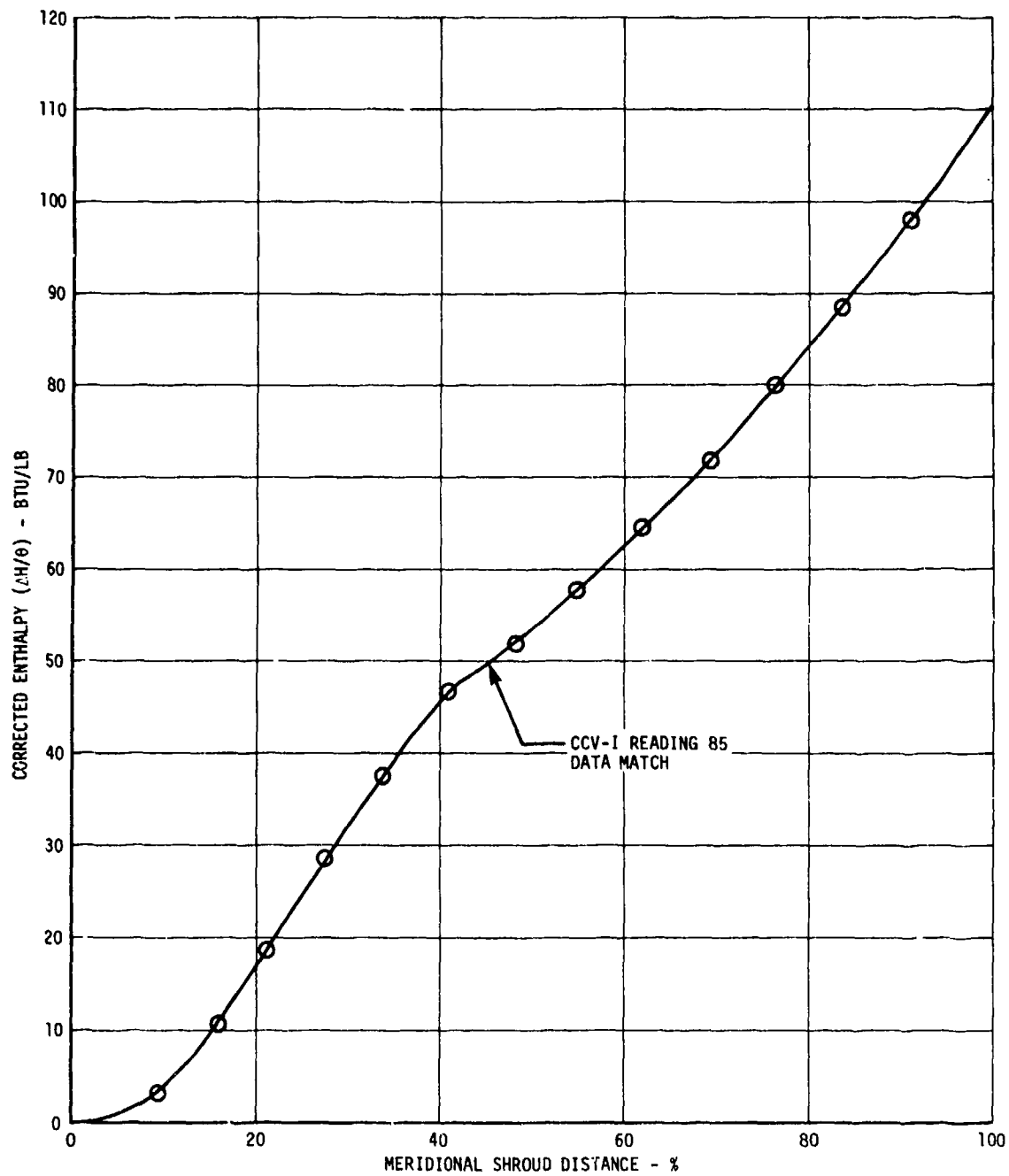


Figure 124. Calculated Enthalpy Rise Through Impeller.

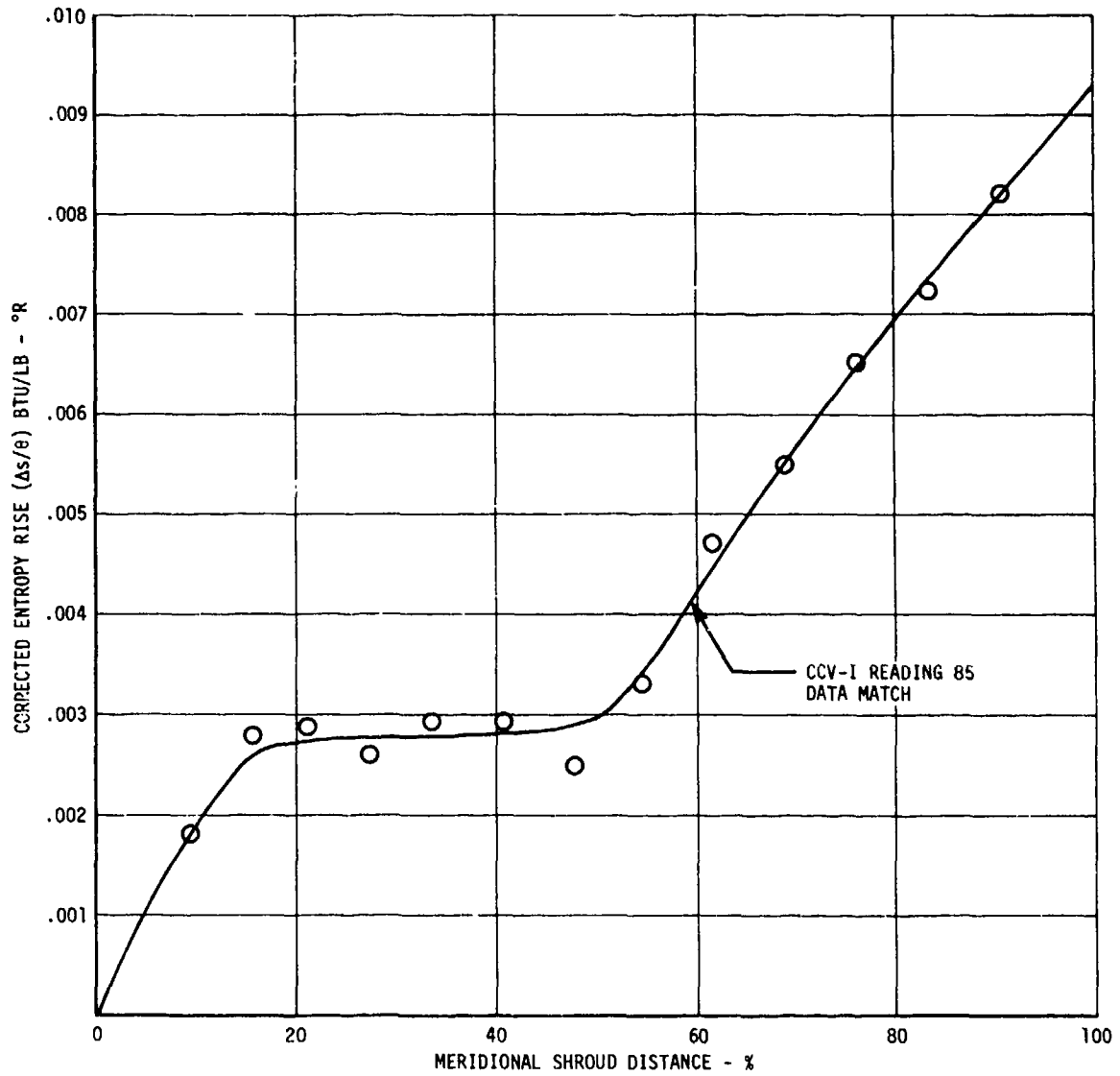


Figure 125. Calculated Entropy Rise Through Impeller.

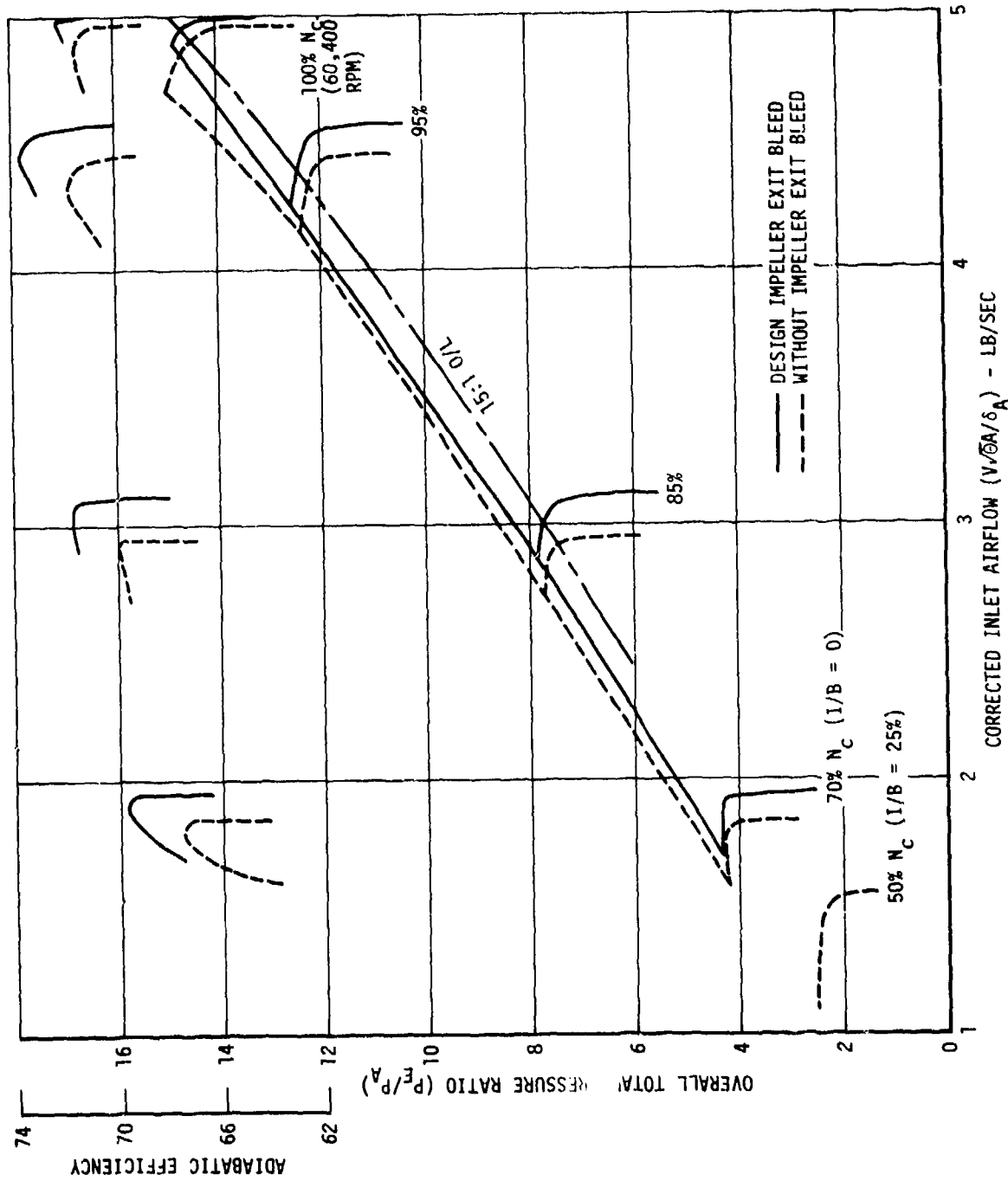


Figure 126. Estimated FCV-I Compressor Performance Using ACV and CCV-I Test Data.

## COMBINED COMPRESSOR TEST (FCV-I)

### Mechanical Performance

In general, the mechanical operation of the combined compressor (FCV-1) was not as smooth as that of the axial and centrifugal compressors (AV and CCV-I). The forward bearing squirrel cage motion went as high as 0.0045 inch peak-to-peak at the maximum speed of 54,000 rpm. The proximity probe located at the vehicle end of the flexible shaft showed a maximum runout of 0.006 inch, of which 0.004 inch was low speed runout. The change in runout between high and low speed was consistent with previous tests.

The front frame horizontal average velocity reached 1.0 in./sec at top speed (23 g's) while the vertical and axial velocity never exceeded 0.5 in./sec (14 g's). The diffuser casing vertical and horizontal vibration pickups indicated a maximum of 0.5 in./sec average velocity at maximum speed (12 g's).

The bearing temperatures and lube oil supply and discharge temperatures were consistent with previous vehicle operation and displayed the same observed response to load and speed fluctuations.

The three load cells were monitored on the strip chart recorder and showed good agreement throughout the test. The sum of the three load cell outputs was used as input for the thrust control system which maintained the required 200-pound thrust load except at very low speeds where the supply pressure was too low and allowed the load to fall off. To get the desired 200-pound load, the vent cavity discharge was capped as in the CCV test.

A sudden increase in thrust load occurred at the end of the test when vibration levels increased. At this time the AC portion of the signal from one load cell was being monitored on an oscilloscope and recorded on tape. Playback of the tape showed a significant increase in the AC signal level at a definite 1/rev frequency. The effect of this type of AC signal on the controller is not completely understood, but tests made later show this may have caused the controller to temporarily malfunction, allowing the load increase.

The stator vane control system provided good tracking with corrected speed and good agreement between the primary and alternate vane angle signals. Some drift in vane angle at constant speed was noted during the test; however, this was corrected by a gain adjustment in the controller.

### Bench Frequency Testing

After the Stage 1 and 2 blisks were tip ground, each blade was frequency checked for the first two modes. The impeller full blades were also frequency checked in the first mode. The results of these frequency measurements were plotted in the Campbell diagram in Figure 127.

### Rotor and Stator Strain Gage Test Results

The amplitudes of vibratory response are evaluated through comparison with a scope limit ( $\sigma_{sc}$ ). The scope limit is the minimum amplitude from a specific strain gage at which failure of the highest responding, weakest blade in the population could be anticipated for a given mode of vibration. It is defined as follows:

$$\sigma_{sc} = \frac{2 \sigma_{av}}{\sigma_{crit}/\sigma_G} \times \frac{1}{K_v} \times \frac{1}{K_t} \quad (20)$$

where  $\sigma_{sc}$  - scope limit (ksi)

$\sigma_{av}$  - minimum allowable vibratory stress from the material Goodman diagram, at the appropriate temperature and mean stress condition existing at the critical location in the vibratory mode in question, (ksi)

$\sigma_{crit}/\sigma_G$  - the ratio of the critical vibratory stress to the stress being read by the strain gage in the mode of vibration in question

$K_v$  - blade-to-blade response variation factor

$K_t$  - blade-to-blade tolerance effect factor

The last two terms are included since normally only a small number of blades are instrumented in a stage relative to the total population, and a range of response can be anticipated for a given stimulus. The assumption is made that the strain-gaged blade is the lowest responding blade in the population.

With reference to the above equation, note that for a given strain gage location, the scope limit varies with:

1. The mode of vibration, since the stress distribution changes significantly from mode to mode.
2. Operating condition, since the allowable vibratory stress is affected by both temperature at the stage and the mean stress on the blade produced by centrifugal effects and gas loading.

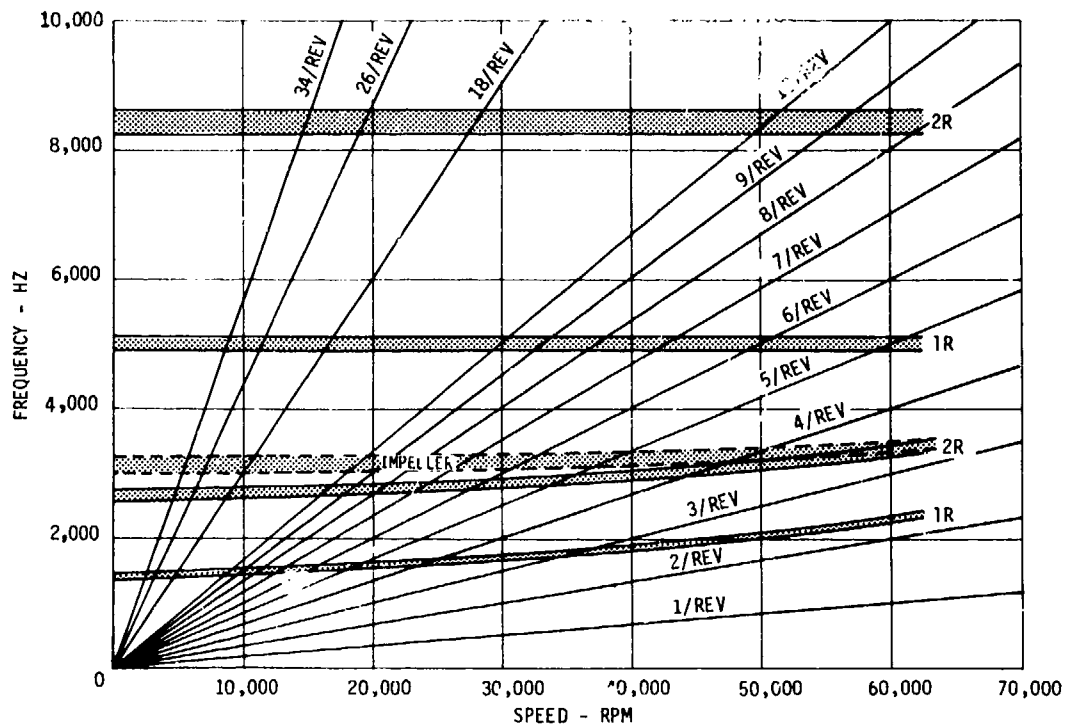


Figure 127. Campbell Diagram for FCV-I Rotor Blade.

Theoretically, then, an infinite number of scope limits exist for a strain gage located on a blade. Practically, limits are calculated prior to test for a number of key operating conditions for use during the test, and are refined during the evaluation process to the degree necessary to establish the integrity of the design.

The airfoil gage response during the conduct of the FCV-I testing indicated no significant stress problem and in general was low (see Table 17). The first stage variable stator which supports a shroud seal at the ID showed a maximum response of 3,000 psi.

The second stage stator in the 5th mode (16,885 rpm) responded to the second rotor passing frequency (22 blades) at 46,000 rpm with a maximum response level of 28% of limits.

The centrifugal impeller showed a maximum response of 48,800 rpm to 43% of limits in the first flexural mode. This stress was the combined effect of a 4/rev, most likely from the front frame struts, and separated flow.

The second rotor responded to the first stator passing frequency (26 vanes) in the second torsional mode (22,500 Hz) at 52,000 rpm. The maximum level of response was 50%, which was considered to be well below acceptable levels.

TABLE 17. COMBINED COMPRESSOR STRESS SUMMARY

Stage	RPM	Mode	Freq	$\eta/\text{rev}$	Source	$\sigma/A$	$\sigma_{sc}$
R1	42,800	1F	$\approx 1,900$	3.7	Sep Flow	8	12%
R1	51,000	3C (15th Mode)	30,500	36	2x IGv	8	a
R1	51,500	1F	1,939	2.25	-	10	b
R1	52,000	7th or 8th	15,700	18	IGv	24	c 52% or 83%
R2	6,000	1F	2,600	26	15	30	36%
R2	44,000	1F	2,960	-	Sep Flow	24	28%
R2	52,000	2T	22,500	26	15	16	50%
IMP	48,800	1F	3,200	4	4x + Sep Flow	40	43%
IMP	51,900	8th or 9th	22,553	26	15	12	c 43% or 29%
IMP	52,400	4th	10,484	12	-	14	21%
S1	All	-	-	-	-	$\leq 3$	-
S2	42,830	1F	3,090	4.34	Sep Flow	20	22%
S2	45,000	5th	16,385	22x	2nd Rotor	10	28%

- a. Requires bench testing for stress distribution.
- b. Recorded on insensitive gage - requires bench test.
- c. Requires bench testing for mode determination.

The maximum observed response of the Stage 1 rotor was at 52,000 rpm, and it was excited at the IGV passing frequency (18 vanes). The resonant frequency was 15,700 Hz with a response level of 24,000 psi. Since this frequency is midway between the 7th and 8th modes, being 4% lower and 4% higher respectively, there is a problem with mode and percent of limit evaluation. The worst case would be mode 8, where the observed stress would reduce to 83% of limits. This level is considered higher than desirable and would require the determination of airfoil response as a function of variable geometry variation (primarily IGV) and operating line. If the 15,700 Hz mode was determined to be the 7th mode, the maximum observed stress would be 52% of limits; this would be considered acceptable.

The FCV-I was stalled at various speeds from 78% to 95%  $N/\sqrt{\theta}$  with a maximum response of 70% limits, which for stall stress is well below acceptable levels (see Figure 128).

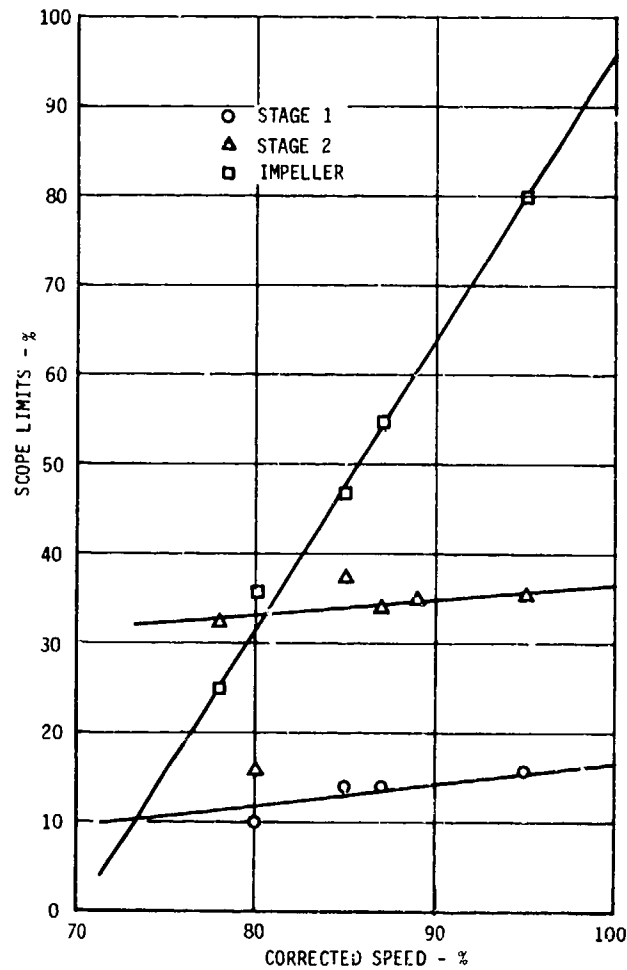


Figure 128. FCV-I Rotor Blade Stall Stresses.

The maximum stall stresses observed on the Stage 1 and 2 rotors were less than 15% and 40% respectively.

The impeller stall stress tends to increase with corrected speed and responded to 70% of limits at 95%  $N/\sqrt{\theta}$ . Extrapolating the data to 100%  $N/\sqrt{\theta}$  the response would be expected to be approximately 95% of the allowable stress.

#### Analysis for Cause of High Vibration

During the disassembly of the test vehicle, extra checks and measurements were made in order to isolate the source of the high vibration noted at the conclusion of the test. All measurements, runouts, and interference fits were correlated with buildup data. No cracked or yielded parts were observed; however, a small chip, 0.025 x 0.05 in., was missing from a balance piston seal tooth. The tie-bolt stretch repeated and both bearing inner races were tight. The conduits, adaptors, and wiring for the rotor strain gages were in place. The only discrepancies noted on teardown were the small chip from the balance piston seal tooth, an increase in rotor unbalance at the balance piston from less than 0.1 gram-in. at buildup to 1.5 gram-in. at disassembly, and some slight fretting under the aft bearing inner race. Fretting had been observed after the previous tests, but this had progressed somewhat further, probably owing to the longer running time for this test. A summary of the vibration cause findings follows:

1. The vibration energy source was a 1/rev stimulus from the compressor rotor.
2. The extent of the vibration at the front frame was about 3 mils and was close to bottoming the front support squeeze film. The double amplitude of the shaft at the flexible coupling was 13 mils and was probably bottoming the aft bearing squeeze film.
3. A rotor critical frequency was not the cause of the vibration but rather a high unbalance or shift in the assembly (forced vibration).
4. The measured 1.5 gram-in. of unbalance of the rotor assembly after the test was not sufficient to cause the high vibrations.
5. The labyrinth seal rubs were heavier at the front frame - both seals were rubbed 360° from a single sector of the rotor.
6. The rear frame balance piston-to-vent cavity seal had some light rubbing as well as a 360° score mark on the CDP seal in line with the chipped seal tooth.

7. The problem occurred at the slowest (90%) and coldest (403°R) speed and inlet temperature. Prior testing at that inlet temperature was at 95 and 100% corrected speed.
8. The high 1/rev axial load fluctuations observed on the load cell could be caused by rotor orbiting.
9. The increase in bearing thrust load can be attributed to the thrust balance control system that was found to be erratic when large ac signals were received from the load cell.
10. The rotor vibration did not cause any blade tip rubs.

The preceding findings indicated a number of possible causes for the apparent shift in the rotor assembly that created the high vibration via misalignment and/or unbalance. The major rotor assemblies were:

1. Axial rotors and impeller piloted together with curvic couplings and restrained with a tie bolt.
2. Impeller to balance-piston rabbetted joint.
3. Aft assembly between thrust bearing inner race and flexible coupling.

The probability of the impeller-to-balance piston joint to be at fault was unlikely because this assembly had operated to higher speeds and temperatures on this test and previous tests. Also, this assembly had the same fits at teardown.

The aft assembly up to the coupling did not have any different mode of operation during the previous hours of test and was tight at teardown.

The forward rotor assembly that was clamped by the tie bolt does offer some probable causes and was subjected to a unique operational point - lowest speed (90%) and coldest low speed temperature (403°R). It has been estimated that half of the tie-bolt load could be lost because of shrinkage of the rotor assembly at cold inlet temperatures while the tie-bolt ends are heated by the impeller bore and the hot oil in the forward sump. This condition is aggravated at lower compressor speeds because the lower temperature rise across the axial rotors results in colder rotor metal temperatures.

Another possibility in the forward sump was an icing condition in the shop air seal pressure line. This might have permitted further cooling of the housing bore and led to a rotor seal rub. A plugged seal pressure line could have permitted the refrigerated inlet air to enter the forward sump seal cavity.

In terms of future action to avoid a repetition of the vibration problem, the following items were implemented:

1. Increase tie-bolt preload, since the present design has margin.
2. Avoid refrigerated testing below 415-420°R inlet temperature.
3. Heat the forward seal supply air.

#### Aerodynamic Performance

The overall performance of the compressor was obtained directly from the instrumentation outlined in the section entitled Aerodynamic Test Results from Combined Compressor Test (FCV-I), whereas performance of the individual axial and centrifugal stages was obtained by measuring the static pressure at the axial compressor discharge and subsequently computing total pressure from data (see Figure 129) derived during the ACV test. The results in Figure 129 were a function of the static-to-total pressure ratio and static flow function at the axial compressor discharge plane. The correlation was made using both Plane B static pressures and wall static taps located at the exit of the second stator vanes. (Items 296 - 307 in Figure 23.)

Performance was obtained with and without intercompressor bleed and vaneless space bleed. In addition, performance effects were observed for 5° closed and opened Stage 2 stator vanes.

#### Nominal Stator Schedule

The overall compressor performance map with the stator schedule set as given in Figure 68 was plotted in Figure 130. This schedule was derived as optimum during the ACV test on the basis of efficiency as well as surge margin of both the axial and centrifugal compressors. Figure 130 shows the overall map superimposed on estimated overall performance based on the matched ACV and CCV test data.

Performance of the individual components of the axial and centrifugal compressors was plotted in Figures 131 and 132, respectively. These were obtained by computation using the correlation in Figure 129. The component test performance obtained during the ACV and CCV test programs was not repeated. In the case of the axial compressor, the peak efficiency appeared to deteriorate faster than demonstrated by the component test. The centrifugal compressor diffuser choke flow was reduced by approximately 4%. At lower speeds the flow reduction was somewhat less.

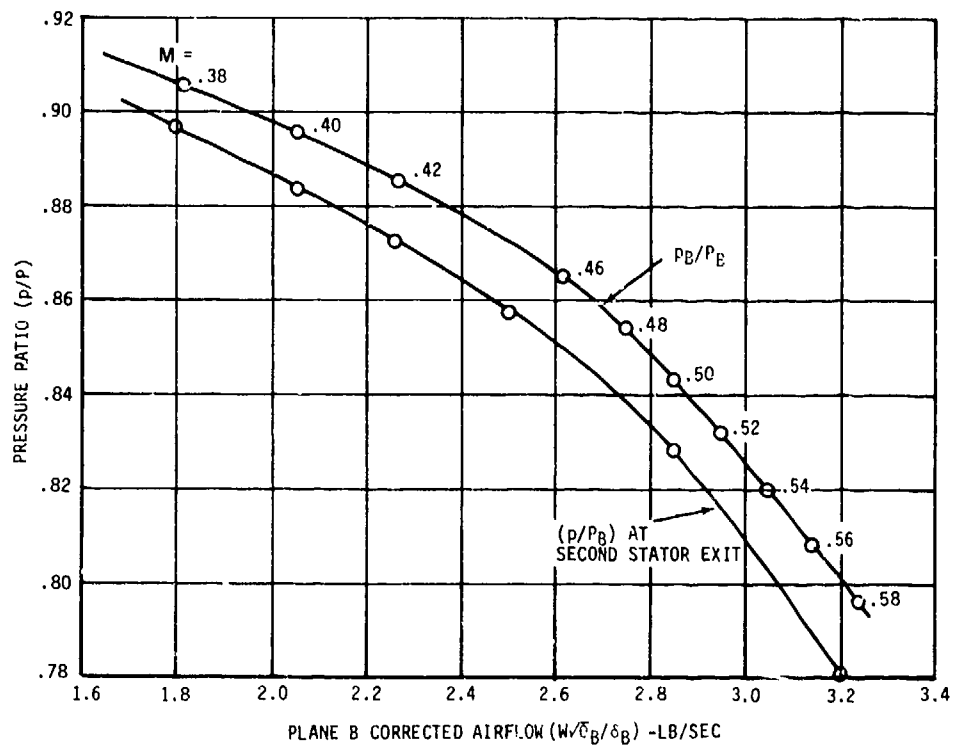


Figure 129. Flow Function Correlation.

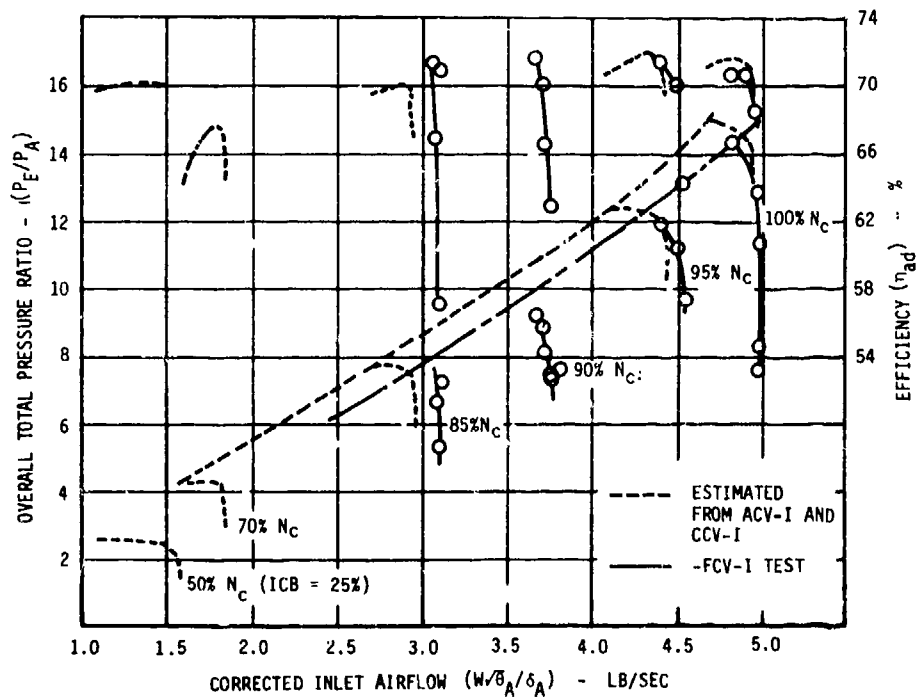


Figure 130. FCV-I Overall Compressor Performance.

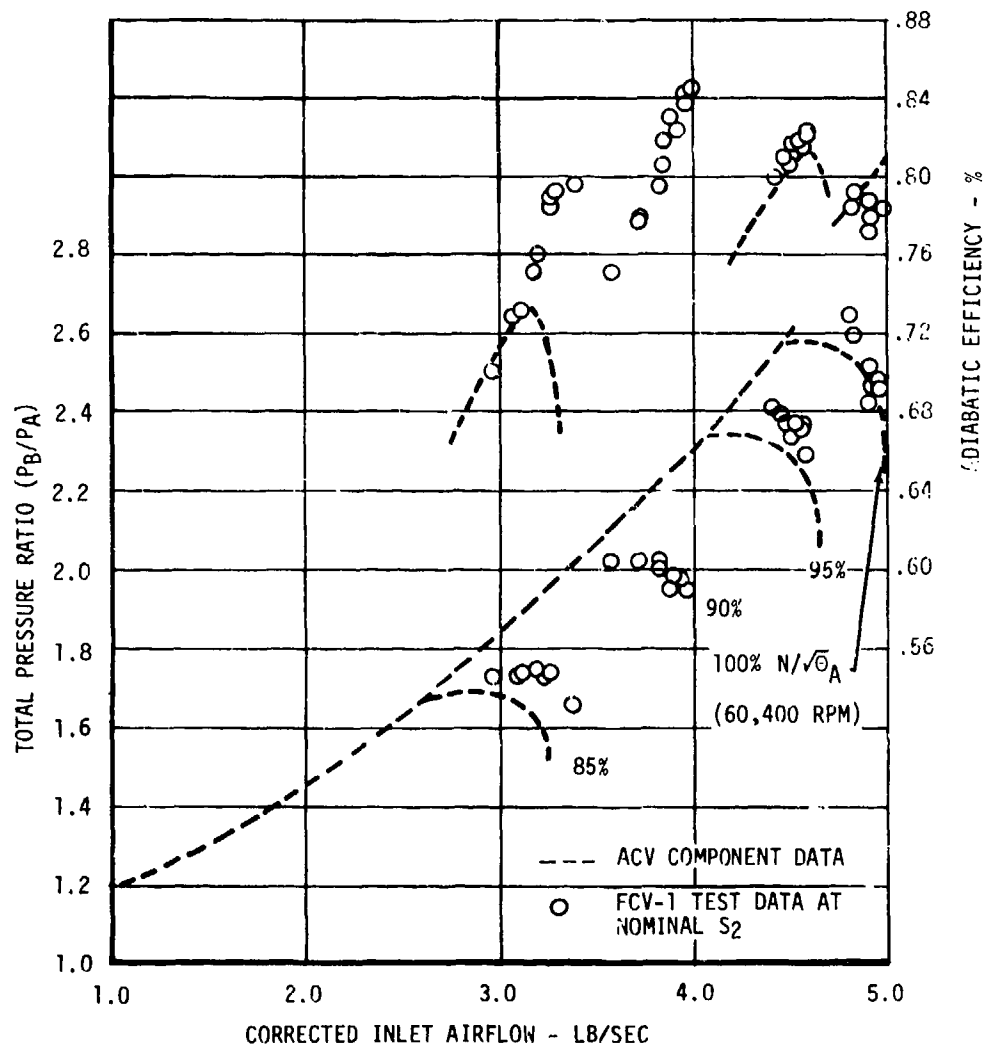
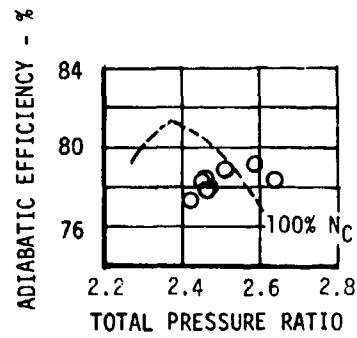


Figure 131. FCV-I Axial Compressor Performance.

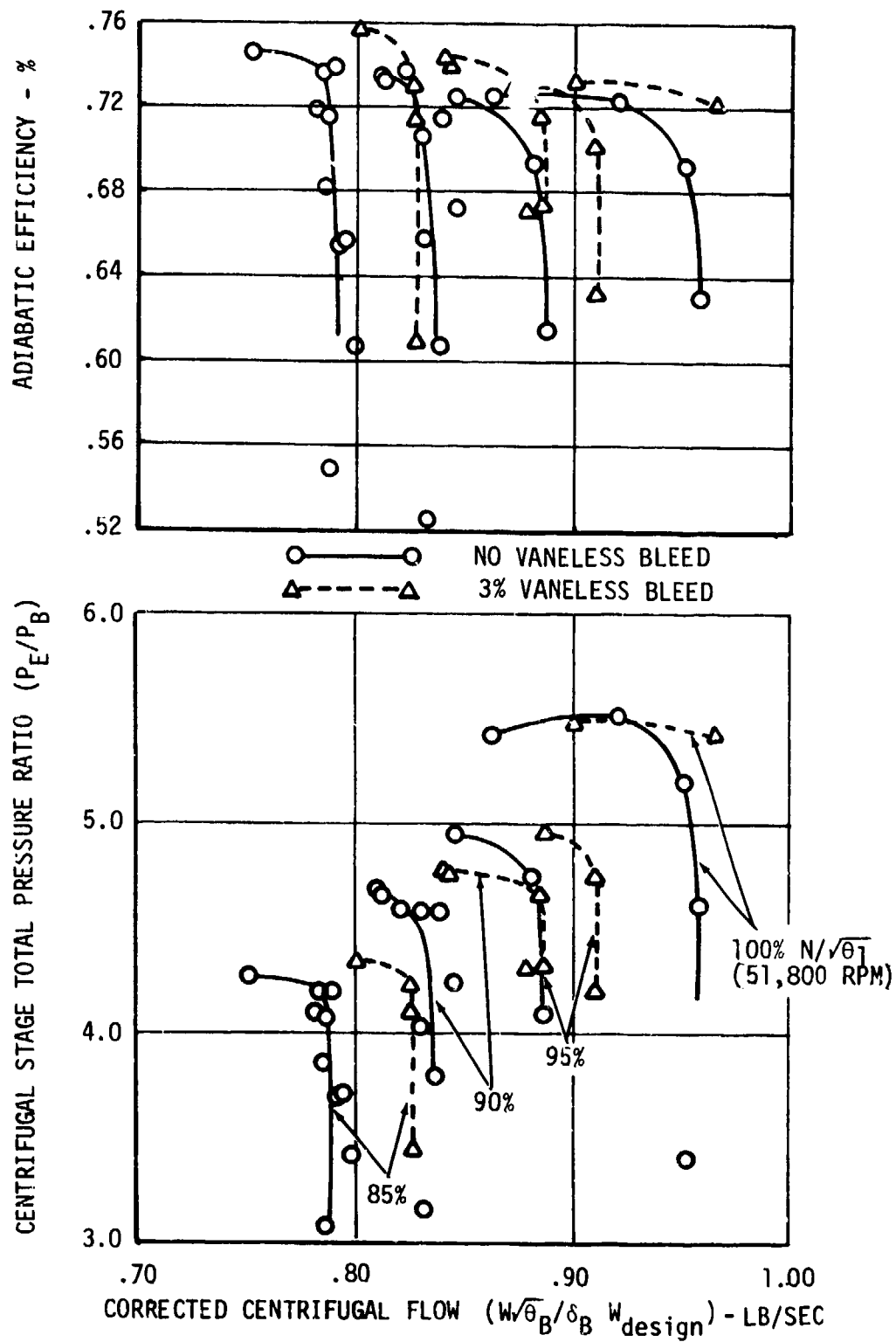


Figure 132. Centrifugal Compressor Performance.

### Effect of Stage 2 Stator Schedule Variation

The compressor performance variation with Stage 2 stator open 5° and closed 5° was obtained at three different speeds. The effect of the schedule variation is plotted in Figures 133 through 135.

Figure 133 shows the respective effect of open and closed schedule on overall performance at 100% corrected speed. Contrary to expectation, the flow at 5° open schedule has not increased. This is due to lower performance in the axial compressor at 100% speed.

The above condition appears to persist at speeds down to 90% (see Figures 134 and 135). The effect of Stator 2 variation at lower speeds was not investigated. The 5° closed Stage 2 stator schedule resulted in a loss of flow and pressure ratio with an increase in adiabatic efficiency at all speeds.

For comparison, the axial compressor stage performance due to the above stator variation (Figures 136 through 138) showed a similar effect. The maximum flow does not increase for 5° open, and the peak efficiency drops approximately 2-1/2 points at 100% speed, 3-1/2 points at 95% speed, and 1 point at 90% speed.

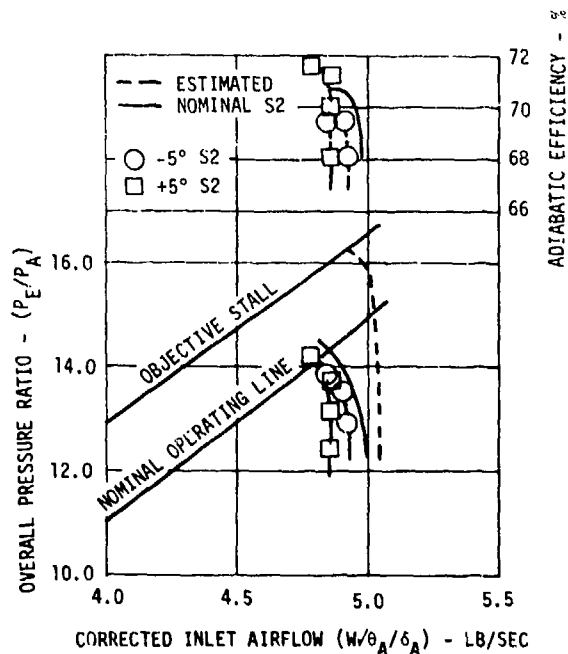


Figure 133. Effect of Stator 2 Schedule on Overall Compressor Performance - 100% Speed.

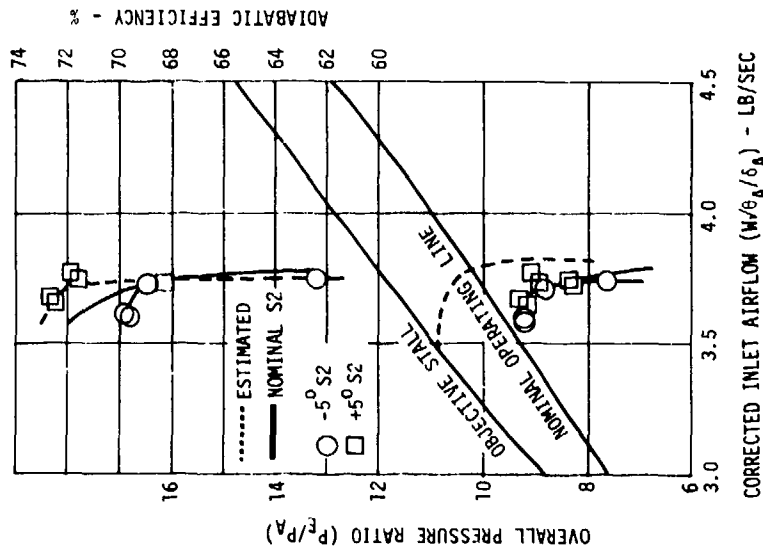


Figure 135. Effect of Stator 2 Schedule on Overall Compressor Performance - 90% Speed.

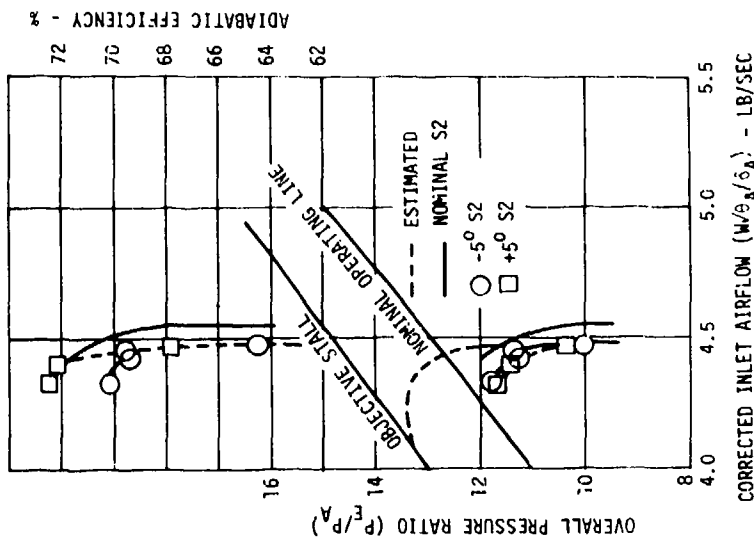


Figure 134. Effect of Stator 2 Schedule on Overall Compressor Performance - 95% Speed.

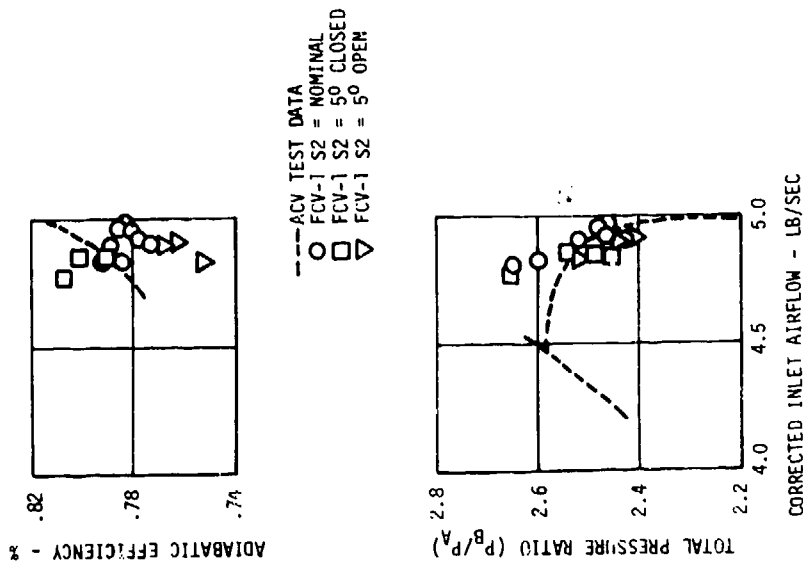


Figure 136. Effect of Stator 2 Schedule on Axial Compressor Performance - 100% Speed.

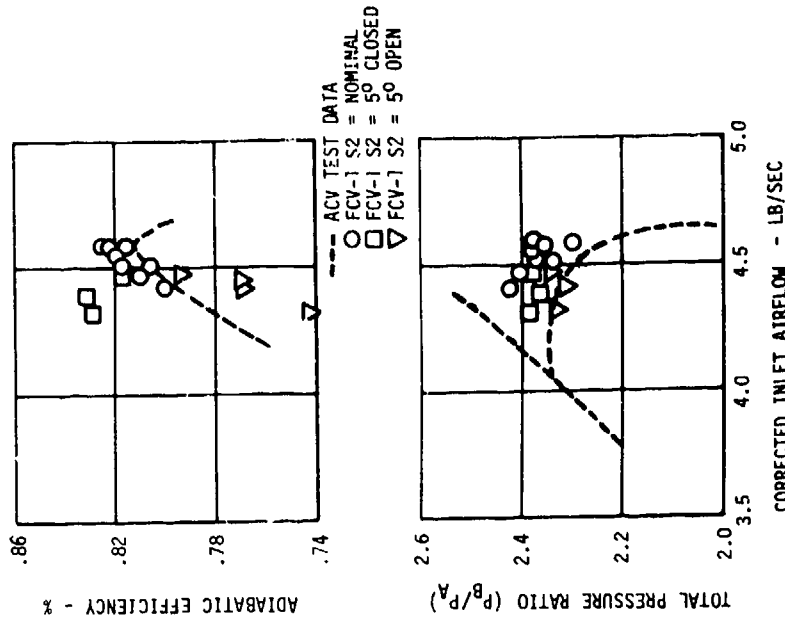


Figure 137. Effect of Stator 2 Schedule on Axial Compressor Performance - 95% Speed.

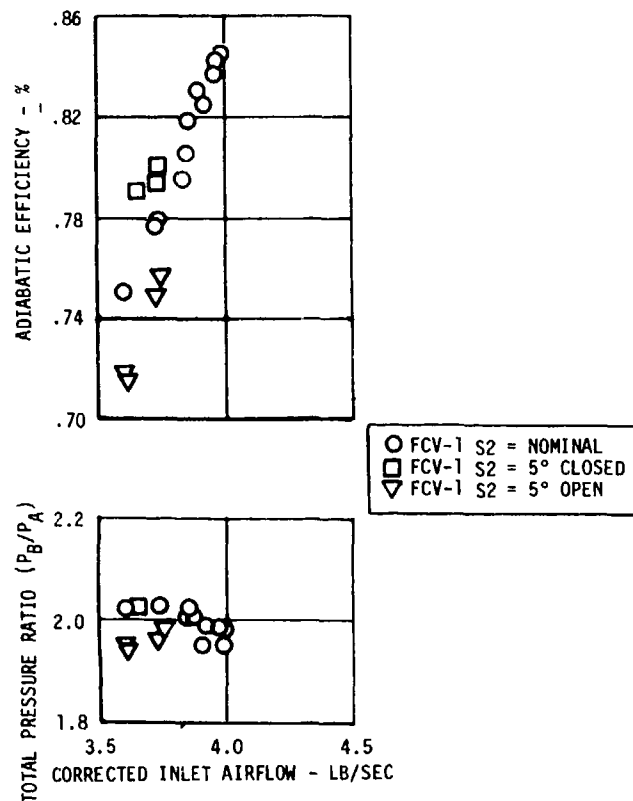


Figure 138. Effect of Stator 2 Schedule on Axial Compressor Performance - 90% Speed.

The effect of stator variation on the centrifugal compressor, on the other hand (Figures 139 through 141), shows a change in performance similar to the CCV map (Figure 108). The maximum flow and efficiency level is lower but the relative change in flow is similar in both cases.

#### Static Pressure Variation

The axial distribution of the wall static pressure at 100% corrected speed was plotted in Figure 142. For comparison, static pressure distribution of the ACV test was also plotted. As may be seen, Stage 1 is unloaded while Stage 2 is loaded up in relation to the ACV data.

#### Analysis of FCV-I Results

The initial operation of the combined compressor indicated stalls occurring in the axial stage before the estimated stall limit. A review of the test results indicated a 4% reduced flow capacity in the centrifugal stage which resulted in higher loading in the axial compressor. The choke airflow in the combined compressor was set by the diffuser throat, and these airflows were at a high throttle setting

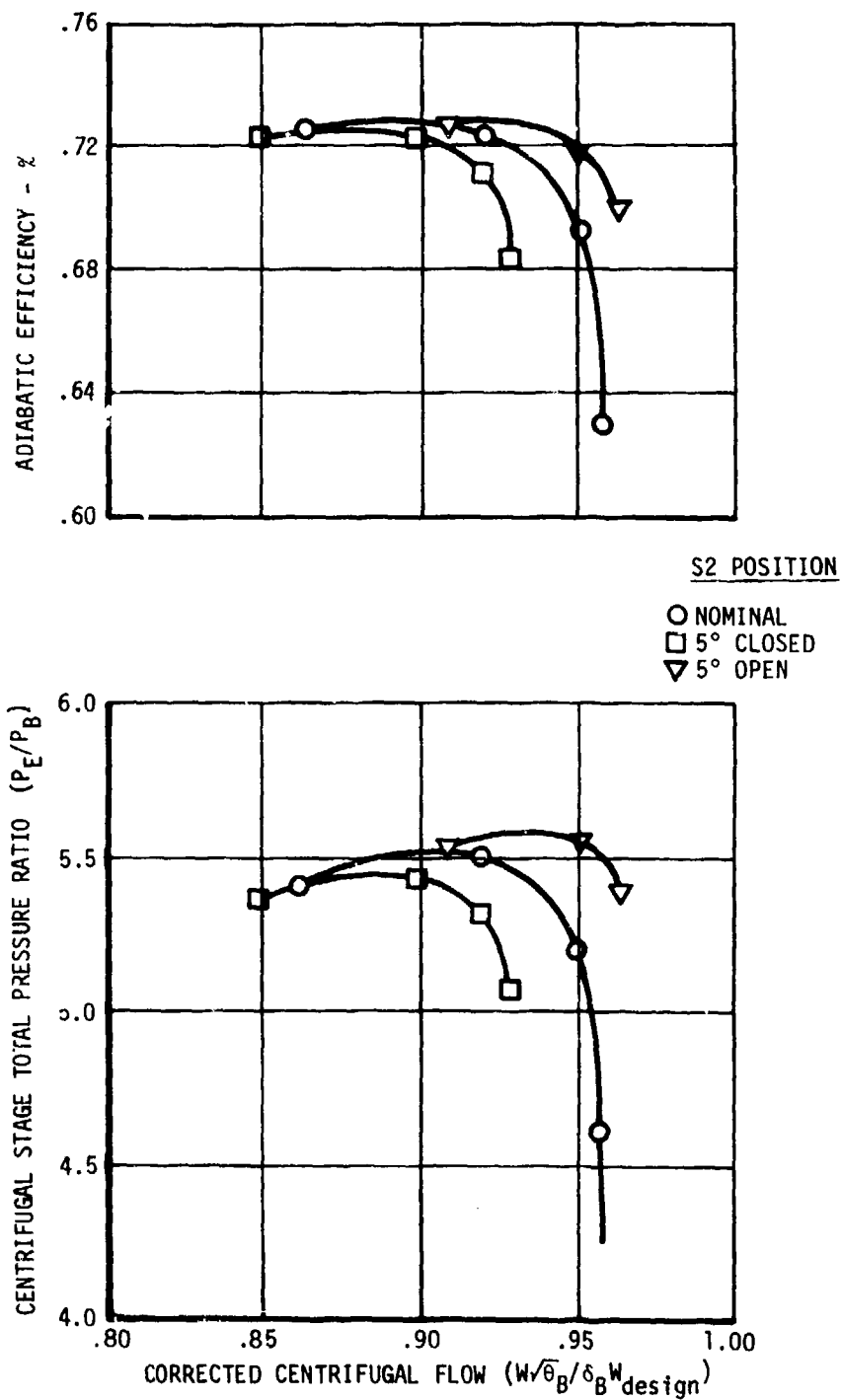


Figure 139. Effect of Stator 2 Schedule on Centrifugal Compressor Performance - 100% Speed.

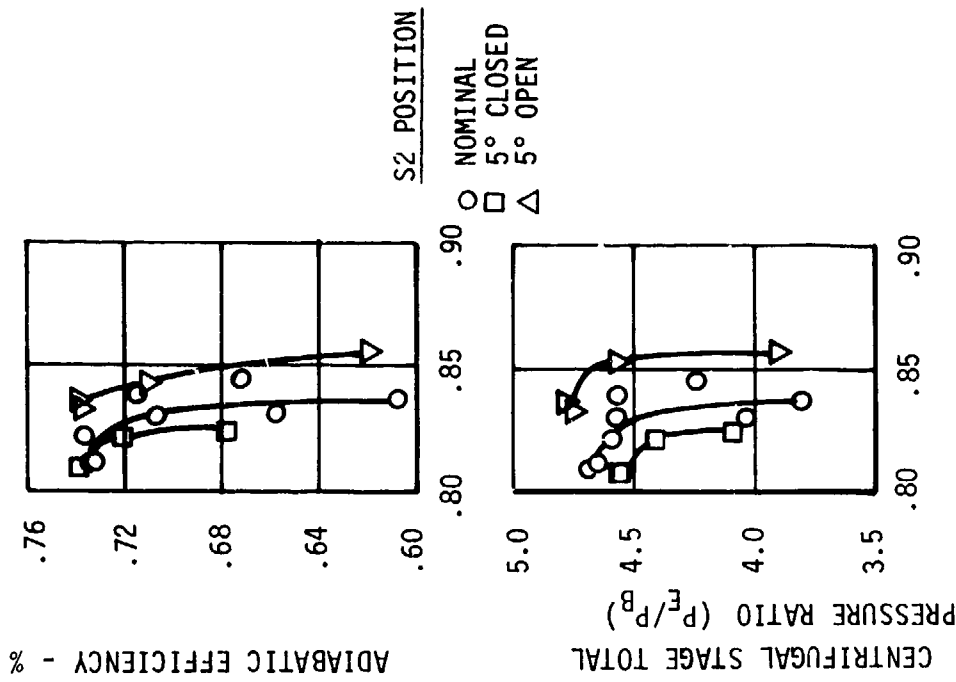


Figure 140. Effect of Stator 2 Schedule on Centrifugal Compressor Performance - 95% Speed.

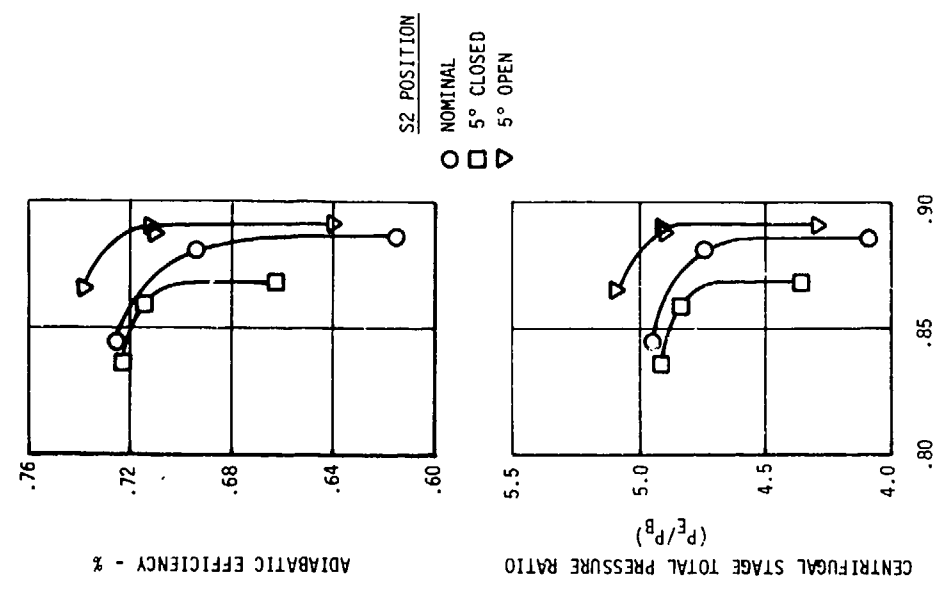


Figure 141. Effect of Stator 2 Schedule on Centrifugal Compressor Performance - 90% Speed.

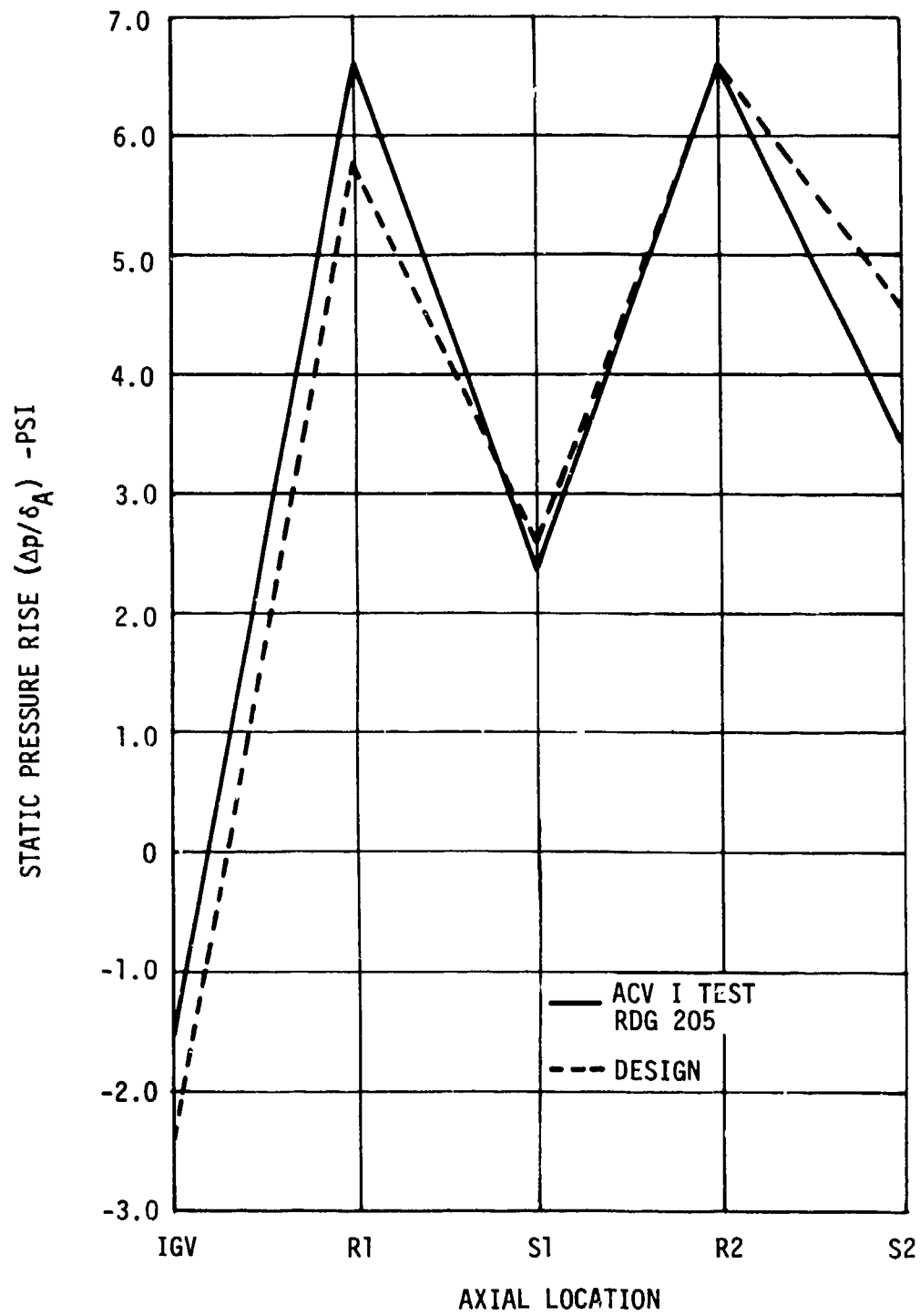


Figure 142. Axial Compressor Static Pressure Distribution - 100% Speed.

in the axial compressor. About 6% intercompressor bleed flow (Plane B) was used to operate the axial stage near its design conditions.

The calculation of the axial compressor performance used the second stator static pressure correlation shown in Figure 129. This correlation was used because the intercompressor bleed affected the Plane B static pressure. The difference in the axial compressor performance from the ACV data (see Figure 131) could possibly be due to the intercompressor bleed affecting the measured outlet temperature and the second stator exit static pressure. The observed differences from ACV levels could not be due to the different set of hardware or build-up clearances used for the FCV-I component test.

The flow-pressure ratio characteristic of the centrifugal stage was lower than the CCV-I component data. The FCV-I centrifugal stage efficiency was about a point lower than CCV-I levels. The outlet conditions from the axial compressor were the suspected cause of this change in the centrifugal stage performance characteristics. The axial stage second stator vanes were opened and closed 5° to alter the axial outlet flow conditions. The overall and axial compressor efficiency was improved by closing the second stator vanes but at the expense of reduced airflow and overall pressure ratio. The centrifugal efficiency was not affected, so the gain in overall efficiency was entirely in the axial stage. Opening the second stator reduced the overall efficiency and pressure ratio at 100% corrected speed from the nominal values (see Figure 133). The axial stage pressure ratio and efficiency were the cause of the lower overall performance (see Figure 133). The centrifugal stage reacted to the opened second stator vanes since its pressure ratio and airflow were increased over the nominal values (see Figure 139). The centrifugal stage efficiency was constant, and this was also observed in the CCV-I component test results (see Figure 108).

As a result of the FCV-I test and analysis, it was decided to increase the diffuser throat area 6.4% to match the axial stage without the use of intercompressor bleed. A review of the ACV traverse data at Plane C (see Figure 79) indicated some improvement in the impeller leading edge incidence could be achieved by cutting back the inducer leading edge. It was also decided to carry out additional traversing at the axial compressor discharge (Plane B) to better define the axial stage outlet flow conditions. This traverse data would be gathered in both the radial and circumferential directions.

## COMBINED COMPRESSOR TEST (FCV-II)

### Summary

The testing of this compressor build was started on 13 December 1973 and completed after six test runs on 28 December 1973. The first test run obtained complete speed lines to stall at 50, 70, 80, 85, and 90% corrected speed using ambient inlet conditions. The test results indicated below predicted airflows at 85 and 90% speed, so additional diagnostic data was obtained at maximum vaneless bleed. Stable operation was demonstrated at 70% speed without intercompressor bleed.

The second run on 14 December obtained test results to 100% corrected speed using refrigerated inlet conditions. The 90% corrected speed line was repeated to compare with earlier data at ambient inlet conditions.

The third test run on 19 December obtained the traverse data behind the axial rotors and at the axial discharge plane. These data were near the design point at 100% speed and the typical operating line at 85% corrected speed. The remaining traverse data at 95% and 100% speed was completed in the fourth test run on 20 December.

Prior to the fifth test run, the traverse equipment was removed and Plane B total pressure and temperature rakes were installed to measure the axial compressor performance prior to increasing the rotor tip clearances. This baseline data was obtained at 85, 95, and 100% corrected speed on 21 December.

The axial rotor clearances were increased prior to Run 6 by the removal of an axial shim between the rear flange of the axial casing and the diffuser casing. Run 6 was on 28 December and completed all required test data. Speed line mapping of the axial compressor was carried out at 85, 95, and 100% corrected speed to compare with prior data obtained during Run 5. At the conclusion of this test the compressor was successfully operated with ambient inlet conditions to 95 and 99% corrected speed (59,540 rpm) for partial speed line mapping.

The FCV-II test acquired a total of 158 data readings in running time of 55:55 hours. Sixteen stall points were determined during the test program.

### Mechanical Operation

The mechanical operation of this test build was as smooth as the earlier ACV and CCV-I tests. Rotor strain gages were not required on this test because the safe stress envelope for the axial compressor was established in the previous FCV-I test with strain gages. Setup and operation of the compressor test vehicle were the same as in the previous

FCV-I test, and all bearing temperatures and vibration readouts were normal.

Prior to the final test run, a shim was removed from the aft flange of the axial compressor to increase the clearance between the rotor tips and the compressor casing. This shim was intentionally designed into the stackup to easily evaluate clearance effects. The tip clearance change before and after the shim removal for each rotor is tabulated below:

	<u>Before</u>	<u>After</u>
Stage One Rotor (% C1/L)	.706	.985
Stage Two Rotor (% C1/L)	.634	1.21

#### Performance Results and Analysis

The overall performance results for the FCV-II combined axial-centrifugal compressor are shown in Figures 143 and 144. The compressor data was obtained with the nominal stator schedule determined from the ACV test results (see Figure 68). The overall performance is plotted as total-to-total with an outlet Mach number 0.10 to 0.11 near the peak efficiency values (see Figure 145).

The predicted performance shown in Figure 143 was based on the ACV-I axial compressor test data and on the adjusted CCV-I centrifugal compressor data for the 6.4% diffuser throat area increase and the impeller inducer leading edge modification. The FCV-II test data was obtained without resorting to intercompressor bleed, demonstrating the ability to match the axial and centrifugal stages. The improved axial-centrifugal matching was a result of the centrifugal stage rework.

The stall limit as shown in Figure 143 was lower than predicted due to centrifugal compressor stall.

The performance of the axial stage is presented in Figure 146 for the data using the fixed total pressure and temperature rakes. The efficiency contour at 100% speed was drawn through the data points using a similar shape as defined in the ACV component test. Experience has shown this to be a more realistic representation of the data than obtained using a straight line through the data points. The calculated axial performance is shown in Figure 147 for all readings on the nominal stator schedule.

The results of the increased clearance over the axial compressor rotors were plotted in Figure 148 at 85%, 95%, and 100% corrected speed. The one point reduction in efficiency level at design speed was similar to

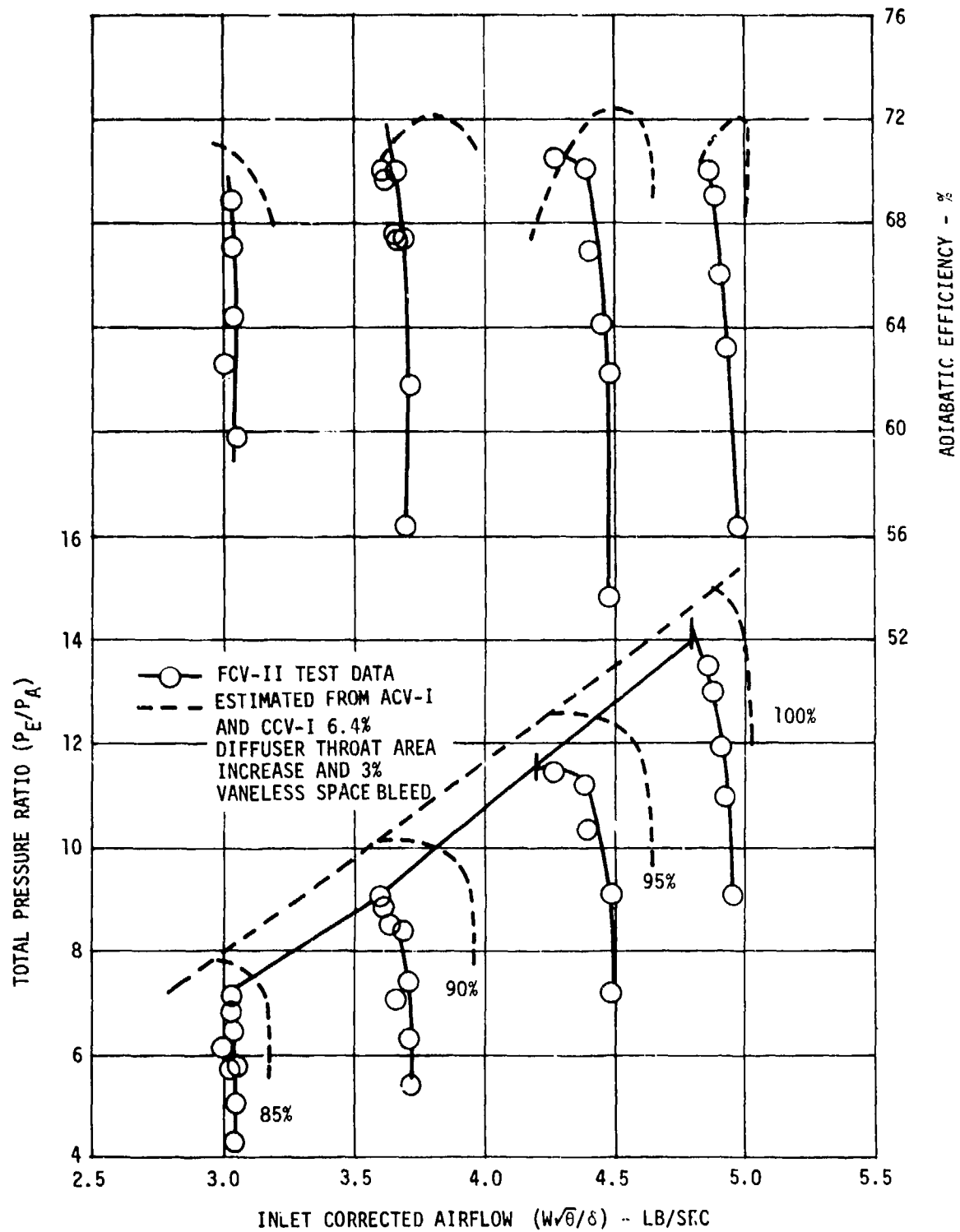


Figure 143. FCV-II Overall Performance Results.

3% VANELESS SPACE BLEED

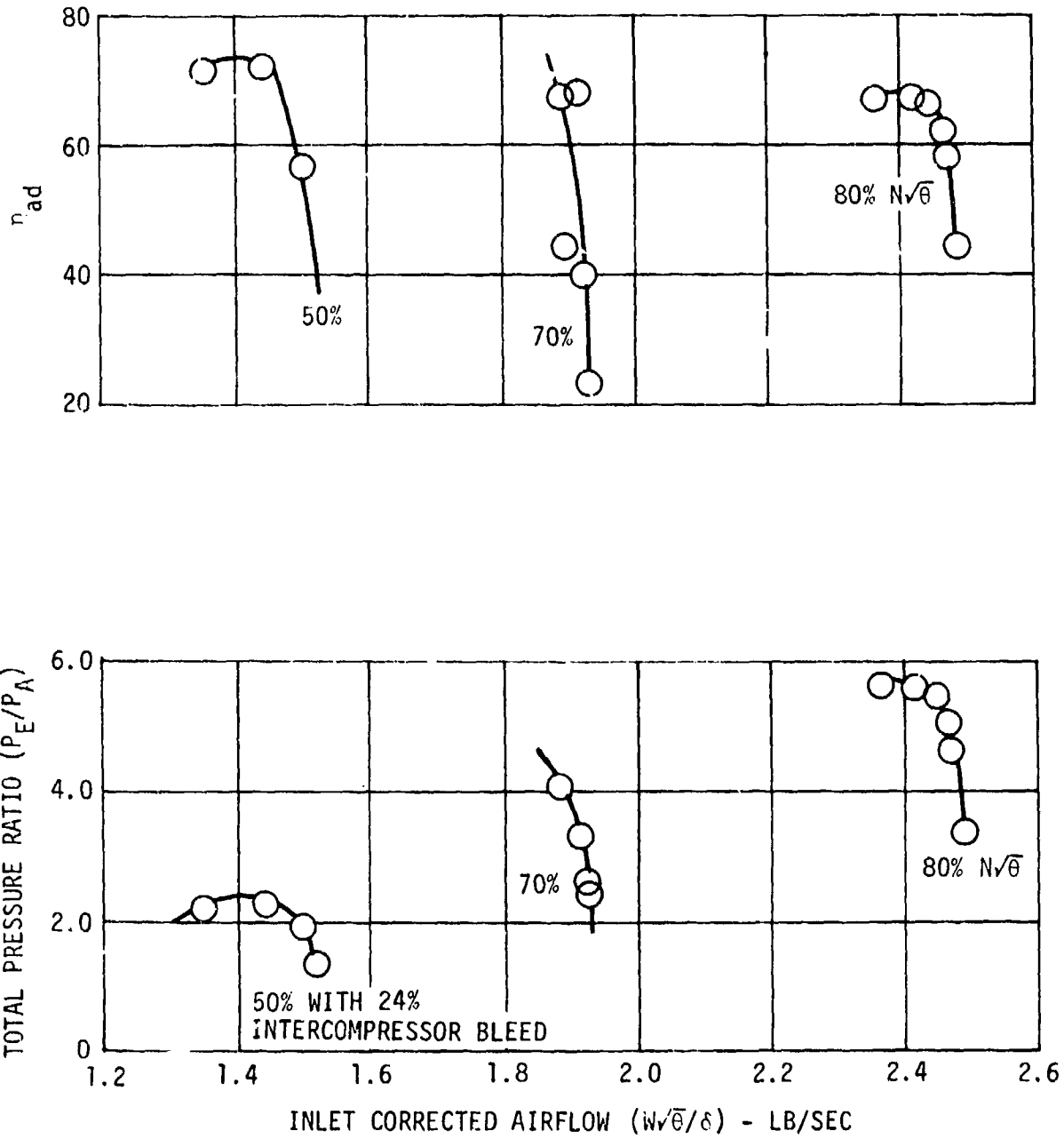


Figure 144. FCV-II Overall Performance - Low Speed.

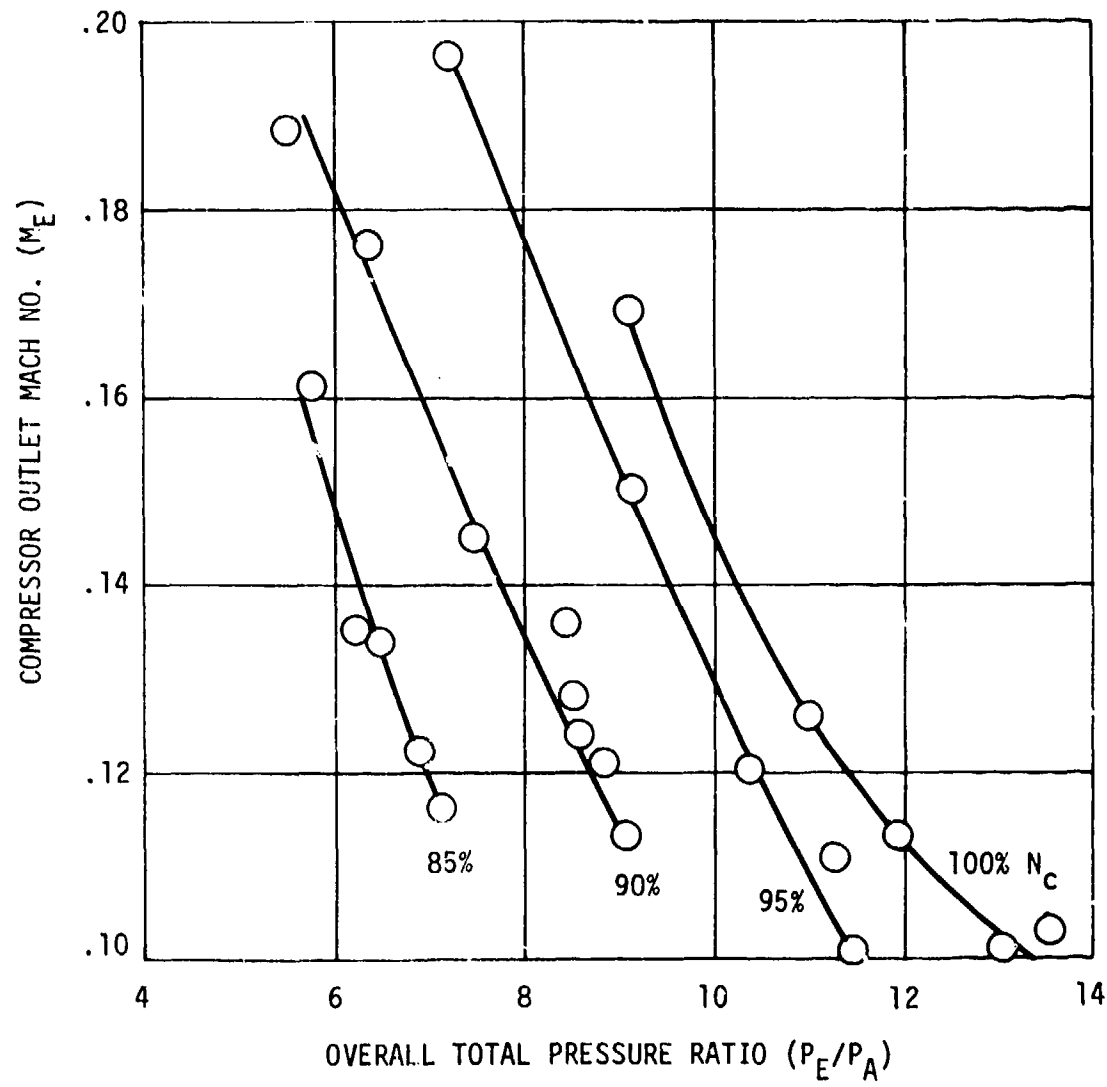


Figure 145. FCV-II Plane E Mach No.

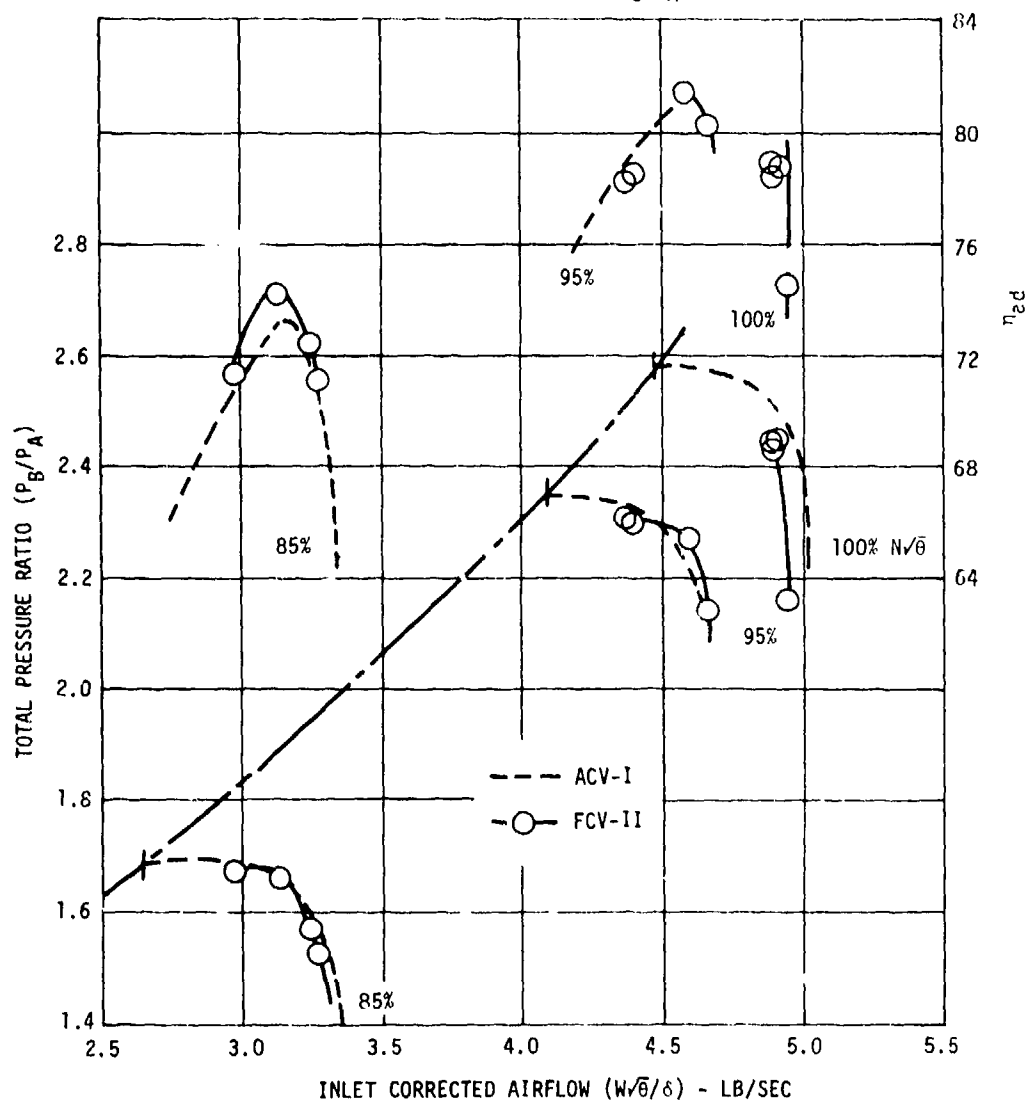
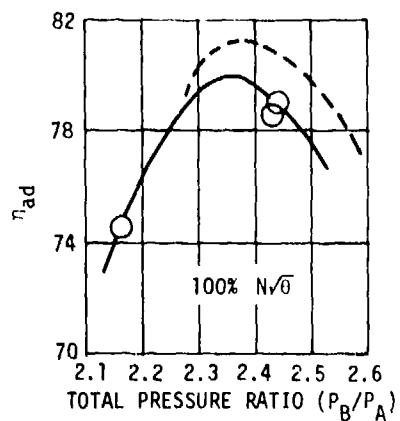


Figure 146. FCV-II Axial Compressor Results With Plane B Rakes.

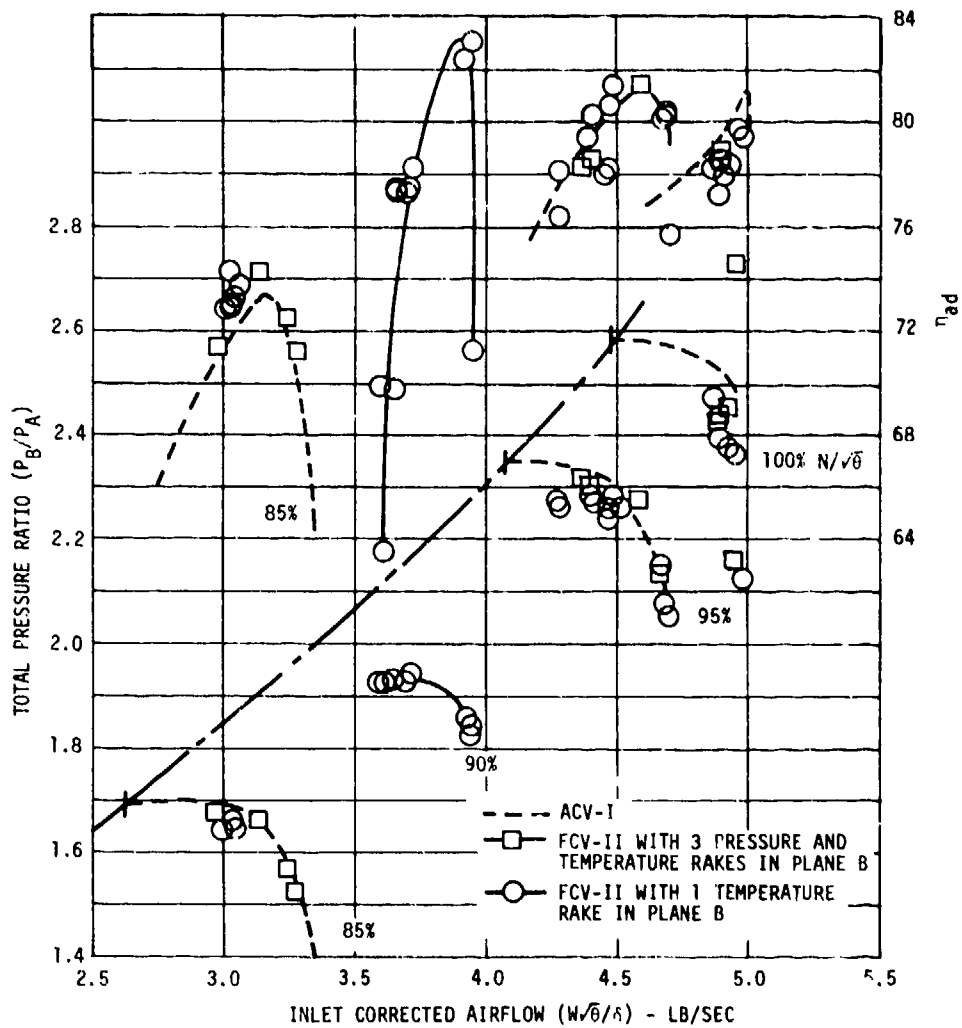
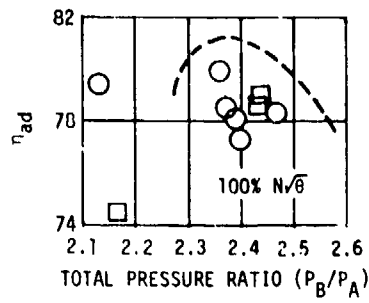


Figure 147. FCV-II Axial Compressor Data.

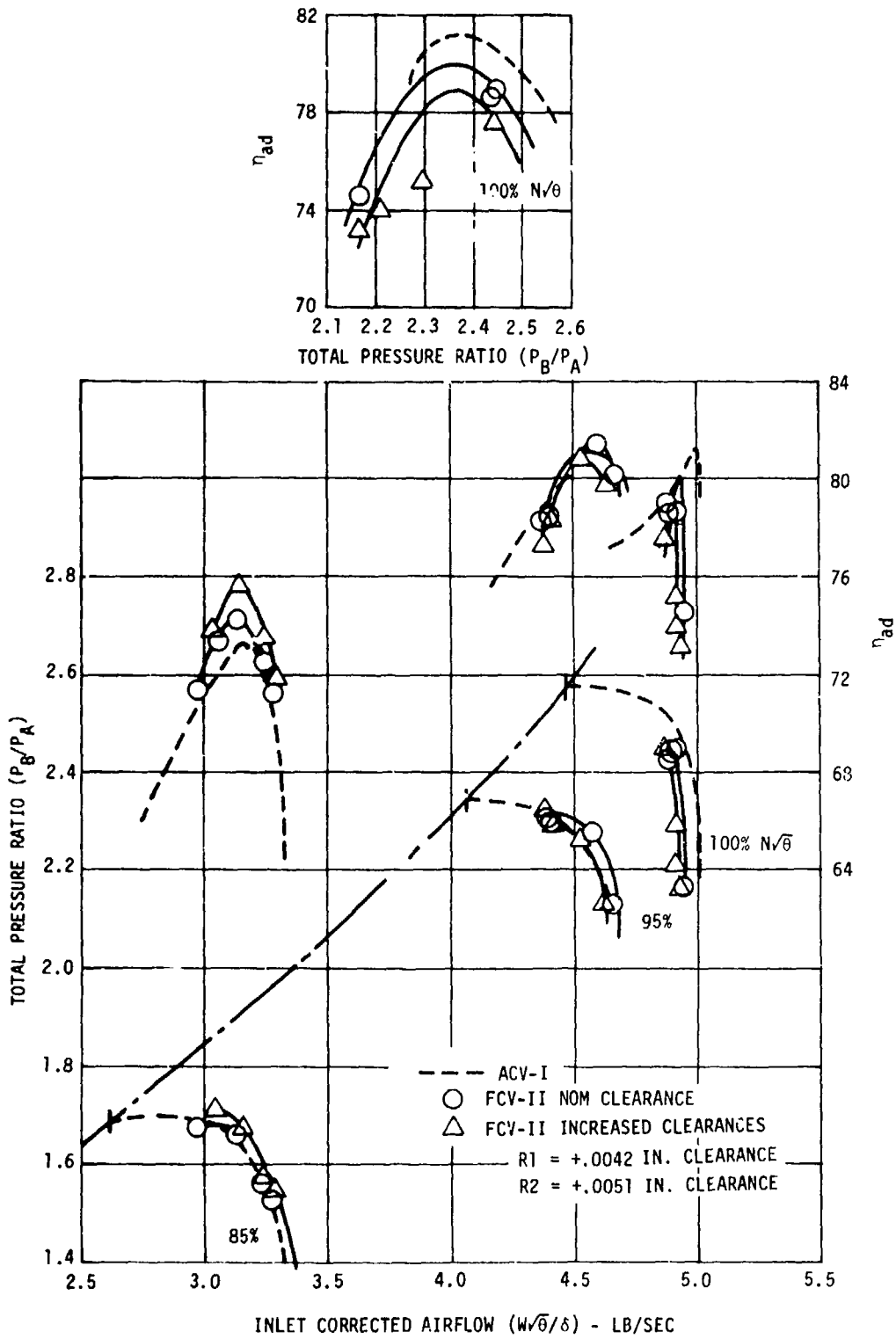


Figure 148. Effect of Increased Axial Rotor Tip Clearance.

experimental correlations on axial compressor efficiency. These test results agreed with the clearance effects presented in Reference 3.

The overall centrifugal compressor map with 3% vaneless space bleed and nominal stator schedule is shown in Figure 149. The predicted centrifugal stage map is shown in Figure 150 with the FCV-II test results where a flow reduction of 5% and a two-point loss in adiabatic efficiency were observed. Because of a lower impeller pressure ratio, the diffuser throat area was too small to pass the required flow. The diffuser static pressure distribution is shown in Figure 151 where a family of curves were plotted for various readings on the 100% corrected speed line. As expected, the results showed a normal diffuser behavior. The impeller shroud static pressure data was shown on Figure 152 along with the CCV-I component results. This lower impeller pressure rise was the cause of the lower observed centrifugal stage efficiency.

#### Plane B Traverse Data

Circumferential and radial traverse test data was obtained at the axial discharge (Plane B) during the ATACC FCV-II component test at 85%, 95%, and 100% corrected speed. At each speed a throttle setting was made near the estimated operating line of an estimated 15:1 pressure ratio turboshaft engine. The data at 85% corrected speed were gathered at ambient inlet conditions, whereas the higher speeds used reduced inlet temperatures and pressures to minimize potential blade stress problems. The data at 100% corrected speed had an inlet temperature and pressure of approximately 427°R and 12.9 psia. A set of data consisted of digitized transverse traverse results for five preset immersions of 13.4, 30, 50, 70, and 90% from the hub. A full automatic data log of all mechanical and aerodynamic parameters was recorded before and after each traverse to determine if stable conditions were maintained. These digitized traverse data were also plotted on a Calcomp plotter as part of the standard output (see Figure 153).

The stator vane settings that were on the optimized schedule tabulated below (see Figure 68):

#### DEGREES FROM DESIGN

%N c	IGV	S1	S2
100	3	5	0
95	6	7	0
85	27	21	0

3. Grieb, H., Schill, G., Gumucio, R., A SEMI-EMPIRICAL METHOD FOR THE DETERMINATION OF MULTISTAGE AXIAL COMPRESSOR EFFICIENCY, ASME 75-GT-11, March 1975.

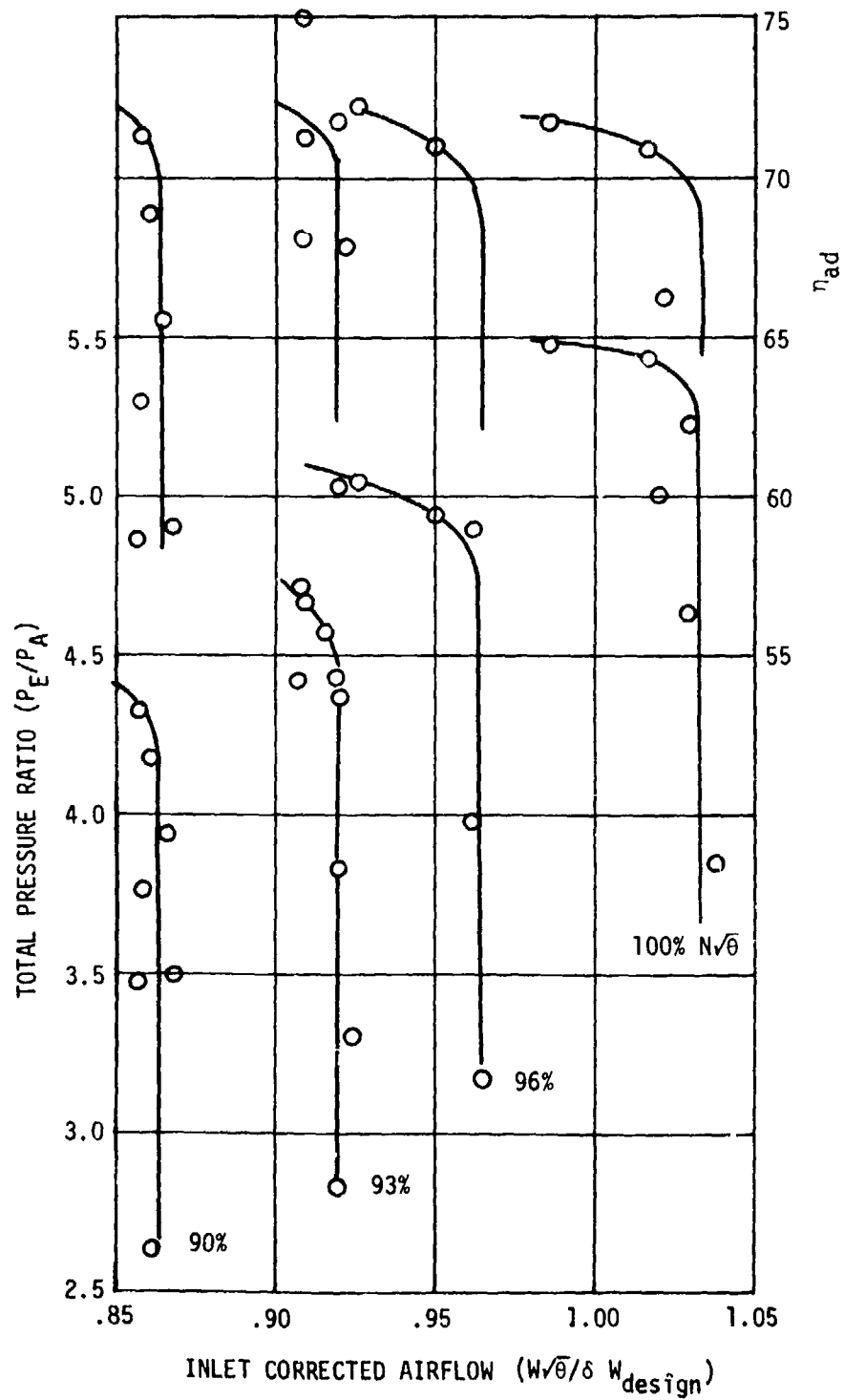


Figure 149. FCV-II Centrifugal Compressor Data.

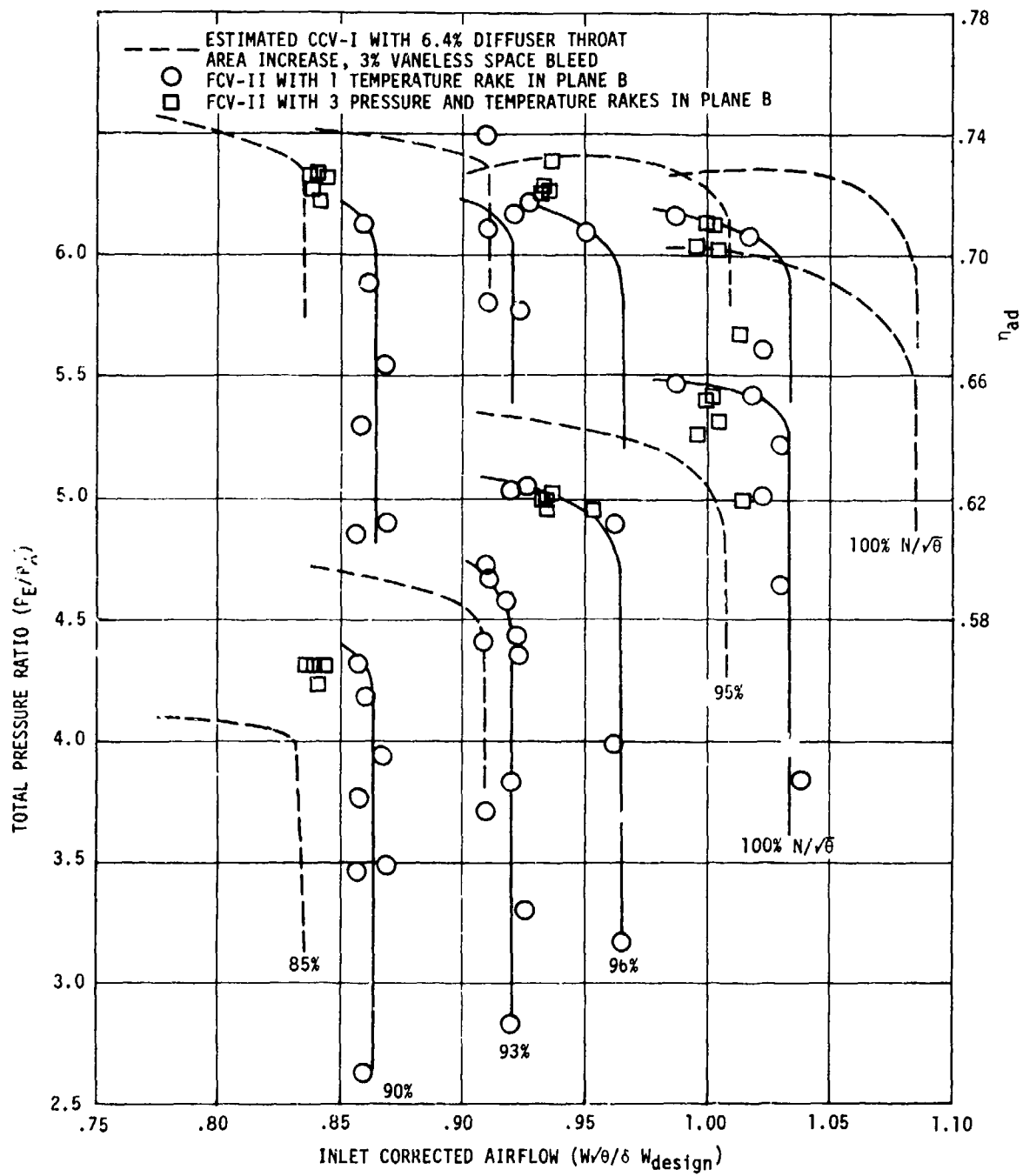


Figure 150. FCV-II Centrifugal Compressor Data With Plane B Rakes.

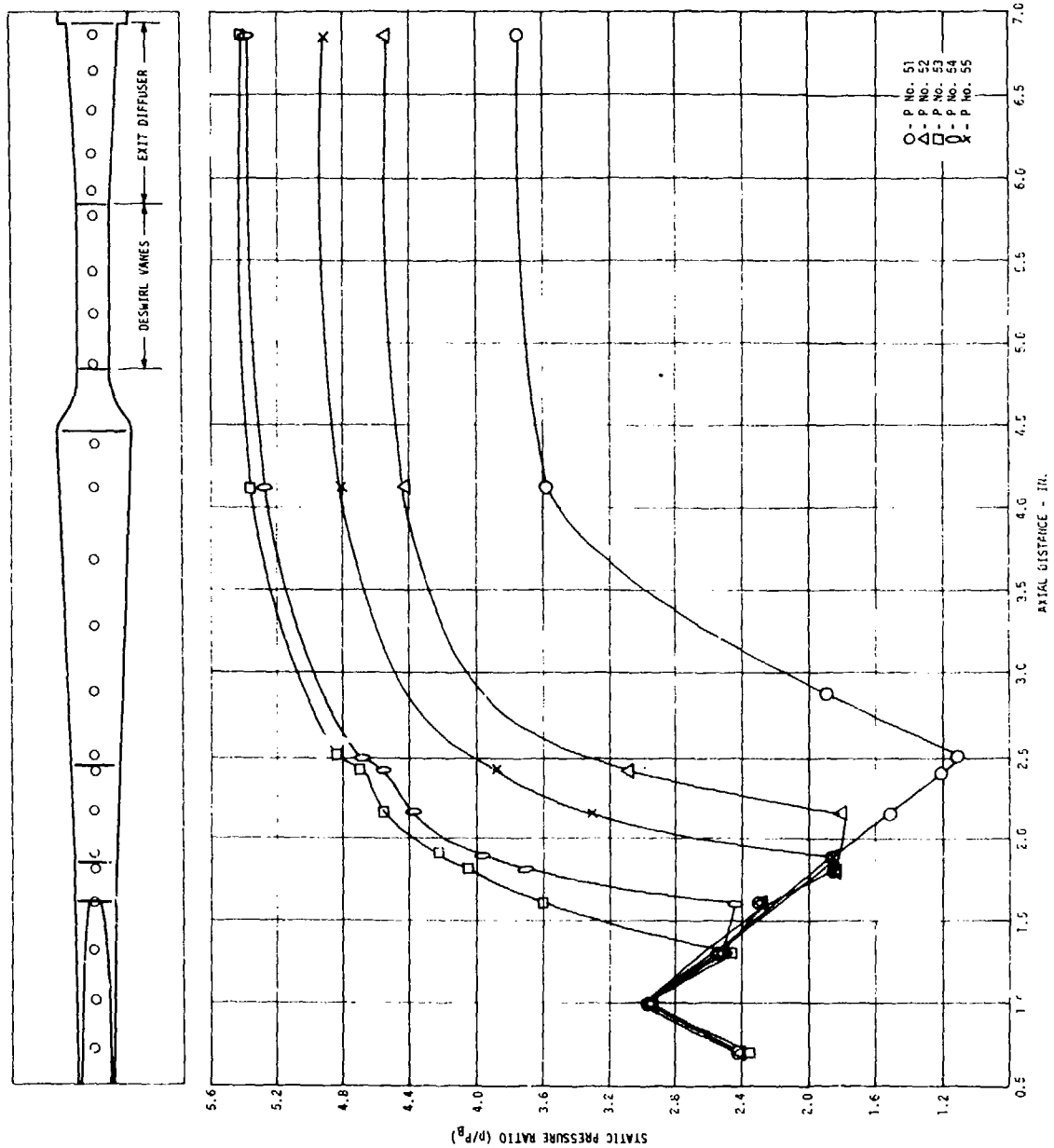


Figure 151. FCV-II Diffuser Static Pressure Rise at 100%  $N/\theta_A$  Throttle Line.

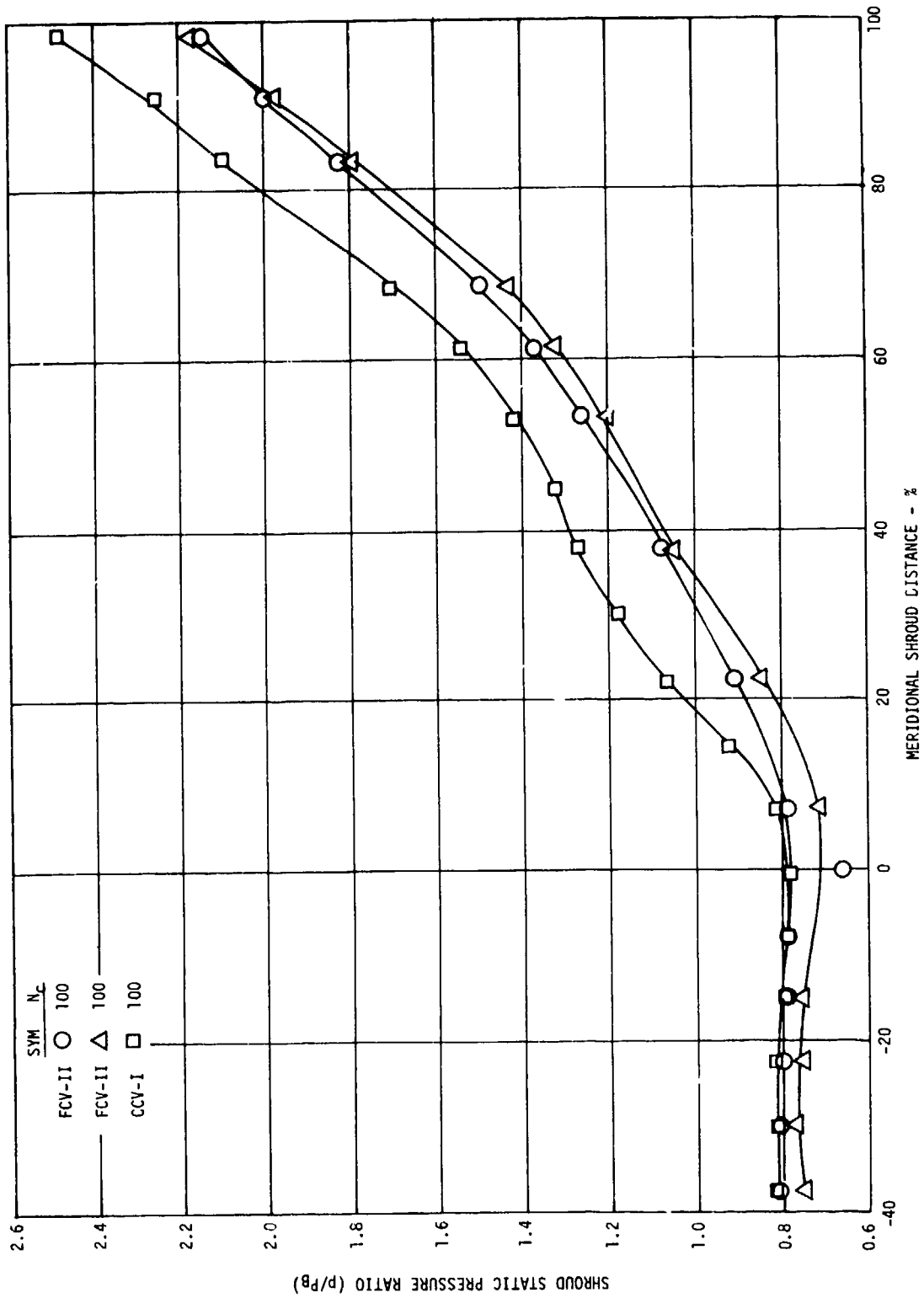


Figure 152. Impeller Static Pressure Rise for FCV-II and CCV-I.

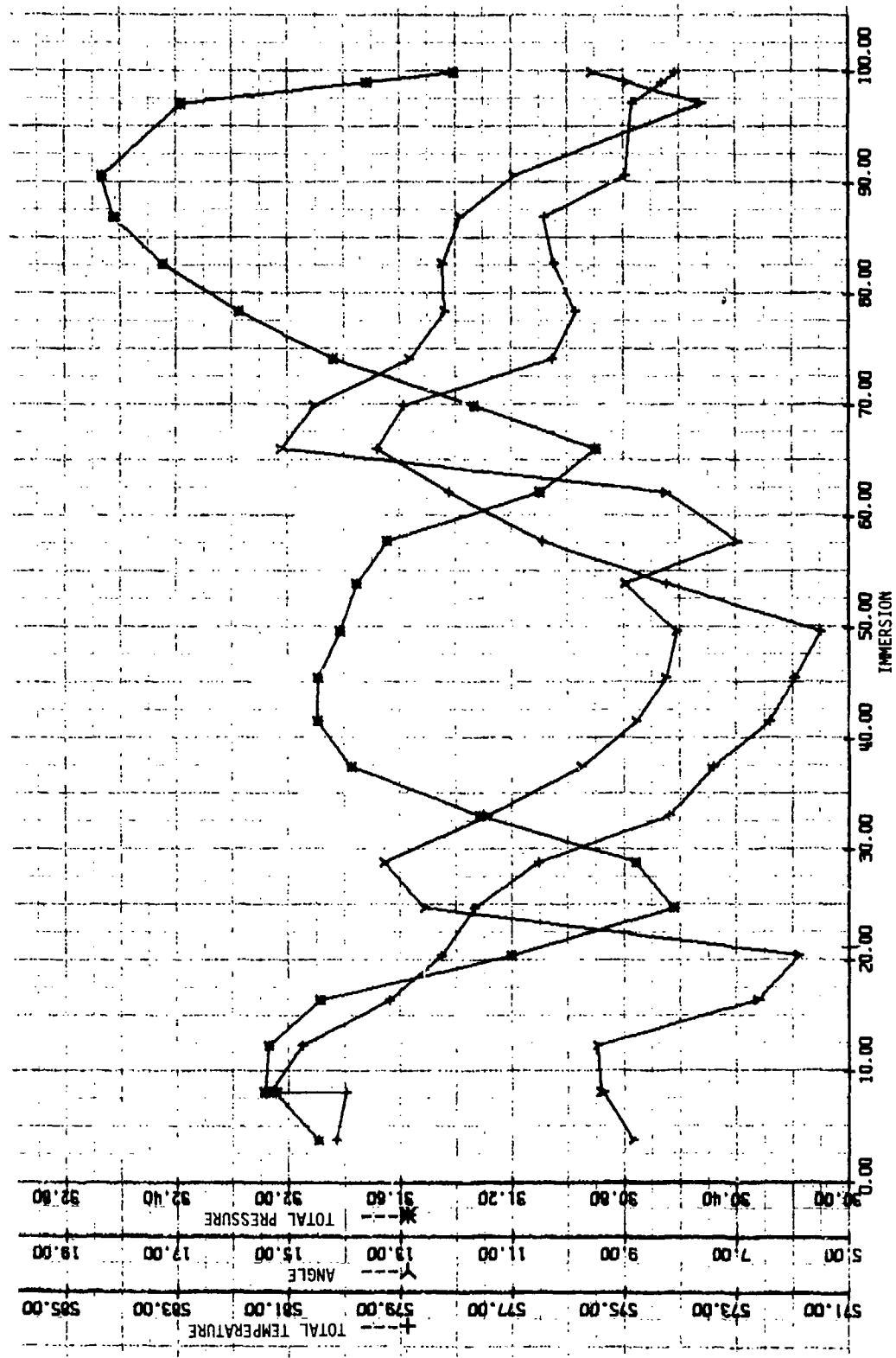


Figure 153. CALCOMP Plot of Test Data (50% Immersion).

An isobar plot of the flow field measured at the 100% speed point is shown in Figure 154 along with the mass-averaged values of total pressure for each immersion. The stator vane wakes were located at approximately 30 and 65% transverse travel. A simpler method of presenting this data is shown in Figure 155 where the mass-averaged value of total pressure ratio is plotted along with the observed maximum and minimum values.

The merits of circumferential data traverse can be seen from Figure 155 since a single radial traverse at a fixed circumferential location could observe data widely different from the average. The mass-averaged temperature ratio results are shown in Figure 156.

The measured angle data also has a large variation in the circumferential direction, as shown in Figure 157 where the mass-averaged, maximum, and minimum values are presented. The extreme angles were exaggerated because the wakes in the flow biased the nulled probe position due to the finite spacing between the Cobra probe angle sensors. The bleed slot would also distort the angle data near the casing. This bias was estimated to be in the order of 3-6 degrees. The angle data shown in Figure 157 indicated that an angle variation of 10-15 degrees was observed with the greatest variation near the hub and casing. This angle variation again emphasized the need for circumferential data since a single traverse could not obtain representative angle data.

The design data are also presented in Figures 155 through 157. The axial outlet conditions agree with the design intent on the lower two-thirds of the blade span. The test data departed from the design intent on the outermost third of the blade span where the total pressure was down and the temperature ratio was above the design. This region of high loss corresponded with the high relative Mach number regions on the rotor blades.

The total pressure traverse results for 85% and 95% corrected speed were plotted in Figure 158. The flow angle data are shown in Figures 159 and 160. The circumferential variations in pressure, temperature, and angle were similar at these part-speed settings.

The Plane B traverse data was used for a data match to arrive at the relative angle at the impeller inlet. The inlet relative air and metal blade angles for the impeller are compared in Figure 161 for the initial design and the reworked impeller for FCV-II.

For the FCV-II test, the impeller leading edge was cut back based on the ACV test results measured at the centrifugal inlet Plane C. As shown in Figure 161, the absolute air angles were considerably different between the ACV and FCV-II tests. The ACV test did not have an impeller in the flow stream, and this may have altered those measured air angles.

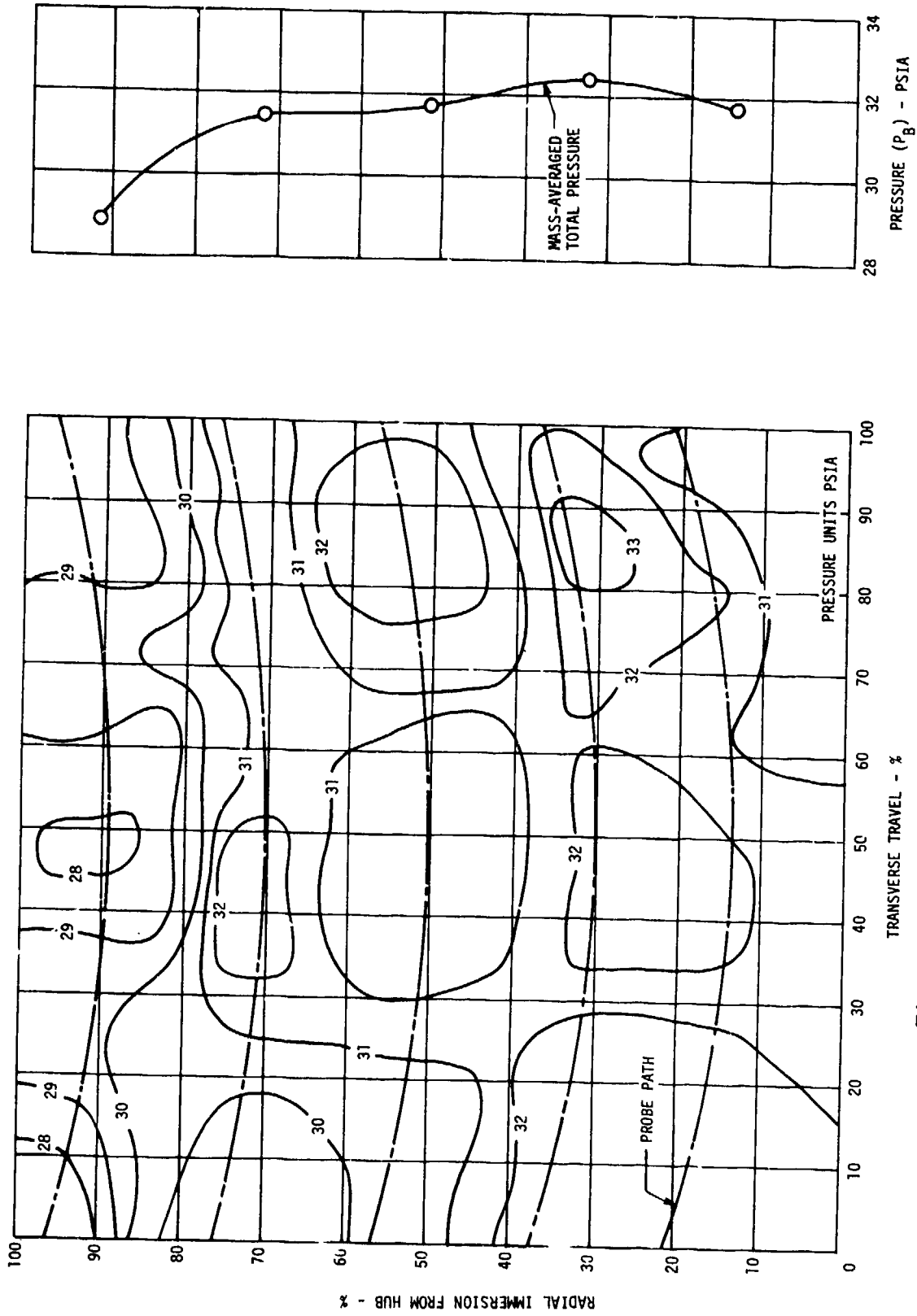


Figure 154. Plane B Traverse - Total Pressure Contours.

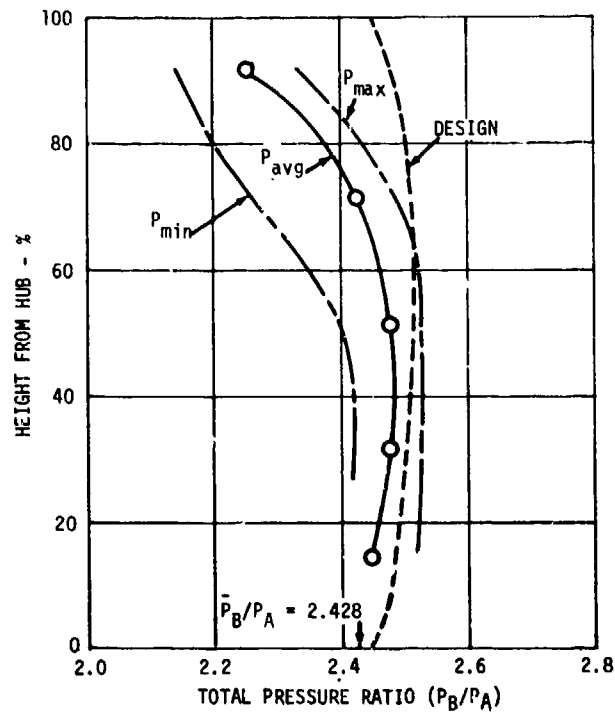


Figure 155. FCV-II Traverse Results - Axial Outlet, Plane B at 100%  $N_c$ .

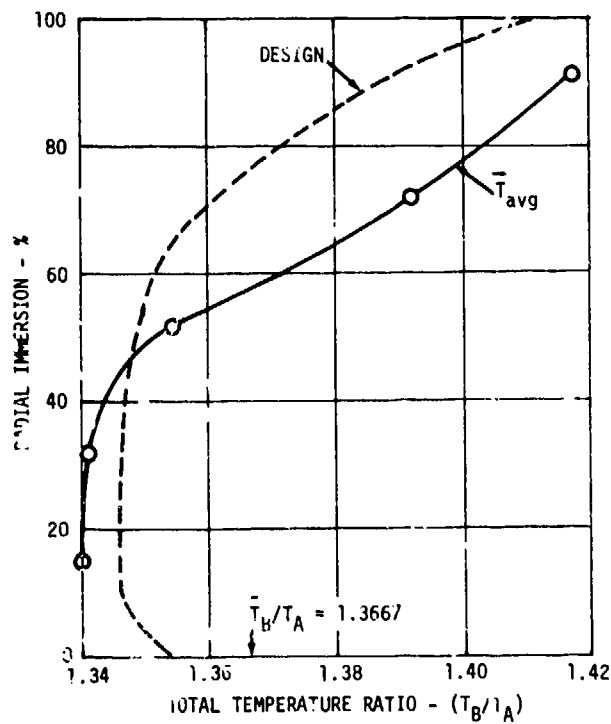


Figure 156. FCV-II Traverse Results - Axial Outlet, Plane B at 100%  $N_c$ .

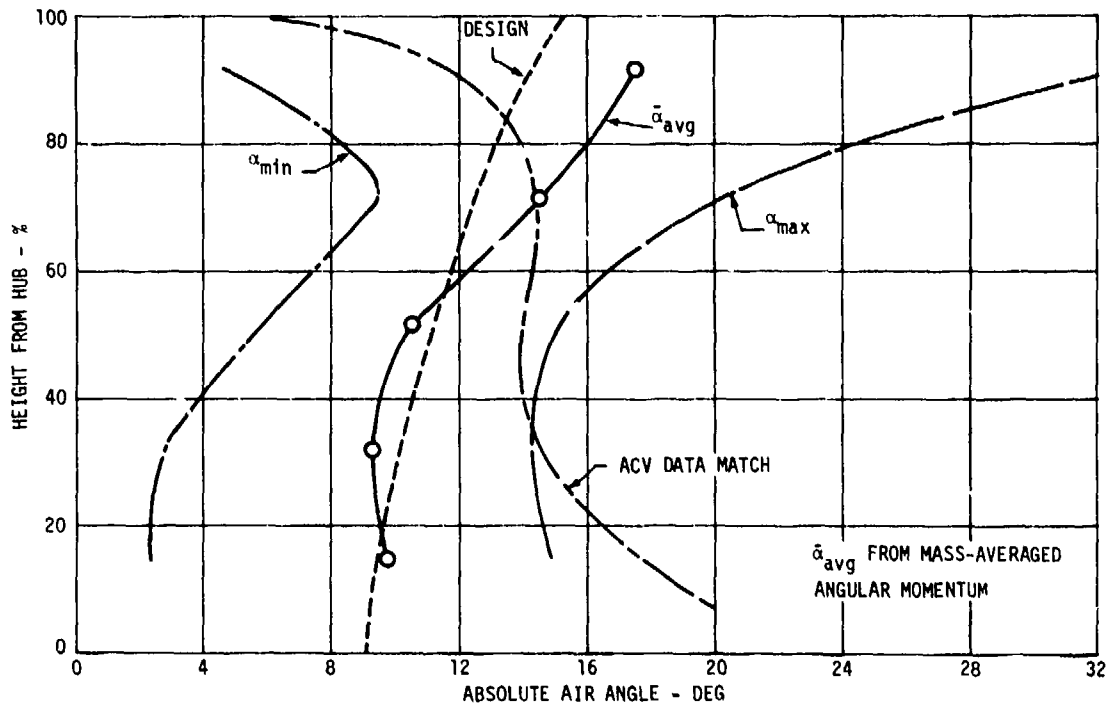


Figure 157. FCV-II Traverse Results - Axial Outlet, Plane B at 100%  $N_c$ .

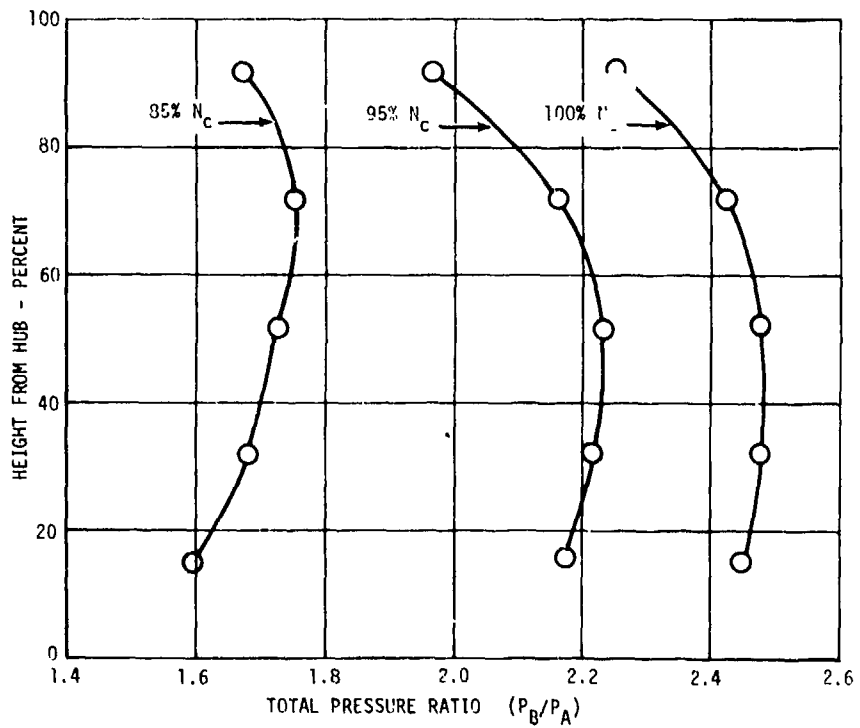


Figure 158. FCV-II Traverse Results - Axial Outlet, Plane B Pressure Ratio.

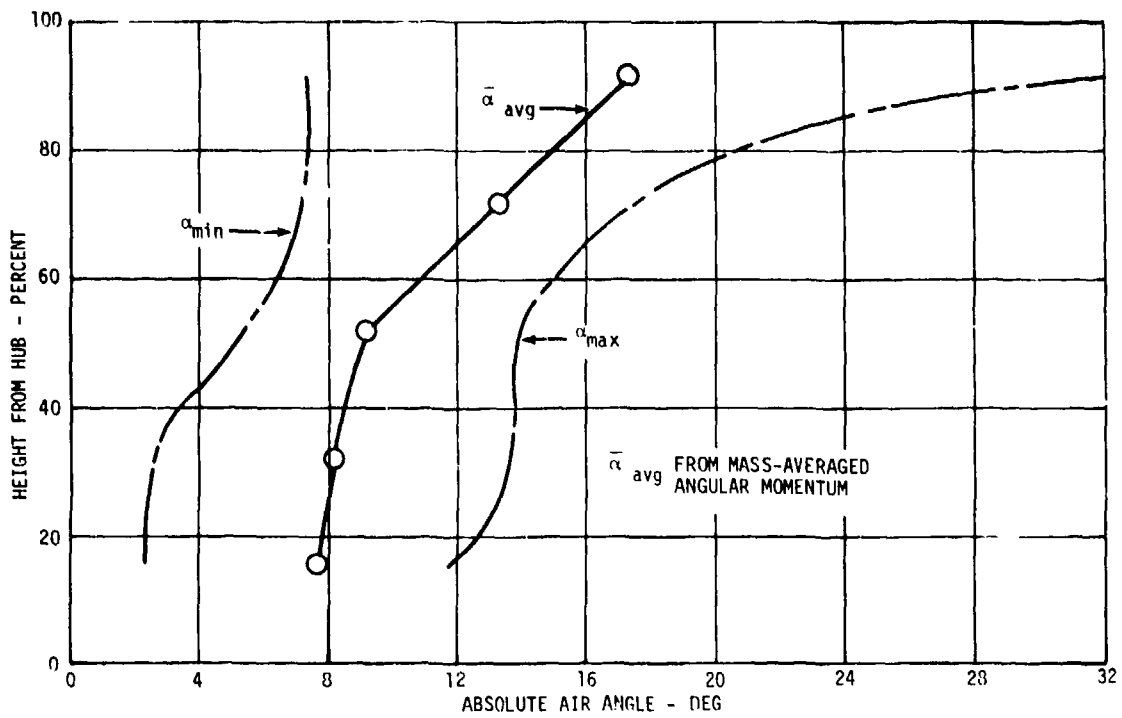


Figure 159. FCV-II Traverse Results - Axial Outlet, Plane B at 95%  $N_c$ .

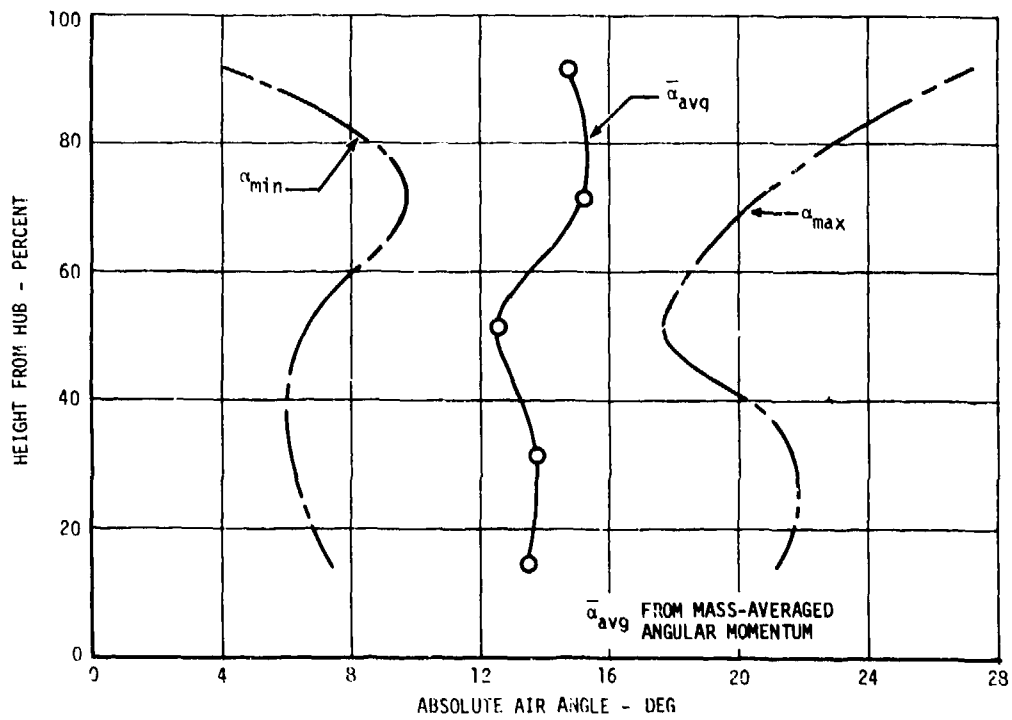


Figure 160. FCV-II Traverse Results - Axial Outlet, Plane B at 85%  $N_c$ .

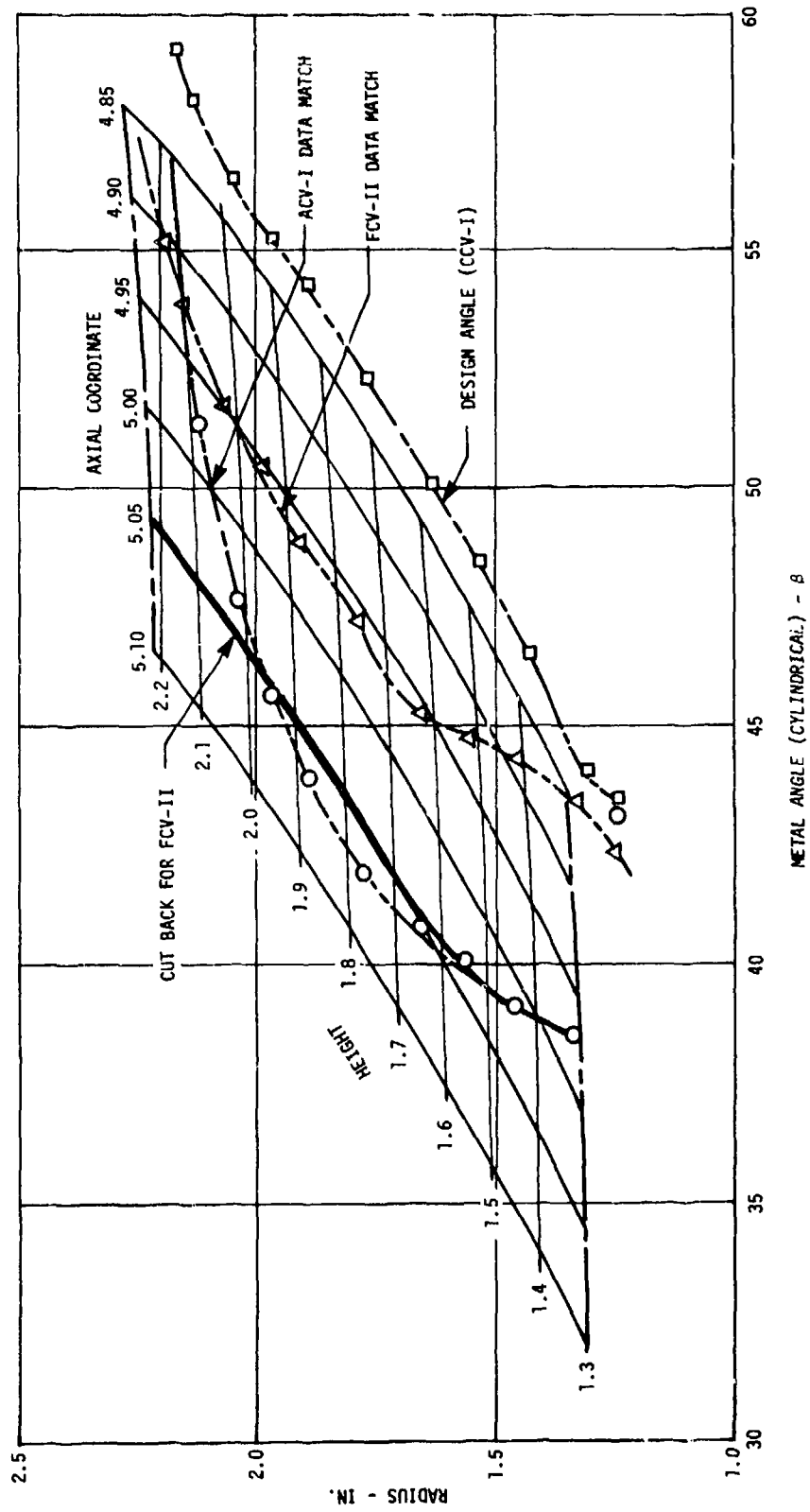


Figure 161. Impeller Metal Angles and Calculated Data Match Inlet Air Angles.

For the FCV-II traverse, the impeller was installed and appropriate downstream conditions were maintained. Also, the ACV intercompressor duct was slightly different, although this is not considered to be significant. Furthermore, the ACV data was obtained using a single radial traverse whereas the FCV data was obtained using a circumferential and radial survey. The measured angle variations observed from the circumferential traverse are shown in Figure 157 as  $\alpha_{\min}$  and  $\alpha_{\max}$  and the ACV angle data generally falls within the range of the observed FCV-II circumferential angle variation. The impeller rework as defined from the available ACV data was excessive and caused large positive leading edge incidence (see Figure 161) which resulted in a reduction of impeller efficiency for FCV-II. The data match using the FCV-II survey data substantiated the measured angles and static pressures; therefore, these data are considered to accurately define the axial outlet conditions. Future impeller designs would utilize these FCV-II traverse results to define the required impeller leading edge metal angles.

Another objective in this test was to determine if the fixed Plane B pressure and temperature rakes have any significant bias from circumferential and radial gradients. An analysis carried out in Reference 1 to evaluate profile effects indicated that six radial probe immersions were required to reduce the bias to an acceptable level. The FCV-II fixed rake and mass-averaged traverse results of efficiency and pressure ratio were plotted in Figure 162. An excellent agreement was obtained; therefore, the fixed rake data do not appear to have any significant bias error using the procedure on page 86.

The blockage ( $\lambda$ ) was calculated for each traverse point from the calculated and measured airflows.

$$\lambda = W_{\text{actual}}/W_{\text{calculate}}$$

The blockage results are tabulated below:

$\%N_c$	$\lambda$
100	.955
95	.995
85	.881

The measured blockage was essentially identical to the design level of 0.952 at 100% corrected speed. The calculated blockage at 95% corrected speed appeared high by 3-5% and this may be due to the design point variation in static pressure assumed across the passages for 95% corrected speed. This assumption will also introduce some uncertainty in the 85% corrected speed blockage.

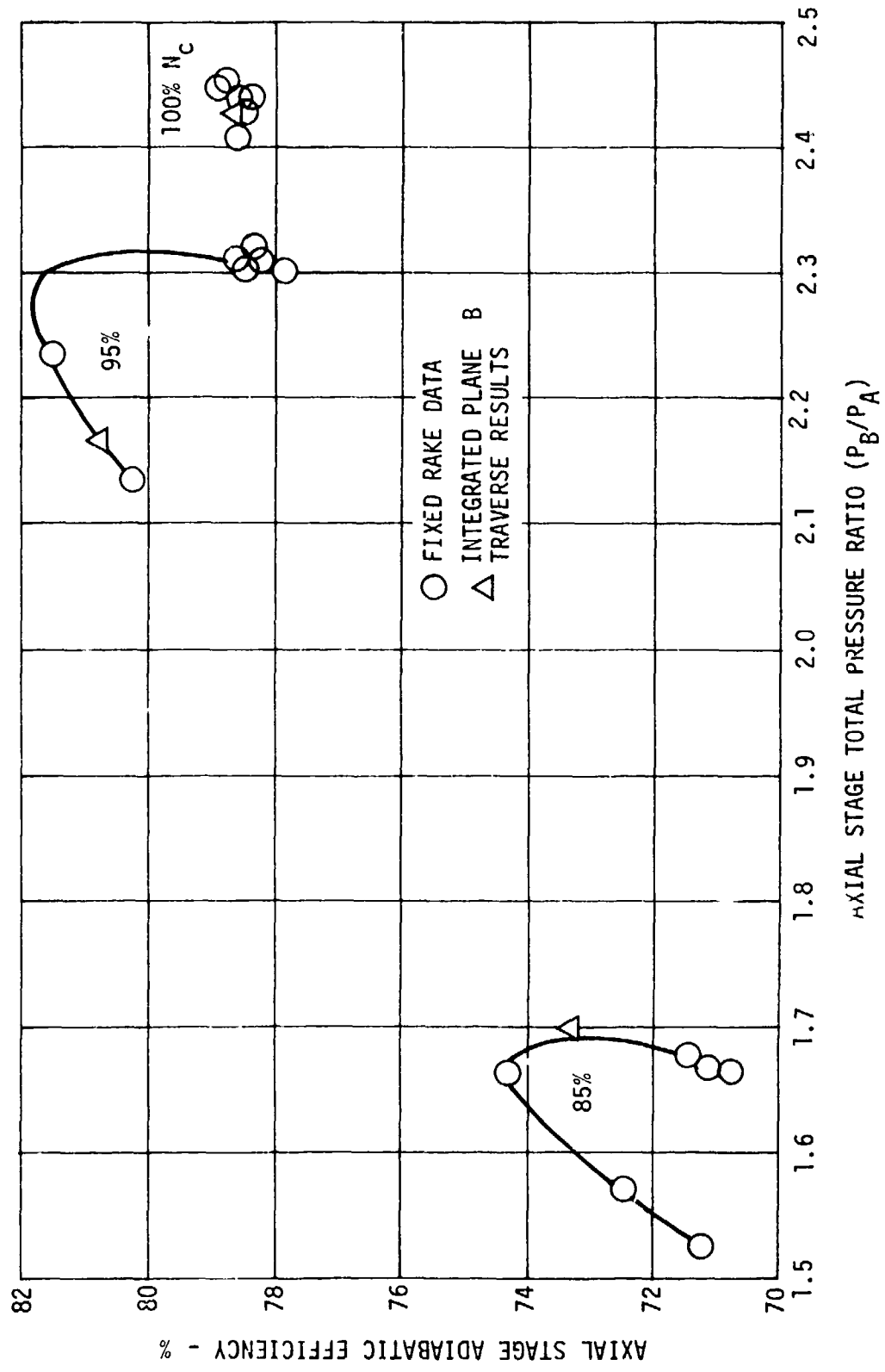


Figure 162. FCV-II Test Results - Comparison of Plane B Rake and Traverse Data.

## RELATED CENTRIFUGAL COMPRESSOR PROGRAM

### CENTRIFUGAL COMPRESSOR AERODYNAMIC DESIGN

The design procedure for centrifugal compressors consisted of a preliminary performance analysis followed by a detailed analysis of the proposed design. A flow chart of the design process is shown in Figure 163.

The preliminary design has been programmed for solution on a high speed digital computer. The program is composed of various semiempirical relationships evolved to represent the interaction of the major parameters in compressor design. The principal effects considered are losses due to viscous shear in the blade passages, losses due to blade loading in the impeller, losses due to flow leakage between the stationary shroud and the impeller vanes, losses due to shroud and backface windage, losses incurred at high relative Mach numbers at the inducer inlet and diffuser loading losses. The normal technique involved in using the program is to successively vary the dominant geometrical parameters such as impeller tip width, tip radius, and inducer hub-tip radius ratio in a systematic manner such that an acceptable envelope evolves.

The detail design analysis consists of three separate sections: an impeller design program, a vaneless diffuser program, and a diffuser program.

Once the component envelope was established in the preliminary design analysis, faired contours were determined for the impeller inner and outer annuli, impeller vane surface, and thickness distribution. This data comprised the initial input for the impeller design program.

The impeller design program solves, simultaneously, the equations of continuity, energy, and momentum for the flow field within the impeller. The equation of motion is formulated as an axisymmetrical quasi three-dimensional equation representing the flow of a compressible fluid in the presence of a force field. By numerical techniques, the principal equations are solved and the internal flow structure is established.

The normal method of using the impeller design program is to start from the flow path established in the preliminary design to obtain a definition of the internal flow structure. The velocity profiles obtained are studied for incipient separation and, where required, the physical contour of the impeller is modified to improve the velocity distribution. This process of modification is continued until an acceptable impeller evolves.

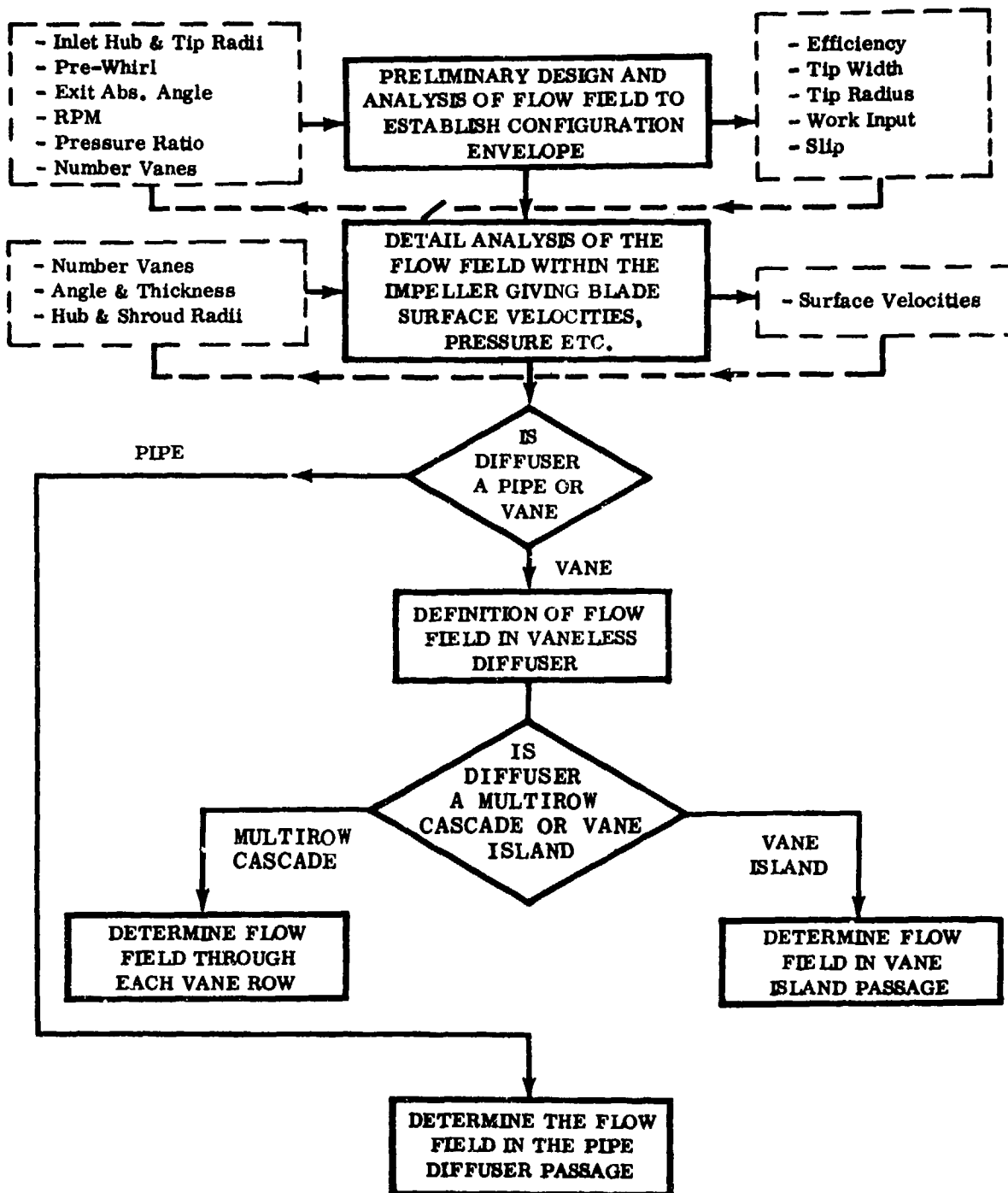


Figure 163. Flow Chart of Design Process.

The design program for the flow in the vaneless diffuser is essentially a one-dimensional method recognizing the conservation of tangential momentum in the presence of viscous shear. Once the inlet flow angle and Mach number to the vaneless diffuser are established by the impeller exit conditions, the inlet-to-exit radius ratio determines the vaneless diffuser performance. All that is required is a check of the stability of the vaneless diffuser flow. The lower limit for the radius ratio of the vaneless diffuser is normally set by the Dean-Senoo criteria, while the upper limit is set by an acceptable Mach number into the vaned diffuser.

The output from the vaneless diffuser program was the absolute flow angle, Mach number, static pressure recovery coefficient, and total pressure loss coefficient. From these data, the inlet conditions to the diffuser passages may be established.

The design of the diffuser passages is dependent on the type used. Currently, techniques are available for three types of diffusers: vane-island diffusers, pipe diffusers, and multirow cascade diffusers.

The vane-island diffuser was analyzed using a channel flow technique which was originally developed for mixed transonic-subsonic flow in stream turbine blades. The method determines the velocity and pressure distribution on the passage walls in the diffuser; once these are available the momentum and displacement thickness of the boundary layer may then be established. Knowing the condition of the boundary layer, the loss and stability of the diffuser may be evaluated.

The pipe diffuser was analyzed using a program which was developed to handle the conditions in the quasi-vaneless space peculiar to this configuration. Essentially, the program considers the flow in the pipe as that prevailing in a conical diffuser. The friction on the walls in the presence of an adverse pressure gradient from diffusion results in a Prandtl-D'Arcy type flow at the exit of the pipe. This exit flow distribution has been used to establish loss and blockage relationships for pipe diffusers.

The normal input required for the program was the number of pipes, the impeller width, the inlet cone angle, the secondary cone angle, and the exit radius. From these data the overall performance is established.

The program for establishing the design and performance of cascade diffuser relates the vane configuration to the diffusion factor for the vane row. Imbedded in the program are cascade data similar to that presented in NASA SP36 which relate blade incidence and deviation at minimum loss to camber, stagger, solidity and thickness-chord ratio. By an iterative procedure, blade settings are determined which satisfy a required level of diffusion parameter. Losses in the diffuser are considered to arise from three sources: profile losses due principally to

the diffusion process on a two-dimensional profile, annulus losses due to the drag on the annulus walls, and secondary losses due to the vorticity induced in deflecting a developed profile. This loss breakdown correlates well with observed performance. The cascade program was used a stage at a time to establish the flow field in a multirow vaned diffuser.

#### CCV-II COMPRESSOR DESIGN

The design of this compressor configuration was directed at a new impeller for operation with the CCV-I pipe diffuser. The same diffuser was used, since the CCV-I test data did not clearly identify a problem with the diffuser. The higher impeller tip-to-diffuser throat losses could be due to the lower CCV-I impeller efficiency and not inherent in the diffuser design. This design had a longer inducer section and a more gradual turning distribution. The inducer inlet hub radius was increased to reduce the hub curvature in the transition duct from the axial stage. This raised the inducer tip Mach number from 0.88 to 0.94, but it was still considered to be an acceptable design level. The various flow paths for the CCV-I, II, and III designs are shown in Figure 164. The principal design details for the CCV-I impeller are repeated in Table 18 (see Reference 1) and the CCV-II design details are presented in Table 19. The number of full and splitter blades were lowered to 23 each, versus 28 each for the CCV-I impeller design.

The calculated blade velocity diagram is presented in Figure 165 along the shroud for the CCV-I, II, and III impeller designs.

#### CCV-III COMPRESSOR DESIGN

This impeller design was directed at an increased loading in overall rotor diffusion so the blade camberline was extended to limit excessive diffusion rates. The flow path, shown in Figure 164, has even less hub curvature in the transition duct and a longer axial chord length than previous designs. The blade velocity diagram along the shroud is shown in Figure 165. The principal design details are shown in Table 20. There were 20 full blades and 20 splitter blades in this design.

This impeller had a wider tip of 0.27 inch versus previous design of 0.21 inch. A new pipe diffuser was designed using the nominal throat area but it reduced the number of passages from 33 to 19 to preserve the geometry in the quasi-vaneless space. A deswirler vane system was not used in this test configuration because of added cost and complexity, so the outlet Mach number was nominally 0.21 at the design point.

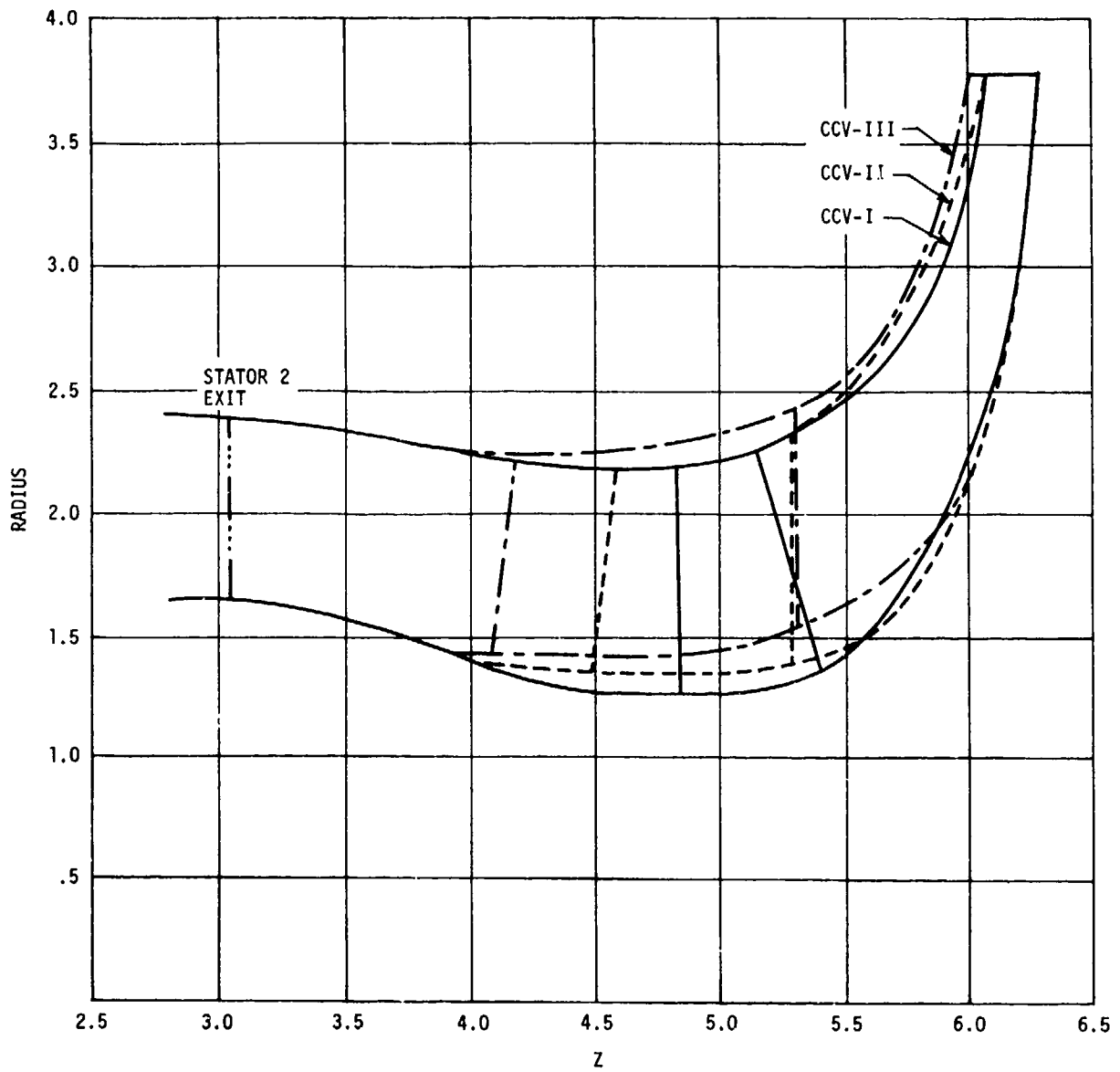


Figure 164. CCV-I, CCV-II, and CCV-III Impeller Flow Paths.

TABLE 18. CCV-I IMPELLER PRINCIPAL DESIGN DETAILS

Inducer Inlet Conditions	Hub	Mean	Shroud
Radius - in.	1.250	1.7708	2.1688
$M_1$ Absolute	0.445	0.493	0.470
$\beta_1$ Absolute - deg	13.706	13.826	15.950
$V_1$ Tangential - ft/sec	134.40	149.09	165.99
$V_1$ Axial - ft/sec	551.10	605.78	580.80
$W_1$ - ft/sec	760.54	991.14	1138.81
$M_1'$ Relative	0.597	0.783	0.878
$W_1$ Tangential - ft/sec	524.13	783.82	976.59
$\beta_1'$ Relative - deg	43.563	52.30	59.259
$U_1$ - ft/sec	658.53	932.90	1142.58
Impeller Tip Exit Conditions			
Radius - in.	3.780		
$U_{tip}$ - ft/sec	1992.2		
$M_2$ Absolute	1.265		
$V_2$ Radial - ft/sec	603.91		
$V_2$ Tangential - ft/sec	1821.1		
$V_2$ Absolute - ft/sec	1918.6		
$W_2$ - ft/sec	627.7		
$M_2'$ Relative	0.414		
$W_2$ Tangential - ft/sec	171.1		
$\beta_2$ Absolute - deg	71.65		
$\beta_2'$ Relative - deg	15.82		
Tip Width - in.	0.21		

TABLE 19. CCV-II IMPELLER PRINCIPAL DESIGN DETAILS

Inducer Inlet Conditions	Hub	Mean	Shroud
Radius - in.	1.3387	1.80965	2.1674
$M_1$ Absolute	0.462	0.552	0.572
$\beta_1$ Absolute - deg	12.339	12.215	13.089
$V_1$ Tangential - ft/sec	125.50	145.88	166.10
$V_1$ Axial - ft/sec	573.69	673.90	714.41
$W_1$ - ft/sec	815.63	1055.24	1209.58
$M_1'$ Relative	0.641	0.838	0.942
$W_1$ Tangential - ft/sec	579.77	807.49	975.74
$\beta_1'$ Relative - deg	45.302	50.153	53.790
$U_1$ - ft/sec	705.26	953.37	1141.84
Impeller Tip Exit Conditions			
Radius - in.	3.78		
$U_{tip}$ - ft/sec	1992.2		
$M_2$ Absolute	1.265		
$V_2$ Radial - ft/sec	603.91		
$V_2$ Tangential - ft/sec	1821.1		
$V_2$ Absolute - ft/sec	1918.6		
$W_2$ - ft/sec	627.7		
$M_2'$ Relative	0.414		
$W_2$ Tangential - ft/sec	171.1		
$\beta_2$ Absolute - deg	71.65		
$\beta_2'$ Relative - deg	15.82		
Tip Width - in.	0.21		

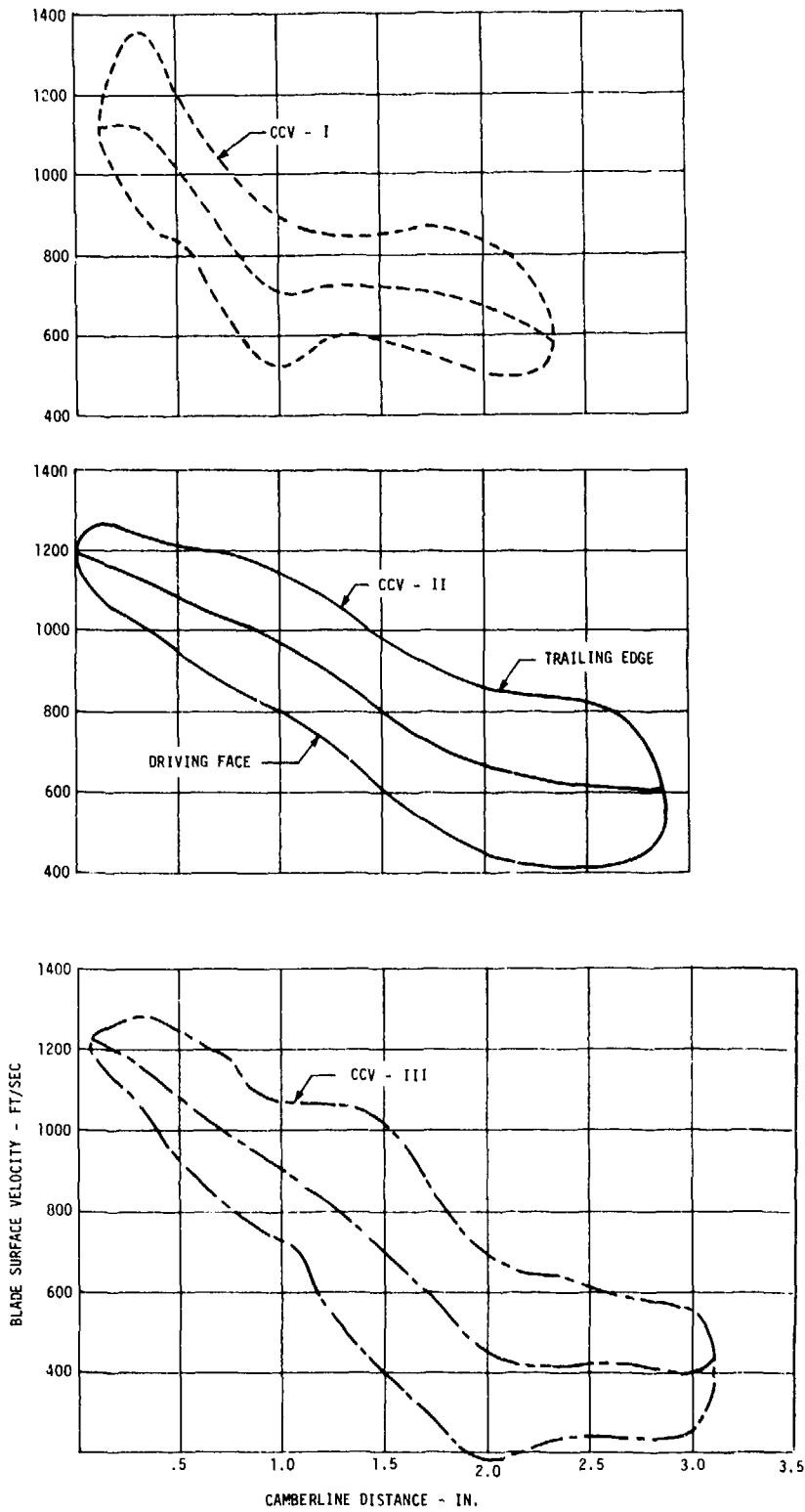


Figure 165. Blade Velocity Diagrams Along the Shrouds.

TABLE 20. CCV-III IMPELLER PRINCIPAL DESIGN DETAILS

Inducer Inlet Conditions	Hub	Mean	Shroud
Radius - in.	1.4181	1.87745	2.235
$M_1$ Absolute	0.468	0.528	0.534
$\beta_1$ Absolute - deg	11.491	12.191	13.537
$V_1$ Tangential - ft/sec	118.47	140.62	161.07
$V_1$ Axial - ft/sec	582.75	650.85	669.03
$\dot{W}_1$ - ft/sec	857.17	1069.85	1216.81
$M_1'$ Relative	0.674	0.848	0.945
$W_1$ Tangential - ft/sec	628.62	848.47	1016.38
$\beta_1'$ Relative - deg	47.168	52.509	56.645
$U_1$ - ft/sec	747.09	989.09	1177.45
Impeller Tip Exit Conditions			
Radius - in.	3.78		
$U_{tip}$ - ft/sec	1991.4		
$M_2$ Absolute	1.228		
$V_2$ Radial - ft/sec	472.6		
$V_2$ Tangential - ft/sec	1812.2		
$V_2$ Absolute - ft/sec	1872.8		
$W_2$ - ft/sec	505.4		
$M_2'$ Relative	0.294		
$W_2$ Tangential - ft/sec	179.02		
$\beta_2$ Absolute - deg	75.38		
$\beta_2'$ Relative - deg	20.77		
Tip Width - in.	0.27		

#### CCV-IV COMPRESSOR DESIGN

This impeller was designed using the outlet conditions from the axial compressor as determined on the FCV-II component test. This impeller has a nearly constant diameter hub and shroud flow path in the transition duct to permit a close-coupled, shorter rotor (see Figure 166). The inducer tip relative Mach number of 0.94 was considered within acceptable limits for this design. The principal design details are presented in Table 21. The blade loading along the shroud was similar to the CCV-II impeller except that the inducer elements were nonradial in order to reduce the blade loading along the hub stream surface. This impeller was designed using the axial compressor flow determination program, and equivalent blade velocity diagrams were not generated for comparison with previous impeller designs. Instead, the static pressure diffusion rates were used for comparison. A comparison of the hub streamtube static pressure coefficient ( $\Delta p/q_1$ ) was plotted in Figure 167 for the CCV-I through CCV-IV impeller designs. This lower static pressure coefficient was achieved for CCV-IV by use of nonradial blades between the hub and tip sections because similar shroud loading was maintained while lowering the hub loading. In effect, the hub section had a more gradual turning rate when compared with radial blade element designs. This impeller had 20 full blades and 20 splitter blades.

The mechanical design of the impeller was similar to the process described in Reference 1. The stress summary is shown in Figure 168 for the mechanical design speed of 63,420 rpm.

A smooth silver-plated impeller shroud was used for this test in place of the previous metal-sprayed nickel-graphite shroud coatings.

The diffuser design incorporated a 7% larger tangency circle than the CCV-I design reported in Reference 1. This design also had the 6.4% larger throat area that was part of the FCV-II rework of the CCV-I diffuser design. The diffuser exit geometry was similar because the existing deswirl vane row was used for this test configuration, but this did not compromise the performance of the pipe diffuser-deswirl system.

#### CCV-V COMPRESSOR DESIGN

This test configuration utilized the CCV-IV impeller and shroud with the FCV-II pipe diffuser. In effect, the primary difference between CCV-IV and V was the passage tangency circle for the pipe diffuser. The same deswirl and rotor assemblies were used, and all alignments and running clearances were repeated. Only a partial teardown of the CCV-IV test vehicle was required for this diffuser change.

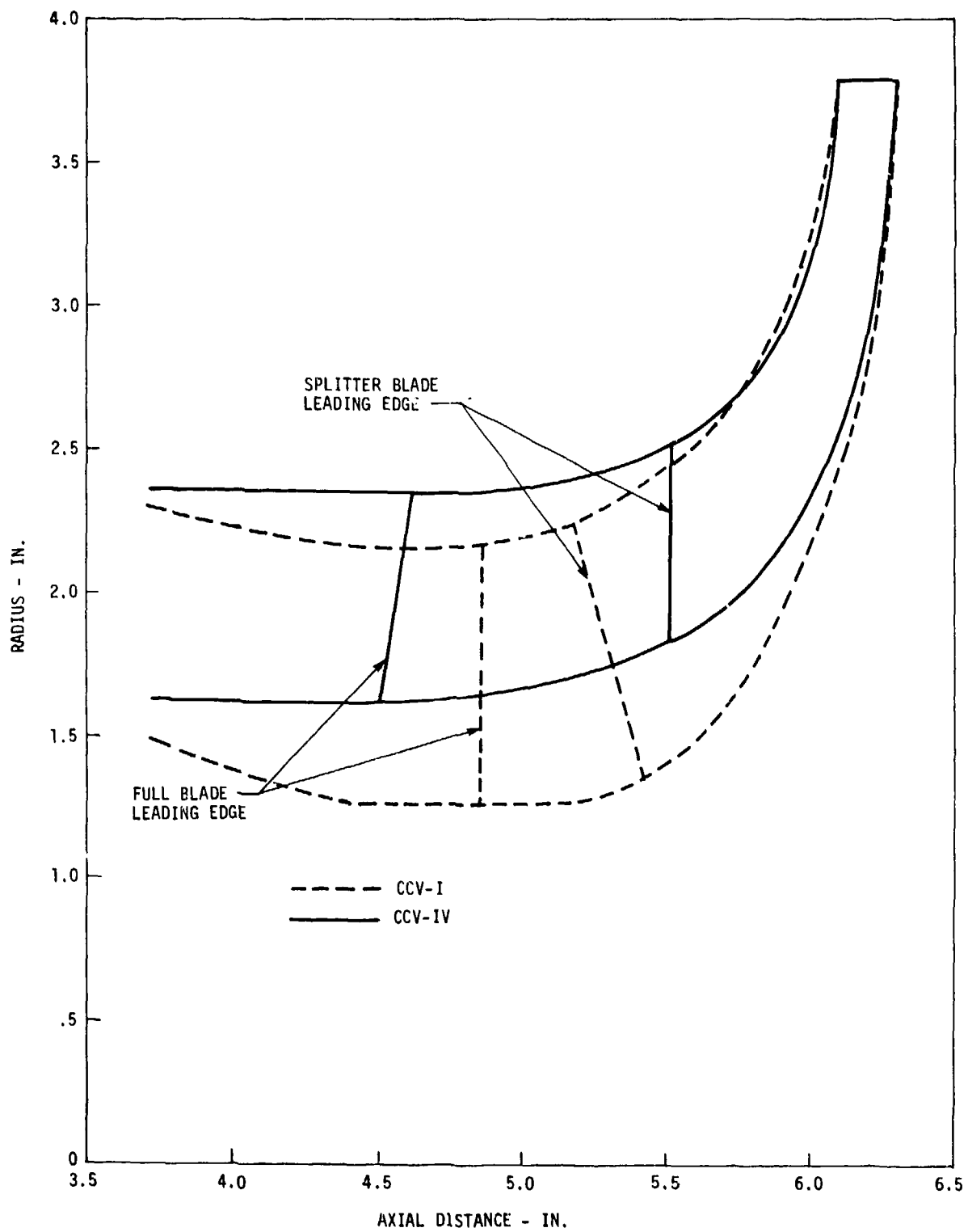


Figure 166. CCV-I and CCV-IV Impeller Flow Paths.

TABLE 21. CCV-IV IMPELLER PRINCIPAL DESIGN DETAILS

Inducer Inlet Conditions	Hub	Mean	Shroud
Radius - in.	1.631	2.009	2.355
$M_1$ Absolute	0.531	0.620	0.463
$\beta_1$ Absolute - deg	10.08	9.86	15.35
$V_1$ Tangential - ft/sec	116.2	132.5	159.1
$V_1$ Axial - ft/sec	653.9	761.7	579.7
$W_1$ - ft/sec	987.5	1196.2	1223.3
$M_1'$ Relative	0.789	0.959	0.943
$W_1$ Tangential - ft/sec	740.0	922.1	1077.1
$\beta_1'$ Relative - deg	48.54	50.45	61.71
$U_1$ - ft/sec	856.2	1054.6	1236.2
Impeller Tip Exit Conditions			
Radius - in.	3.78		
$U_{tip}$ - ft/sec	1984.2		
$M_2$ Absolute	1.249		
$V_2$ Radial - ft/sec	602.7		
$V_2$ Tangential - ft/sec	1791.3		
$V_2$ Absolute - ft/sec	1890.0		
$W_2$ - ft/sec	632.9		
$M_2'$ Relative	0.418		
$W_2$ Tangential - ft/sec	192.9		
$\beta_2$ Absolute - deg	71.40		
$\beta_2'$ Relative - deg	17.75		
Tip width - in.	0.21		

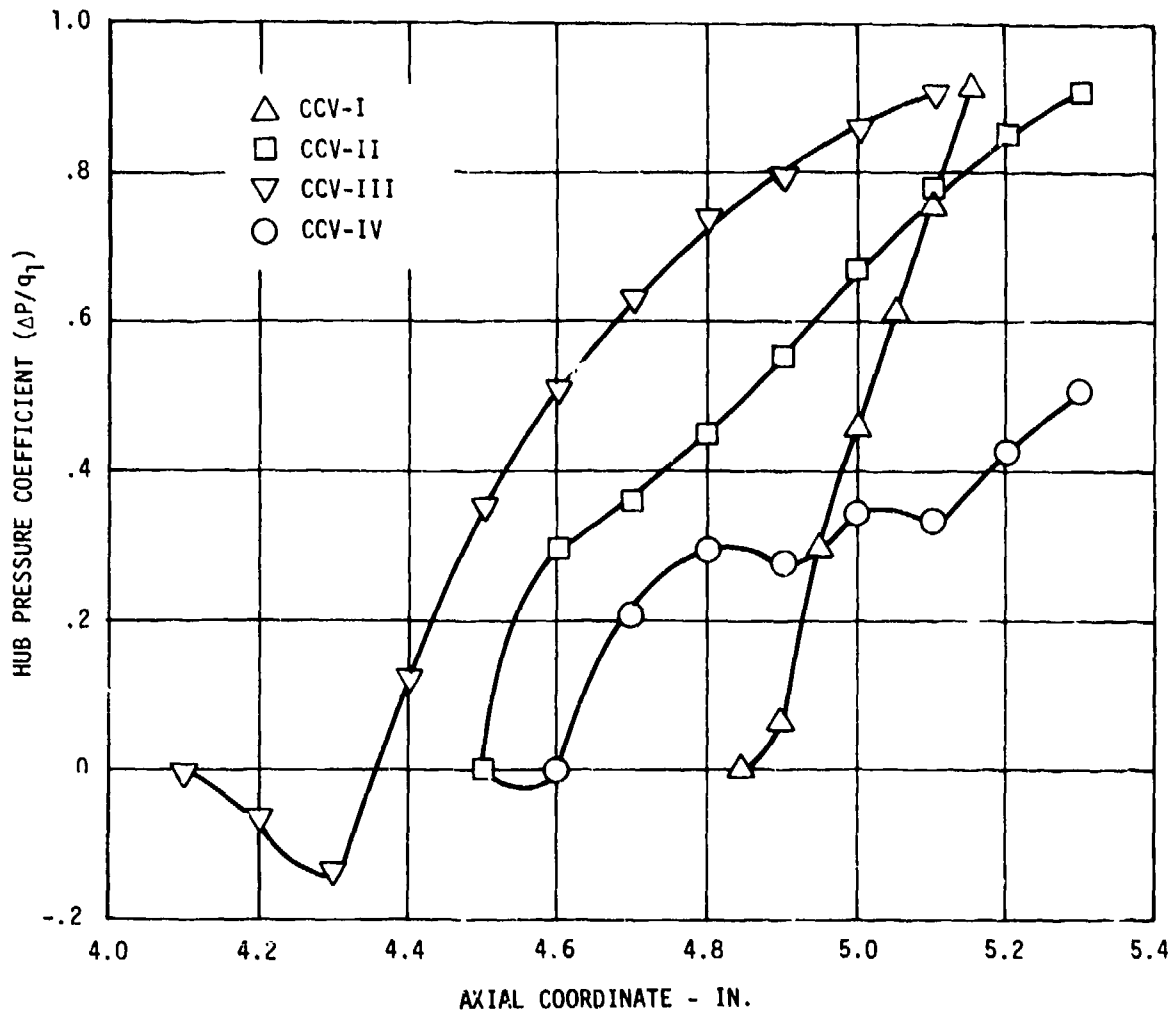


Figure 167. Hub Static Pressure Coefficient.

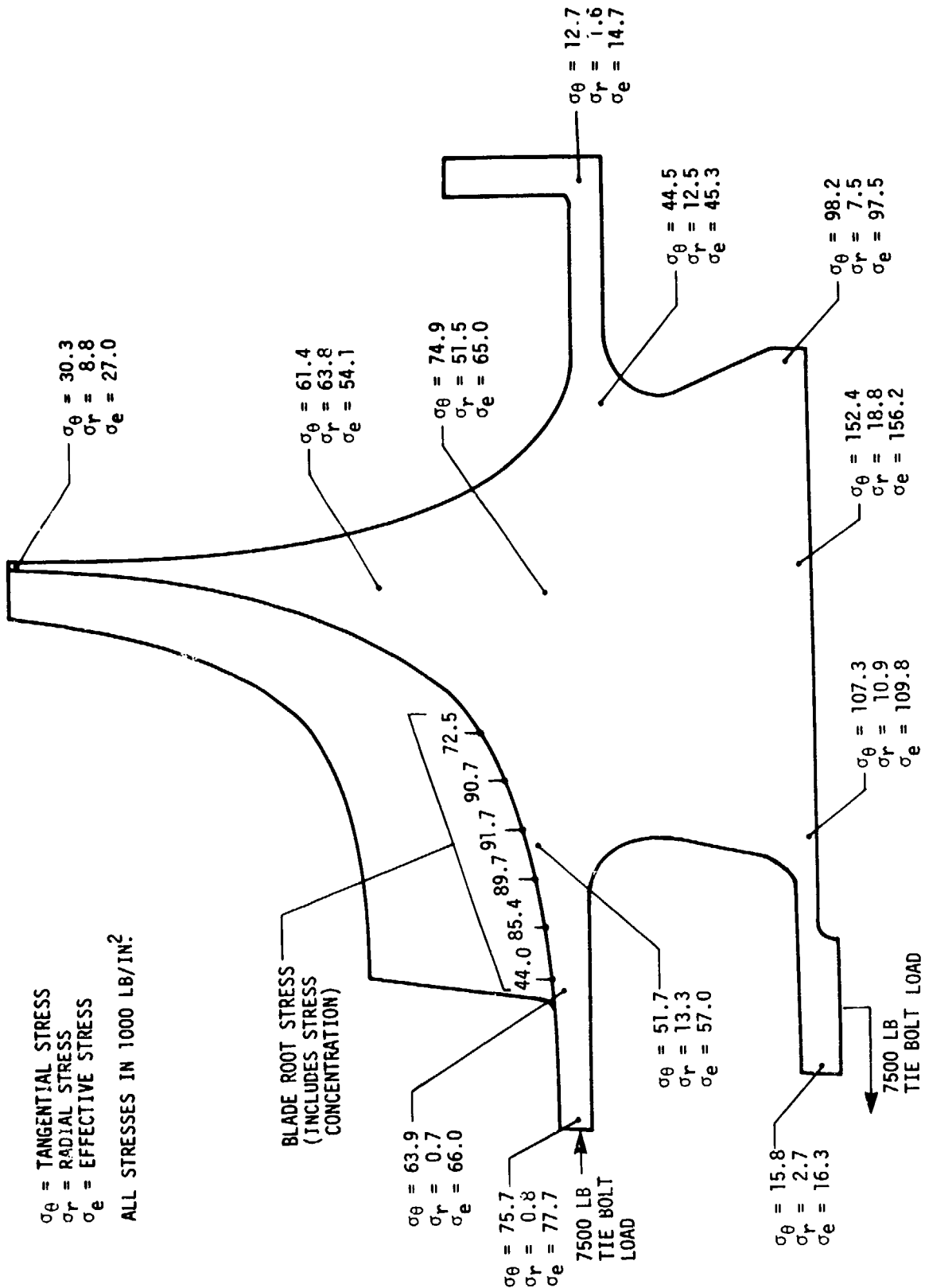


Figure 168. CCV-IV Impeller Disk and Blade Stresses.

## Test Results

The CCV-II and III test results did not indicate any improvement over the levels demonstrated in the CCV-I test. Some nickel-graphite shroud coating material was lost during the testing. This coating loss resulted in increased rotor clearances in the inducer region for CCV-II and in the tip region for CCV-III. Corrections were made to the test data to reflect the coating loss; however, the corrected performance levels were not sufficiently different from the CCV-I tests to warrant further testing of these redesigned impellers.

The CCV-IV test evaluated a new impeller and diffuser design at various levels of vaneless space bleed. Similar testing was carried out during the CCV-V component test. The results for the CCV-IV and CCV-V tests are shown in Figure 169 for the nominal IGV setting and design vaneless space bleed (3%). The CCV-V results indicate that the smaller tangency diameter pipe diffuser had better overall compressor performance. The CCV-V test results are compared with the FCV-II centrifugal stage data in Figure 170 and with the CCV-I test data in Figure 171. These CCV-5 test results indicated a substantial improvement in efficiency over prior data albeit it was still below the objective efficiency. Objective choke flow and stall flow were achieved in the CCV-5 test. The design point pressure ratio was 5.9:1 versus the objective of 6.0:1 (see Figure 169). The broad efficiency and flow range characteristics of the CCV-5 data made it very attractive for matching with the axial compressor stage.

The performance for the CCV-IV impeller is shown in Figure 172 where 87.2% efficiency at 7.04:1 total pressure ratio was demonstrated at the design point versus an objective of 88.4 at 6.85:1 total pressure ratio. The slip factor for this impeller was also lower than the CCV-1 impeller as evidenced in Figure 173. This reduction in slip factor was much greater than what would be expected from the reduced number of impeller blades used in the CCV-IV impeller. The smooth impeller shroud contributed to this lower impeller work input observed in CCV-IV. The shroud static pressure rise at design speed and airflow is shown in Figure 174 for the CCV-IV impeller.

The effect of vaneless space bleed on the overall performance of the CCV-V test configuration is shown in Figures 175 and 176 at 95 and 90% corrected speed, respectively. The diffuser losses were reduced with increasing quantities of vaneless space bleed. The CCV-V test results are shown in Figure 177 for the range of bleed flows tested at 90%, 95%, and 100% corrected speed. The diffuser outlet Mach number is plotted in Figure 178 for the nominal bleed and IGV settings.

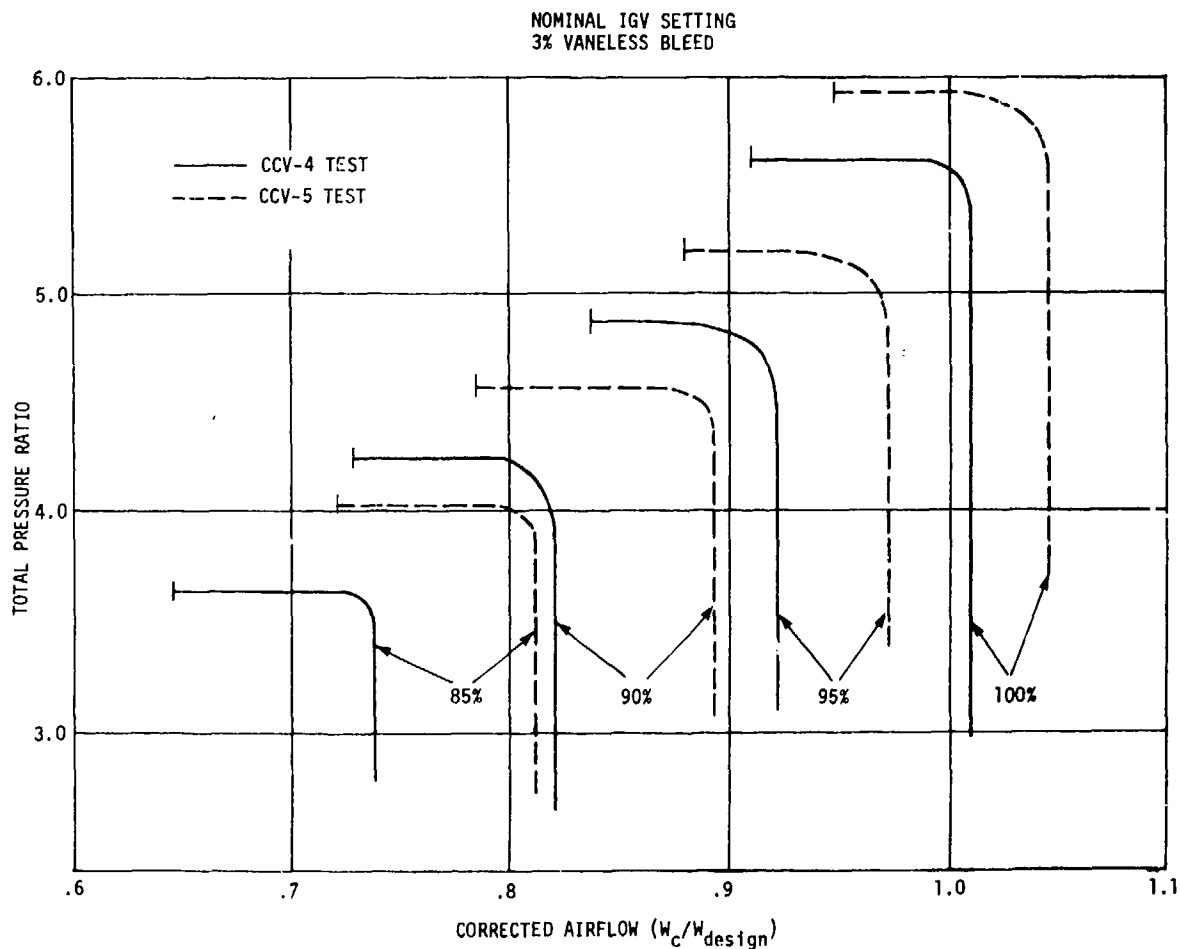
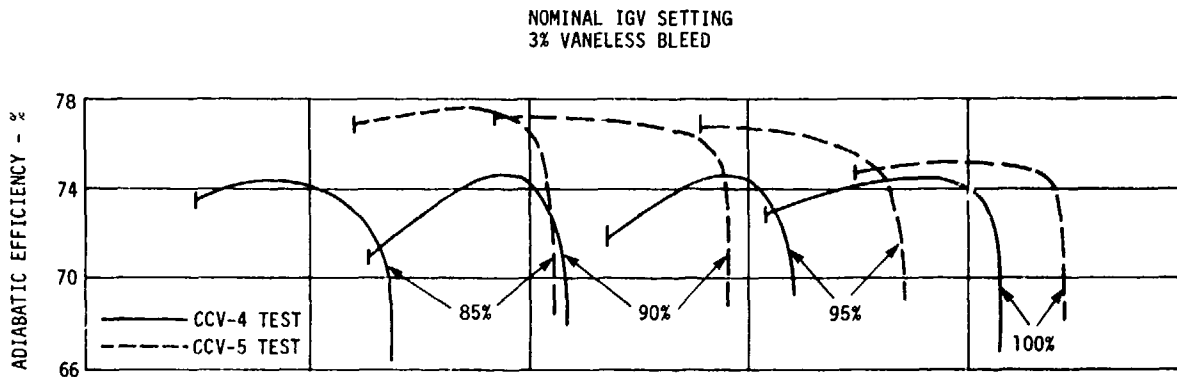


Figure 169. CCV-IV and CCV-V Test Results.

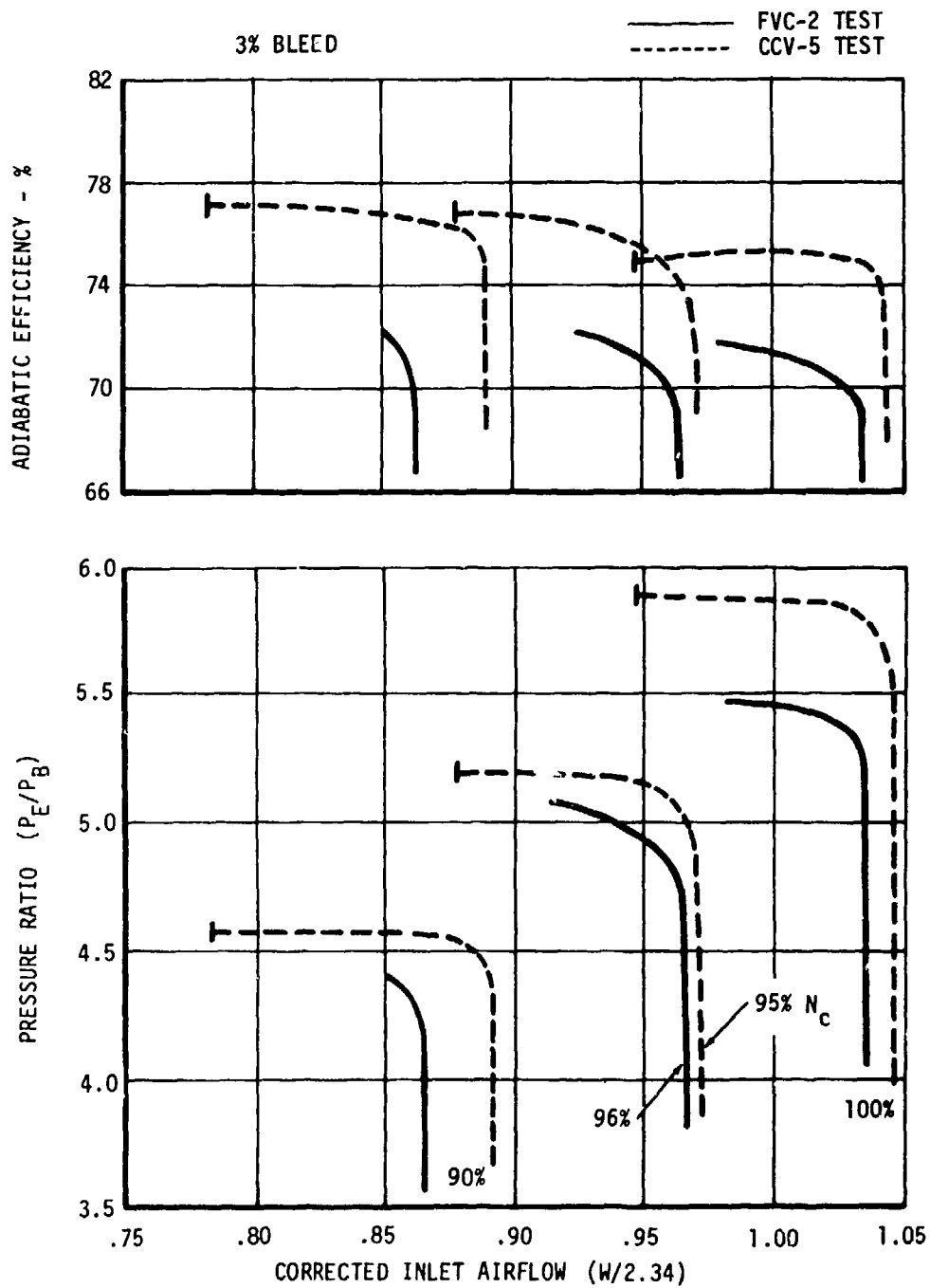


Figure 170. CCV-V and FCV-II Centrifugal Stage Performance.

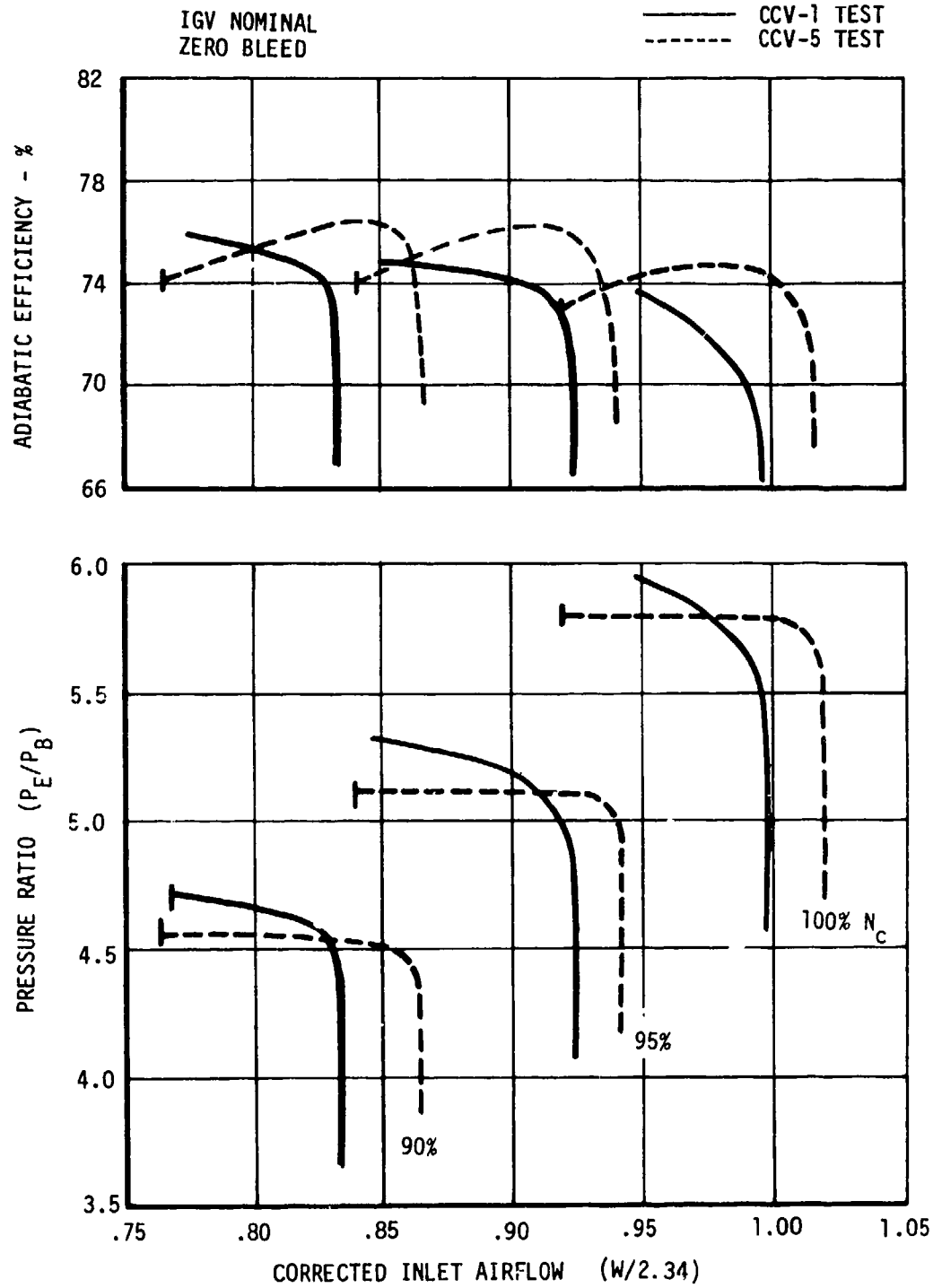


Figure 171. Centrifugal Stage Performance.

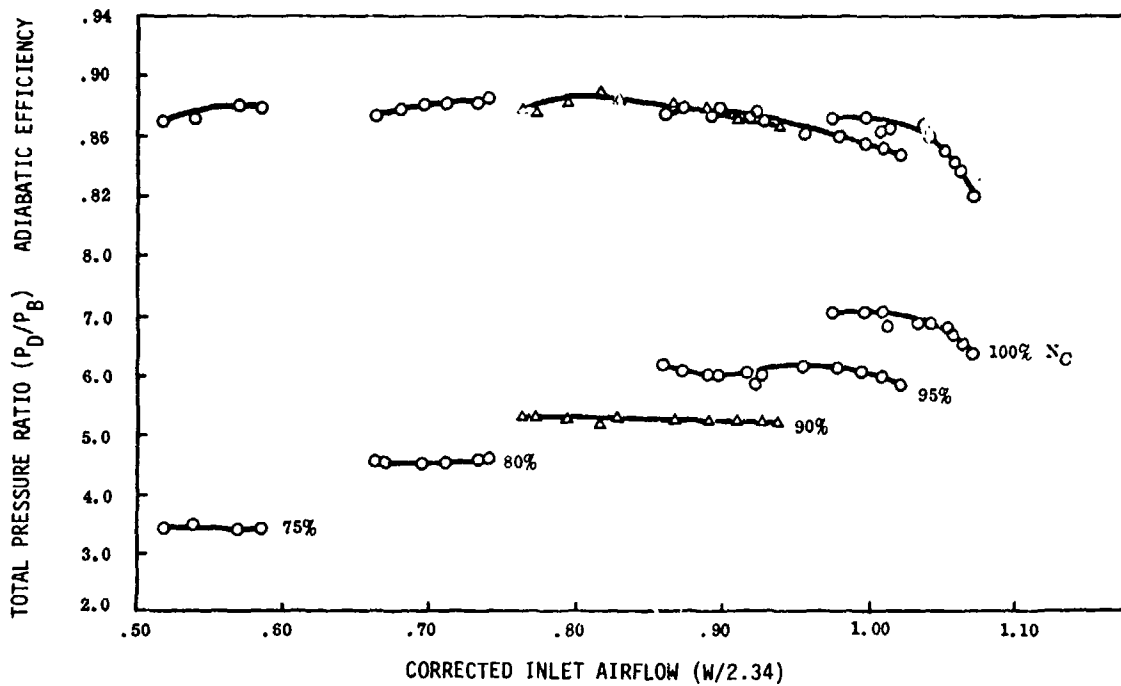


Figure 172. CCV-IV Impeller Performance.

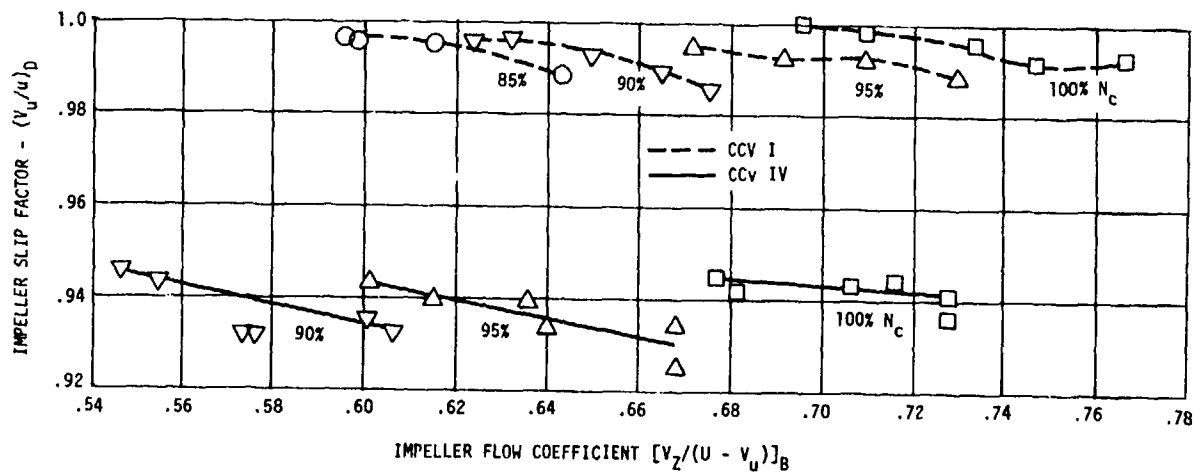


Figure 173. Slip Factor for CCV-I and CCV-IV Impellers.

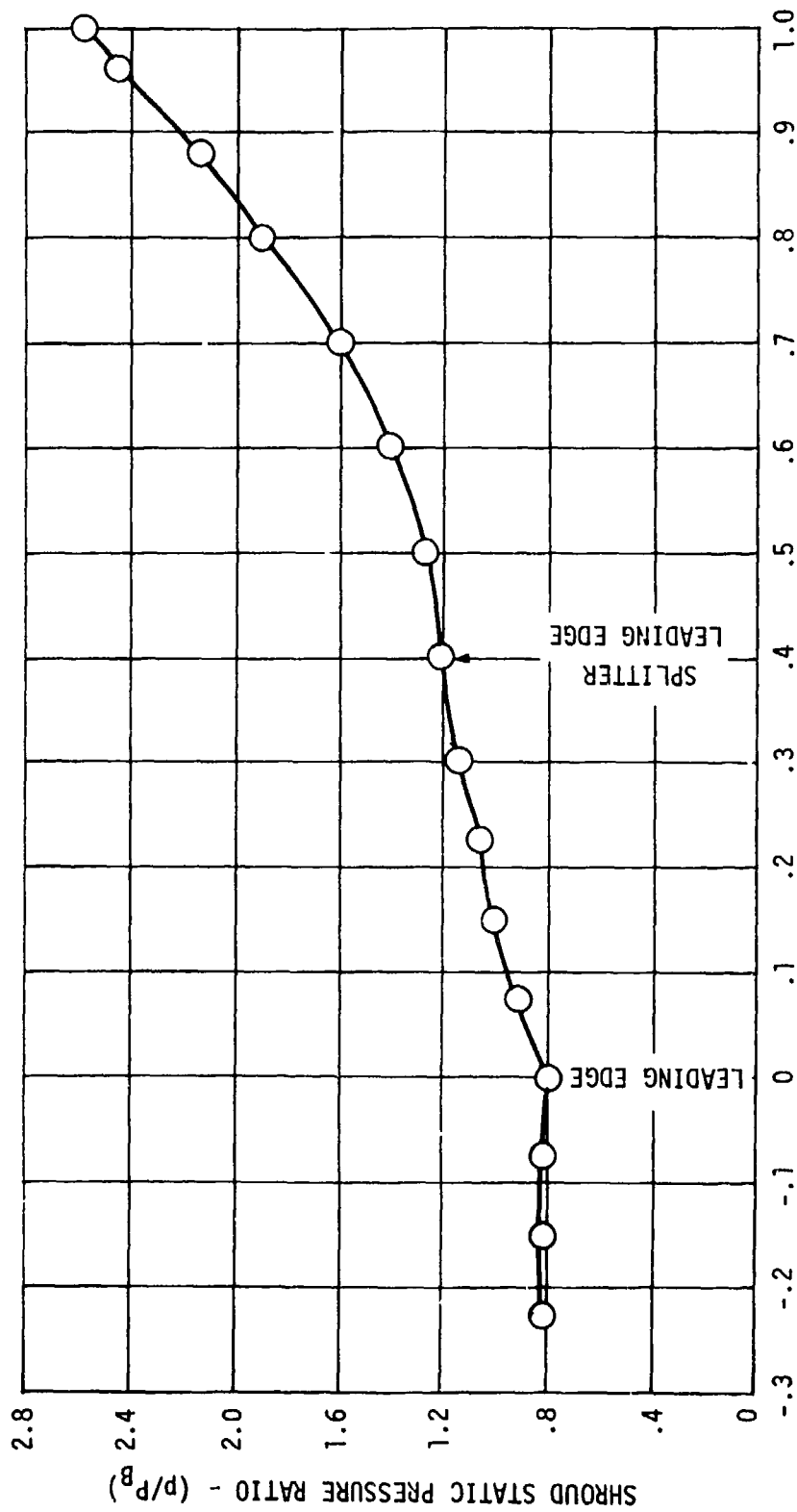


Figure 174. CCV-IV Impeller Shroud Static Pressures.

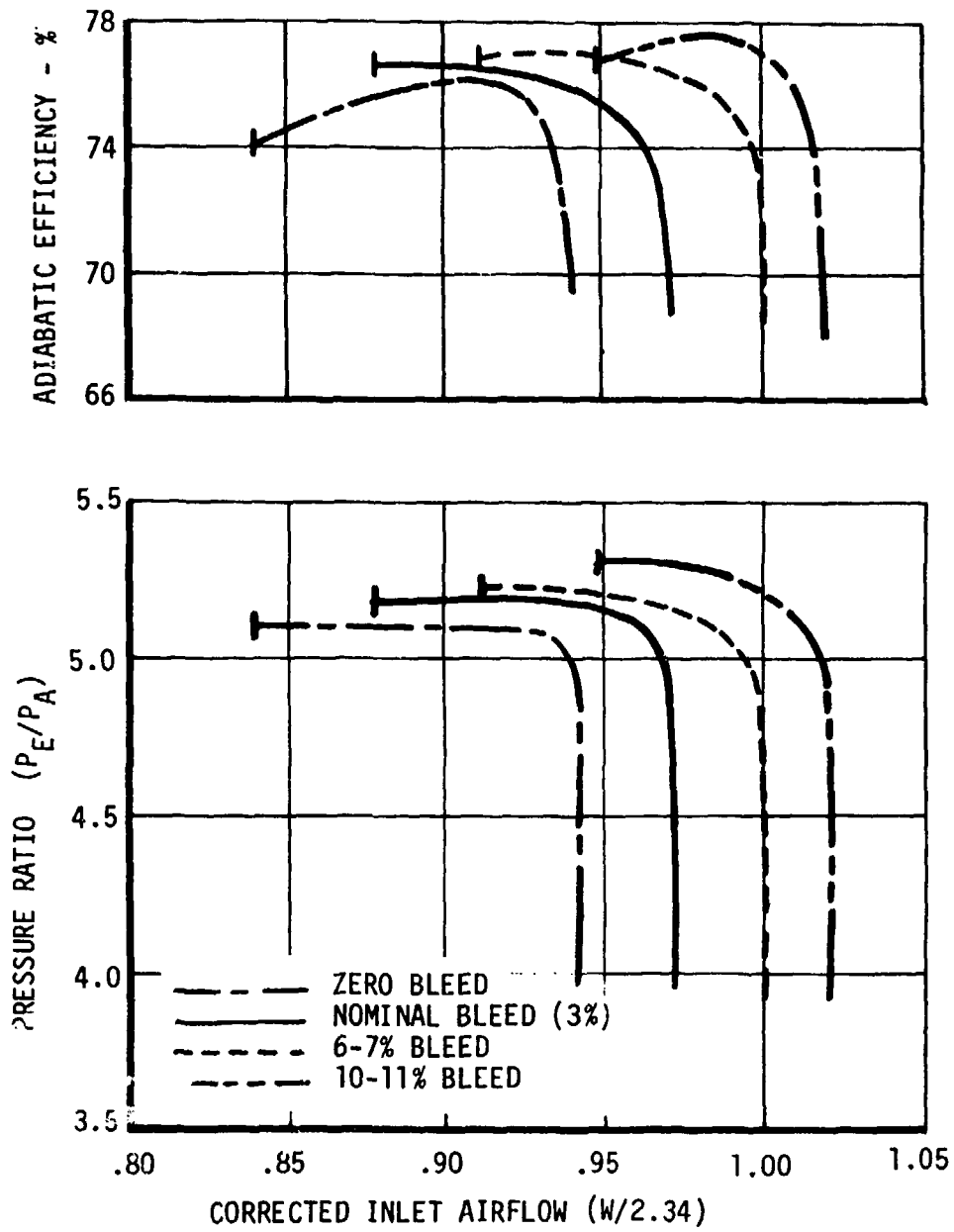


Figure 175. Effect of Vaneless Space Bleed at 95%  $N_c$ .

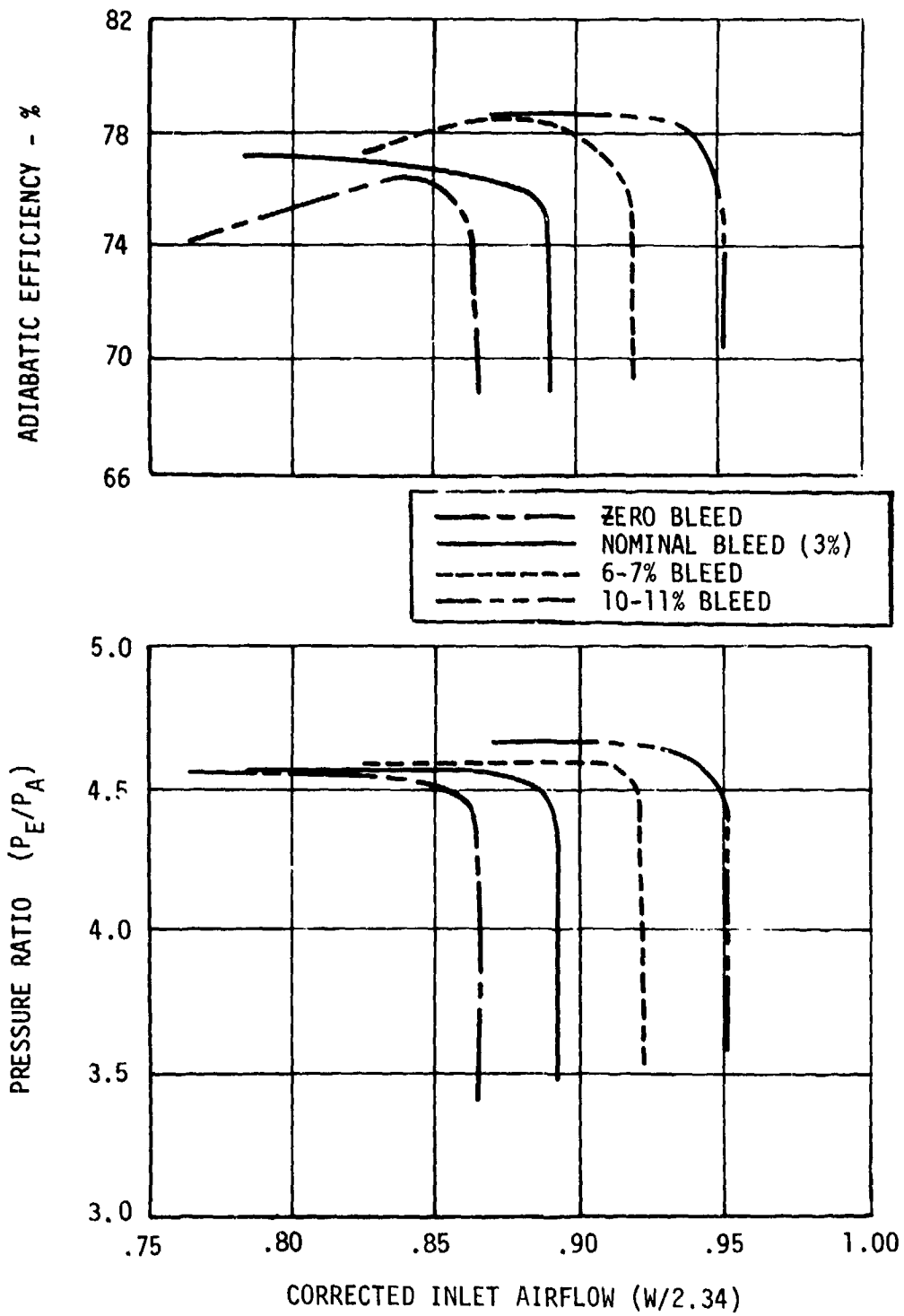


Figure 176. Effect of Vaneless Space Bleed at 90%  $N_c$ .

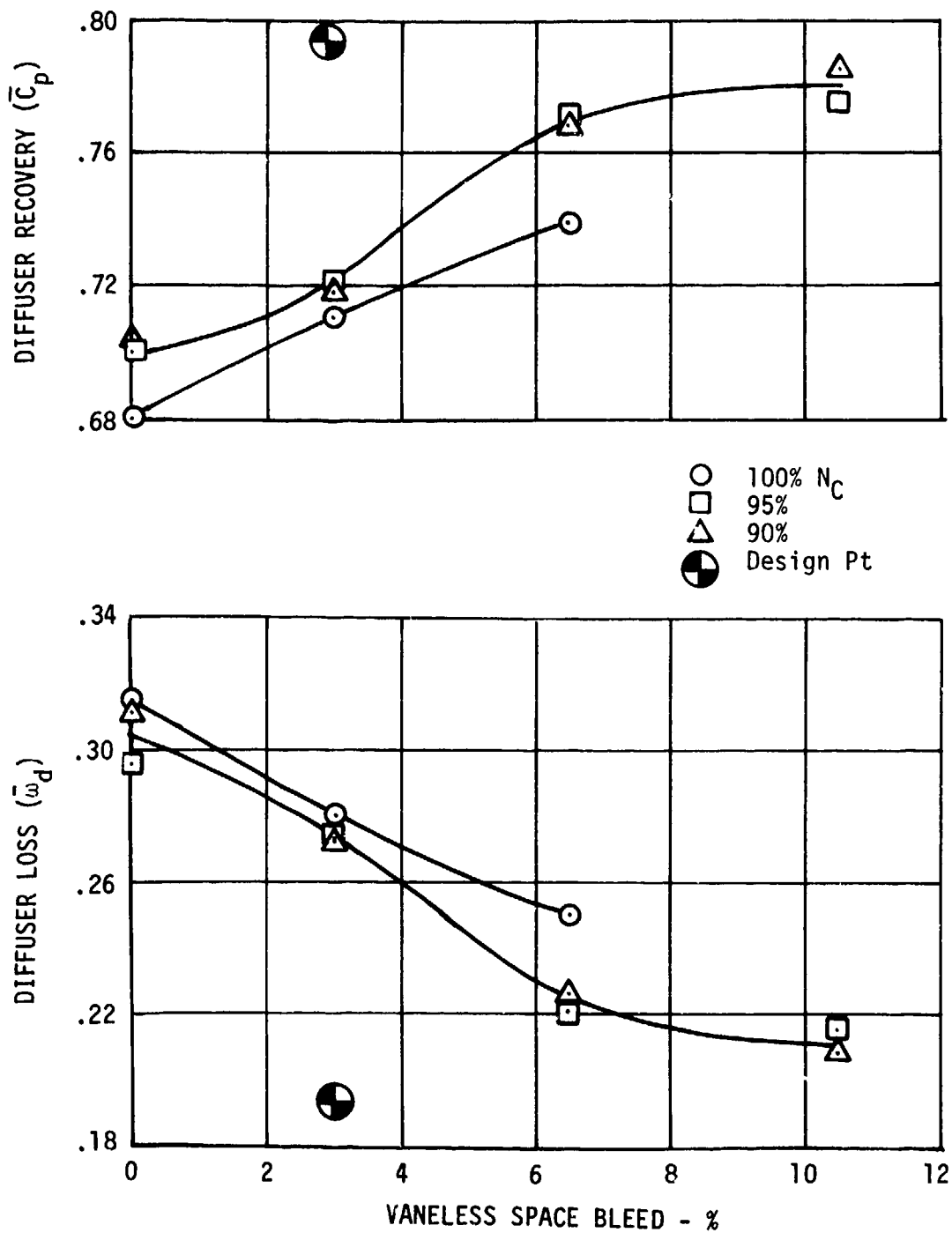


Figure 177. CCV-V Diffuser Performance.

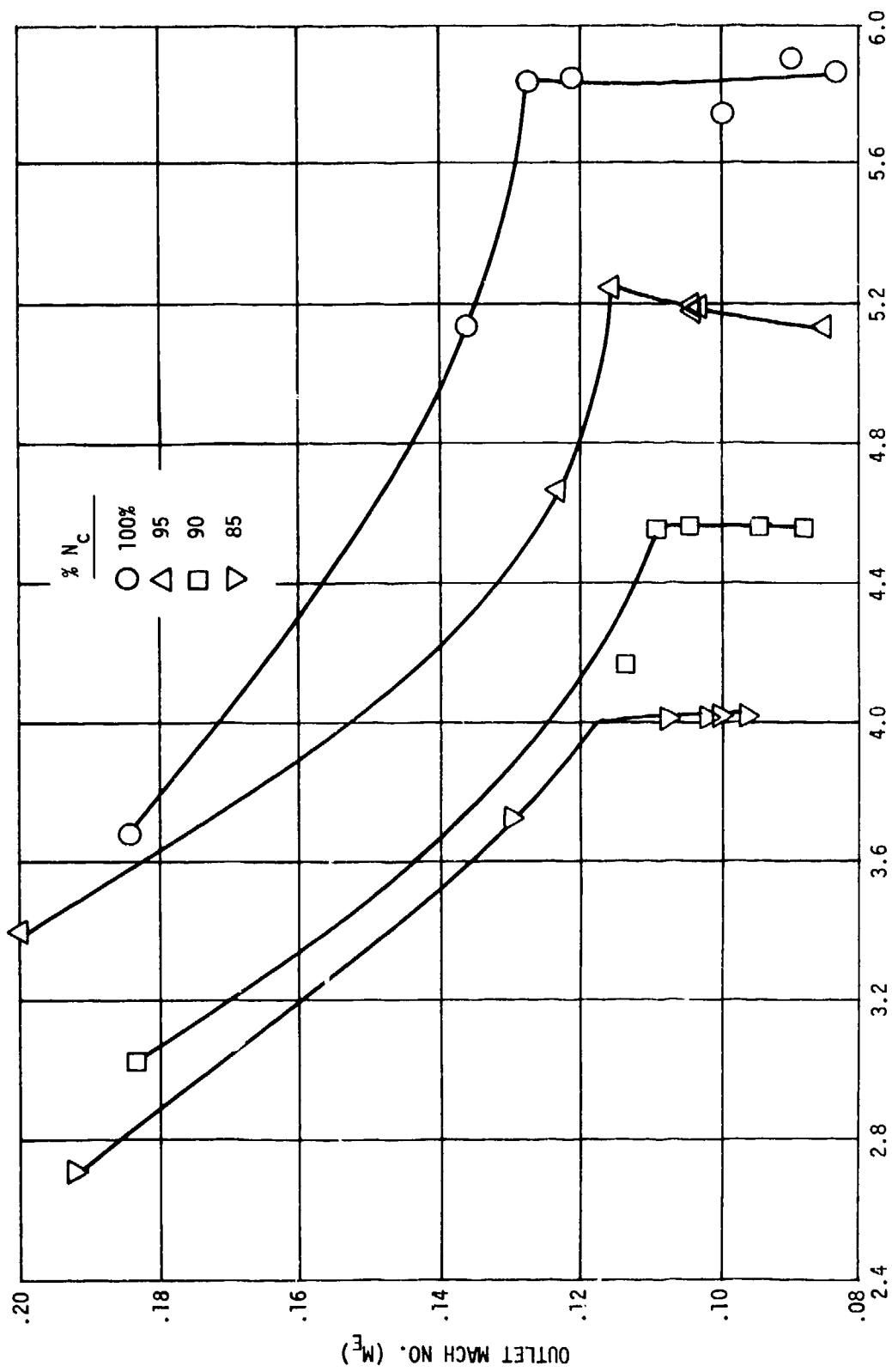


Figure 178. CCV-V Diffuser Outlet Mach Number.

### PHASE V MATCHING STUDIES

The results of the CCV-V component test were used to predict the combined axial-centrifugal compressor performance. The axial compressor performance characteristic was based on the test results from the Phase III axial component test and the Phase V, FCV-II component test. The predicted combined compressor performance is shown in Figure 179 for the nominal axial stator schedule with the design vaneless space bleed. These results indicate a considerable improvement in compressor performance over levels demonstrated during FCV-II. The improvement in usable compressor efficiency is shown in Figure 2 where the efficiency versus pressure ratio data are plotted for 10% stall margin.

The results of these matching studies were used to formulate recommendations for future compressor development effort.

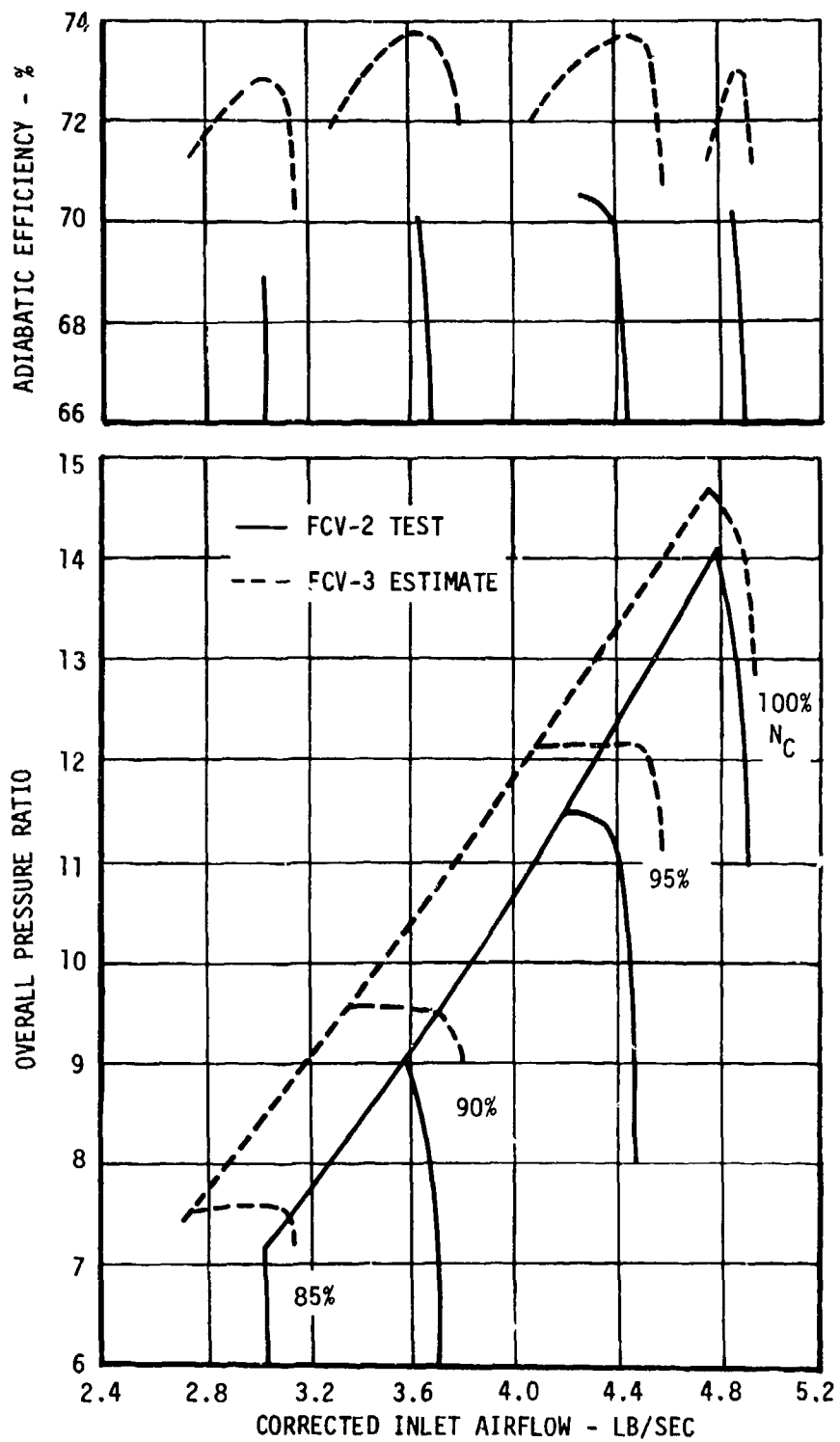


Figure 179. Combined Axial-Centrifugal Compressor.

## CONCLUSIONS

The test vehicle and its mechanical drive operated to 61,000 rpm with very low vibration levels. There were no fretting or wear problems experienced over the 200 hours of testing. Low rotor runouts and balance limits were demonstrated with the curvic coupling rotor assembly. The low vibration level coupled with a stable rotor-assembly permitted very close blade tip clearances during the various tests. The roller bearing design operated satisfactorily; however, the thrust bearings were reworked to increase the bearing contact angle after the axial component test. Reasonable bearing thrust loads were maintained during the various component tests using an externally pressurized balance piston regulated with a thrust load cell.

The 5-lb/sec, 2.5:1 pressure ratio axial compressor demonstrated the wide variation of flow-pressure ratio characteristics made possible with variable stator vanes. This wide variation permitted improved matching with the centrifugal compressor in order to optimize the performance for best efficiency at a 60% power setting for a typical turboshaft engine. The axial compressor demonstrated flows up to 5.2 lb/sec and pressure ratios up to 2.72:1. Best efficiency at 100% speed occurred at a 2.4:1 pressure ratio and 81.4% efficiency. The flow range and stall margin of the axial compressor were adequate for matching with the centrifugal stage. The axial compressor efficiency was somewhat below the objective level of 83.3%; however, a redesign was not carried out because of the smaller impact of the axial compressor on the overall compressor efficiency. The second stage of the axial compressor appeared to meet the objective efficiency level, so the deficiency was in the first stage.

During the axial compressor test a failure at the blade root of the first stage rotor occurred and a subsequent investigation revealed the cause to be high mean stress levels coupled with some marginal material properties. The rotor material was changed to a contour-forged 6-4 Titanium. The rotor blades were strain-gaged on the combined compressor test and no excessive stress regions were observed; the maximum alternating stress was 80% of scope limits.

The initial design of the centrifugal compressor was tested up to 100% corrected speed and achieved the design pressure ratio of 6.0:1 at 2.34 lb/sec with the inlet guide vanes opened 5° from the nominal setting. The choke airflow without vaneless space bleed was 2.4% below the objective level but appeared adequate for matching with the axial compressor. The best efficiency at 100% speed was 74.2% for the inlet guide vanes closed 5° from nominal. Vaneless space bleed indicated a 1 to 1-1/2% improvement in efficiency for the design bleed level of 3%. Unusually high impeller slip factors (approximately unity) were observed during the CCV-I component test,

and the impeller adiabatic efficiency of 84.7% was below the objective level (88.4%). This higher work input accounted for the near design pressure ratio levels at lower than design efficiencies. The outlet conditions from the centrifugal compressor were at an average Mach number of 0.09 which was below the design level of 0.112. This lower exit Mach number was attributed to reduced outlet blockage, as indicated by the outlet flow coefficient of 0.836 versus the design level of 0.72.

The FCV-I component test evaluated the replacement axial compressor with the CCV-I centrifugal compressor. A reduction in centrifugal compressor performance resulted in a lower centrifugal stage pressure ratio and flow capacity. However, a suitable match was obtained by use of intercompressor bleed. A pressure ratio of 14.34 was demonstrated at 100% corrected speed and 4.92 lb/sec corrected inlet airflow. The efficiency was below the predicted level because of the lower centrifugal stage performance. Closing the second stator 5° improved the overall efficiency, whereas opening the second stator had a deleterious effect. The nominal second stator position appeared best for the overall performance and matching.

The FCV-II component test evaluated a reworked centrifugal compressor stage where the diffuser throat area was increased 6.4% and the impeller leading edge was cut back. This test configuration rematched the axial and centrifugal stages above 70% speed without intercompressor bleed, but the overall efficiency and pressure ratio were not at predicted levels due to a lower impeller efficiency. Traverse data in the intercompressor duct were obtained in both the transverse and radial directions and indicated higher swirl values than previous test results. Consequently, the impeller rework was excessive and resulted in the lower impeller efficiency. The axial compressor clearance was increased during this test to evaluate efficiency effects, and a one point loss in efficiency was noted for a 0.43% C1/L clearance change.

Circumferential traverse data were obtained at the outlet of the axial inlet guide vanes. The measured total pressure loss was 0.04 versus the design level of 0.03; however, the impact of this additional loss on stage efficiency is small. Contour plots of constant pressure and angle prepared from these data showed a considerable circumferential variation across the vane pitch. A secondary flow analysis could not entirely explain angle variation from the design intent. Additional cascade data on this type of anti-iced inlet guide vane would be useful in understanding the observed pressure loss level and angle variation.

The related centrifugal compressor component test (CCV-IV) indicated a significant improvement in impeller efficiency (87.2% at design speed and airflow) and a lower slip factor (0.94). This design, based on the FCV-II axial outlet flow conditions, had a smooth impeller shroud

coating. The CCV-V test of this impeller and the FCV-II pipe diffuser demonstrated objective flow range, stall flow, and improved stage efficiency (see Figure 171). Increased amount of vaneless space bleed had further improvements in the diffuser performance (see Figure 177). The 7% increased tangency circle pipe diffuser tested in CCV-IV was inferior to the CCV-V design where the passages were tangent to the impeller tip radius (see Figure 169).

Matching studies carried out using the axial stage with the CCV-V centrifugal stage indicated a 3-4 point improvement in overall efficiency along an operating line (see Figure 2).

### RECOMMENDATIONS

From the test results and analysis during this program, the following recommendations are made:

1. A test of the axial compressor should be conducted with an improved centrifugal stage to demonstrate higher efficiency levels.
2. Additional analysis and test should be directed at the losses generated in the impeller exit-to-diffuser throat region.
3. Smooth impeller shrouds of 16-32  $\mu$ -inches should be considered for any high wheel speed centrifugal impeller to reduce shroud windage. Impeller backface windage losses should also be carefully estimated for the specific design.
4. Additional cascade data would be useful on small inlet guide vanes modified for anti-icing.

#### REFERENCES

1. Blair, L.W., and Tapparo, D.J., AXIAL CENTRIFUGAL COMPRESSOR PROGRAM-PHASES I AND II, USAAMRDL TR-72-74, U.S. Army Air Mobility Research and Development Laboratory, Fort Eustis, Virginia, February 1973, CONFIDENTIAL.
2. Reeves, G.B., and Schweitzer, J.K., MODIFIED CENTRIFUGAL COMPRESSOR, USAAMRDL TR-74-96, U.S. Army Air Mobility Research and Development Laboratory, Fort Eustis, Virginia, November 1974, AD004002.
3. Grieb, H., Schill, G., Gumucio, R., A SEMI-EMPIRICAL METHOD FOR THE DETERMINATION OF MULTISTAGE AXIAL COMPRESSOR EFFICIENCY, ASME 75-GT-11, March 1975.

APPENDIX  
TEST DATA TABLES

TABLE 22. AXIAL COMPRESSOR TEST DATA (ACV)							
Reading No.	Stator Schedule			Corrected Speed (%)	Corrected Airflow (lb/sec)	Total Pressure Ratio ( $P_B/P_A$ )	Adiabatic Efficiency ( $\eta_{BA}$ )
	IGV	S1	S2				
1	Check Out						
10	Data Readings						
11	43	34	0	80.045	2.2353	1.1381	.3082
12	43	33	0	79.9769	2.2317	1.1647	.3455
13	31.4	24.4	0	84.9749	3.0773	1.3027	.5384
14	31.5	25	0	85.049	2.8578	1.5712	.6680
15	20.2	15.8	0	89.953	3.8527	1.6816	.7565
16	20.1	16	0	89.923	3.6931	1.8855	.7680
17	8.2	7.5	0	95.109	4.6422	2.0669	.8058
18	8.2	7.3	0	95.103	4.2985	2.3168	.7808
19	8.1	7.5	0	95.101	4.5427	2.2318	.8093
20	8.1	7.5	0	95.102	4.5393	2.2283	.8093
21	-4	-1	0	100.00	5.2412	2.3945	.7481
22	0	0	0	99.962	5.1126	2.3320	.7563
23	0	0	0	100.06	5.1092	2.4199	.7734
24	42	32.5	0	79.974	2.2694	1.0102	.0307
25	42	32.5	0	80.089	2.1681	1.2441	.4395
26	42	32.5	0	80.063	1.7599	1.3081	.4033
27	42	32.5	0	80.053	1.3067	1.3132	.3145
28	20.4	16.3	0	90.099	3.6086	1.9250	.7660
29	20.4	16.3	0	90.179	3.3906	1.9335	.7251
30	20.4	16.3	0	90.176	3.2521	1.9089	.6945
31	8.2	7.4	0	95.228	4.2776	2.3208	.7815
32	8.2	7.4	0	95.112	4.1299	2.3249	.7589
33	30.9	24.5	0	85.320	3.0154	1.4123	.6093
34	30.9	24.5	0	85.340	2.9533	1.5334	.6633
35	30.9	24.5	0	85.399	2.7399	1.6020	.6547
36	30.9	24.5	0	85.327	2.5370	1.6094	.6186
37	30.9	24.5	0	85.349	2.4339	1.6058	.5915
38	30.9	24.5	0	85.358	2.7365	1.5956	.6572
39	30.9	24.5	0	85.415	2.4207	1.6019	.5916
40	26	21	0	85.444	3.3258	1.4258	.6460
41	26	21	0	85.176	3.2203	1.6154	.7249
42	26	21	0	85.159	2.9633	1.6941	.7031
43	26	21	0	85.187	2.7278	1.6906	.6597
44	26	26	0	85.164	3.0483	1.3067	.4969
45	26	26	0	85.148	2.8520	1.5806	.6504
46	26	26	0	85.136	2.6454	1.6096	.6247
47	26	26	0	85.169	2.4447	1.5959	.5786

TABLE 22. - Continued

Reading No.	Stator Schedule			Corrected Speed (%)	Corrected Airflow (lb/sec)	Total Pressure Ratio ( $P_B/P_A$ )	Adiabatic Efficiency ( $\eta_{BA}$ )
	IGV	S1	S2				
48	26	16	0	85.038	3.3827	1.6323	.7611
49	26	16	0	85.093	3.1768	1.7490	.7523
50	26	16	0	85.116	2.9649	1.7301	.6975
51	30	21	0	85.130	3.1141	1.5678	.7128
52	30	21	0	85.031	2.7890	1.6327	.6605
53	30	21	0	85.064	3.0123	1.6083	.7039
54		21	0	85.093	7.3322	1.6639	.7304
55	21	21	0	85.070	3.1358	1.7438	.7123
56	21.8	21	0	85.083	2.8813	1.7329	.6633
57	13	0	0	85.037	4.0181	1.8792	.8163
58	13	0	0	85.104	3.8650	1.9539	.7996
59	13	0	0	84.997	3.4789	1.9523	.7044
60	13	0	0	85.027	4.0963	1.8017	.8208
61	0	0	0	85.006	4.4171	1.9544	.8130
62	0	0	0	84.993	4.2928	2.0270	.8116
63	0	0	0	84.980	4.1998	2.0596	.8033
64	26	0	0	85.130	3.6999	1.6042	.7550
65	26	0	0	85.029	3.6055	1.7169	.7719
66	31	24.5	0	85.129	3.0324	1.4094	.6100
67	31	24.5	0	85.136	3.3544	1.5310	.6598
68	31	24.5	0	85.117	2.5501	1.6079	.6163
69	26	21	0	85.0	1.5218	1.6131	-
70	26	21	0	85.0	3.0375	1.6136	-
71	26	21	0	85.130	3.2180	1.6134	.7139
72	45	35.4	0	0	0	-	-
73	45	35.4	0	69.079	2.1065	1.0368	.1298
74	45	35.4	0	69.928	1.1408	1.2193	.2800
75	45	35.4	0	69.905	1.6188	1.1923	.3763
76	45	35.4	0	70.047	1.5676	1.0370	.1261
77	45	35.4	0	70.046	1.5677	1.0370	.1222
78	45	35.4	0		VOID		
79	45	35.4	0	70.047	1.5676	1.0370	.1261
80	45	35.4	0	69.613	1.1383	1.1790	.3362
81	45	35.4	0	70.078	1.4678	1.1076	.2950
82	45	35.4	0	70.349	1.4621	1.1076	.2644
83	45	35.4	0	70.078	1.4678	1.1076	.2950
84	45	35.4	0	70.078	1.4678	1.1076	.2950
85	45	35.4	0	69.759	1.7258	1.0355	.1231
86	45	35.4	0	69.759	1.7258	1.0355	.1196
87	45	35.4	0	70.135	1.0794	1.2147	.3018
88	45	35.4	0	70.174	1.5306	1.1675	.3710

TABLE 22. - Continued

Reading No.	Stator Schedule			Corrected Speed (%)	Corrected Airflow (lb/sec)	Total Pressure Ratio ( $P_B/P_A$ )	Adiabatic Efficiency ( $\eta_{BA}$ )
	IGV	S1	S2				
89	45	35.4	0		VOID		
90	45	35.4	0	92.821	4.5974	2.0486	.7997
91	8.0	7.5	0	95.015	4.4915	2.1987	.8075
92	10	9.1	0	95.058	4.4975	2.0088	.7946
93	10	9.1	0	95.058	4.4975	2.0088	.7932
94	10	9.1	0	95.013	4.0469	2.2496	.7524
95	10	9.1	0	94.998	4.3688	2.1572	.7855
96	10	0	0	94.972	4.6061	2.0711	.7892
97	10	0	0	94.970	4.2524	2.2798	.7450
98	10	0	0	94.891	4.5198	2.2367	.7909
99	10	5	0	97.824	4.5589	2.0402	.7913
100	10	5	0	95.014	4.1622	2.2952	.7567
101	10	5	0	95.126	4.4387	2.2261	.7968
102	6	5	0	95.055	4.6828	2.1062	.8036
103	6	5	0	95.052	4.6829	2.1062	.7909
104	6	5	0	95.072	4.1621	2.3449	.7552
105	6	5	0	94.046	4.4167	2.3230	.7952
106	6	0	0	95.012	4.7301	2.1389	.7753
107	6	0	0	95.083	4.3487	2.3335	.7536
108	6	0	0	94.882	4.5915	2.3051	.7974
109	14	9	0	94.997	4.3434	1.9480	.7756
110	14	8	9.0	94.961	3.9368	2.1779	.7474
111	14	9	0	94.873	3.9442	2.1853	.7463
112	14	9	0	94.943	4.2190	2.1109	.7715
113	14	13	0	94.903	4.2416	1.9012	.7828
114	14	13	0	94.820	3.9496	2.1443	.7349
115	14	13	0	94.831	4.1445	2.0569	.7802
116	0	0	0	95.168	4.9404	2.2393	.8019
117	0	0	0	95.098	4.5804	2.4372	.7682
118	0	0	0	95.082	4.8273	2.3959	.7970
119	10	9	0	95.223	4.3748	2.1622	.7993
120	10	9	0	95.249	4.4846	2.0115	.7940
121	10	9	0		VOID		
122	25.8	16.2	0	84.014	3.3979	1.6051	.7578
123	25.8	16.2	0	83.988	3.4022	1.6040	.7481
124	25.8	16.2	0	89.402	3.2001	1.6053	
125	25.8	16.2	0	83.883	3.4024	1.6030	.7586
126	25.8	16.2	0	83.997	3.4058	1.6049	.7563
127	25.8	16.2	0		VOID		
128	6	7	0	94.883	4.6110	2.1989	.8111
129	6	7	0	94.919	4.6039	2.2002	.8113
130	6	7	0	94.768	4.5972	2.1959	.8116

TABLE 22. - Continued

Reading No.	Stator Schedule			Corrected Speed (%)	Corrected Airflow (lb/sec)	Total Pressure Ratio ( $P_B/P_A$ )	Adiabatic Efficiency ( $\eta_{BA}$ )
	IGV	S1	S2				
131	6	7	0	94.747	4.5936	2.1970	.8118
132	6	7	0	94.723	4.6098	2.2047	.8161
133	-2	0	0	99.890	5.1724	2.3731	.7607
134	-2	0	0	99.918	5.1657	2.5223	.7772
135	-2	0	0	99.735	5.1218	2.6517	.7859
136	-2	0	0	99.848	5.1670	2.4622	.7751
137	-2	0	0	99.800	5.1824	2.4623	.7780
138	-2	0	0	99.941	5.1781	2.4618	.7804
139	-2	0	0	99.803	5.1594	2.4545	.7809
140	-2	0	0	38.546	5.1741	2.4594	.7812
141	-2	0	0	100.27	5.2021	2.4719	.7744
142	-2	0	0	100.14	5.1888	2.4682	.7743
143	-2	0	0	100.08	5.0826	2.6901	.7792
144	0	0	0	100.22	5.1280	2.4423	.7803
145	0	0	0	100.20	5.1287	2.5051	.7834
146	0	2.5	0	100.21	5.1164	2.5066	.7923
147	-4	2.5	0	100.26	5.2116	2.5633	.7859
148	-4	0	0	100.27	5.2223	2.5667	.7782
149	0	5	0	100.35	5.1005	2.5018	.7957
150	3	5	0	100.32	5.0053	2.2500	.7992
151	3	2.5	0	100.23	5.0249	2.4540	.7952
152	0	5	0	100.08	5.0736	2.5414	.7976
153	0	5	0	100.16	4.8800	2.6385	.7767
154	0	5	0	100.19	5.0203	2.6078	.7728
155	-4	2.5	0	100.14	5.2168	2.5716	.7892
156	VOID						
157	-4	5	0	100.19	5.1941	2.5574	.7926
158	-4	7	0	100.16	5.1692	2.5402	.7936
159	-4	7	0		VOID		
160	46	36	0	69.950	1.8658	1.0628	.2018
161	46	36	0	72.317	1.6612	1.1439	-
162	46	36	0	69.773	1.9116	1.1438	.3445
163	46	36	0	69.689	1.7194	1.1433	.3446
164	46	36	0	69.658	1.4710	1.1816	.3333
165	38	28	0	69.725	2.2173	1.2902	.6387
166	38	28	0	69.575	1.9721	1.3237	.6030
167	38	28	0	69.666	1.6567	1.2982	.4747
168	38	28	0	50.179	1.8537	1.0324	.2782
169	38	28	0	50.084	1.7307	1.1134	.6194
170	38	28	0	50.047	1.5070	1.1676	.5911
171	38	28	0	85.060	3.0909	1.7103	.7463
172)				System			
185)				Checkout			
186	26	21	0	84.939	2.8148	1.5627	.6584

TABLE 22. - Continued

Reading No.	Stator Schedule			Corrected Speed (%)	Corrected Airflow (lb/sec)	Total Pressure Ratio ( $P_B/P_A$ )	Adiabatic Efficiency ( $\eta_{BA}$ )
	IGV	S1	S2				
187	26	21	0	0	-	-	-
188	31.4	24.3	0	84.766	2.8063	1.5643	.6611
189	31.4	24.3	0	84.712	2.7934	1.5648	.6586
190	31.4	24.3	0	0	-	-	-
191	31.4	24.3	0	84.909	2.8000	1.5620	.6598
192	31.4	24.3	0	84.958	2.7967	1.5634	.658
193	20	16	0	90.051	3.5682	1.9078	.7569
194	8.2	7.5	0	95.151	4.2154	2.3006	.7714
195	-2	0	0	100.14	5.1784	2.4572	.7787
196	3	7	0	95.273	4.7567	2.1418	.8118
197	3	7	0	95.584	4.7007	2.2679	.8153
198	3	7	0	95.394	4.3653	2.3743	.7811
199	14	6	0	95.182	4.4178	1.9795	.7949
200	14	6	0	95.186	4.3309	2.1528	.8016
201	14	6	0	101.27	3.6541	2.2078	.6151
202	14	6	0	95.806	3.8753	2.2072	.7225
203	3	5	0	100.13	4.9951	2.2737	.7898
204	3	5	0	100.14	4.9942	2.3593	.8126
205	3	5	0	100.12	4.9208	2.5005	.7977
206	3	5	0	100.20	4.6719	2.5771	.7755
207	-4	5	0	100.16	5.1920	2.3891	.7761
208	-4	5	0	100.16	5.1886	2.4799	.7887
209	-4	5	0	0	-	-	-

TABLE 23. CENTRIFUGAL TEST DATA (CCV-I)

Reading No.	Corrected Speed (%)	Corrected Flow (%)	Total Pressure Ratio ( $P_E/P_B$ )	Adiabatic Efficiency ( $\eta_{E-B}$ )	IGV Setting (deg from design)
1	49.80	58.89	1.0837	.0348	0
2	49.96	32.40	1.1520	.0215	0
3	49.96	41.14	1.0766	.0735	0
4	75.22	60.06	1.9107	.4071	0
5	85.52	73.55	2.4834	.4617	0
6					
7	91.28	83.74	2.0653	.3218	0
8	96.34	92.42	2.3204	.3433	0
9					
10	101.67	95.53	4.3811	.5787	0
11	75.14	57.61	2.5029	.5946	0
12	75.13	49.84	2.9875	.7134	0
13	74.97	.5489	2.9405	.7136	0
14	85.11	72.36	2.9776	.5648	0
15	84.91	69.20	3.8886	.7349	0
16	85.12	74.24	3.1075	.5806	0
17	85.01	71.68	4.0379	.7473	0
18	84.81	76.84	4.1410	.7573	0
19	94.95	93.98	4.7467	.6862	0
20	94.76	85.88	5.1077	.7259	0
21	100.08	94.30	4.5265	.5957	0
22	100.07	92.96	5.1874	.6639	0
23	99.98	91.98	5.5775	.7014	0
24	95.02	87.32	5.1513	.7356	0
25	94.93	86.25	5.1606	.7389	0
26	94.90	86.13	5.1578	.7337	0
27	95.02	85.68	5.1736	.7345	0
28	94.97	87.93	5.1447	.7387	0
29	94.95	88.26	5.1390	.7373	0
30	94.98	84.74	5.1839	.7395	0
31	95.03	84.35	5.1569	.7380	0
32	84.88	67.88	4.0871	.7536	0
33	84.82	70.94	3.1959	.7303	0
34	57.77	69.17	1.1260	.0470	0
35	75.19	73.53	2.5134	.5787	0
36	90.13	83.22	3.6624	.6139	0
37	90.08	82.22	4.3576	.7170	0
38	90.06	80.76	4.6300	.7511	0
39	90.04	79.01	4.6759	.7537	0
40	90.01	78.16	4.6930	.7571	0

TABLE 23. - Continued

Reading No.	Corrected Speed (%)	Corrected Flow (%)	Total Pressure Ratio ( $P_E/P_B$ )	Adiabatic Efficiency ( $\eta_{E-B}$ )	IGV Setting (deg from design)
41	85.09	76.33	3.0518	.5837	5
42	85.10	71.65	4.0480	.7573	5
43	85.09	70.00	4.0973	.7612	5
44	95.10	89.35	3.8693	.5876	5
45	95.01				
46	95.03	85.60	5.2628	.7508	5
47	100.24	97.94	4.7233	.6231	5
48	99.92	96.68	5.6958	.7254	5
49	99.99	92.20	5.9220	.7433	5
50	90.09	82.77	3.6710	.6219	5
51	90.04	81.17	4.5191	.7471	5
52	90.12	78.02	4.6391	.7570	5
53	85.16	77.41	3.0931	.5736	-5
54	85.15	75.07	4.1052	.7504	-5
55	85.04	71.07	4.1620	.7552	-5
56	90.22	85.49	3.6368	.6012	-5
57	90.12	84.98	4.5898	.7361	-5
58	90.06	81.57	4.7432	.7525	-5
59			DELETED		
60	95.07	93.10	4.1543	.6088	-5
61	94.81	93.33	5.2495	.7382	-5
62	95.03	89.37	5.4062	.7471	-5
63	100.13	100.61	4.5473	.5908	-5
64	99.92	100.83	5.9295	.7259	-5
65	99.98	97.50	6.0887	.7363	-5
66			DELETED		
67	50.13	30.00	1.7218	.7247	0
68	50.20	27.86	1.7380	.7228	0
69	50.22	28.63	1.7343	.7197	0
70	75.06	61.48	2.4254	.5652	0
71	74.91	59.36	3.1154	.7475	0
72	74.94	55.06	3.1533	.7570	0
73	85.02	76.05	3.1860	.6020	0
74	84.98	76.04	3.9981	.7418	0
75	85.06	73.43	4.0889	.7552	0
76	84.98	71.64	4.0930	.7565	0
77	85.08	71.49	4.1235	.7587	0
78	90.03	84.82	3.5405	.5948	0
79	94.99	92.35	3.9429	.5924	0
80	94.89	90.41	5.1826	.7400	0
81	94.90	88.70	5.2332	.7449	0
82	95.12	86.96	5.2879	.7448	0
83	94.93	85.42	5.2423	.7489	0

TABLE 23. - Continued

Reading No.	Corrected Speed (%)	Corrected Flow (%)	Total Pressure Ratio ( $P_E/P_B$ )	Adiabatic Efficiency ( $\eta_{E-B}$ )	IGV Setting (deg from design)
84	99.97	99.67	4.5255	.5990	0
85	99.86	97.77	5.6502	.7140	0
86	99.90	96.63	5.8581	.7293	0
87	99.90	95.37	5.9276	.7306	0
88	99.82	95.36	5.9295	.7331	0
89	99.81	96.51	5.9304	.7319	0
90	99.78	95.01	5.9244	.7314	0
91	99.82	95.70	5.9383	.7314	0
92	99.75	99.09	5.7961	.7311	0
93	99.86	97.52	5.9580	.7398	0
94	95.00	92.08	5.2542	.7484	0
95	94.95	90.99	5.3183	.7481	0
96	94.81	87.70	5.2466	.7430	0
97	94.80	88.82	5.2445	.7426	0
98	97.01	87.85	5.2422	.7395	0
99	94.80	87.07	5.2489	.7426	0
100	94.81	87.70	5.2469	.7430	0
101	89.92	81.79	4.5975	.7447	0
102			DELETED		
103	89.77	81.11	4.6003	.7462	0
104	89.96	82.18	4.6064	.7447	0
105	89.93	81.50	4.6058	.7442	0
106	84.95	77.69	4.0677	.7606	0
107					
108	75.01	54.91	2.4457	.5754	0
109	74.97	52.59	3.1083	.7548	0
110	74.97	52.37	3.1444	.7598	0
111	74.99	56.37	3.1083	.7540	0

Note - RDGS 1 - 35 were not processed for IGV loss.

TABLE 24. COMBINED COMPRESSOR DATA SETTINGS (FCV-I)

RDG	Stator Schedule			Plane B Bleed (%)	Vaneless Bleed (%)		Run No.
	IGV	S1	S2		FWD	AFT	
1	38	28	0		0	0	1
2	38	28	0		0	0	2
3	38	28	0		0	0	2
4	38	28	0		0	0	2
5	38	28	0		0	0	3
6	38	28	0	17.65	0	0	3
7	38	28	0	14.57	0	0	3
8	38	28	0	0	0	0	3
9	38	28	0		0	0	3
10	38	28	0		0	0	3
11	38	28	0		0	0	3
12	38	28	0		0	0	5
13	27	21	0		0	0	6
14	27	21	0		0	0	6
15	27	21	0		0	0	6
16	27	21	0		0	0	6
17	27	21	-5		0	0	7
18	27	21	-5	1.265	0	0	7
19	17	14	0	0	0	0	7
20	6	7	0	0	0	0	7
21	6	7	0	2.385	0	0	7
22	6	7	0	2.406	0	0	7
23	17	14	-	2.867	0	0	7
24	3	5	0	3.760	0	0	7
25	3	5	0	3.751	0	0	7
26	3	5	0	3.886	0	0	7
27	16.3	13.7	0	2.465	0	0	10
28	17	14	0	2.490	0	0	10
29	17	14	0	11.19	0	0	10
30	17	14	0	7.224	0	0	10
31	17	14	0	8.542	0	0	10
32	17	14	0	8.609	0	0	10
33	17	14	0	8.803	0	0	10
34	17	14	0	8.458	0	0	10
35	17	14	0	8.161	0	0	10
36	17	14	0	8.145	1.696	0	10
37	17	14	0	7.851	2.109	0	10
38	17	14	0	8.123	2.134	.925	10
39	17	14	0	8.013	1.806	1.882	10
40	17	14	0	8.088	2.135	1.884	10

RDG 4 Aborted

TABLE 24. - Continued

RDG	Stator Schedule			Plane B Bleed (%)	Vaneless Bleed (%)		Run No.
	IGV	S1	S2		FWD	AFT	
41	17	14	0	8.568	2.129	1.919	10
42	17	14	0	8.386	1.998	1.840	10
43	6	7	0	3.857	2.508	1.665	10
44	27	21	0	4.364	2.028	1.936	10
45	27	21	0	11.262	1.739	1.769	10
46	27	21	0	7.304	1.795	1.857	10
47	27	21	0	7.052	1.672	1.763	10
48	27	21	0	7.292	1.839	1.839	10
49	27	21	0	7.526	2.136	1.881	10
50	27	21	0	7.013	1.882	1.730	10
51	27	21	0	7.640	0	0	10
52	27	21	0	7.506	0	0	10
53	27	21	0	8.404	0	0	10
54	27	21	0	7.467	0	0	10
55	17	14	0	2.531	0	0	11
56	6	7	0	6.405	0	0	11
57	6	7	0	6.400	0	0	11
58	6	7	0	6.530	0	0	11
59	6	7	0	6.674	0	0	11
60	6	7	0	7.104	0	0	11
61	6	7	0	4.638	2.030	1.387	11
62	6	7	0	4.545	2.340	1.058	11
63	6	7	0	4.815	2.363	1.350	11
64	3	5	0	5.901	0	0	11
65	3	5	0	5.957	0	0	11
66	3	5	0	5.981	0	0	11
67	3	5	0	6.397	0	0	11
68	3	5	0	6.908	0	0	11
69	3	5	0	4.183	1.576	0	11
70	3	5	0	4.388	2.085	.973	11
71	3	5	0	4.271	2.085	0	11
72	17	14	0	7.203	0	0	11
73	17	14	0	6.970	0	0	11
74	17	14	0	6.998	0	0	11
75	17	14	0	6.910	0	0	11
76	17	14	0	6.593	0	0	11
77	27	21	0	7.478	0	0	11
78	27	21	0	7.467	0	0	11

Repeat RDG 23

TABLE 24. - Continued

RDG	Stator Schedule			Plane B Bleed (%)	Vaneless Bleed (%)		Run No.
	IGV	S1	S2		FWD	AFT	
79	17	14	-5	7.047	0	0	12
80	17	14	-5	7.249	0	0	12
81	17	14	-5	7.439	0	0	12
82	17	14	-5	7.331	0	0	12
83	6	7	-5	6.389	0	0	12
84	6	7	-5	6.461	0	0	12
85	6	7	-5	6.454	0	0	12
86	6	7	-5	7.026	0	0	12
87	3	5	-5	5.945	0	0	12
88	3	5	-5	6.671	0	0	12
89	3	5	-5	5.721	0	0	12
90	3	5	+5	6.202	0	0	12
91	3	5	+5	6.166	0	0	12
92	3	5	+5	6.520	0	0	12
93	3	5	+5	6.781	0	0	12
94	6	7	+5	7.022	0	0	12
95	6	7	+5	6.700	0	0	12
96	6	7	+5	6.778	0	0	12
97	17	14	+5	7.042	0	0	12
98	17	14	+5	7.152	0	0	12
99	17	14	+5	7.279	0	0	12

TABLE 25. COMBINED COMPRESSOR TEST RESULTS (FCV-I)

RDG NO.	PCT. RPM	AXIAL STAGE			CENT. STAGE			OVERALL	
		FLOW LB/SEC	PRES. RATIO	EFF. RATIO	FLOW W/WDSN	PRES. RATIO	EFF. RATIO	PRES. RATIO	EFF. RATIO
1	4.99	0.526	1.027	59.961	0.219	0.794	0.	0.816	0.
2	12.91	0.493	1.047	3.072	0.202	0.794	0.	0.832	0.
3	24.16	0.817	1.087	1.414	0.227	0.953	0.	1.036	0.138
4	0.	0.	-0.000	0.	0.	0.	0.	1.000	0.001
5	24.53	1.189	1.106	1.968	0.368	0.937	0.	1.036	0.130
6	50.04	1.558	1.214	0.732	0.469	1.361	0.351	1.652	0.427
7	70.01	2.093	1.361	0.663	0.599	2.245	0.536	3.054	0.543
8	69.97	1.893	1.349	0.585	0.644	2.320	0.545	3.128	0.529
9	70.01	2.000	1.362	0.597	0.674	2.749	0.668	3.743	0.624
10	80.37	2.518	1.483	0.677	0.787	3.579	0.668	5.307	0.644
11	80.36	2.557	1.484	0.680	0.798	3.596	0.671	5.336	0.648
12	70.08	2.235	1.378	0.737	0.639	2.412	0.560	3.323	0.579
13	85.10	2.797	1.706	0.673	0.782	4.099	0.719	6.991	0.674
14	85.10	2.851	1.712	0.677	0.794	3.709	0.658	6.350	0.629
15	85.11	2.840	1.707	0.678	0.792	3.695	0.656	6.308	0.628
16	85.47	2.912	1.718	0.691	0.799	3.413	0.607	5.863	0.597
17	85.06	2.811	1.668	0.632	0.805	3.369	0.599	5.619	0.572
18	85.09	2.876	1.674	0.654	0.807	3.437	0.609	5.753	0.586
19	90.05	3.416	2.011	0.705	0.832	3.151	0.525	6.337	0.541
20	95.06	4.438	2.552	0.819	0.871	2.574	0.394	6.570	0.489
21	95.08	4.351	2.417	0.782	0.880	2.612	0.400	6.314	0.479
22	94.99	4.362	2.391	0.789	0.887	2.623	0.328	6.274	0.413
23	89.94	3.579	2.027	0.735	0.837	2.454	0.402	4.975	0.464
24	97.86	4.775	2.510	0.714	0.921	3.221	0.484	8.086	0.536
25	99.07	4.936	2.541	0.805	0.938	3.333	0.482	8.469	0.542
26	99.12	4.939	2.536	0.800	0.940	3.345	0.484	8.484	0.542
27	90.00	3.605	2.044	0.751	0.839	2.428	0.391	4.964	0.460
28	90.10	3.587	2.022	0.751	0.841	2.450	0.394	4.955	0.461
29	90.04	3.981	1.949	0.845	0.866	2.990	0.468	5.827	0.533
30	89.94	3.828	2.009	0.795	0.854	2.925	0.476	5.877	0.530
31	89.96	3.843	2.010	0.806	0.845	4.235	0.673	8.513	0.681
32	89.95	3.720	2.024	0.776	0.812	4.644	0.733	9.399	0.714
33	89.98	3.727	2.034	0.778	0.811	4.666	0.736	9.489	0.717
34	90.00	3.839	2.026	0.806	0.839	4.565	0.715	9.249	0.712
35	90.00	3.849	2.000	0.818	0.849	2.916	0.468	5.833	0.530
36	90.01	3.910	1.985	0.824	0.869	2.921	0.468	5.797	0.531
37	90.02	3.889	1.946	0.830	0.880	2.947	0.469	5.735	0.531
38	89.95	3.949	1.983	0.837	0.878	4.303	0.672	8.532	0.689
39	89.94	3.973	1.980	0.843	0.885	4.321	0.674	8.555	0.692
40	89.95	3.975	1.981	0.840	0.884	4.662	0.717	9.235	0.724
41	89.98	3.842	2.012	0.813	0.842	4.754	0.740	9.564	0.733
42	90.00	3.830	2.018	0.809	0.840	4.778	0.744	9.641	0.735
43	94.98	4.676	2.405	0.847	0.923	3.001	0.461	7.217	0.540
44	84.94	3.200	1.749	0.761	0.828	2.622	0.463	4.585	0.509
45	84.98	3.388	1.656	0.796	0.848	2.707	0.462	4.482	0.511
46	84.97	3.286	1.733	0.792	0.830	2.630	0.456	4.558	0.510
47	84.95	3.266	1.728	0.788	0.827	3.435	0.608	5.937	0.626
48	84.93	3.269	1.734	0.784	0.826	4.224	0.731	7.322	0.720
49	84.93	3.179	1.742	0.751	0.801	4.330	0.757	7.543	0.728

TABLE 25. - Continued

RDG NO.	PCT. RPM	AXIAL STAGE			CENT. STAGE			OVERALL	
		FLØW LR/SEC	PRES. RATIO	EFF. RATIO	FLØW W/WDSN	PRES. RATIO	EFF. RATIO	PRES. RATIO	EFF. RATIO
50	84.93	3.263	1.730	0.782	0.826	4.094	0.714	7.082	0.705
51	85.00	3.121	1.734	0.731	0.790	4.194	0.739	7.273	0.707
52	85.00	3.087	1.726	0.728	0.784	4.197	0.736	7.245	0.704
53	84.97	2.964	1.729	0.700	0.751	4.264	0.746	7.375	0.702
54	85.00	3.115	1.738	0.732	0.787	4.057	0.716	7.050	0.691
55	90.10	3.606	2.038	0.753	0.840	2.430	0.392	4.953	0.461
56	94.94	4.509	2.330	0.805	0.895	2.644	0.400	6.159	0.483
57	94.98	4.578	2.350	0.822	0.898	2.652	0.400	6.233	0.487
58	94.97	4.548	2.376	0.818	0.886	4.088	0.615	9.713	0.642
59	94.90	4.507	2.363	0.817	0.881	4.742	0.694	11.204	0.699
60	94.93	4.416	2.418	0.798	0.845	4.942	0.725	11.952	0.715
61	94.93	4.582	2.376	0.825	0.909	4.203	0.632	9.986	0.657
62	95.03	4.583	2.393	0.814	0.909	4.748	0.702	11.359	0.704
63	94.89	4.487	2.395	0.810	0.886	4.956	0.728	11.867	0.722
64	99.91	4.901	2.424	0.772	0.952	3.406	0.484	8.255	0.529
65	99.91	4.983	2.455	0.783	0.957	4.620	0.630	11.340	0.638
66	99.89	4.977	2.467	0.784	0.950	5.198	0.693	12.823	0.684
67	99.89	4.916	2.516	0.788	0.919	5.504	0.723	13.849	0.707
68	99.89	4.837	2.647	0.784	0.862	5.416	0.726	14.339	0.707
69	99.89	4.930	2.464	0.777	0.962	4.629	0.640	11.409	0.644
70	99.89	4.968	2.473	0.779	0.964	5.419	0.721	13.401	0.702
71	99.88	4.839	2.597	0.792	0.900	5.480	0.732	14.232	0.714
72	89.84	3.729	2.020	0.789	0.830	4.021	0.658	8.121	0.664
73	89.89	3.723	2.022	0.788	0.830	4.375	0.707	8.848	0.701
74	89.88	3.681	2.022	0.772	0.821	4.581	0.737	9.263	0.716
75	89.92	3.774	2.032	0.791	0.837	3.686	0.608	7.491	0.628
76	89.92	3.778	2.022	0.797	0.843	2.840	0.468	5.742	0.527
77	84.86	3.107	1.730	0.741	0.787	3.069	0.549	5.311	0.569
78	84.87	3.094	1.732	0.738	0.785	3.849	0.682	6.667	0.668
79	90.03	3.741	1.962	0.756	0.856	3.894	0.618	7.641	0.624
80	89.98	3.719	1.953	0.749	0.853	4.571	0.710	8.930	0.689
81	90.05	3.600	1.931	0.714	0.836	4.781	0.739	9.234	0.697
82	90.04	3.599	1.944	0.716	0.832	4.756	0.737	9.248	0.696
83	94.98	4.470	2.330	0.773	0.891	4.297	0.640	10.011	0.645
84	95.02	4.450	2.321	0.769	0.890	4.907	0.712	11.390	0.694
85	94.94	4.420	2.306	0.769	0.889	4.893	0.711	11.281	0.693
86	94.94	4.324	2.321	0.742	0.865	5.083	0.738	11.797	0.701
87	100.00	4.918	2.404	0.762	0.963	5.389	0.699	12.956	0.679
88	99.89	4.836	2.515	0.751	0.908	5.524	0.726	13.893	0.694
89	99.96	4.900	2.437	0.766	0.950	5.555	0.717	13.536	0.694
90	100.03	4.851	2.450	0.791	0.928	5.072	0.683	12.429	0.680
91	99.93	4.854	2.484	0.792	0.919	5.312	0.711	13.194	0.700
92	99.96	4.860	2.541	0.801	0.898	5.418	0.722	13.766	0.712
93	99.90	4.775	2.653	0.807	0.848	5.364	0.723	14.231	0.714
94	94.99	4.466	2.373	0.817	0.868	4.361	0.663	10.346	0.677
95	94.99	4.396	2.360	0.832	0.859	4.837	0.715	11.414	0.721
96	94.98	4.317	2.380	0.829	0.836	4.914	0.723	11.695	0.724
97	89.83	3.722	2.027	0.794	0.825	4.086	0.678	8.281	0.681
98	89.80	3.729	2.037	0.800	0.822	4.400	0.721	8.962	0.715
99	89.75	3.644	2.018	0.790	0.809	4.544	0.739	9.172	0.724

TABLE 26. COMBINED COMPRESSOR DATA SETTINGS (FCV-II)

Reading No.	Stator IGV	Schedule		Plane B	Vaneless Bleed (%)		Test Run
		S1	*S2	Bleed (%)	FWD	AFT	
1	38	28		24.6	0	0	1
2	38	28		16.7	0	0	1
3	38	28		15.7	2.0	1.0	1
4	38	28		12.6	2.0	1.0	1
5	38	28		0	2.0	1.0	1
6	27	21		0	2.0	1.0	1
7	17	14		0	2.0	1.0	1
8	38	28		0	2.0	1.0	1
9	38	28		0	2.0	1.0	1
10	38	28		0	2.0	1.0	1
11	38	28		0	2.0	1.0	1
12	38	28		0	2.0	1.0	1
13	27	21		0	2.0	1.0	1
14	27	21		0	2.0	1.0	1
15	27	21		0	2.0	1.0	1
16	27	21		0	2.0	1.0	1
17	27	21		0	2.0	1.0	1
18	27	21		0	2.0	1.0	1
19	17	14		0	2.0	1.0	1
20	17	14		0	2.0	1.0	1
21	17	14		0	2.0	1.0	1
22	17	14		0	7.8	2.5	1
23	17	14		0	8.0	2.5	1
24	17	14		0	7.8	2.4	1
25	17	14		0	2.0	1.0	1
26	17	14		0	2.0	1.0	1
27	38	28		0	2.0	1.0	1
28	38	28		0	2.0	1.0	1
29	38	28		0	2.0	1.0	1
30	38	28		0	2.0	1.0	1
31	38	28		0	2.0	1.0	1
32	38	28		0	2.0	1.0	1
33	38	28		0	2.0	1.0	1
34	38	28		0	2.0	1.0	1
35	38	28		0	2.0	1.0	1
36	38	28		26.1	2.0	1.0	1
37	38	28		24.1	2.0	1.0	1
38	38	28		23.3	2.0	1.0	1
39	38	28		21.3	7.3	2.6	2
40	38	28		13.2	8.1	2.9	2
41	17	14		0	2.0	1.0	2
42	17	14		0	2.0	1.0	2

\*S2 = 0

TABLE 26. - Continued

Reading No.	Stator IGV	Schedule		Plane B Bleed (%)	Vaneless Bleed (%)		Test Run
		S1	*S2		FWD	AFT	
43	22	19		0	2.0	1.0	2
44	22	19		0	2.0	1.0	2
45	22	19		0	2.0	1.0	2
46	6	7		0	2.0	1.0	2
47	6	7		0	2.0	1.0	2
48	6	7		0	2.0	1.0	2
49	6	7		0	2.0	1.0	2
50	6	7		0	2.0	1.0	2
51	3	5		0	2.0	1.0	2
52	3	5		0	2.0	1.0	2
53	3	5		0	2.0	1.0	2
54	3	5		0	2.0	1.0	2
56	3	5		0	7.2	2.4	2
57	8	10		0	2.0	1.0	2
58	6	7		0	7.5	2.4	2
59	6	7		0	7.4	2.4	2
60	11	12		0	2.0	1.0	2
61	11	12		0	2.0	1.0	2
62	6	7		2.1	2.0	1.0	2
63	6	7		2.2	2.0	1.0	2
64	6	7		2.6	2.0	1.0	2
65	6	7		1.8	7.3	2.4	2
66	6	7		1.9	7.2	2.3	2
67	17	14		0	2.0	1.0	2
68	27	21		0	2.0	1.0	3
69	27	21		0	2.0	1.0	3
70	27	21		0	2.0	1.0	3
71	27	21		0	2.0	1.0	3
72	27	21		0	2.0	1.0	3
73	27	21		0	2.0	1.0	3
74	27	21		0	2.0	1.0	3
75	27	21		0	2.0	1.0	3
76	27	21		0	2.0	1.0	3
77	3	5		0	2.0	1.0	3
78	3	5		0	2.0	1.0	3
79	3	5		0	2.0	1.0	3
80	3	5		0	2.0	1.0	3
81	3	5		0	2.0	1.0	3
82	3	5		0	2.0	1.0	3
83	3	5		0	2.0	1.0	3
84	3	5		2.1	2.0	1.0	3

\*S2 = 0

TABLE 26. - Continued

Reading No.	Stator IGV	Schedule		Plane B Bleed (%)	Vaneless Bleed (%)		Test Run
		S1	*S2		FWD	AFT	
85	3	5		2.1	2.0	1.0	3
86	3	5		2.0	2.0	1.0	3
87	22	19		0	2.0	1.0	3
88	22	19		0	2.0	1.0	4
89	3	5		0	2.0	1.0	4
90	3	5		0	2.0	1.0	4
91	3	5		0	2.0	1.0	4
92	3	5		0	2.0	1.0	4
93	3	5		0	2.0	1.0	4
94	3	5		0	2.0	1.0	4
95	6	7		0	6.5	2.4	4
96	6	7		0	6.5	2.4	4
97	6	7		0	6.5	2.4	4
98	6	7		0	6.5	2.4	4
99	6	7		0	6.5	2.4	4
100	6	7		0	6.5	2.4	4
101	6	7		0	6.5	2.4	4
102	6	7		0	6.5	2.4	4
103	6	7		5.6	2.0	1.0	4
104	6	7		5.5	2.0	1.0	4
105	27	21		0	2.0	1.0	5
106	27	21		0	2.0	1.0	5
107	27	21		0	2.0	1.0	5
108	27	21		0	2.0	1.0	5
109	27	21		0	2.0	1.0	5
110	27	21		0	8.3	2.5	5
111	27	21		2.0	8.1	2.4	5
112	27	21		0	3.5	2.6	5
113	6	7		0	2.0	1.0	5
114	6	7		0	2.0	1.0	5
115	6	7		0	2.0	1.0	5
116	6	7		0	2.0	1.0	5
117	6	7		0	2.0	1.0	5
118	6	7		0	7.9	2.4	5
119	6	7		0	3.9	2.5	5
120	6	7		0	2.1	1.6	5
121	3	5		0	2.0	1.0	5
122	3	5		0	2.0	1.0	5
123	3	5		0	2.0	1.0	5
124	3	5		0	2.0	1.0	5
125	3	5		0	2.0	1.0	5
126	3	5		0	2.0	1.0	5

\*S2 = 0

TABLE 26. - Continued

Reading No.	Stator IGV	Schedule		Plane B	Vaneless Bleed (%)		Test Run
		S1	*S2	Bleed (%)	FWD	AFT	
127	3	5		0	2.0	1.0	5
128	3	5		0	7.6	2.3	5
129	22	19		0	2.0	1.0	5
130	22	19		0	2.0	1.0	5
131	27	21		0	2.0	1.0	6
132	27	21		0	2.0	1.0	6
133	27	21		0	8.2	2.5	6
134	27	21		2.3	8.0	2.5	6
135	6	7		0	3.7	2.6	6
136	6	7		0	8.3	2.6	6
137	6	7		0	7.9	2.5	6
138	6	7		0	3.9	2.6	6
139	6	7		0	3.9	2.6	6
140	6	7		0	2.0	1.7	6
141	3	5		0	2.0	1.0	6
142	3	5		0	7.6	2.4	6
143	3	5		0	5.7	2.4	6
144	3	5		0	3.3	2.5	6
145	0	0		0	3.3	2.5	6
146	0	0		0	7.6	2.4	6
147	17	14		0	8.1	2.4	6
148	17	14		0	2.0	1.0	6
149	17	14		0	5.2	0.6	6
150	17	14		2.5	5.1	0.3	6
151	27	21		0	3.8	0.4	6
152	3	5		0	2.0	1.0	6
153	3	5		0	2.0	1.0	6
154	3	5		0	2.0	1.0	6
155	6	7		0	2.0	1.0	6
156	6	7		0	2.0	1.0	6
157	6	7		0	2.0	1.0	6
158	6	7		0	2.0	1.0	6

\*S2 = 0

TABLE 27. COMBINED COMPRESSOR TEST RESULTS FCV-II

Reading No.	Axial Stage				Centrifugal Stage				Overall	
	Corrected Speed (%)	Corrected Airflow (lb/sec)	Pressure Ratio ( $P_B/P_A$ )	Adiabatic Efficiency ( $\eta_{B-A}$ )	Corrected Airflow (W/2.34)	Pressure Ratio ( $P_T/P_B$ )	Adiabatic Efficiency ( $\eta_{B-A}$ )	Pressure Ratio ( $P_E/P_A$ )	Adiabatic Efficiency ( $\eta_{E-A}$ )	
1	50.083	1.454						1.3071	.221	
2	70.015	2.202						2.4422	.414	
3	69.964	2.284						2.4703	.425	
4	79.874	2.627						3.1054	.428	
5	79.861	2.486						3.4044	.449	
6	84.844	3.043	1.663	.7332	.8612	2.626	.4355	4.3491	.478	
7	89.859	3.723	1.946	.7815	.9203	2.833	.4449	5.4780	.502	
8	79.813	2.470						4.6490	.587	
9	79.945	2.467						5.0666	.627	
10	79.887	2.364						5.6609	.675	
11	79.846	2.412						5.6306	.676	
12	79.871	2.447						5.4731	.665	
13	84.786	3.015	1.652	.7420	.8828	3.472	.5863	5.7383	.576	
14	84.805	3.050	1.652	.7382	.8675	3.502	.5909	5.7898	.598	
15	84.848	3.026	1.659	.7284	.8587	4.335	.7126	7.1797	.689	
16	84.853	3.025	1.652	.7300	.8613	4.180	.6878	6.8933	.671	
17	84.858	3.037	1.649	.7312	.8658	3.941	.6545	6.4920	.645	
18	84.861	3.003	1.642	.7291	.8591	3.771	.6298	6.1802	.676	
19	89.705	3.705	1.938	.7751	.9197	3.841	.6026	7.4331	.618	
20	89.786	3.658	1.934	.7751	.9099	4.682	.7122	7.0373	.700	
21	89.738	3.641	1.924	.7743	.9074	4.423	.6805	8.5065	.676	
22	89.733	3.942	1.834	.8302	1.0174	4.610	.6873	8.4358	.698	
23	89.719	3.917	1.861	.8235	.9996	4.598	.7341	9.2045	.733	
24	89.719	3.935	1.844	.7111	1.0262	4.785	.7640	8.8034	.717	
25	89.753	3.692	1.927	.7745	.9209	4.372	.6779	8.4278	.674	
26	89.785	3.702	1.928	.7743	.9237	3.298	.5300	6.3478	.564	
27	69.881	2.252						3.3420	.599	
28	69.917	2.144						4.1453	.718	
29	69.939	2.242						3.9864	.701	
30	69.884	1.914						3.3443	.571	
31	69.851	1.888						4.1178	.688	
32	69.829	1.894						4.0075	.670	
33	67.826	1.923						2.6392	.447	
34	69.820	1.927						2.4106	.402	
35	49.886	1.515						1.3158	.234	
36	47.868	1.348						2.253	.714	

TABLE 27. - Continued

Reading No.	Axial Stage			Centrifugal Stage			Overall		
	Corrected Speed (%)	Corrected Airflow (lb/sec)	Pressure Ratio ( $P_B/P_A$ )	Adiabatic Efficiency ( $\eta_{B-A}$ )	Corrected Airflow ( $W/2.34$ )	Pressure Ratio ( $P_E/P_B$ )	Adiabatic Efficiency ( $\eta_{B-A}$ )	Pressure Ratio ( $P_E/P_A$ )	Overall Adiabatic Efficiency ( $\eta_{E-A}$ )
37	49.934	1.444						2.250	.723
38	49.935	1.507						1.906	.567
39	49.937	1.636						1.418	.304
40	49.911	1.497						1.444	.314
41	89.947	3.648	1.929	.6982	.9200	4.428	.7165	8.531	.675
42	89.592	3.603	1.927	.6990	.9094	4.705	.7496	9.050	.699
43	89.810	3.489	1.790	.7304	.9308	3.773	.5916	6.751	.595
44	89.851	3.464	1.802	.7223	.9201	4.817	.7309	8.667	.697
45	89.831	3.478	1.804	.7251	.9225	4.694	.7154	8.459	.686
46	94.897	4.472	2.285	.8072	.9649	3.159	.4765	7.207	.536
47	94.825	4.483	2.288	.8154	.9649	3.985	.5898	9.131	.623
48	94.825	4.265	2.277	.7821	.9263	5.052	.7205	11.474	.705
49	94.829	4.388	2.279	.7952	.9503	4.942	.7087	11.230	.702
50	94.829	4.398	2.282	.8028	.9504	4.554	.6610	10.362	.670
51	99.831	4.950	2.368	.7979	1.0384	3.854	.5237	9.198	.564
52	99.781	4.950	2.380	.7845	1.0300	4.639	.6217	10.996	.632
53	99.831	4.864	2.475	.7828	.9862	5.484	.7173	13.538	.701
54	99.868	4.883	2.401	.7731	1.0169	5.440	.7091	13.014	.692
55	99.760	4.901	2.397	.7813	1.0205	4.998	.6618	11.935	.660
56	99.785	4.969	2.130	.7952	1.1383	5.792	.6918	12.307	.686
57	99.810	4.684	2.240	.7639	1.0344	5.535	.7078	12.351	.688
58	74.762	4.651	2.155	.8028	1.0542	5.242	.7343	11.270	.723
59	94.773	4.672	2.132	.8041	1.0633	5.072	.7126	10.779	.708
60	44.818	4.123	2.132	.7500	.7483	5.172	.7358	11.023	.705
61	94.829	4.207	2.132	.7657	.9759	4.998	.7416	10.634	.695
62	94.791	4.460	2.256	.7822	.9560	4.879	.7131	10.981	.700
63	94.826	4.446	2.266	.7797	.9484	5.069	.7320	11.449	.713
64	94.815	4.268	2.273	.7641	.9074	5.096	.7347	11.529	.709
65	94.785	4.670	2.084	.8990	1.0757	5.354	.6951	11.119	.722
66	94.813	4.687	2.056	.7573	1.0910	5.204	.7315	10.668	.706
67	87.818	3.605	1.928	.6359	.9175	4.579	.7782	8.823	.699
68	84.906	3.030						7.066	.687
69	84.884	3.052						6.860	.675
70	84.821	3.038						7.031	.690
71	84.856	3.031						7.075	.691
72	84.866	3.025						7.088	.671

TABLE 27. - Continued

Reading No.	Axial Stage				Centrifugal Stage				Overall	
	Corrected Speed (Z)	Corrected Airflow (lb/sec)	Pressure Ratio (P <sub>B</sub> /P <sub>A</sub> )	Adiabatic Efficiency (η <sub>B-A</sub> )	Corrected Airflow (W/2.34)	Pressure Ratio (P <sub>E</sub> /P <sub>B</sub> )	Adiabatic Efficiency (η <sub>B-A</sub> )	Pressure Ratio (P <sub>E</sub> /P <sub>A</sub> )	Adiabatic Efficiency (η <sub>E-A</sub> )	
73	84.856	3.006						7.088	.692	
74	84.874	3.029						7.079	.693	
75	84.853	3.026						7.103	.694	
76	84.843	3.025						7.122	.694	
77	99.709	4.915	2.4442	.7849	1.0063	5.4998	.7233	13.401	.707	
78	99.429	4.906						13.132	.703	
79	99.356	4.916	2.4382	.7848	1.0141	5.3883	.7190	13.095	.704	
80	99.709	4.913						13.151	.701	
81	99.659	4.900						13.142	.702	
82	99.641	4.913						13.154	.701	
83	99.611	4.895	2.4359	.7838	1.0052	5.4029	.7173	13.112	.702	
84	99.719	4.935	2.3514	.7669	1.0475	5.4962	.7220	12.875	.609	
85	99.719	4.941	2.3381	.7628	1.0535	5.3292	.7040	12.418	.684	
86	99.724	4.948	2.3313	.7603	1.0580	5.0329	.6766	11.700	.664	
87	89.737	3.518	1.8451	.7238	.9163	4.3469	.7035	8.016	.677	
88	89.805	3.522	1.8401	.7196	.9200	3.8621	.6359	7.098	.626	
89	99.748	4.511						13.188	.701	
90	99.748	4.887						13.225	.703	
91	99.664	4.905	2.4138	.7694	1.0174	5.4419	.7241	13.094	.701	
92	99.602	4.916	2.4271	.7750	1.0142	5.4471	.7244	13.177	.704	
93	99.682	4.917	2.4222	.7735	1.0163	5.3999	.7146	13.038	.696	
94	97.634	4.898	2.4183	.7725	1.0140	5.4259	.7196	13.075	.699	
95	94.722	4.633	2.1730	.7882	1.0543	5.1339	.7720	11.124	.724	
96	94.780	4.636	2.1757	.7908	1.0452	5.1624	.7453	11.205	.725	
97	94.859	4.640						11.246	.726	
98	94.929	4.655	2.1780	.7911	1.0476	5.1938	.7443	11.280	.727	
99	94.945	4.655						11.241	.724	
100	94.998	4.656						11.260	.724	
101	95.003	4.654						11.274	.723	
102	94.787	4.654	2.1793	.7959	1.0461	5.1811	.7384	11.264	.724	
103	94.940	4.610	2.2024	.7973	1.0361	5.0621	.7513	11.107	.713	
104	94.917	4.600	2.1993	.7938	1.0265	5.0600	.7245	11.087	.713	
105	85.084	2.982	1.678	.6993	.8415	4.304	.7341	7.216	.695	
106	84.977	2.967	1.666	.7079	.8414	4.318	.7315	7.186	.696	
107	84.945	2.972	1.678	.7144	.8372	4.321	.7326	7.238	.699	
108	84.914	2.971	1.670	.7116	.8406	4.315	.7338	7.200	.699	

TABLE 27. - Continued

Reading No.	Axial Stage			Centrifugal Stage			Overall		
	Corrected Speed (%)	Corrected Airflow (lb/sec)	Pressure Ratio ( $P_B/P_A$ )	Adiabatic Efficiency ( $\eta_{B-A}$ )	Corrected Airflow (W/2.34)	Pressure Ratio ( $P_E/P_B$ )	Adiabatic Efficiency ( $\eta_{B-A}$ )	Pressure Ratio ( $P_E/P_A$ )	Adiabatic Efficiency ( $\eta_{E-A}$ )
109	84.959	2.994	1.676	.7144	.8442	4.309	.7329	7.221	.699
110	84.985	3.240	1.570	.7250	.9619	4.471	.7406	7.009	.712
111	84.990	3.274	1.527	.7121	.9960	4.553	.7453	6.941	.713
112	84.977	3.128	1.664	.7432	.8841	4.308	.7245	7.152	.703
113	94.889	4.357	2.318	.7834	.9322	5.000	.7264	11.505	.710
114	94.869	4.346	2.305	.7787	.9348	4.961	.7249	11.407	.708
115	94.811	4.362	2.313	.7825	.9351	4.971	.7258	11.472	.710
116	94.856	4.358	2.317	.7839	.9329	4.991	.7273	11.536	.711
117	94.866	4.365	2.311	.7857	.9362	5.001	.7284	11.531	.713
118	94.790	4.660	2.135	.8029	1.0646	5.211	.7327	11.095	.723
119	94.834	4.584	2.279	.8154	.9898	4.835	.7060	11.059	.708
120	94.866	4.394	2.305	.7850	.9444	5.055	.7342	11.615	.717
121	99.745	4.886	2.439	.7860	1.0020	5.428	.7138	13.208	.700
122	99.758	4.889	2.445	.7897	.9999	5.435	.7142	13.245	.702
123	99.818	4.884	2.442	.7861	1.0005	5.446	.7156	13.266	.701
124	99.854	4.914	2.452	.7878	1.0032	5.441	.7150	13.313	.702
125	49.916	4.860	2.441	.7840	.9964	5.479	.7167	13.318	.701
126	99.823	4.878	2.426	.7849	1.0050	5.334	.7036	12.892	.692
127	99.877	4.898	2.413	.7863	1.0141	5.001	.6681	12.029	.666
128	99.937	4.941	2.167	.7462	1.1247	5.126	.6606	11.074	.654
129	89.666	3.466	1.840	.7464	.9021	4.628	.7275	8.504	.702
130	89.753	3.462	1.840	.7445	.9012	4.518	.7130	8.302	.691
131	84.916	3.043	1.716	.7392	.8388	4.279	.7268	7.332	.703
132	84.757	3.031	1.703	.7391	.8407	4.242	.7216	7.211	.699
133	84.791	3.243	1.576	.7349	1.0055	4.499	.7415	7.073	.716
134	84.747	3.284	1.548	.7177	.9866	4.528	.7451	7.003	.714
135	84.730	3.135	1.674	.7574	.8801	4.332	.7288	7.241	.711
136	94.980	4.373	2.323	.7733	.9355	5.020	.7387	11.632	.715
137	94.945	4.631	2.136	.7977	1.0581	5.218	.7375	11.115	.724
138	94.813	4.533	2.269	.7085	.9850	5.023	.7283	11.357	.717
139	94.836	4.531	2.264	.8091	.9846	5.040	.7247	11.376	.719
140	94.825	4.407	2.292	.7829	.9518	4.995	.7302	11.409	.713
141	97.858	4.864	2.448	.7760	.9962	5.267	.7025	12.851	.688
142	99.869	4.932	2.168	.7324	1.1247	5.499	.7025	11.885	.677
143	99.907	4.910	2.212	.7400	1.0920	5.497	.6878	13.115	.680
144	99.930	4.912	2.299	.7521	1.0640	5.449	.7098	12.478	.685

TABLE 27. - Continued

Reading No.	Axial Stage				Centrifugal Stage				Overall	
	Corrected Speed (%)	Corrected Airflow (lb/sec)	Pressure Ratio ( $P_B/P_A$ )	Adiabatic Efficiency ( $\eta_{B-A}$ )	Corrected Airflow (W/2.34)	Pressure Ratio ( $P_E/P_B$ )	Adiabatic Efficiency ( $\eta_{B-A}$ )	Pressure Ratio ( $P_E/P_A$ )	Adiabatic Efficiency ( $\eta_{E-A}$ )	
145	99.858	4.988	2.411	.7420	1.0408	5.303	.7146	12.727	.683	
146	99.815	5.010	2.256	.7158	1.1093	5.442	.7226	12.240	.680	
147	89.949	3.920	1.871	.8138	.8976	4.733	.7211	8.837	.719	
148	89.901	3.659	1.985	.7790	.8905	4.587	.7190	9.095	.706	
149	89.906	3.763	1.920	.7875	.9402	4.719	.7317	9.053	.719	
150	89.939	3.837	1.895	.7909	.9692	4.742	.7273	8.963	.717	
151	84.924	3.121	1.680	.7549	.8741	4.324	.7408	7.252	.719	

LIST OF SYMBOLS

A	area, in. <sup>2</sup>
ACV	axial component vehicle
CCV	centrifugal component vehicle
C <sub>l/L</sub>	clearance-to-blade height ratio
C	chord - in.
C <sub>D</sub>	bellmouth flow coefficient
C <sub>p</sub>	static pressure recovery or specific heat at constant pressure, Btu/lb - °R
C <sub>θ</sub>	absolute angular velocity, ft/sec
FCV	combined or full vehicle
g <sub>o</sub>	gravitational constant 32.174, lb-ft/lb-sec <sup>2</sup>
h	blade height, in.
ICB	intercompressor bleed at Plane B
J	Joule's constant, 778.16 ft-lb <sub>f</sub> /Btu
LE	leading edge
M	Mach number
N <sub>c</sub>	corrected speed, rpm
N <sub>CENT</sub>	centrifugal compressor speed, rpm
N <sub>g</sub>	measured compressor speed, rpm
P	total pressure, lb/in. <sup>2</sup>
P <sub>P</sub>	mass-averaged total pressure, lb/in. <sup>2</sup>
p	static pressure, lb/in. <sup>2</sup>
Q̄	mass-averaged velocity head (P - p), lb/in. <sup>2</sup>

$q_i$	velocity head ( $1/2 \rho V^2$ ), lb/in <sup>2</sup>
R	rotor
r	radius, in.
S	stator
s	enthropy, Btu/lb - °R
T	total temperature, °R
t	static temperature, °R
TE	trailing edge
U	wheel speed, ft/sec
V	velocity, ft/sec
$V_u$	tangential velocity, ft/sec
$V_z$	axial velocity, ft/sec
W	airflow, lb/sec
$W_c$	corrected airflow, lb/sec
$\alpha$	absolute flow angle from axial, deg
$\bar{\alpha}$	absolute mass-averaged flow angle from axial, deg
$\beta$	relative flow angle from axial, deg
$\gamma$	specific heat ratio
$\delta$	P/14.696
$\Delta\bar{P}$	mass-averaged pressure differential, lb/in. <sup>2</sup>
$\eta$	efficiency
$\eta_{ad}$	adiabatic efficiency
$\theta$	T/518.7

$\lambda$	blockage factor
$\sigma$	slip factor, solidity, or stress
$\phi_n$	normalized flow coefficient
$\psi_n$	normalized pressure coefficient
$\psi_n$	normalized work coefficient
$\omega_d$	total pressure loss coefficient
$\rho$	density, lb/ft <sup>3</sup>

#### SUBSCRIPTS

A	axial compressor inlet (see Figure 21)
B	axial compressor exit (see Figure 21)
C	centrifugal impeller inlet (see Figure 21)
D	centrifugal impeller exit (see Figure 21)
E	centrifugal diffuser exit (see Figure 21)
F	discharge plenum (see Figure 21)
	inlet
2	outlet